



# THE UNIVERSITY *of*ADELAIDE

The transport of high energy cosmic rays in a TeV  
gamma ray Pulsar Wind Nebula

Tiffany Collins  
Faculty of Sciences  
School of Physical Sciences  
University of Adelaide

July 19, 2023

supervised by  
A. Prof. Gavin Rowell and Dr. Sabrina Einecke



# Contents

<b>Abstract</b>	<b>i</b>
<b>Declaration of Originality</b>	<b>ii</b>
<b>Acknowledgements</b>	<b>iii</b>
<b>1 Introduction</b>	<b>1</b>
<b>2 Pulsar Wind Nebulae</b>	<b>4</b>
2.1 Pulsar Wind Nebulae . . . . .	4
2.1.1 Neutron Stars/ Pulsars . . . . .	4
2.1.2 Time Evolution of Pulsar Wind Nebulae . . . . .	8
2.1.3 TeV Pulsar Wind Nebula . . . . .	12
2.1.4 Mysteries of Pulsar Wind Nebulae . . . . .	13
2.1.5 HESS J1825-137 and HESS J1826-130 . . . . .	14
2.2 Cosmic Rays . . . . .	18
2.2.1 Acceleration of Charged Particles . . . . .	19
2.2.2 Propagation of charged particles . . . . .	21
2.2.3 Cosmic Ray Spectrum . . . . .	24
2.2.4 PeVatrons . . . . .	24
2.3 Gamma-rays: messengers of cosmic rays . . . . .	26
2.3.1 A brief history . . . . .	26
2.3.2 Hadronic Gamma-Ray Emission . . . . .	26
2.3.3 Leptonic Gamma-Ray emission . . . . .	29
<b>3 Gamma Ray Astronomy</b>	<b>37</b>
3.1 Air Showers . . . . .	37
3.1.1 Gamma-ray Air Showers . . . . .	38
3.1.2 Cosmic-ray Air Showers . . . . .	40
3.1.3 Cherenkov Light and Cherenkov Telescopes . . . . .	42
3.2 TeV Gamma-ray Observatories . . . . .	44
3.2.1 The High Energy Stereoscopic System . . . . .	45
3.2.2 <i>Fermi</i> -LAT . . . . .	46
3.2.3 LHAASO . . . . .	47
3.2.4 HAWC . . . . .	48
3.2.5 The Cherenkov Telescope Array . . . . .	48
<b>4 ISM towards HESS J1825-137 and HESS J1826-130</b>	<b>50</b>
4.1 Detecting the interstellar medium . . . . .	51
4.1.1 Specific Intensity, Specific Flux and Bolometric flux . . . . .	51
4.1.2 Radiative Transfer . . . . .	52
4.1.3 Black Bodies . . . . .	53
4.1.4 Spectral Line Excitation and Emission . . . . .	54
4.2 Probing the interstellar medium . . . . .	55
4.2.1 Molecular Tracers . . . . .	55
4.2.2 Doppler Shift . . . . .	56
4.2.3 Galactic Rotation Curve . . . . .	57
4.2.4 Magnetic fields in molecular clouds . . . . .	59
4.2.5 H $\alpha$ emission . . . . .	59
4.2.6 Nanten2 Observatory . . . . .	61

<b>5 Time evolution of CR particles</b>	<b>63</b>
5.1 Radiation losses . . . . .	63
5.1.1 Impulsive source of cosmic rays . . . . .	65
5.1.2 Continuous source of cosmic rays . . . . .	68
5.2 Transport of Cosmic Rays . . . . .	72
5.2.1 Propagation of Cosmic Rays . . . . .	72
5.3 Modelling the energy density distribution of cosmic rays . . . . .	78
5.3.1 <code>Newsedprod</code> . . . . .	78
5.3.2 Including particle escape in <code>Newsedprod</code> . . . . .	82
5.3.3 Investigation of magnetic field turbulence regimes . . . . .	84
5.3.4 Applications of <code>Newsedprod</code> . . . . .	84
<b>6 Explaining the extended GeV gamma-ray emission adjacent to HESS J1825-137</b>	<b>88</b>
<b>7 Modelling the 3D environment around Pulsar Wind Nebulae</b>	<b>105</b>
7.1 The Transport Equation . . . . .	105
7.1.1 Particle Transport literature review . . . . .	106
7.1.2 Numerical Solution of the Transport Equation . . . . .	107
7.1.3 <code>Multizone</code> . . . . .	108
7.1.4 Analytical Solution: Diffusion-only . . . . .	110
7.1.5 Diffusion and Radiative Energy Losses: Analytical and Numerical Solution Comparison . . . . .	112
7.2 Advection . . . . .	114
7.2.1 Numerical Solution . . . . .	116
7.2.2 Analytical Solution . . . . .	116
7.3 Summary and Application . . . . .	120
<b>8 A 3D Diffusive and Advective Model of Electron Transport Applied to the Pulsar Wind Nebula HESS J1825-137</b>	<b>122</b>
<b>9 Conclusion and Future Work</b>	<b>146</b>
<b>A Supernova Remnants</b>	<b>149</b>
A.1 The supernova . . . . .	149
A.2 Stages of a Supernova Remnant . . . . .	150
A.2.1 Free Expansion Phase . . . . .	150
A.2.2 Sedov-Taylor Phase . . . . .	150
A.2.3 Snow-Plough Phase . . . . .	151
<b>B Diffusive Shock Acceleration</b>	<b>152</b>
B.1 Fermi's Original Theory . . . . .	152
B.2 Diffusive Shock Acceleration . . . . .	153
<b>C Finite Difference Techniques applied to the Transport Equation</b>	<b>157</b>
C.1 Diffusion . . . . .	157
C.1.1 Stability of the Finite Difference . . . . .	158
C.2 Advection . . . . .	160

<b>D Variance of diffusion in <math>n</math> dimensions</b>	<b>162</b>
D.1 1D Diffusion . . . . .	162
D.2 2D Diffusion . . . . .	163
D.3 3D Diffusion . . . . .	163
<b>E Spectral Energy Distribution towards Cl* 1806-20</b>	<b>165</b>
<b>F Miscellaneous Tables</b>	<b>166</b>

# Abstract

Pulsars are dense, rapidly spinning remnants of massive stars. Charged particles are stripped off the surface of the pulsar by extreme magnetic fields and are accelerated beyond TeV energies, forming the powerful winds known as pulsar wind nebulae (PWNe). These particles, known as cosmic rays, escape into the interstellar medium (ISM) and interact with soft photon fields to produce gamma rays or with magnetic fields to produce radio to X-ray emission. One of the major mysteries in modern-day astrophysics is how cosmic rays escape from PWN environments.

HESS J1825-137 is a bright, extended TeV PWN, making it an ideal laboratory to study cosmic-ray transport in PWN. Both the HAWC and LHAASO observatories have observed gamma-ray emission from HESS J1825-137 greater than 50 TeV, indicative of a PeVatron; a source capable of accelerating cosmic rays up to energies greater than  $10^{15}$  eV. This thesis focuses on understanding the origin of the X-ray to gamma-ray emission towards HESS J1825-137.

*Fermi*-LAT observations revealed extended GeV emission to the Galactic south of HESS J1825-137. The first portion of this thesis investigated whether this GeV emission originated from the PWN associated with HESS J1825-137, the progenitor supernova remnant (SNR) or a source linked to the nearby object LS 5039. ISM gas analysis was first conducted towards this region in order to constrain the multi-wavelength emission. The analysis highlighted a dense cloud of CO(1-0) gas lying towards the GeV region at the same distance as LS 5039 that is coincident with the H $\alpha$  SNR rim associated with HESS J1825-137. The results of the gas analysis was combined with spectral energy distribution (SED) modelling to show that neither a source associated with HESS J1825-137 or LS 5039 is likely to be the sole origin of high-energy cosmic rays towards the GeV region. A combination of both sources could result in the gamma-ray emission. This study emphasised the complexity of the region towards HESS J1825-137.

The second part of this thesis investigated the multi-wavelength SED and gamma-ray morphology towards HESS J1825-137 to disentangle the transport mechanisms of electrons from the pulsar. Electrons escaping the PWN experience diffusion (where particles scatter off turbulence, resulting in 'random-walk') and/or advection (the bulk motion of particles). The region towards HESS J1825-137 was divided into a 3D grid of ISM gas and magnetic fields based on ISM observations. The transport of electrons from the pulsar was then modelled to reproduce the multi-wavelength SED and gamma-ray morphology seen towards HESS J1825-137. A diffusive model with an advective velocity of  $0.002c$  ( $c$  is the speed of light) towards lower Galactic longitudes could explain observations. Additionally, a turbulent region of gas with a magnetic field between  $20 - 60 \mu\text{G}$  is required to prevent significant gamma-ray contamination towards nearby northern TeV source, HESS J1826-136.

The modelling conducted in this thesis is not constrained to HESS J1825-137 and can be applied to other TeV PWN or other gamma-ray sources to develop understanding of how cosmic-ray sources evolve in their respective environments.

# **Declaration of Originality**

I certify that this work contains no material which has been accepted for the award of any other degree or diploma in my name, in any university or other tertiary institution and, to the best of my knowledge and belief, contains no material previously published or written by another person, except where due reference has been made in the text. In addition, I certify that no part of this work will, in the future, be used in a submission in my name, for any other degree or diploma in any university or other tertiary institution without the prior approval of the University of Adelaide and where applicable, any partner institution responsible for the joint-award of this degree.

I acknowledge that copyright of published works contained within this thesis resides with the copyright holder(s) of those works.

I also give permission for the digital version of my thesis to be made available on the web, via the University's digital research repository, the Library Search and also through web search engines, unless permission has been granted by the University to restrict access for a period of time.

I acknowledge the support I have received for my research through the provision of an Australian Government Research Training Program Scholarship.

Tiffany Collins

---

Signature

---

Date

## **Acknowledgements**

This is the acknowledgement section.

# Chapter 1

## Introduction

The Aurora Borealis (aka the Northern lights) have fascinated humans as far back as the Stone Ages and have been integrated into the mythology of many cultures (see Eather, (1980) and references within). These lights (and the Southern lights) are the result of charged particles emitted by solar flares that are channelled by the Earth’s magnetic field to the poles. When they collide with the Earth’s atmosphere, they excite oxygen and nitrogen atoms that then decay back into their ground state to produce dazzling green and red light. Charged particles from the sun have energies up to  $10^{10}$  eV and are only the tip of the iceberg (Longair, 2011).

The Earth’s atmosphere is constantly bombarded by charged particles known as cosmic rays (CRs) that can have energies up to  $10^{20}$  eV (Stanev, 2010). These cosmic rays originate from outside the solar system from Galactic sources such as pulsar wind nebulae (PWNe), supernova remnants (SNRs) and stellar clusters or extra-Galactic sources like Galaxy clusters and active Galactic nuclei.

Cosmic rays must then traverse through extreme environments in the Milky Way to reach Earth. On their journey, cosmic rays interact with magnetic fields or collide with gas and the cosmic microwave background to release electromagnetic energy from X-rays to gamma rays. Gamma rays convey information about their cosmic-ray predecessors such as where cosmic rays are accelerated, their energy and how they propagate from their source. Essentially, gamma rays are a highly accessible tracer or ‘smoking gun’ of cosmic rays!

While our ancestors used the naked eye to observe celestial bodies, modern day astronomers have access to instruments that can observe the highest energy gamma rays. The cutting-edge High Energy Stereoscopic System (H.E.S.S.) is one such observatory that has the capability of observing gamma-rays with energies up to 100 TeV (*HESS*). In 2018, the H.E.S.S. collaboration released their second Galactic plane survey which consisted of 78 TeV gamma-ray sources (H.E.S.S. Collaboration et al., 2018a). Of these sources, 20 are confirmed TeV pulsar wind nebulae and a further 36 are possible PWNe candidates. This makes pulsar wind nebulae the most numerous class of the Galactic TeV gamma-ray sources.

Supernovae occur when a massive star core collapses or when a white dwarf ‘re-ignites’ and triggers runaway nuclear fusion. The supernova as well as gravitational collapse can compress the core of massive stars past the density of a white dwarf to the nuclear saturation density. This compact object, known as a neutron star, emits two beams of electromagnetic radiation from its magnetic poles. This can be observed as a series of pulses when the direction of the beam points towards Earth and the neutron star is

classified as a pulsar. The high magnetic fields of the pulsar can strip cosmic rays from its surface to form powerful winds known as pulsar wind nebula. PWNe has been observed across the electromagnetic spectrum, from low frequency radio waves (Hewish et al., 1968) up to high-energy PeV gamma-rays (The LHAASO Collaboration et al., 2021).

Cosmic rays escaping the PWN experience diffusion (where cosmic rays scatter off magnetic fields and ISM gas and its overall motion is described by a random walk) and/or advection (an overall bulk motion of cosmic rays in a certain direction). It has been proposed that advection dominates particle transport close to the pulsar while diffusion dominates the outer reaches of the PWN (Giacinti et al., 2020; Recchia et al., 2021). Additionally, cosmic rays interact with their environment to radiate photons at a rate related to their energy. The combination of diffusion, advection and radiative processes will influence the morphology and spectral information of the PWN.

This thesis will model the multi-wavelength emission towards the TeV PWN HESS J1825-137 by combining cosmic ray transport theory and observations from state-of-the-art instruments. HESS J1825-137 is one of the brightest TeV PWN with extended GeV emission  $\approx 2.5^\circ$  to the south (Araya et al., 2019). This makes HESS J1825-137 an ideal laboratory to study the relativistic transportation of cosmic rays towards PWN. By modelling the emission towards HESS J1825-137, insight into the cosmic ray transportation will be gained.

The thesis will be structured as following: Chapter 2 will provide an overview in TeV Pulsar Wind Nebulae, cosmic rays and the processes in which cosmic rays convert their energy into gamma rays. Chapter 3 describes some of the instruments whose data products were used in this thesis and their observational techniques. Chapter 4 discusses interstellar gas, its implications in this thesis and how the gas can be detected. Chapter 5 will delve deeper into cosmic ray propagation how their energy distribution evolves in time for a simple region of interstellar gas. The techniques discussed in Chapter 5 will be applied to the GeV gamma-ray emission to south of HESS J1825-137 in order to gain insight into underlying particle acceleration and transportation of this region. This original work was published in the peer reviewed journal Monthly Notices of the Royal Astronomical Society (MNRAS) and can be viewed in Chapter 6. Chapter 7 will expand on the cosmic ray propagation theory discussed in Chapter 5 by modelling the transport of CRs in complex regions of ISM with varying magnetic fields, gas distribution and diffusion rates. Chapter 8 applies this model to HESS J1825-137 in order to explain the extended multi-wavelength emission towards HESS J1825-137 and to constrain the gamma-ray contamination of nearby unidentified TeV object HESS J1826-130 by HESS J1825-137. Chapter 9 will summarise the work conducted in this thesis and discuss any future work.

## Acronyms and Abbreviations

**Bremsstrahlung:** brem

**CMB:** cosmic microwave background

**CTA:** Cherenkov Telescope Array

**FIR:** far-infrared

**Fermi-LAT:** *Fermi* Large Area Telescope

**GC:** Galactic centre

**HAWC:** High Altitude Water Cherenkov Experiment

**H.E.S.S.**: High Energy Stereoscopic System

**HGPS**: HESS Galactic Plane Survey

**IC**: inverse Compton

**IR**: infrared

**ISM**: interstellar medium

**LSR**: local standard of rest

**LHAASO**: Large High Altitude Air Shower Observatory

**NIR**: near-infrared

**p-p**: proton-proton

**PWN**: pulsar wind nebula

**SED**: Spectral Energy Distribution

**SNR**: supernova remnant

**sync**: synchrotron

**UV**: Ultra Violet

**VHE**: Very High Energy

# Chapter 2

## Pulsar Wind Nebulae

The last couple of centuries have seen astronomy being turned from a navigators map into a diverse field full of extremes. High-energy astrophysics is one of these extremes and investigates cosmic-rays and gamma-ray released by the most energetic events in the Universe. One source of cosmic rays are PWNe, which can be seen across the electromagnetic spectrum from radio waves up to gamma rays. The linking of fundamental physics to gamma-ray observations can provide a window into the understanding of PWNe. This chapter is divided as follows: Section 2.1 discusses the structure and evolution of PWN before highlighting the TeV PWN HESS J1825-137 and nearby northern source HESS J1826-130. Cosmic rays are then investigated in further detail in Section 2.2 before describing the pathways of gamma ray production by cosmic rays in Section 2.3.

### 2.1 Pulsar Wind Nebulae

#### 2.1.1 Neutron Stars/ Pulsars

In 1967 Jocelyn Bell and Antony Hewish observed a series of radio pulses every 1.33s originating from the same location in the night sky. The object was label LGM-1, short for ‘little green men’ and eventually, became the first known neutron star/pulsar. First proposed by Walter Baade and Fritz Zwicky in the 1930’s (Baade and Zwicky, 1934c), neutron stars are the rotating, highly dense, magnetised remnants of massive stars that emits a beam of photons from its magnetic poles. The magnetic and rotational axes do not necessarily align and the beams of photons rotate around the neutron star. A neutron star is a pulsar when the beam of light points in the direction of earth, forming the characteristic pulse.

Neutron stars are formed during a supernova when a massive star ( $\gtrsim 8 M_{\odot}$ ) can no longer able support the immense gravitational pressure due to accumulation of iron in the core and undergoes core collapse. Gravitational pressure overcomes electron-degeneracy pressure, forcing electrons and protons in the core to combine to form neutrons. At this



Figure 2.1: The neutron star/pulsar structure is composed of an inner & outer core, inner & outer crust and an atmosphere (Haensel et al., 2007).

point, neutron-degeneracy and the strong force prevents further collapse and the neutron star is created. If the neutron star mass exceeds the Tolman–Oppenheimer–Volkoff limit ( $1.5 - 3 M_{\odot}$ ), further collapse can result in a black hole (Bombaci, 1996; Slane et al., 2015).

Neutron stars have a mass of  $1 - 3 M_{\odot}$ , average density  $\rho_0 = 2.8 \times 10^{14} \text{ g cm}^{-3}$  (nuclear saturated mass density) and a radius  $10 - 15 \text{ km}$  which is subdivided into the following layers (see Fig. 2.1) (Haensel et al., 2007): the **atmosphere** consists of a thin layer of plasma (electrons and light nuclei) up to  $10 \text{ cm}$  thick with temperature around  $10^5 - 10^6 \text{ K}$  (Zavlin and Pavlov, 2002). The magnetic field of  $10^{11} - 10^{14} \text{ G}$  controls the dynamics of the atmosphere. Ions and electrons make up the **outer crust** in a layer of  $0.3 - 0.5 \text{ km}$  thickness of density  $\rho = 4 \times 10^{11} \text{ g cm}^{-3}$ . Just below the atmosphere, a thin non-degenerate electron gas form the edges of the outer crust. This gives way to a liquid/solid crust where nuclei undergo electron capture forming neutrons. The **inner crust** is around  $1 \text{ km}$  thick and has average density of  $0.3 - 0.5 \rho_0$ . The inner crust is composed of electrons, neutrons and neutron-rich nuclei. Both the inner and outer crust have been postulated to contain ‘nuclear pasta’, degenerate matter where neutrons and electrons arrange themselves into complex structures (Schneider et al., 2013). The **outer core** is the thickest part of the neutron star at around  $9 - 12 \text{ km}$  thick and has density  $0.5 - 2.0 \rho_0$ . The **inner core** exists at the centre of the more massive neutron stars with conditions so extreme, it has been postulated that protons and neutrons break up into their constituent quarks (Haensel et al., 2007).

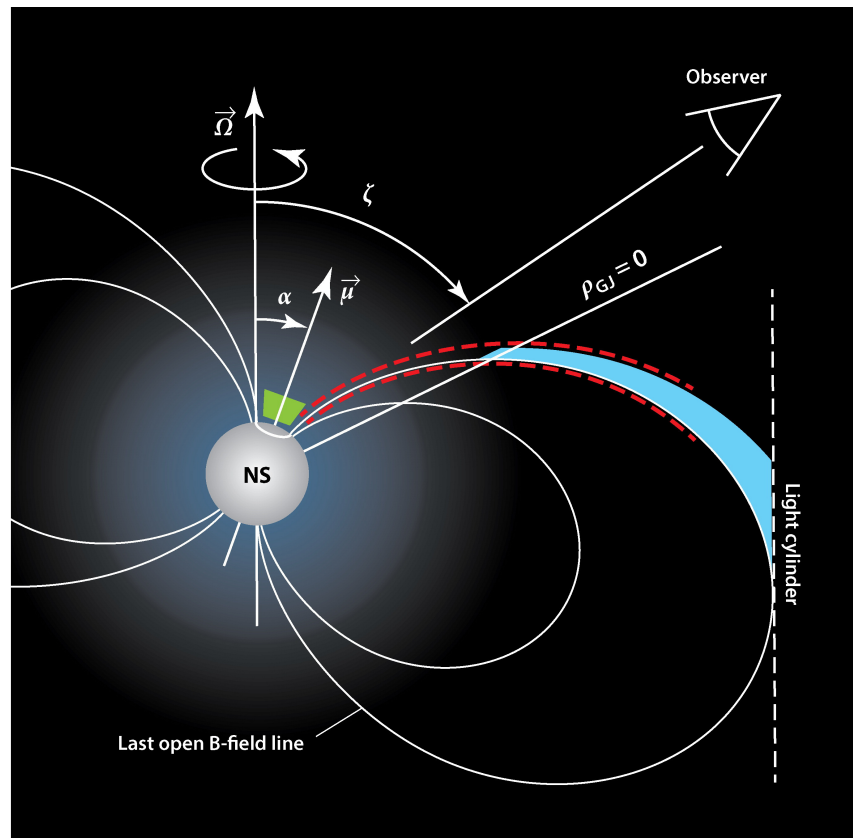


Figure 2.2: Magnetosphere structure of a pulsar with spin velocity  $\vec{\Omega}$  at angle  $\alpha$  to the magnetic field axis and angle  $\zeta$  to the observer. The acceleration site for the polar cap model and outer gap model is shown in green and blue respectively while the site for the slot gap model is enclosed by the red-dashed lines. Image courtesy of Caraveo, (2014).

After core collapse, pulsars retain the majority of a progenitor star's angular momentum ( $L = m\omega r$ ;  $m$  = mass,  $\omega$  = spin velocity and  $r$  = radius), leading to the pulsar spinning rapidly on its axis. Based on the assumption that the magnetic flux of the progenitor star is conserved, Woltjer, (1964) proposed that the pulsar's magnetic field could be as strong as  $10^{14} - 10^{16}$  G. The rotation coupled with the magnetic field,  $\vec{B}$ , generates an electric field given by:

$$\vec{E} = \vec{v} \times \vec{B} , \quad (2.1)$$

where  $\vec{v}$  is the linear velocity of rotation. The magnetic field rips particles from the surface of the pulsar to form the magnetosphere Gold, (1968); Goldreich and Julian, (1969). The magnetosphere of the pulsar extends out to the light cylinder of radius  $R_{LC}$ :

$$R_{LC} = c/\Omega , \quad (2.2)$$

where  $c$  is the speed of light and  $\Omega$  is the angular frequency of the pulsar.

To explain the pulsed radio and gamma-ray emission from the pulsar, Sturrock, (1971) developed the polar-cap model where particles are accelerated at the poles of the pulsar (see Fig. 2.2) and interact with the magnetic field to produce an electron-positron pair ( $e^-e^+$ ). The electron-positron pair emit photons via synchrotron radiation, which then produce a second electron-positron pair. This process cascades until the produced photon can no longer undergo pair production and contributes to the beamed radio emission. The polar-cap model predicts gamma-ray emission due to synchrotron and inverse Compton scattering from the  $e^-e^+$  pair. The slot-gap model (Arons, 1983) extends the acceleration site to higher altitudes until the last open magnetic field line (see Fig. 2.2). The outer-gap model predicts gamma-ray emission due to particle acceleration between the region where  $\vec{\Omega} \cdot \vec{B} = 0$  and the light cylinder (Cheng et al., 1986).

Over time, the rotational kinetic energy is dissipated at a rate described by:

$$\dot{E} = I\Omega\dot{\Omega} , \quad (2.3)$$

where  $I$  is the moment of inertia of the pulsar and  $\dot{\Omega}$  is the time derivative of the angular frequency. Some of the spin down power is channelled into the acceleration of particles by the magnetic field. If the pulsar is treated as a simple magnetic dipole, the energy loss becomes (Slane, 2017):

$$\dot{E} = -\frac{BR^6\Omega^4}{6c^2} \sin^2\alpha , \quad (2.4)$$

where  $B$  is the magnetic dipole strength at the poles,  $R$  is the radius of the pulsar and  $\alpha$  is the angle between the rotational and magnetic axes. The angular frequency decreases over time in a manner described by the braking index of the pulsar,  $n$ :

$$\dot{\Omega} \propto \Omega^n . \quad (2.5)$$

The braking index typically takes values between 2 to 3, where  $n = 3$  represents a situation where the pulsar loses all its rotational energy through magnetic dipole radiation (Livingstone et al., 2007). However ‘glitches’ (sudden speed up events that are thought to be due to transfer of angular momentum within the pulsar) may result in a braking index  $> 3$  (Parthasarathy et al., 2019; Parthasarathy et al., 2020). In the case where a pulsar

does not have a companion star, the characteristic age/spin-down timescale is defined to be (Haensel et al., (2007) and references within):

$$\tau = \frac{P_0}{(n - 1)\dot{P}} . \quad (2.6)$$

If the pulsar has a companion star, the extreme gravitational force of the pulsar can strip the companion of its mass and its angular rotation increases. Therefore, the characteristic age may not reflect the true age of the pulsar. The accretion of matter onto the pulsar is believed to be the origin for millisecond pulsars; pulsars with a period less than 10ms (Alpar et al., 1982).

At the surface of the pulsar, the magnetic field depends on the period and spin down period (Lorimer and Kramer, (2012) and references within):

$$B_s = 3.2 \times 10^{19} (P\dot{P})^{\frac{1}{2}} \text{ [G]} . \quad (2.7)$$

Pulsars with extremely strong magnetic fields are known as magnetars and may be linked to the origin of short gamma-ray bursts and soft gamma ray repeaters (Duncan and Thompson, 1992). For ‘regular’ pulsars, the surface magnetic field has strength  $B = 10^{11-13}$  G while magnetars have magnetic fields up to  $10^{14-15}$  G (Haensel et al., 2007). Possible theories for the extreme magnetic field of a magnetar include; conservation of magnetic field flux of a star with an extreme magnetic field, collapse of a highly magnetized white dwarf or the magnetic field amplification during the birth of the neutron through a dynamo mechanism (the mechanism where a magnetic field is produced by charged plasma in a rotating celestial body) (Duncan and Thompson, 1992; Thompson and Duncan, 1993; Duncan and Thompson, 1996).

The distance to a pulsar can be determined by considering the line of sight ISM. For ISM with electron density  $n_e$ , electrons naturally oscillate at plasma frequency,  $\omega_p$ :

$$\omega_p^2 = \frac{4\pi n_e e^2}{m_e} , \quad (2.8)$$

where  $e$  and  $m_e$  are the charge and the mass of an electron respectively. A photon (with angular frequency  $\omega = 2\pi f$ ) in the interstellar medium (ISM) gas will then propagate with velocity (Draine, 2011):

$$v = c \left( 1 - \frac{\omega_p^2}{\omega^2} \right)^{1/2} . \quad (2.9)$$

Therefore, photons of frequencies  $\nu_1$  and  $\nu_2$  emitted simultaneously by the pulsar will experience a time delay  $\Delta t = t_2 - t_1$  in a manner related to the ISM. The dispersion measure (DM) is defined to be the integrated column density of free electrons over the distance ( $d$ ) to the pulsar(Draine, 2011):

$$\begin{aligned} DM &= \frac{\Delta t}{4.15 \text{ ms} [(\nu_2/\text{GHz})^{-2} - (\nu_1/\text{GHz})^{-2}]} \\ &= \int_0^d n_e \text{ d}\ell . \end{aligned} \quad (2.10)$$

Combining Galactic models of the free electron density (e.g. Yao et al., (2017)) with time delay measurements, the distance to the pulsar can then be estimated.

### 2.1.2 Time Evolution of Pulsar Wind Nebulae

Charged particles (electrons, positrons, protons and nuclei) from the pulsar escape the magnetosphere (which extends up to the light cylinder, see Fig. 2.2) and form the powerful winds known as a PWN. These charged particles emit photons isotropically and are not tied to the pulsar beam. Therefore, the PWN emission is said to be ‘unpulsed’. PWNe typically evolve inside a supernova remnant (SNR) (see Appendix A).

The characteristics (e.g. morphology, spectral energy distribution) of a PWN depends on the age of the powering pulsar. The PWN can be divided into three stages: the expansion phase, a compression-expansion phase and the formation of a halo.



Figure 2.3: (left) Structure of a composite SNR and PWN. Image courtesy of Gaensler and Slane, (2006). (right) A PWN evolves within the SNR and is eventually crushed by the reverse shock. The pulsar escapes the SNR and the electrons escaping into the ISM form a TeV halo around the PWN. Image courtesy of Giacinti et al., (2020).

#### Stage 1: Expansion Phase (< 10 kyr)

As the pulsar wind expands into the shocked region of the SNR, the outer winds of the PWN are decelerated by the ISM until the ram pressure of the interstellar wind counteracts the internal pressure of the PWN,  $P_{\text{PWN}}$  (see Fig. 2.3). This forms the termination shock at radius (Gaensler and Slane, 2006):

$$r_{\text{ts}} = \left( \frac{\dot{E}}{4\pi\omega c P_{\text{PWN}}} \right)^{\frac{1}{2}}, \quad (2.11)$$

where  $\dot{E}$  is the spin-down power and  $\omega$  is the filling factor of the PWN ( $\omega \approx 1$  for isotropic winds) (Bogovalov and Khangoulyan, 2002). Typical PWN have a termination shock occurring at  $r_s \approx 0.1$  pc (Gaensler and Slane, 2006). Particles are re-accelerated at the termination shock and are believed to be the source of the radio to [unpulsed](#) TeV emission from PWN. For a PWN in its first stage of evolution, the radius evolves as (Chevalier, 1977):

$$r_{\text{PWN}} = 1.5 \dot{E}_0^{\frac{1}{5}} E_{\text{SNR}}^{\frac{3}{10}} M_{\text{ej}}^{-\frac{1}{2}} t^{\frac{6}{5}}, \quad (2.12)$$

where  $E_{\text{SNR}}$  and  $M_{\text{ej}}$  are the energy and ejected mass of the SNR. At this stage the spin down energy of the pulsar,  $E_0$ , is roughly constant.

Asymmetry in the progenitor supernova will result in the pulsar gaining a so-called kick velocity of  $300 \text{ km s}^{-1}$  (Kolb et al., 2017), however at early stages the pulsar appears towards the centre of the SNR.

### Stage 2: (10 – 100 kyr)

As the PWN evolves inside the SNR, the outer edges of the SNR collide with the ISM and forms a reverse shock (see Appendix A). The reverse shock travels radially inwards and crushes the PWN, increasing its pressure and magnetic field. The pressure inside the PWN increases until it is greater than its surroundings, resulting in a subsonic expansion of the nebula. This compression and expansion phase repeats itself over a time scale of a few thousand years. The crushing of the PWN by the reverse shock is anti-symmetric due to the kick velocity of the pulsar and non-uniformity in the ISM, which leads to complex morphology of the PWN.

At the edge of the PWN,  $r_{\text{PWN}}$ , the pressure is balanced with that of the associated SNR. During stage 2, the SNR will be in its Sedov-Taylor phase of its evolution (see Appendix A) with radius  $r_{\text{SNR}} \propto t^{\frac{2}{5}}$ . Therefore the radius of the PWN is thought to be related to the SNR radius via (van der Swaluw et al., 2001):

$$r_{\text{PWN}} \propto t^{\frac{1}{3}} r_{\text{SNR}} = t^{11/15}. \quad (2.13)$$

High-energy electrons can escape the PWN into the ISM and can emit TeV  $\gamma$ -rays via inverse Compton interactions, forming a TeV halo (Giacinti et al., 2020).

### Stage 3: Formation of TeV halos ( $t \gtrsim 100$ kyr)

At this stage, the kick velocity of the pulsar has allowed it to escape the SNR (which is now fading into the ISM). The pulsar is travelling faster than the speed of the sound in the ISM, forming a bow shock with the PWN trailing behind (see Fig. 2.3) (Giacinti et al., 2020). At this point a TeV halo is formed around the PWN. Extended TeV emission, indicative of a TeV halo, has been seen towards the Geminga and PSR B0656+14 pulsars (Abeysekara et al., 2017).

## Time Evolution of the PWN Magnetic Field Structure

The charged winds of PWNe are influenced by the presence of magnetic fields. The magnetic field structure of PWNe is believed to be toroidal in nature, with the viewing angle affecting observations at Earth (Kothes et al., 2006; Reynolds et al., 2012). If the axis of rotation aligns with the viewing angle, the magnetic field appears to be toroidal (see left hand panel of Fig. 2.4). In contrast, the magnetic field of the pulsar will appear to be radially dependent if the viewing angle and axis of rotation is perpendicular to each other. More complex observed magnetic field structures occur when the viewing angle is between these two extremes (see the right hand panel of Fig. 2.4).

The magnetic field evolves with the PWN. The average magnetic field of the PWN,  $B_{\text{PWN}}$ , at time  $t$  can be found by considering the conservation of magnetic energy density (see Tanaka and Takahara, (2010) and references within):



Figure 2.4: (left) Expansion of the PWN magnetic field lines and how the viewing angle alters the way the magnetic field structure appears at Earth. Image courtesy of (Kothes et al., 2006)(right) Simulated magnetic field lines of a stage 1 PWN. Azimuthal orientated field lines are shown in blue while radial field lines are shown in red. The termination shock is indicated by magenta and indicated by the arrow. Image adapted from Porth et al., (2014)

$$V_{\text{PWN}} \frac{B_{\text{PWN}}^2(t)}{8\pi} = \int_0^t \eta L(t') dt' \\ = \eta E_{\text{spin}}(t) , \quad (2.14)$$

where  $V_{\text{PWN}}$  is the volume of the PWN,  $L$  is the injection luminosity (of particles) of the PWN,  $\eta$  ( $0 \leq \eta \leq 1$ ) is the ratio of the magnetic energy and the pulsars' spin down power and  $E_{\text{spin}}$  is the time-integrated spin down energy. The resulting magnetic field is then:

$$B(t) = \sqrt{\frac{3(n-1)\eta L_0 \tau_0}{R_{\text{PWN}}^3} \left[ 1 - \left( 1 + \frac{t}{\tau_0} \right)^{-\frac{2}{n-1}} \right]} , \quad (2.15)$$

where  $R_{\text{PWN}}$  is the size of the PWN and  $\tau_0$  is the initial spin down timescale (see Eq. 2.6). For  $t > \tau_0$ , the magnetic field of the PWN can be approximated by  $B(t) \propto t^{-1.5}$ .

### Time Evolution of the Spectral Energy Distribution

A spectral energy distribution (SED) describes how the energy flux of photons (or particles) from a source varies with energy. Fig. 2.5 from the study Gelfand et al., (2009) shows the SED time evolution for an example PWN with braking index 3 and electron injection luminosity of  $10^{40} \text{ erg s}^{-1}$ , where electrons follow a power-law spectrum ( $\propto E^{-1.6}$ ).

At  $t = 0$  (stage 1), the injected electrons have not experienced any energy losses and form a strong peak in the X-ray regime through synchotron emission. The same electrons will interact with the cosmic microwave background (CMB) through inverse Compton interactions and form a strong peak in the GeV regime (top-left panel of Fig. 2.5). As the PWN expands within the SNR, the overall magnetic field strength of the PWN decreases and the synchotron luminosity peak migrates to lower energies in the optical regime. This leaves more energy to be lost through inverse Compton (IC) interactions (see Section 2.3.3) and the IC peak transitions from the GeV to the TeV regime.



Figure 2.5: Theoretical time evolution of the multi-wavelength SED of a PWN inside a SNR. See text for more information. Image courtesy of (Gelfand et al., 2009).

As the reverse shock compresses the PWN (stage 2), the increased magnetic field turbulence within the PWN strengthens the magnetic field. (see Appendix A). Thus, electrons injected into the PWN lose more energy to synchrotron losses and the ratio of synchrotron to IC flux increases (top-right panel of Fig. 2.5). At this point, two distinct peaks start to form in the synchrotron and inverse Compton spectra due to the two populations of young high-energy electrons and the older lower energy electrons that were initially injected into the PWN. During this compression, the pulsar may leave the PWN and no new electrons are injected into the system. The synchrotron and IC peak from the young high electrons subsequently disappears (black line in the top-right panel of Fig. 2.5).

The pressure inside the PWN increases due to compression until it is greater than the surrounding ISM and the PWN expands. Before the pulsar re-enters the PWN, the overall magnetic field strength of the PWN decreases and the IC flux from the electron population increases at the expense of the synchrotron flux (top-right and bottom-left panel of Fig. 2.5). New electrons are injected in the PWN when the pulsar re-enters the system, creating two populations of old low-energy electrons and young high-energy electrons. This is reflected in the IC and synchrotron emission (dotted orange line in the bottom-left panel of Fig. 2.5).

As the PWN re-expands, the pressure inside the PWN decreases until it is less than the pressure due to the associated SNR and the PWN is compressed. Similarly to the first compression, the magnetic field strength inside the PWN increases and the ratio of synchrotron to IC flux increases. The pulsar will again leave the PWN (dotted yellow line

in the bottom right-panel of Fig. 2.5) and no new electrons are injected into the system (stage 3). The synchrotron and IC peak from the young high-energy electrons migrates to lower energies due to high energy losses. However, the energy of the synchrotron peak from old low-energy electrons increases while the energy of the IC peak decreases as a result of the increasing magnetic field.

### 2.1.3 TeV Pulsar Wind Nebula

It was postulated by Gould, (1965) that PWN are a source of TeV gamma rays via IC emission, but it wasn't until Weekes et al., (1989) reported the first detection of TeV emission from the Crab Nebula. A TeV PWN is predicted to be physically larger than the X-ray nebula (Aharonian et al., 1997).

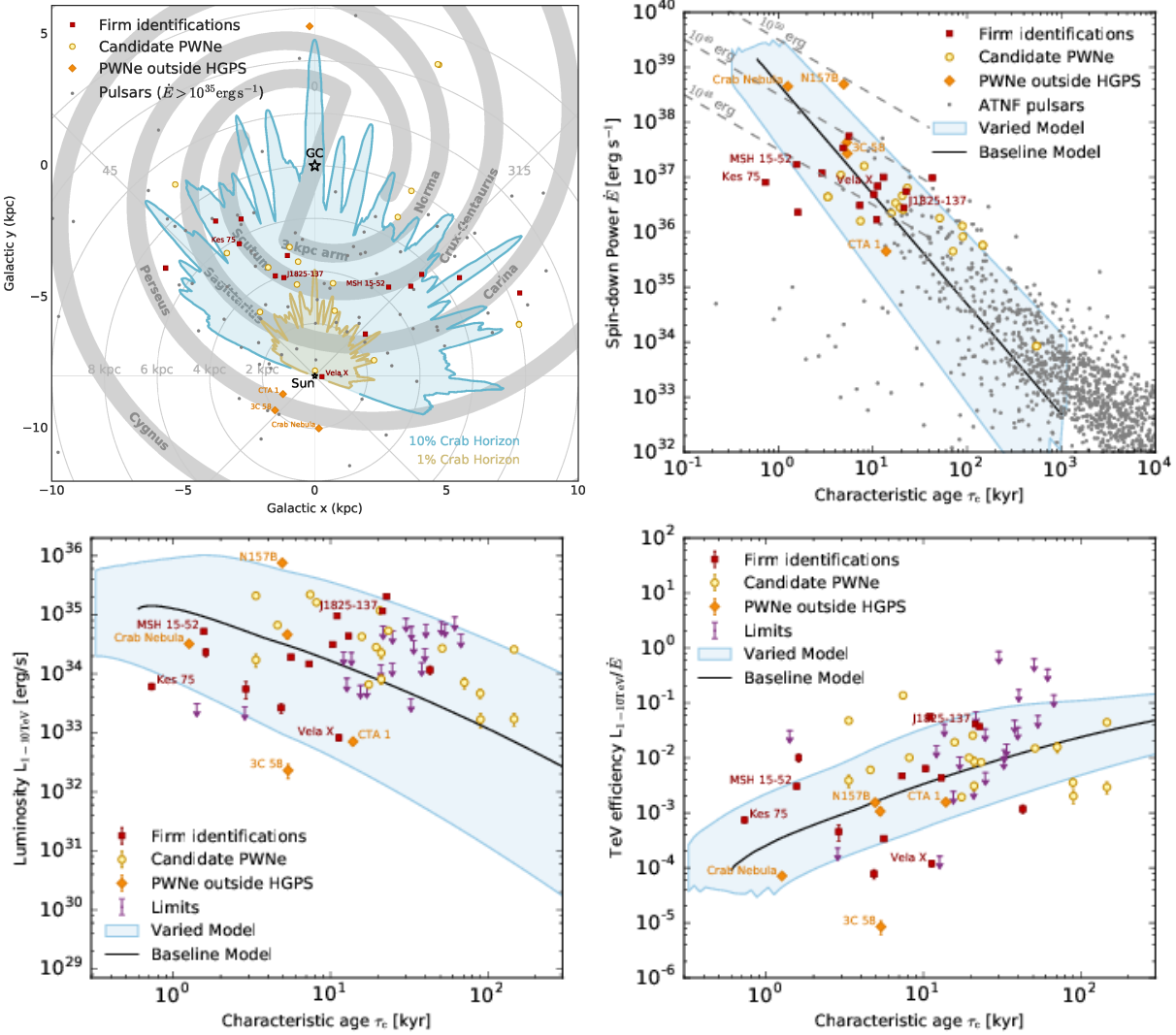


Figure 2.6: (top-left) An illustration of the Milky Way spiral arm structure and the location of identified and candidate PWN from the H.E.S.S. HPGS. Spin down power (top-right), TeV luminosity (bottom-left) and TeV efficiency (bottom-right) vs the characteristic age of known PWN. Images from H.E.S.S. Collaboration et al., (2018b).

The H.E.S.S. TeV gamma-ray survey revealed 78 very high-energy (VHE) gamma-ray sources (H.E.S.S. Collaboration et al., 2018a): 12 are confirmed TeV PWNe, 8 are composite objects (PWN + SNR) and a further 36 are identified as TeV PWNe

candidates. The H.E.S.S. observatory will be discussed further in Section 3.2.1. H.E.S.S. Collaboration et al., (2018b) reviewed the H.E.S.S. Galactic Plane Survey (HGPS) in order to investigate the evolution and nature of TeV PWNe. It was found that the majority of PWN are located on or near the Milky Way spiral arms, with the Crux-Scutum arm hosting half of the PWN from the HGPS (see Fig. 2.6).

Through time-dependent modelling of TeV PWN, H.E.S.S. Collaboration et al., (2018b), it was noted that as PWNe age: 1) The physical offset between the pulsar and TeV PWN increases (at a rate of  $\approx 0.5\text{pc}/\text{kyr}$ ) due to the kick-velocity of the pulsar and the SNR reverse shock crushing the PWN. 2) The TeV luminosity ( $L_{1-10 \text{ TeV}}$ ) of known PWN varies widely with characteristic age (from  $\approx 10^{35} \text{ erg s}^{-1}$  at 1 kyr to  $\approx 10^{34} \text{ erg s}^{-1}$  at 10 kyr) with no clear statistical correlation. 3) The TeV efficiency ( $L_{1-10 \text{ TeV}}/\dot{E}$ ) increases (from  $2 \times 10^{-4}$  at 1 kyr to  $3 \times 10^{-3}$  at 10 kyr) possible due to the physical offset between the pulsar and TeV PWN.

### 2.1.4 Mysteries of Pulsar Wind Nebulae

Even though multiple PWNe have been observed and studies such as H.E.S.S. Collaboration et al., (2018b) have modelled trends of TeV PWN, there are still many open questions. The following will summarise some of these questions.

#### **How are electrons transported within pulsar wind nebula?**

Electrons released by a pulsar are subject to varying transportation processes and energy losses. In a non-uniform environment (due to gas and magnetic field turbulence), electrons scatter off the ISM atoms and magnetic field turbulence resulting in diffusive motion outwards from the acceleration site (see Section 2.2.2). Electrons in PWNe may also experience an overlying bulk transport in a particular direction, i.e. advection. It has been proposed that advection dominates the particle transport close to the pulsar while diffusion dominates the outer reaches of the nebula (Giacinti et al., 2020; Recchia et al., 2021). Electrons undergo energy loss through inverse-Compton, synchrotron and Bremsstrahlung emission (see section Section 2.3.3). The rate at which an electron loses energy depends heavily on the surrounding environment.

A challenge in modelling PWN will be balancing the transportation of electrons and energy losses with respect to the surrounding environment to order to explain the multi-wavelength emission.

#### **Can pulsar wind nebula accelerate particles up to PeV energies?**

The break between the knee ( $1 \text{ PeV} = 10^{15} \text{ eV}$ ) and the ankle ( $10^{18} \text{ EeV}$ ) in the cosmic ray proton and nuclei spectrum at Earth suggests the transition from Galactic to extra-Galactic cosmic rays (see Section 2.2.3). Thus, what type of Galactic source is capable of accelerating cosmic rays up to PeV energies, i.e. a PeVatron?

Due to their large energy budget ( $\approx 10^{51} \text{ erg}$  of kinetic energy) and production rate ( $\approx 2 - 3$  supernova occur in the Milky Way per century), SNRs have been the most likely candidates for Galactic PeVatrons (Lagage and Cesarsky, 1983; Hillas, 1984; Bell, 2004; Cristofari et al., 2018). Recently, the suitability of SNRs by themselves as PeVatrons has been called into question (Cristofari et al., 2020) and PWNe are now being considered as

additional candidates (Ohira et al., 2018; Xin et al., 2019; de Oña Wilhelmi et al., 2022; Breuhaus et al., 2022).

In 2021, the LHAASO facility identified 12 gamma-ray sources with the detection of photons between 100 TeV to 1.4 PeV (Cao et al., 2021). These sources are prime PeVatron candidates; two being firmly identified PWNe and a further nine having possible PWN counterparts. One of the twelve PeVatron candidates is the Crab Nebula. The MeV synchrotron emission from the Crab Nebula and maximum gamma-ray energy of  $\approx 0.9$  PeV heavily implies the presence of PeV electrons within the nebula (The LHAASO Collaboration et al., 2021).

### Is there a hadronic component to the pulsar wind nebula?

Spectral and spatial analysis of known PWNe indicate that leptonic emission is the main source of gamma-ray emission. With the detection of PeV emission towards known PWNe (The LHAASO Collaboration et al., 2021), further studies suggest that PWN may have an additional hadronic component (Li et al., 2010; Xin et al., 2019; Liu and Wang, 2021). The majority of literature consider the winds of the PWN to consist of electrons and positrons (e.g. H.E.S.S. Collaboration et al., (2018b)). However, in the polar cap model (see Fig. 2.2) electrons, positrons and protons are stripped from the surface of the pulsar. Gallant and Arons, (1994) proposed that a fraction of the spin-down power of the pulsar is converted into a wind of protons. These protons undergo proton-proton collisions to produce pions (see Section 2.3.2). Charged pions decay into muons, which subsequently decay into electrons and positrons. Amato et al., (2003) suggested that signatures of these ‘secondary’ electrons/positrons can be found in the production of TeV gamma rays and neutrinos. Moreover, the SNR reverse shock can re-introduce protons into the PWN and accelerate protons greater than 1 PeV (Bell, 1992; Ohira et al., 2018).

#### 2.1.5 HESS J1825-137 and HESS J1826-130

This thesis will focus on the PWN associated with TeV source HESS J1825-137. The following will briefly summarise the literature of HESS J1825-137 and nearby TeV source HESS J1826-130.

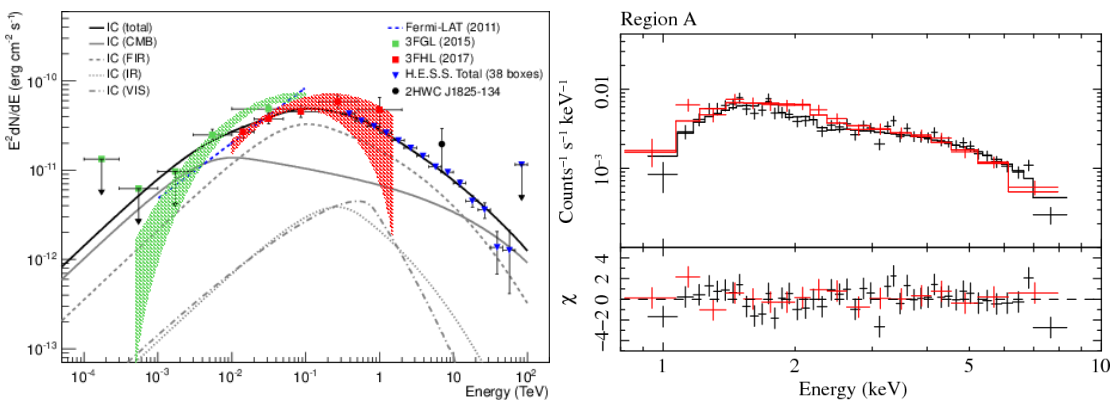


Figure 2.7: (left) Gamma-ray SED of HESS J1825-137 as seen by HESS together with the *Fermi*-LAT 3FGL and 4FHL equivalent sources. (right) X-ray SED towards PSR J1826-1334. Images courtesy of H.E.S.S. Collaboration et al., (2019) and Uchiyama et al., (2009).



Figure 2.8: HESS excess counts map towards HESS J1825-137 from H.E.S.S. Collaboration et al., (2019). The spatial position and extent of HESS J1825-137, HESS J1826-130, 4FGL J1824.5-1351e, eHWC J1825-134 and LHAASO 1825-1326 are shown together with PSR J1826-1334 (star) and PSR J1826-1256 (cross).

Table 2.1: Fit parameters to the spectrum of HESS J1825-137 and equivalent *Fermi*-Lat and HAWC sources. Power law (PL):  $\frac{dN}{dE} \propto \left(\frac{E_p}{E_0}\right)^{-\Gamma}$ . Exponential Cutoff Power Law (ECPL):  $\frac{dN}{dE} \propto \left(\frac{E_p}{E_0}\right)^{-\Gamma} \exp\left(-\frac{E}{E_c}\right)$ . Log Parabola (LP):  $\frac{dN}{dE} \propto \left(\frac{E_p}{E_0}\right)^{-\Gamma+\beta \log(E/E_0)}$ . Broken Power Law (BPL):  $\frac{dN}{dE} \propto \left(\frac{E_p}{E_b}\right)^{-\Gamma}$  where  $\Gamma = \Gamma_1$  if  $E < E_b$  and  $\Gamma = \Gamma_2$  otherwise.  $E_0 = 1$  TeV unless specified.

Model	$\Gamma$	Parameters	RA	DEC	extent ( $^{\circ}$ )	References
<b>HESS J1825-137</b>	-	-	18h25m49s	-13°46m35s	0.66*	a
PL	$2.23 \pm 0.02 \pm 0.04$	-	-	-	-	a
ECPL	$2.06 \pm 0.05 \pm 0.08$	$E_c = 15 \pm 5 \pm 6$ TeV	-	-	-	a
LP	$2.21 \pm 0.03 \pm 0.04$	$\beta = 0.08 \pm 0.02 \pm 0.03$	-	-	-	a
<b>4FGL J1824.5-1351e</b>	-	-	18h24m31.2s	-13°51m07.2s	0.75	b
LP	$1.96 \pm 0.68$	$E_0 = 145 \pm$ GeV	-	-	-	c
-	-	$\beta = 0.046 \pm 0.013$	-	-	-	-
BPL	$1.70 \pm 0.04$	$E_b = 115 \pm 8$ GeV	-	-	-	c
-	$2.29 \pm 0.15$	-	-	-	-	-
<b>3HWC J1825 - 134</b>	-	-	18h25m50.4s	-13°24m03.6s	-	d
PL	$2.35 \pm 0.02$	-	-	-	-	d
<b>eHWC J1825 - 134</b>	-	-	18h25m36s	-13°22m12s	0.34	e
ECPL	$2.12 \pm 0.15$	$E_c = 61 \pm 12$ TeV	-	-	-	e
<b>LHAASO 1825-1326</b>	-	-	18h25m48s	-13°27m00s	0.3	f

\*: Average of the southern and northern extent

#### References

- a: (H.E.S.S. Collaboration et al., 2019)
- b: (Abdollahi et al., 2020)
- c: (Principe et al., 2020)
- d: (Albert et al., 2020)
- e: (Abeysekara et al., 2020)
- f: (Cao et al., 2021)

Discovered in 2005, HESS J1825-137 is one of the most luminous and extensive TeV PWN (Aharonian et al., 2005b; Aharonian et al., 2006a). HESS J1825-137 is powered by PSR J1826-1334, which has a spin down power, period, period derivative and DM distance of  $2.8 \times 10^{36}$  erg s $^{-1}$ , 101.5 ms,  $7.5 \times 10^{-14}$  ss $^{-1}$  and 3.6 kpc respectively (Manchester et al., 2005). Eq. 2.6 gives the characteristic age of PSR J1826-1334 as 21.4 kyr, placing the PWN in its second phase of its evolution (see Section 2.1.2). In support of this, a TeV halo appears to be forming around HESS J1825-137 (Principe et al., 2020). The High Altitude Water Cherenkov (HAWC) observatory has observed gamma-rays towards equivalent source eHWC J1825-134 with energies greater than 100 TeV (Abeysekara et

al., 2020). Similarly, LHAASO identified HESS J1825-137 (LHAASO J1825-1326) as a possible PeVatron candidate (see section. Section 2.2.4) (Cao et al., 2021). The equivalent GeV *Fermi*-LAT source is 4FGL J1824.5-1351e. See Table 2.1 and Fig. 2.8 for the spectral and spatial information of HESS J1825-137 and equivalent sources.

The TeV morphology towards HESS J1825-137 (see Fig. 2.8) is asymmetric around the pulsar, with more extensive emission towards the southern side of the nebula (in Galactic coordinates). The extent (defined to be the point at which the emission drops to  $1/e$  of its highest value) towards the south of HESS J1825-137 was found (H.E.S.S. Collaboration et al., 2019) to be  $0.66^\circ \pm 0.03^\circ_{\text{stat}} \pm 0.04^\circ_{\text{sys}}$ , while the northern side is extended by  $0.41^\circ \pm 0.03^\circ_{\text{stat}} \pm 0.09^\circ_{\text{sys}}$ . At a distance of 4.0 kpc, this equates to a physical distance of  $91 \pm 4 \pm 6$  pc and  $57 \pm 4 \pm 13$  pc to the south and north respectively. The southern side of the nebula is also extensive in GeV gamma-rays as revealed by Araya et al., (2019). This region of gamma-ray emission has a hard spectrum with photon index 1.9 and also suggested to be powered by high-energy electrons from the PWN associated with HESS J1825-137.

The progenitor SNR associated with HESS J1825-137 will likely be in its Sedov-Taylor phase stage of evolution based on the characteristic age of PSR J1826-1334 (see Appendix A). van der Swaluw et al., (2001) suggests that the size of a SNR will be approximately four times the size of the PWN. The radius of the TeV PWN associated with HESS J1825-137 is 38 pc for a distance of 4 kpc (see Table 2.1), giving an estimated SNR radius of 150 pc. Voisin et al., (2016) noted a large H $\alpha$ -rim like structure indicative of a SNR shock lying 120 pc to the south of PSR J1826-1334, consistent with the predicted SNR size. Voisin et al., (2016) further postulated a connection between this H $\alpha$  rim and a second H $\alpha$  rim (discovered by Stupar et al., (2008)) lying at a similar angular distance to the pulsar.

## HESS J1826-130



Figure 2.9: TeV (*left*) and X-ray (*right*) SED towards HESS J1826-130 as seen by H.E.S.S. and Suzaku respectively. Images courtesy of H.E.S.S. Collaboration et al., (2020) and Duvidovich et al., (2019) respectively.

HESS J1826-130, an unidentified gamma-ray source situated  $\approx 0.7^\circ$  to the Galactic north of HESS J1825-137 (see Fig. 2.8). Due to its proximity, HESS J1826-130 was originally thought to be an extension of HESS J1825-137 until it was classified as a separate source through its energy-dependent morphology (Angüner et al., 2017). HESS J1826-130 becomes more distinct from HESS J1825-137 at higher gamma-ray energies. The analysis

Table 2.2: Fit parameters to the spectrum of HESS J1826-130. Power law (PL):  $\frac{dN}{dE} \propto \left(\frac{E_p}{E_0}\right)^{-\Gamma}$ . Exponential Cutoff Power Law (ECPL):  $\frac{dN}{dE} \propto \left(\frac{E_p}{E_0}\right)^{-\Gamma} \exp\left(-\frac{E}{E_c}\right)$ . Broken Power Law (BPL):  $\frac{dN}{dE} \propto \left(\frac{E_p}{E_b}\right)^{-\Gamma}$  where  $\Gamma = \Gamma_1$  if  $E < E_b$  and  $\Gamma = \Gamma_2$  otherwise.  $E_0 = 1$  TeV unless specified.

Model	$\Gamma$	Parameters	RA	DEC	extent ( $^{\circ}$ )	References
<b>HESS J1826-130</b>	-	-	18h26m02.1s	-13°01m02.6s	0.15*	a
PL	$2.12 \pm 0.04$	-	-	-	-	a
ECPL	$1.78 \pm 0.10$	$E_c = 15.2 \pm 5$	-	-	-	a
BPL	$1.96 \pm 0.06$	$E_b = 11.2 \pm 2.7$ TeV $3.59 \pm 0.69$	-	-	-	a

#### References

a: (H.E.S.S. Collaboration et al., 2020)



Figure 2.10: XMN-Newton 0.5 – 10 keV X-ray images towards HESS J1826-130. The positions of PSR 1826-1256 and the Eel Nebula are shown by the red cross and ellipse respectively. The orange lines represent the H.E.S.S. 3 $\sigma$  and 5 $\sigma$  significance contours. Nearby SNR G18.45-0.42 and star cluster Bica 3 are shown by the dashed blue and black circles respectively. Image courtesy of Burgess et al., (2022).

conducted by H.E.S.S. Collaboration et al., (2020) showed that HESS J1825-137 contaminates the SED of HESS J1826-130 by approximately 40% below 1.5 TeV and 20% above 1.5 TeV. As shown by Fig. 2.8, the position of eHWC J1825-134 lies approximately midwway between HESS J1825-137 and HESS J1826-130. Due to the coarse angular resolution of HAWC, eHWC J1825-134 may represent the combined emission from both HESS J1825-137 and HESS J1826-130.

Several objects towards HESS J1826-130 have been associated with the gamma-ray emission based on spatial correlation. This includes the Eel nebula (PWN G18.5-0.4), a PWN with a long faint trail ( $0.1^{\circ}$ ) of hard X-ray emission above 2 keV (see Fig. 2.10) (Roberts et al., 2007; Burgess et al., 2022). Similarly, H.E.S.S. Collaboration et al., (2018a) proposed two possible SNRs as a source of protons interacting with the interstellar gas to produce the observed gamma-ray emission; SNR G018.1-0.1 and SNR G018.6-0.2. As shown by the purple cross in Fig. 2.8, PSR 1826-1256 is located towards HESS J1826-130 and may be a source of electrons powering the PWN. PSR 1826-1256 has spin down power and characteristic age of  $3.6 \times 10^{36}$  erg s $^{-1}$  and 14 kyr respectively (Abdo et al., 2010).

Voisin et al., (2016) revealed dense turbulent molecular gas between HESS J1825-137 and HESS J1826-130. The same study places the majority of these clouds in the  $40 - 60 \text{ km s}^{-1}$  velocity range, equivalent to a distance of  $3.5 - 4.5 \text{ kpc}$  as given by the Galactic rotation model (see Section 4.2.3 (Brand and Blitz, 1993)). This is consistent with the DM distance of PSR J1826-1334. Therefore, protons from the associated SNR may interact with these dense clouds through p-p collisions (see Section 2.3.2) to emit the high-energy gamma-rays as seen by eHWC J1825-134.

## 2.2 Cosmic Rays

As discussed in Section 2.1, PWN are a source of high-energy cosmic rays. Therefore, it is vital to understand the properties of cosmic rays in order to explain PWN characteristics.



Figure 2.11: Victor HESS about to ascend to an altitude  $> 5 \text{ km}$  to discover cosmic rays (Hess, 1912)

In 1896 Henri Becquerel discovered that uranium salts emitted a form of invisible radiation that could penetrate through solid matter. At the beginning of the 20th

century, it was generally believed that only elements in the Earth could emit such radiation. However in 1912, Victor HESS ascended 5 km with an electroscope in a hot air balloon. He noticed that as altitude increased, the amount of radiation measured by the electroscope increased (Hess, 1912). In contrast, Millikan submerged electroscopes in Muir Lake located in the Rocky Mountains (Millikan and Cameron, 1926). As the electroscopes descended, less radiation was detected. The findings of Hess and Millikan showed that ionising radiation, later dubbed ‘cosmic rays’, originate from the sky. In the mid 20th century, the level of cosmic-ray ionisation was found to be dependent on latitude (Sandström et al., 1960) were being deflected by the Earth’s magnetic field.

Cosmic rays comprise of protons, electrons, nuclei, neutrinos and anti-matter. Within this thesis, cosmic rays will be referred to as protons and electrons. Protons consist of three quarks (two up and one down-quark) and are classified as hadrons, a composite subatomic particle made of two or more quarks held together by the strong force. Meanwhile, electrons are elementary particles that belong in the lepton ‘family’ in the standard model of particle physics. Hence hadronic cosmic rays refer to protons while leptonic cosmic rays refer to electrons.

Supernovae were proposed as a source for cosmic rays by Baade and Zwicky, (1934a) in the 1930s. In his 1949 paper, Enrico Fermi provided a method where shock fronts (including those generated by SNRs) accelerate cosmic ray protons up to ultra-high energies (Fermi, 1949). SNRs also accelerate cosmic ray electrons up to high energies as indicated by X-ray emission produced through synchrotron interactions at the rims of SNRS such as SN 1006 (Koyama et al., 1995).

Other sources that have been proposed as accelerators of cosmic rays include PWN (as discussed in Section 2.1), star clusters, binary systems and active Galactic nuclei.

### 2.2.1 Acceleration of Charged Particles

#### Acceleration by pulsars

As discussed in Section 2.1.1, pulsars are the highly dense, magnetised remnants of a supernova. The Lorentz equation,

$$\vec{F} = q\vec{E} + q\vec{v} \times \vec{B} , \quad (2.16)$$

shows that a magnetic field of strength  $\vec{B}$  applies a perpendicular force,  $\vec{F}$ , on a particle with charge  $q$ . In other words, a uniform magnetic field does not change the energy of the particle. However, the rotation of a pulsar coupled with its strong magnetic field generates an electric field,  $\vec{E}$ . This is described by Faraday’s law:

$$\nabla \times \vec{E} = -\frac{\partial \vec{B}}{\partial t} . \quad (2.17)$$

The integral form of Eq. 2.17 describes a changing magnetic field across a surface with cross sectional area  $d\vec{A}$ :

$$\oint_S \vec{E} \cdot d\vec{l} = - \int_S \frac{\partial \vec{B}}{\partial t} \cdot d\vec{A} . \quad (2.18)$$

Where the cross sectional area is the area swept up by expanding surface  $S$  in segment  $d\ell$  and velocity  $\vec{v}$  over time  $dt$  ( $d\vec{A} = d\vec{\ell} \times \vec{v} dt$ ). Eq. 2.18 becomes:

$$\oint_S \vec{E} \cdot d\vec{l} = \int_S \vec{v} \times \vec{B} \cdot d\vec{\ell} . \quad (2.19)$$

i.e. the electric field generated by the pulsar is proportional to the rotation and magnetic field of the pulsar.

The change in energy,  $\mathcal{E}$ , of particles in the presence of an electric field is given by:

$$\frac{d\mathcal{E}}{dt} = \frac{d}{dt} \left( \frac{1}{2} m \vec{v}^2 \right) = m \vec{v} \cdot \frac{d\vec{v}}{dt} = \vec{v} \cdot \vec{F} = q \vec{v} \cdot \vec{E} . \quad (2.20)$$

Therefore, the electric field generated by the pulsar strips particles from its surface and accelerates them up to high energies. The maximum electric field strength produced by a fluctuating magnetic field is described by  $E_{\max} = v_{\text{plasma}} B$ , giving the maximum energy gain rate:

$$\frac{d\mathcal{E}}{dt}_{\max} = q v^2 B . \quad (2.21)$$

For relativistic particles:

$$\frac{d\mathcal{E}}{dt}_{\text{acc}} = \zeta Z e c^2 B , \quad (2.22)$$

where  $0 < \zeta < 1$  is an “acceleration rate parameter” that depends on the acceleration mechanism and  $Z$  is the charge of the particle (The Pierre Auger Collaboration et al., 2022). Naively, taking the surface magnetic field strength of  $B = 10^{11}$  G, pulsar radius of 10 km and the average period of  $P = 0.8$  s (Manchester et al., 2005), the maximum energy gain rate of particles is  $\approx 10^{17}$  eV s $^{-1}$ . Simply, it would take  $10^{-5}$  s for a pulsar to accelerate an electron/proton up to 1 TeV. This assumes that the particle does not escape the pulsar and suffers no energy losses.

### Acceleration by the pulsar wind nebula termination shock

A termination shock forms where the internal pressure of the PWN counteracts the ram pressure of the interstellar wind at approximately  $r_{\text{ts}} = 0.1$  pc (see Section 2.1.2). Particles can be accelerated by the TS through diffusive shock acceleration (DSA) where a particle can scatter back and forth a shock due to magnetic field irregularities, resulting in an overall gain of energy (see Appendix B).

The magnetic field of the PWNe is toroidal in nature where the magnetic field lines are perpendicular to the propagation of the shock. For a pulsar injecting electrons/positrons, the structure of the shock depends on the ratio,  $\sigma$ , of the upstream magnetic energy and plasma energy (Gallant et al., 1992):

$$\sigma = \frac{B^2 / 4\pi}{nm\gamma c^2} , \quad (2.23)$$

where  $B$  and  $n$  is the upstream magnetic field and electron energy density respectively and  $\gamma$  is the Lorentz factor of the electrons. Models of PWN suggest that the magnetization parameter takes values  $10^{-3} - 10^{-2}$  (Rees and Gunn, 1974; Kennel and Coroniti, 1984; Komissarov and Lyubarsky, 2004). The magnetic field turbulence is too weak for particles to scatter back and forth across the termination shock and DSA is suppressed (Lemoine and Pelletier, 2010; Sironi et al., 2015). In general, diffusive shock acceleration for magnetic fields perpendicular to the shock propagation is too suppressed to accelerate

electrons up the energies required to explain PWN emission (Meli and Quenby, 2003; Caprioli and Spitkovsky, 2014).

It has been suggested pre-acceleration of particles driven by magnetic reconnection at the shock front (Lyubarsky and Kirk, 2001; Lyubarsky, 2003; Lemoine, 2016) or resonant cyclotron absorption of electrons/positrons Lyubarsky and Kirk, (2001) followed by diffusive shock acceleration may overcome these issues.

Any modelling conducted in this thesis will assume an injection of accelerated electrons.

### 2.2.2 Propagation of charged particles

Neglecting any electric fields, the Lorentz equation (Eq. 2.16) shows that the magnetic force applied to a charged particle is perpendicular to its motion and the particle will travel in a circular motion described by:

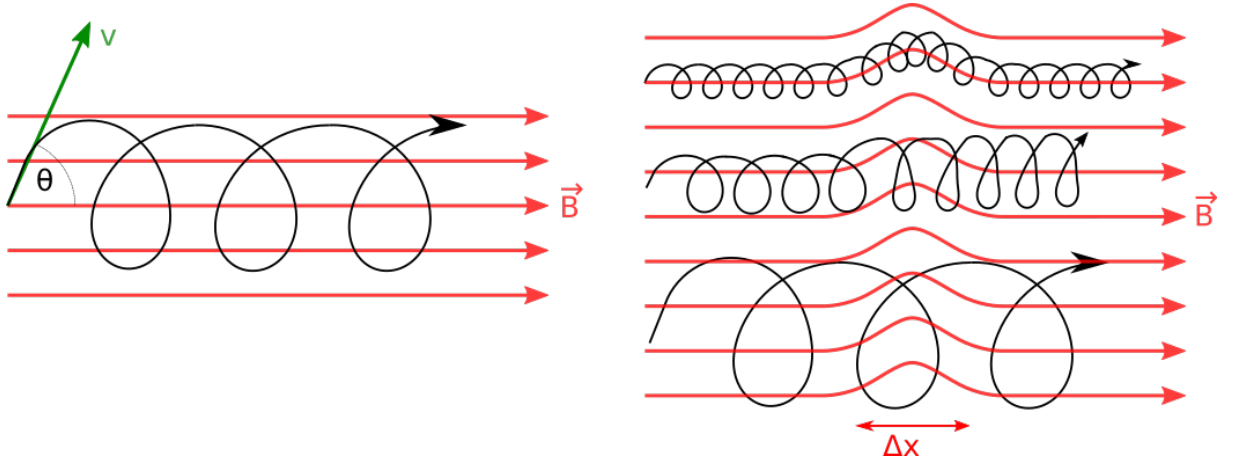


Figure 2.12: (left) The path (black) of motion taken by a charged particle with initial velocity  $v$  at angle  $\theta$  to a uniform magnetic field  $B$  (red). (right) Propagation of a charged particle in a magnetic field with turbulence of length  $\Delta x$  when  $r_g < \Delta x$  (top),  $r_g \approx \Delta x$  (middle) and  $r_g > \Delta x$ . (bottom)

$$\vec{F} = \frac{mv_\perp^2}{r^2} \hat{r}, \quad (2.24)$$

where  $v_\perp$  is the velocity perpendicular to the magnetic field and  $\hat{r}$  represents the direction perpendicular both to the motion and the magnetic field. Combining Eq. 2.16 and Eq. 2.24, we find the particle gyroradius,  $r_g$  (the radius of the circular motion induced by a uniform magnetic field):

$$r_g = \frac{mv_\perp}{qB} = \frac{p}{qB}, \quad (2.25)$$

where  $p$  is the momentum of the charged particle. For relativistic cosmic rays  $p \approx E/c$ . If the charged particle has velocity at an angle  $\theta$  to a magnetic field, it will spiral around the magnetic field direction as shown in the left panel of Fig. 2.12.

The magnetic field around PWNe and within dense gas clouds (see Section 4.2.4) is not uniform and will affect the propagation of charged particles. The presence of magnetic

field turbulence of length  $\Delta x$  in an otherwise uniform field will affect the propagation of charged particles (see the right panel of Fig. 2.12). For charged particles where the gyroradius is much less than the magnetic turbulence ( $r_g \ll \Delta x$ ), the particle will follow the magnetic field lines with no change to its pitch angle. When the gyroradius is much greater than the turbulence ( $r_g \gg \Delta x$ ), the propagation will be unaffected. For charged particles where the gyroradius is similar in scale to the perturbation ( $r_g \approx \Delta x$ ), the pitch angle  $\theta$  changes and alters the direction of travel. In other words, charged particles scatter on the magnetic field turbulence that is of similar scale to the gyroradius.

The gyroradius of ultra-high energy particles ( $r_g = 3.6$  kpc at  $10^{19}$  eV and  $B = 3$   $\mu\text{G}$ ) is so large that they tend to travel in a ballistic manner (for distances less than  $r_g$ ) and thus point back to their place of origin. Lower energy particles (e.g.  $r_g \approx 10^{-4}$  pc at 1 TeV and  $B = 3$   $\mu\text{G}$ ) scatter multiple times and their trajectory tends to follow a random walk, i.e. diffusion.

### Diffusion of charged particles

The diffusion coefficient,  $D$  [ $\text{cm}^2 \text{s}^{-1}$ ], describes the rate that charged particles diffuse per unit area of time and is related to the magnetic field of the medium. In a magnetic field with average field strength  $B_0$ , the mean square variation  $\delta B^2$  depends on the spatial power spectrum of the magnetic field turbulence  $I(k) \propto k^{-\Gamma}$  (Drury, 1983; Nava et al., 2016):

$$\int I(k) d \ln k = \left( \frac{\delta B}{B_0} \right)^2, \quad (2.26)$$

where  $k \propto 1/r_g$  is the wave number. As the charged particle spirals around the magnetic field lines (see Fig. 2.12), the pitch angle of the particle is changed by order  $\delta B$ . The pitch angle is randomised after approximately  $N = B_0^2/kI(k)$  rotations such that the mean free path parallel to the field is given by  $\lambda_{\parallel} = Nr_g$ . Therefore the diffusion coefficient parallel to the magnetic field lines:

$$D_{\parallel} = \frac{r_g v}{3} \frac{B_0^2}{kI(k)}, \quad (2.27)$$

where  $v$  is the velocity of the particle. The mean free path perpendicular to the field lines takes values  $\lambda_{\perp} \approx r_g$  such that the perpendicular diffusion coefficient becomes:

$$D_{\perp} = \frac{r_g v}{3} \frac{kI(k)}{B_0^2} = D_{\parallel} \left( \frac{kI(k)}{B_0^2} \right)^2. \quad (2.28)$$

Hence:

$$D_{\perp} D_{\parallel} = \left( \frac{r_g v}{3} \right)^2 = D_B^2, \quad (2.29)$$

where  $D_B = r_g v / 3$  is known as the Bohm diffusion coefficient representing the case when  $\lambda \approx r_g$ .

Three different regimes of turbulence are considered: Bohm ( $\Gamma = 1$ ), Kraichnan ( $\Gamma = \frac{3}{2}$ ) and Kolomogrov ( $\Gamma = \frac{5}{3}$ ). Quasi-linear theory states that diffusion perpendicular to the magnetic field lines is negligible (Nava et al., (2016) and references within). As  $r_g \propto E$  and  $k \propto 1/E$ , Eq. 2.27 becomes:

$$D \propto \frac{r_g}{kI(k)} \propto E^{2-\Gamma} . \quad (2.30)$$

This results in energy dependent diffusion:  $D \propto E$  in the Bohm regime,  $D \propto E^{\frac{1}{2}}$  in the Kraichnan regime and  $D \propto E^{\frac{1}{3}}$  in the Kolmogrov regime. From cosmic ray observations, values of the diffusion coefficient follows a power law spectrum ( $D \propto E^\delta$ ) with  $\delta$  taking values between 0.3 – 0.6 implying a situation in the Kraichnan/Komogrov regime (e.g. see Strong et al., (2007)).

Neglecting acceleration, (Gabici et al., 2007) parameterized the diffusion coefficient for cosmic rays of energy  $E$  travelling in a molecular cloud with a magnetic field  $B$  to be:

$$D(E, B) = \chi D_0 \left( \frac{E/\text{GeV}}{B/3 \mu\text{G}} \right)^\delta \quad [\text{cm}^2 \text{s}^{-1}] \quad (2.31)$$

where  $D_0 = 1 \times 10^{27} \text{ cm}^2 \text{s}^{-1}$  is the Galactic diffusion coefficient at 1 GeV and the factor,  $\chi$ , takes values < 1 and accounts for the suppression of the diffusion coefficient inside turbulent clouds (Berezinskii et al., 1990). Aharonian and Atoyan, (1996) consider  $\chi = 0.01$  to be ‘slow’ diffusion representing dense ISM clouds (Ormes et al., 1988) and  $\chi = 1$  to be ‘fast’ diffusion. The diffusion suppression factor is poorly constrained but studies towards SNR W28: (Li and Chen, 2010), (Giuliani et al., 2010) and Gabici et al., (2010) assume  $\chi = 0.1, 0.01$  and  $0.06$  respectively for  $D_0 = 10^{28} \text{ cm}^2 \text{s}^{-1}$  at cosmic ray energy 10 GeV. Similarly, Protheroe et al., (2008) highlighted the variation of the suppression factor ( $\chi = 0.01, 0.1, 1$  and  $\chi \gg 1$ ) in studies towards star forming region Sgr B2.

### Local and Galactic Magnetic Fields

Magnetic fields affect the propagation of charged particles through the Galaxy. Faraday rotation (the rotation of polarised light in magnetised plasma) can be used to measure the magnetic field strength in the Galaxy (Faraday, 1846):

$$\langle B_{\parallel} \rangle = 1.232 \frac{\text{RM}}{\text{DM}} , \quad (2.32)$$

where  $B_{\parallel}$  is the magnetic field component along the line of sight, RM is the rotation measure due to Faraday rotation and DM (see Eq. 2.10 is the dispersion measurement of the pulsar. Magnetic fields are also measured through observations of synchrotron emission, where the intensity is proportional to the magnetic field strength and electron energy density (see Beck and Wielebinski, (2013) and references within).

The magnetic field in the ‘local’ vicinity takes value  $1 - 6 \mu\text{G}$  based on both rotation measure and synchrotron measurements (Rand and Kulkarni, 1989; Beck, 2001). Using the rotation measures from 223 pulsars, Han et al., (2006) found the magnetic field strength in the Galactic disk was found to depend on the distance to the Galactic centre:

$$B = B_0 \exp \left[ -\frac{R - R_{\odot}}{R_B} \right] , \quad (2.33)$$

where  $B_0 = 2.1 \pm 0.3 \mu\text{G}$  and  $R_B = 8.5 \pm 4.7 \text{ kpc}$ . This gives the average Galactic magnetic field to be approximately  $3 \mu\text{G}$ . Local sources such as PWN (see Section 2.1), SNRs (see (Reynolds et al., 2012) and references within) and turbulent molecular clouds (Crutcher et al., 2010) provide an ‘additional’ magnetic field component to their surrounding environment.

### 2.2.3 Cosmic Ray Spectrum

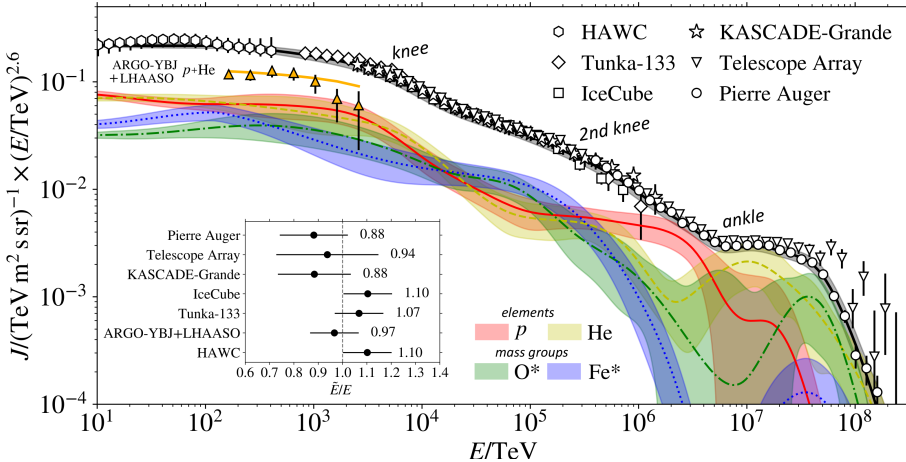


Figure 2.13: Cosmic ray (and high-energy electrons) energy spectrum at Earth as measured by multiple ground based observatories. Image courtesy of Schroeder et al., (2019)

The energy spectrum of cosmic rays (see Fig. 2.13) has been measured up to  $10^{20}$  eV (The Pierre Auger Collaboration et al., 2022) and broadly follows a power-law:

$$\frac{dN}{dE} \propto E^{-\Gamma}. \quad (2.34)$$

Below 10 GeV, the cosmic ray energy spectrum is dominantly composed of high-energy particles originating from the Sun. Below this energy, there are few cosmic rays that originate from outside the solar system due to “frozen in” magnetic fields carried by the solar wind. Cosmic rays below 10 GeV have a gyro-radius (see Eq. 2.25) smaller than the magnetic irregularities within this structure and are scattered out of the solar system (Schlickeiser, 2002). The cosmic ray spectrum broadly follows a power law with spectral index  $\Gamma \approx 2.7$  until the ‘knee’ at  $10^{15}$  eV = 1 PeV when it steepens to an index of 3. Ground-based cosmic ray detectors have reported a second knee at  $10^{17}$  eV where the spectrum steepens further to 3.3 until it flattens out to  $\approx 2.6$  at the ankle ( $10^{18}$  eV = 1 EeV) (Amenomori et al., 2008; Abraham et al., 2010; Apel et al., 2013; Aartsen et al., 2013; Abu-Zayyad et al., 2013). The knee and ankle feature is believed to be created due to the transition of Galactic cosmic-rays (from sources such as SNRs and PWNe) to extra-Galactic cosmic rays possibly originating from AGN (Thoudam et al., 2016). The cosmic ray spectrum then experiences a sharp cutoff at  $29 \times 10^{18}$  eV = 29 EeV due to the GKZ cutoff, where cosmic ray protons and nuclei interact with the CMB and rapidly lose their energy (Greisen, 1966; Zatsepin and Kuz'min, 1966).

### 2.2.4 PeVatrons

The transition from Galactic to extra-Galactic cosmic rays in the cosmic ray spectrum occurs between  $10^{15}$  eV and  $10^{18}$  eV with Galactic cosmic rays expected to contribute up to  $10^{17}$  eV = 100 PeV (Thoudam et al., 2016). Sources capable of accelerating particles up to and beyond 1 PeV =  $10^{15}$  eV are known as PeVatrons. Finding Galactic PeVatrons are key to understanding the mechanism of accelerating particles up to PeV energies.

Cosmic rays with energies 1 PeV and 100 PeV have gyroradii of  $\approx 0.4$  pc and 40 pc respectively, making their direct origin impossible to determine. However, cosmic rays interact with interstellar gas and magnetic fields near their birthplace to produce gamma rays with energies greater than 100 TeV (see Section 2.3). Therefore, any gamma-ray source with significant gamma-ray emission above 100 TeV is an indicator of a PeVatron

Table 2.3: Observed HAWC and LHAASO sources with significant gamma-ray emission greater than 100 TeV (Abeysekara et al., 2020; Cao et al., 2021). The sources equivalent to HESS J1825-137 are highlighted in blue.

	Source	TeV counterpart*	Accelerator*	$\sqrt{\text{TS}}$
<b>HAWC</b>	eHWC J1825-134	HESS J1825-137, HESS J1826-130	PWN	41.1
	eHWC J1907+063	HESS J1908+063	Unidentified	37.8
	eHWC J2019+368	2HWC J2019+367	Possible PWN <sup>a</sup>	32.2
<b>LHAASO</b>	LHAASO J0534+2202	Crab Nebula	PWN	17.8
	<b>LHAASO J1825-1326</b>	<b>HESS J1825-137</b>	PWN	<b>16.4</b>
	LHAASO J1839-0545	HESS J1837-069	Possible PWN	7.7
	LHAASO J1843-0338	HESS J1843-033, HESS J1844-030, SNR G28.6-0.1	Possible SNR	8.5
	LHAASO J1849-0003	HESS J1849-000, W43W	Possible PWN <sup>b</sup>	10.4
	LHAASO J1908+0621	HESS J1908+063, MGRO J1908+06	Possible SNR or PWN	17.2
	LHAASO J1929+1745	HESS J1930+188	Possible PWN or SNR	7.4
	LHAASO J1956+2845	2HWC J1955+285, SNR G66.0-0.0	Possible PWN SNR	7.4
	LHAASO J2018+3651	MGRO J2019+37	Possible PWN	10.4
	LHAASO J2032+4102	-	Possible PWN	10.5
	LHAASO J2108+5157	-	Possible PWN	8.3
	LHAASO J2226+6057	Boomerang Nebula	Possible SNR or PWN	13.6

\*: Counterparts are based on spatial correlation.

#### References

<sup>a</sup> Brisbois et al., (2018)

<sup>b</sup> Kuiper and Hermse, (2015)

The High-Altitude Water Cherenkov Gamma-ray observatory (HAWC) and the Large High Altitude Air Shower observatory (LHAASO) are observatories that detect the air shower triggered by gamma-rays (*LHAASO*; *HAWC*). Table 2.3 lists observed HAWC and LHAASO sources with significant gamma-ray emission above 100 TeV with possible counterparts and accelerator type (Abeysekara et al., 2020; Cao et al., 2021). In the past, SNRs have been regarded as the most likely source capable of accelerating protons up to PeV energies. However, there has been no firm identification of a SNR PeVatron and their suitability as a PeVatron has been called into question (Cristofari et al., 2018; Gabici et al., 2019; Cristofari, 2021; Brose et al., 2022). However, both the Crab Nebula and HESS J1825-137 are confirmed TeV PWN counterparts of LHAASO J0534+2202 and LHAASO J1825-1326 respectively. Out of the remaining LHAASO candidates, at least eight have possible PWN counterparts. PWN are now being considered as possible candidates to accelerate electrons up to PeV energies (Breuhaus et al., 2021; de Oña Wilhelmi et al., 2022). Vecchiotti et al., (2022) suggests that unresolved PWNe provides significant contribution to the diffuse gamma-ray emission above 100 TeV.

H.E.S.S. has only discovered one PeVatron that is postulated to be associated with the Galactic Center during an active phase HESS Collaboration et al., (2016). They highlighted that the current rate of particle acceleration is not powerful enough to explain the cosmic-ray flux at Earth. Alternatively, superbubbles and massive stellar clusters have been proposed as PeVatron candidates. Stellar clusters form within dense molecular clouds, creating an expanding ‘bubble’ of low density ISM (Ikeuchi, 1998). It has been suggested that turbulent plasma within superbubbles confine cosmic rays, allowing multiple shock fronts to accelerate them to high energies (e.g. see Vieu et al., (2022) and references within).

The Tibet AS $\gamma$  collaboration revealed the detection of diffuse gamma rays with energies between 100 TeV to  $10^3$  TeV = 1 PeV in the Galactic disk, indicating the presence of PeVatrons in the Galaxy (Amenomori et al., 2021). Similarly, LHAASO reported measurements of the diffusive gamma-ray emission up to 1000 PeV and suggests that TeV halos (see Section 2.1.2) significantly contribute to the diffusive emission up to the ultra-high energy band (Cao et al., 2023).

## 2.3 Gamma-rays: messengers of cosmic rays

Section 2.2.2 and Section 2.2.4 discussed how Galactic cosmic rays ( $E < 100$  PeV) scatter off magnetic field turbulence, thus do not preserve information about their origin. Therefore, alternate messengers for Galactic cosmic rays must be turned to. Gamma-rays are produced via hadronic (cosmic ray proton) and leptonic (cosmic ray electron) interactions with the ISM and/or radiation fields. This section will describe the history of gamma-ray astronomy and then delve deeper into their production processes.

### 2.3.1 A brief history

Gamma rays were first discovered in 1900 by Paul Villard while studying radium. Ernest Rutherford later realised in 1903 that this radiation was fundamentally different to alpha, beta and delta-rays and subsequently classified them as gamma rays. By reflecting gamma-rays from a crystal surface, Rutherford and Edward Andrade in 1913 proved the electromagnetic nature of gamma-rays and measured their wavelength (Rutherford and Andrade, 1913). Gamma-rays have the largest energy per photon and smallest frequency of the electromagnetic spectrum. On Earth, gamma rays are created by radioactive decay within the crust and the interaction of cosmic rays with the Earth's atmosphere. Gamma-ray astronomy began with the 1957 publication by Philip Morrison, with the prediction that solar flares produce gamma-rays (Morrison, 1958). We now know of many astrophysical sources that can produce gamma-rays. These include PWNe, SNRs, quasars and active Galactic nuclei. Current gamma-ray observatories include *Fermi* Gamma-ray Space Telescope (*The Fermi Gamma-ray Space Telescope* n.d.), the High Energy Stereoscopic System (*HESS*), MAGIC (*The Magic Telescopes*), HAWC (*HAWC*), VERITAS (*VERITAS*) and LHAASO (*LHAASO*). Details of gamma-ray detection will be discussed in Chapter 3.

### 2.3.2 Hadronic Gamma-Ray Emission

Relativistic protons (and nuclei) can collide with gas in the ISM to form charged and neutral pions via proton-proton (p-p) interactions:

$$p + p \rightarrow \pi^0 + \pi^+ + \pi^- \quad (2.35)$$

During p-p interactions, about half of the energy of the initial cosmic-ray proton is split among the neutral and charged pions (Hinton and Hofmann, 2009). The subsequent decay of the neutral pions produces gamma rays as per:

$$\pi^0 \rightarrow \gamma + \gamma \quad (2.36)$$

with each gamma ray carrying approximately one sixth of the initial proton energy (Hinton and Hofmann, 2009). The charged pions decay into muons, neutrinos and anti-neutrinos:

$$\begin{aligned}\pi^+ &\rightarrow \mu^+ + \nu_\mu \\ \pi^- &\rightarrow \mu^- + \bar{\nu}_\mu\end{aligned}\quad (2.37)$$

Similarly, muons go on to decay into electrons, positrons, neutrinos and anti-neutrinos:

$$\begin{aligned}\mu^- &\rightarrow e^- + \bar{\nu}_e + \nu_\mu \\ \mu^+ &\rightarrow e^+ + \nu_e + \bar{\nu}_\mu\end{aligned}\quad (2.38)$$

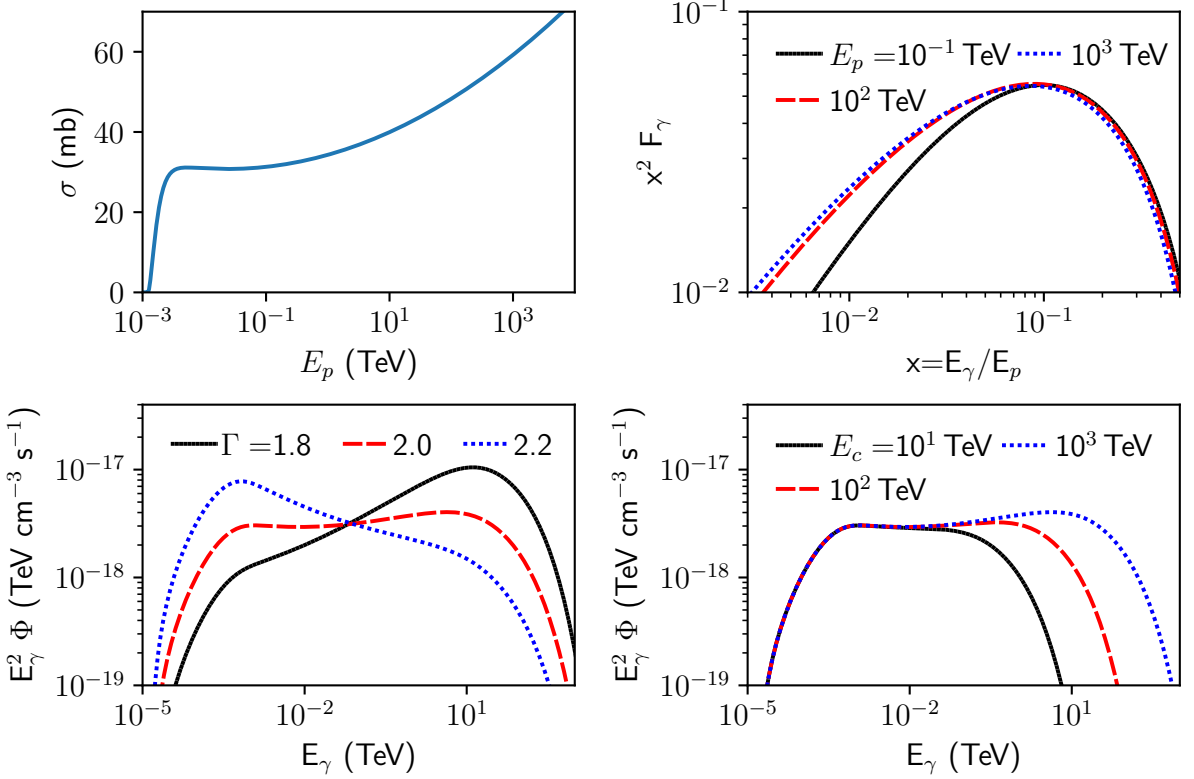


Figure 2.14: (top-left) Proton-proton interaction cross section as given by Eq. 2.41. (top-right) Hadronic gamma ray emission from a cosmic ray proton with energy  $E_p$  and target density  $n_H = 1 \text{ cm}^{-3}$  (bottom) Gamma ray spectra from p-p interactions from cosmic rays protons with an exp cutoff power law distribution ( $dN/dE \propto E^{-\Gamma} \exp(-E/E_c)$ ) with  $E_c = 10^3$  TeV (left) and  $\Gamma = 2.0$  (right).

For a distribution of protons with spectral index  $\Gamma$  and exponential cutoff energy  $E_c$ :

$$J_P(E_p) = A E_p^{-\Gamma} \exp\left(-\frac{E_p}{E_C}\right) \quad [\text{TeV}^{-1} \text{cm}^{-3}], \quad (2.39)$$

where  $A$  is a normalisation constant, the energy spectra of gamma-rays from proton-proton collisions is expected to follow:

$$\Phi(E_\gamma) = \frac{dN_\gamma}{dE_\gamma} = c n_H \int_{E_\gamma}^{\infty} \sigma_{pp}(E_p) J_p(E_p) F_\gamma(T_p, E_\gamma) \frac{dE_p}{E_p}, \quad (2.40)$$

where  $c$  is the speed of light and  $n_H$  is the density of the ambient medium. From the bottom panels in Fig. 2.14 it can be seen that the shape of the p-p gamma-ray SED is influenced by the distribution of cosmic ray protons. While the spatial morphology of

hadronic gamma-rays is shaped by interstellar gas, as seen in Eq. 2.40. In summary, gamma rays act as messengers for hadronic cosmic rays and carry information about the source and its surrounding environment.

The total inelastic cross section of p-p interactions for a proton of kinetic energy  $T_p$  (where the total energy is  $E_p = m_p c^2 + T_p$ ) is given by (Kafexhiu et al., 2014):

$$\sigma_{pp}(T_p) = \left( 30.7 - 0.96 \ln\left(\frac{T_p}{T_{\text{thr}}}\right) + 0.18 \ln^2\left(\frac{T_p}{T_{\text{thr}}}\right) \right) \left( 1 - \left(\frac{T_{\text{thr}}}{T_p}\right)^{1.9} \right)^3 \quad [\text{mb}] , \quad (2.41)$$

where  $T_{\text{thr}} = 2m_\pi + m_\pi^2/2m_p \approx 0.28$  GeV is the minimum proton kinetic energy to form a neutral pion ( $E_{\text{thr}} = 1.22$  GeV). The top-left panel of Fig. 2.14 shows the total inelastic cross section at different proton energies.

The time it takes for a proton to lose its energy (or ‘cool’) to a lower energy through p-p interactions in a medium with ambient density  $n_H$  is given by (Hinton and Hofmann, 2009):

$$\begin{aligned} \tau_{pp} &= \frac{1}{n c \kappa \sigma_{pp}(E)} \\ &\approx 5.3 \times 10^7 \left( n/\text{cm}^{-3} \right)^{-1} \quad [\text{yr}] . \end{aligned} \quad (2.42)$$

Eq. 2.42 shows that the cooling rate of protons is inversely proportional to the density of interstellar gas and approximately independent of the proton energy. Therefore, the brightness of gamma-rays towards a source of cosmic ray protons will correlate with the density morphology of the surrounding ISM gas.

Using GEANT4 models, Kafexhiu et al., (2014) parameterized the spectra of gamma-rays of energy ( $E_\gamma$ ) from a single proton with kinetic energy  $T_p$  to be:

$$F_\gamma(T_p, E_\gamma) = A_{\max}(T_p) F(T_p, E_\gamma) , \quad (2.43)$$

where  $A_{\max}$  is a function of the pion production and  $F(T_p, E_\gamma)$  describes the shape of the spectrum:

$$A_{\max}(T_p) = \sigma_\pi(T_p) \begin{cases} b_0/E_\pi^{\max} & , T_{\text{thr}} \leq T_p < 1 \text{ GeV} \\ b_1 \theta_p^{-b_2}/m_p \times \exp(b_3 \ln^2 \theta_p) & , T_p \geq 1 \text{ GeV} \end{cases} \quad (2.44a)$$

$$F_\gamma(T_p, E_\gamma) = \frac{\left(1 - X_\gamma^{\alpha(T_p)}\right)^{\beta(T_p)}}{\left(1 + X_\gamma/C\right)^{\gamma(T_p)}} , \quad (2.44b)$$

with  $\sigma_\pi$  being the  $\pi_0$  production cross section (see Kafexhiu et al., (2014) for parameterisation),  $\theta_p = T_p/m_p$ ,  $E_\pi^{\max}$  is the maximum total  $\pi_0$  energy in the laboratory frame,  $C = \lambda m_\pi/Y_\gamma^{\max}$ ,  $Y_\gamma = E_\gamma + m_\pi^2/(4E_\gamma)$ ,  $X_\gamma = (Y_\gamma - m_\pi)/(Y_\gamma^{\max} - m_\pi)$  and  $b_0 = 5.9$ ,  $b_1$ ,  $b_2$ ,  $b_3$ ,  $\alpha(T_p)$ ,  $\beta(T_p)$  and  $\gamma(T_p)$  are coefficients for the GEANT4 modelling (see Appendix F). The top-right panel of Fig. 2.14 shows the expected gamma-ray spectra from a proton with energy  $E = 0.1$  TeV, 100 TeV and 1000 TeV.

### 2.3.3 Leptonic Gamma-Ray emission

Cosmic ray electrons produce GeV to TeV gamma rays through synchrotron, inverse Compton and Bremsstrahlung interactions.

#### Synchrotron Radiation

Synchrotron radiation occurs when charged particles gyrate in a magnetic field of strength  $B$ . For a particle with mass  $m$ , charge  $q$  and Lorentz factor  $\gamma$ , the angular velocity is given by:

$$\omega = \frac{qB}{\gamma m} . \quad (2.45)$$

The total power radiated by a charged particle is given by Larmor's formula:

$$P = \frac{q^2 a^2}{6\pi\epsilon_0 c^3} \quad [\text{erg/s}] , \quad (2.46)$$

where  $a$  is the acceleration of the particle.



Figure 2.15: An electron travelling at velocity  $\vec{v}$  in the x-direction of the lab frame (*left*) with a uniform magnetic field on the x-y plane at angle  $\alpha$  to the x-axis. The rest frame of the particle (*right*) travels at velocity  $\vec{v}$  to the lab frame. The pure magnetic field  $\vec{B}$  (i.e. no electric fields) in the lab frame appears as a mixture of magnetic field  $\vec{B}'$  and electric field  $\vec{E}'$  in rest frame.

In the particles rest frame ( $\vec{v} = 0$ ), the force acted on the particle is described by:

$$\begin{aligned} \vec{F} &= m\vec{a} = -e(\vec{E} + \vec{v} \times \vec{B}) \\ &= -e\vec{E} , \end{aligned} \quad (2.47)$$

where  $\vec{E}$  is the electric field strength in the particle's rest frame. For the example shown in Fig. 2.15, the parallel and perpendicular component of the electric field in the particle's rest frame can be obtained using Lorentz transformations:

$$\vec{E}'_{\parallel} = \vec{E}_{\parallel} = 0 \quad (2.48a)$$

$$\vec{E}'_{\perp} = \gamma(\vec{E}_{\perp} + \vec{v} \times \vec{B}_{\perp}) = E'_z = \gamma v B \sin \alpha . \quad (2.48b)$$

Therefore the power radiated is given by:

$$P = -\frac{(\gamma evB \sin \alpha / m)^2 e^2}{6\pi\epsilon_0 c^3} , \quad (2.49)$$

where the negative in Eq. 2.49 represents the energy lost by the particle. Power is Lorentz invariant, hence Eq. 2.49 applies to both the lab and rest frame in Fig. 2.15. While both protons and electrons can emit synchrotron radiation, electrons radiate more power than protons of the same energy due to the inverse proportionality of the particles mass in Eq. 2.49. Henceforth, only synchrotron radiation from electrons will be considered. The power radiated by a single electron through synchrotron radiation is:

$$P = -2\sigma_T \gamma^2 c U_B \sin^2 \alpha , \quad (2.50)$$

with the magnetic energy density defined to be  $U_B = B^2/2\mu_0$  and the Thompson cross section is defined as:

$$\sigma_T = \frac{8\pi}{3} \left( \frac{e^2}{4\pi\epsilon_0 m_e c^2} \right)^2 = \frac{8\pi}{3} r_0^2 , \quad (2.51)$$

where  $r_0 = e^2/4\pi\epsilon_0 m_e c^2$  is the classical electron radius. For electrons travelling in random directions:

$$\langle \sin^2 \alpha \rangle = \frac{1}{2} \int_{-1}^1 \sin^2 \alpha d\cos \alpha = \frac{2}{3} . \quad (2.52)$$

The mean power loss is given by:

$$\langle P \rangle = \frac{dE}{dt} = -\frac{4}{3} \sigma_T \gamma^2 c U_B . \quad (2.53)$$

The spectrum,  $P(\nu)$ , of synchrotron emission emitted by a single electron with pitch angle  $\alpha$  and magnetic field  $B$  is given by (Manolakou et al., 2007):

$$j(\nu) = \frac{dN}{dE} = \frac{\sqrt{3}e^3 B \sin \alpha}{mc^2} \frac{\nu}{\nu_c} \int_{x=\nu/\nu_c}^{\infty} K_{\frac{5}{3}}(t) dt , \quad (2.54)$$

where  $K_{\frac{5}{3}}$  is the modified Bessel function of the second kind. The synchrotron spectrum,

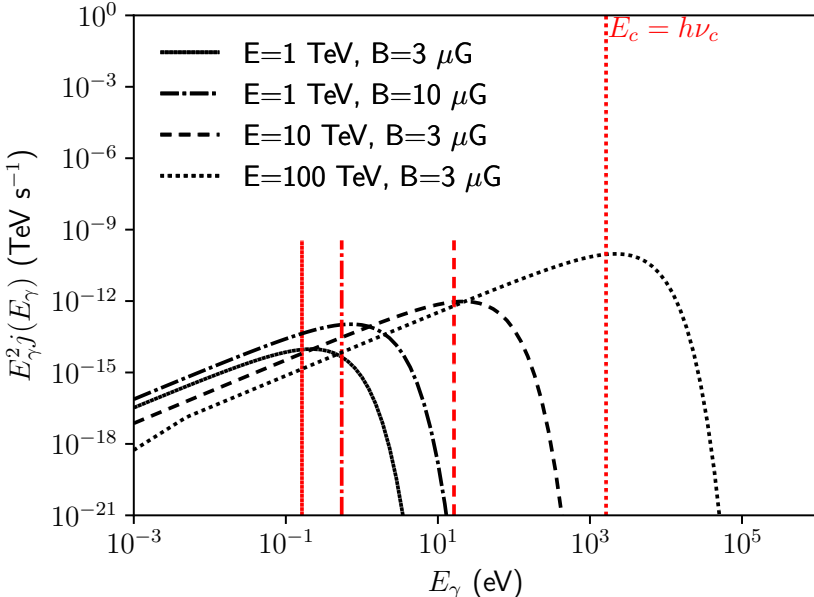


Figure 2.16: Synchrotron emission from an electron with energy  $E$  in magnetic field  $B$ . The red vertical lines represent the equivalent critical energy ( $E_c = h\nu_c$ ).

$P(\nu)$ , peaks at ‘critical frequency’  $\nu = \nu_c$  (see Fig. 2.16):

$$\nu_c = \gamma^2 \frac{3eB \sin \alpha}{4\pi mc} . \quad (2.55)$$

Equivalently, the synchrotron spectrum peaks at photon energy  $E_\gamma$  (Hinton and Hofmann, 2009):

$$\frac{E_\gamma}{\text{eV}} = 0.087 \left( \frac{E_e}{\text{TeV}} \right)^2 \frac{B}{\mu\text{G}} , \quad (2.56)$$

where  $E_e$  is the energy of the initial electron. Therefore, observations of synchrotron emission  $\gtrsim 300$  keV is a strong indicator of a source accelerating electrons up to PeV energies.

### Inverse-Compton emission

Inverse-Compton emission occurs when an electron scatters off a photon:

$$\gamma_{\text{low E}} + e^-' \rightarrow \gamma_{\text{TeV}} + e^- , \quad (2.57)$$

where the final photon energy is greater than the original photon energy at cost of the electron energy ( $E_{e^-'} > E_{e^-}$ ). Photon fields such as the CMB, infra-red photons, visible light, UV and X-rays provide target photons for the electron to scatter up to  $\gamma$ -ray energies.

Fig. 2.17 shows a photon with momentum  $\left[ \frac{E_i}{c}, \frac{E_i}{c} \cos \theta_i, \frac{E_i}{c} \sin \theta_i, 0 \right]$  scattering off an electron in the lab and rest frame of the electron. The Lorentz transformation of the initial photon energy from the lab frame ( $E_i$ ) to the rest frame ( $E'_i$ ) is given by:

$$E'_i = \gamma E_i (1 - \beta \cos \theta_i) , \quad (2.58)$$

where  $\beta = v/c$  and  $v$  is the electron velocity. The Lorentz transformation of the final photon energy from the rest frame to the lab frame is given by:

$$E_f = \gamma E'_f (1 + \beta \cos \theta'_f) . \quad (2.59)$$

Assuming elastic scattering, the photon has the same energy before and after the collision in the rest frame of the electron ( $E'_i = E'_f$ ). Therefore the final energy in the lab frame is:

$$E_f = \gamma^2 E_i (1 - \beta \cos \theta_i) (1 + \beta \cos \theta'_f) . \quad (2.60)$$

The photon scatters off the electron isotropically (*i.e.*  $\langle \cos \theta'_f \rangle \approx 0$ ):

$$\langle E_f \rangle = (1 - \beta \cos \theta_i) \gamma^2 E_i . \quad (2.61)$$

The rate of interaction,  $R$ , for electrons in photon field with density  $n$  at angle  $\theta_i$  can be described by:

$$R = n \sigma_T (1 - \beta \cos \theta_i) , \quad (2.62)$$

where  $\sigma_T$  is the Thompson cross section. The rate of electron energy loss over a solid angle  $d\Omega = 2\pi \sin \theta_i d\theta = 2\pi d(\cos \theta_i)$  is given by:

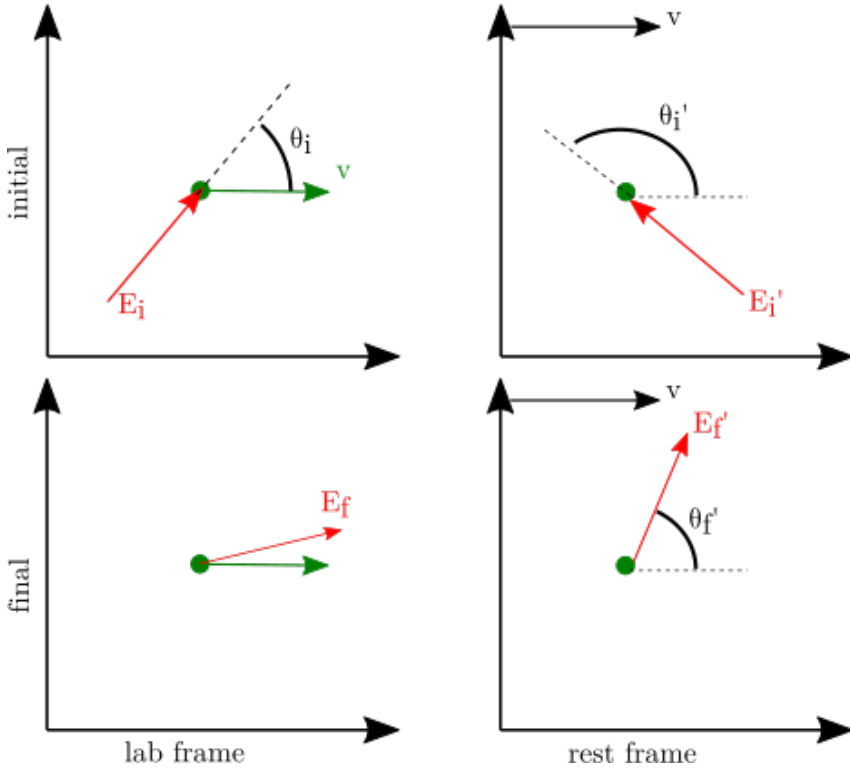


Figure 2.17: A photon with energy  $E_i$  scatters off an electron (travelling at velocity  $v$ ) at angle  $\theta$  in the lab frame (*left*). In the rest frame of the electron (*right*), the photon collides with electron at angle  $\theta'$  and energy  $E'_i$ . The top and bottom panels describe the situation before and after the collision respectively. After scattering the photon has energy  $E_f$  and  $E'_f$  in the lab frame and electron rest frame respectively

$$\begin{aligned} \frac{dE}{dt} &= -\frac{d\Omega}{4\pi} R c \langle E_f \rangle \\ &= -n E_i \sigma_T c \gamma^2 \frac{d \cos \theta}{2} (1 - \cos \theta_i)^2 . \end{aligned} \quad (2.63)$$

Integrating over all  $\theta_i$  gives the electron energy loss for Inverse Compton Interactions as:

$$\frac{dE_e}{dt} = -\frac{4}{3} U_{\text{rad}} \sigma_T c \gamma^2 , \quad (2.64)$$

where  $U_{\text{rad}} = n(E_i) E_i$  is the radiation energy density and  $n(E_i)$  is the number density.

The number density of target photons provided by photon fields such as the CMB can be described by a blackbody spectrum (see Section 4.1.3). Therefore, the spectrum from a single electron with energy  $E_e$  scattering of a target photon with energy in range  $\epsilon + d\epsilon$  is described by (BLUMENTHAL and GOULD, 1970):

$$\begin{aligned} \frac{dN}{dE_\gamma} &= \frac{3\sigma_T m c^3}{4\gamma} \int_{E_\gamma/4\gamma^2}^{E_\gamma} \frac{n(\epsilon) d\epsilon}{\epsilon} f(q, \Gamma) \\ f(q, \Gamma) &= 2q \ln q + (1+2q)(1-q) + \frac{1}{2} \frac{(\Gamma q)^2}{1+\Gamma q} (1-q) , \end{aligned} \quad (2.65)$$

where:

$$q = \frac{E_\gamma}{\Gamma(E_e - E_\gamma)} \quad (2.66a)$$

$$\Gamma = \frac{4\epsilon\gamma}{m_e c^2} . \quad (2.66b)$$

$\Gamma_E$  determines whether the scattering falls under the Thompson limit ( $\Gamma \ll 1$ ) or Klein-Nishina limit ( $\Gamma \gtrsim 1$ ). The Thompson limit applies when the product of the incident and scattered photon energy is much less than the square of the rest mass of the electron (BLUMENTHAL and GOULD, 1970). The Klein-Nishina limit takes in account the suppression of IC scattering for relativistic electrons.



Figure 2.18: IC spectrum from an electron of energy  $E$  interacting with the CMB. The red vertical lines represent the energy at which the IC emission approximately peaks assuming a CMB photon has energy  $\approx 7 \times 10^{-4}$  eV.

In the Thompson regime, the inverse-Compton emission peaks at (Hinton and Hofmann, 2009):

$$\begin{aligned} \frac{E_{\gamma,p}}{\text{TeV}} &\approx \frac{E_e}{\text{TeV}} \frac{2.1b}{\left(1 + (2.1b)^{0.8}\right)^{1/0.8}} \\ b &\approx 15 \frac{E_e}{\text{TeV eV}} \frac{\epsilon}{e} . \end{aligned} \quad (2.67)$$

Eq. 2.67 is used to approximate the energy range of the cosmic ray electron population. In the Klein-Nishina regime, The LHAASO Collaboration et al., (2021) makes the approximation:

$$\frac{E_e}{\text{PeV}} = 2.15 \left( \frac{E_{\gamma,p}}{\text{PeV}} \right)^{0.77} , \quad (2.68)$$

which is accurate to within 10% for electrons within energy range [30 TeV, 3 PeV]. Therefore, observations of gamma rays with energy  $\gtrsim 200$  TeV from IC interactions is a strong indicator that the source is a leptonic PeVatron (see Section 2.2.4).

### Bremsstrahlung Emission

Bremsstrahlung emission occurs when an electron experiences deacceleration due to the presence of an atomic nucleus. For a single electron with energy  $E_e$  passing through a gas with number density  $n$ , the radiated photon spectrum per electron can be described by (BLUMENTHAL and GOULD, 1970):

$$\frac{dN}{dt dk} = cn d\sigma , \quad (2.69)$$

where the electron has initial & final energy,  $E_i$  &  $E_f$  respectively. By conservation of energy, the final photon has energy  $k = E_i - E_f$ . The differential cross section,  $d\sigma$ , can be written as (Bethe and Heitler, 1934):

$$d\sigma = \alpha r_0^2 \left( \frac{dk}{k} \right) \frac{1}{E_i^2} \left[ (E_i^2 + E_f^2) \phi_1 - \frac{2}{3} E_i E_f \phi_2 \right] , \quad (2.70)$$

with  $\alpha = 1/137$  is the fine structure constant and for a unshielded charge:

$$\phi_1 \approx \phi_2 = 4Z^2 \left[ \ln \left( \frac{2E_i E_f}{k} \right) - \frac{1}{2} \right] . \quad (2.71)$$

The SED of Bremsstrahlung emission is proportional to the density of the ambient medium (see Eq. 2.69). Therefore in cases such as pulsar wind nebulae, where the ISM has been “swept” out by the progenitor stellar wind, inverse Compton and synchrotron emission will generally dominate over Bremsstrahlung emission. The electron energy loss rate, as derived by BLUMENTHAL and GOULD, (1970), for an electron interacting with ambient gas with density  $n_z$  and atomic number  $Z$  is related by:

$$\frac{dE_e}{dt} = -\frac{n_z Z(Z+1.3)e^6}{16\pi^3 \hbar \epsilon_0^3 m_e c^4} E_e \left[ \ln \left( \frac{183}{Z^{1/3}} \right) + \frac{1}{8} \right] . \quad (2.72)$$

### Total Leptonic Radiative Processes

The cooling time of an interaction, the time it takes for an electron to cool to a lower kinetic energy, can be used to determine the dominant process amongst the three leptonic processes (synchrotron, inverse Compton and Bremsstrahlung). The cooling time is defined to be:

$$\begin{aligned} \tau &= \int_{\gamma'}^{\gamma} \frac{d\gamma''}{\dot{\gamma}} \\ &\approx \frac{\gamma}{\dot{\gamma}} \text{ for } \gamma' \approx \gamma , \end{aligned} \quad (2.73)$$

where an electron cools from Lorentz factor  $\gamma'$  to  $\gamma$  at rate  $\dot{\gamma}(\gamma'')$ . The cooling time for synchrotron, inverse Compton and Bremsstrahlung interactions are given by (Hinton and Hofmann, 2009):

$$\tau_{\text{sync}} \approx 1.3 \times 10^7 \left( \frac{B}{\mu\text{G}} \right)^{-2} \left( \frac{E_e}{\text{TeV}} \right)^{-1} \text{[yr]} \quad (2.74\text{a})$$

$$\tau_{\text{IC}} = 3 \times 10^5 \left( \frac{U_{\text{rad}}}{\text{eV cm}^{-3}} \right)^{-1} \left( \frac{E_e}{\text{TeV}} \right)^{-1} \ell^{-1} \text{[yr]} \quad (2.74\text{b})$$

$$\tau_{\text{brem}} \approx 3.9 \times 10^7 \left( n/\text{cm}^{-3} \right)^{-1} \text{[yr]}, \quad (2.74\text{c})$$

where:

$$\ell(\gamma, \epsilon_0) = (1 + 4\gamma\epsilon_0)^{-\frac{3}{2}}, \quad (2.75)$$

considers the Thompson limit or Klein-Nishina limit of inverse-Compton scattering with



Figure 2.19: Cooling times for electrons at different energies in a uniform cloud with density  $n = 10 \text{ cm}^{-3}$  and magnetic field  $B = 0.1, 1, 10 \& 100 \mu\text{G}$ . The solid blue line shows the cooling time for inverse-Compton interactions against the CMB ( $U_{\text{CMB}} = 0.26 \text{ eV cm}^{-3}$ ). The dashed yellow line shows the cooling time for synchrotron interactions while the dotted green line shows the cooling time for Bremsstrahlung interactions.

a photon with dimensionless energy  $\epsilon_0 = h\nu/m_ec^2$  and frequency  $\nu$ . Manolakou et al., (2007) describes the total cooling rate as:

$$\dot{\gamma}_{\text{total}} = b_s \gamma^2 + \sum_i b_{\text{IC}} \gamma^2 F_{\text{KN}}(\gamma) + b_C \left( \ln \gamma + b_C^0 \right) + b_B \gamma \left( \ln \gamma + b_B^0 \right), \quad (2.76)$$

where  $\sum_i$  sums over all radiation fields contributing to the Inverse-Compton gamma-ray flux. The coefficients  $b$ :

- $b_s = \frac{4\sigma_T}{3m_e c} u_B = 1.292 \times 10^{-15} (B/\text{mG})^2 [\text{s}^{-1}]$  is a synchrotron loss constant.
- $b_{\text{IC}} = b_s \frac{u_0}{u_B} = 5.204 \times 10^{-20} (u_0/\text{eV cm}^{-3}) [\text{s}^{-1}]$  is an inverse Compton constant.
- $b_C = \frac{2\pi e^4 n_e}{m_e^2 c^3} = 1.491 \times 10^{-14} n_e [\text{s}^{-1}]$  is the Coulomb loss constant.
- $b_B = \frac{4e^6 n_e}{m_e^2 c^4 \hbar} = 1.37 \times 10^{-16} n_e [\text{s}^{-1}]$  is the Bremsstrahlung loss constant.
- $b_C^0 = \ln\left(\frac{m_e^3 c^4}{4e^2 n_e \hbar^2}\right) + \frac{3}{4} = -\ln n_e + 73.4$
- $b_B^0 = \ln 2 - \frac{1}{3} = 0.36$

and  $m_e$  and  $e$  being the mass & charge of the electron respectively,  $u_0$  and  $u_B$  are the energy densities of the photon and magnetic fields and  $n_e$  is the electron density number. The function  $F_{\text{KN}}$  takes account the full Klein-Nishina cross section for Inverse Compton scattering (Manolakou et al., 2007):

$$F_{\text{KN}} = \frac{1}{u_0} \int_0^\infty \mathcal{J}(\gamma, \epsilon_0) u_{\epsilon_0} d\epsilon_0 . \quad (2.77)$$

For a Planckian black body distribution of photon energies,  $F_{\text{KN}}$  can be approximated by:

$$\begin{aligned} F_{\text{KN}} &= (1 + 4\gamma\epsilon_{\text{eff}})^{-3/2} \\ \epsilon_{\text{eff}} &= \frac{2.8kT}{m_e c^2} . \end{aligned} \quad (2.78)$$

For Bremsstrahlung losses in neutral hydrogen, Eq. 2.76 becomes:

$$\dot{\gamma}_{\text{total}} = b_s \gamma^2 + \sum_i b_{\text{IC}} \gamma^2 F_{\text{KN}}(\gamma) + b_C (3 \ln \gamma + 18.8) + 5.3b_B . \quad (2.79)$$

Fig. 2.19 shows the individual and total cooling time for electrons for different electron energies in a uniform cloud with varying magnetic field strengths. Synchrotron losses dominate in high magnetic fields and/or high electron energies. For example, synchrotron losses are dominant for electrons greater  $\approx 85$  TeV than in a magnetic field of 3  $\mu\text{G}$  and dominant for magnetic fields greater than  $\approx 12$   $\mu\text{G}$  for 1 TeV electrons scattering against CMB photons ( $u_0 = 0.26 \text{ eV cm}^{-3}$  and  $T = 2.7 \text{ K}$ ).

Fig. 2.16 and Fig. 2.18 shows the synchrotron and IC emission from a single electron energy. The SED from an electron distribution  $J_e(E_e)$  is described by:

$$\Phi(E_\gamma) = \int_{E_\gamma}^\infty J_e(E_e) F_\gamma(E_\gamma, E_e) dE_e , \quad (2.80)$$

where  $F_\gamma(E_\gamma, E_e) dE_e$  is given by Eq. 2.54, Eq. 2.65 and Eq. 2.69. Overall, the flux ratio of IC to and synchrotron emission in the Thompson regime is related by (Aharonian et al., 1997):

$$\frac{f_{\text{IC}}(E)}{f_s(E)} = \frac{U_{\text{rad}}}{U_B} . \quad (2.81)$$

Electrons escaping the PWN cool at a rate that is dependent on the surrounding environment (Eq. 2.79), affecting the energy distribution of cosmic rays and the subsequent multiwavelength emission (Eq. 2.80). Therefore, Chapter 5 will describe the evolution of cosmic rays (leptonic and hadronic) and the subsequent SED.

# Chapter 3

## Gamma Ray Astronomy

Chapter 2 discussed how PWNe like HESS J1825-137 accelerate cosmic rays up to TeV energies and how gamma-rays can be used as alternative messengers. To study accelerators like HESS J1825-137, astronomers require instruments that are capable of observing gamma-rays up to TeV energies.

Upon reaching the Earth atmosphere, gamma rays produce air showers comprising of billions of secondary particles and photons. Astronomers in the early 20th century placed Geiger counters on balloons to detect gamma rays at high altitude. Now, satellites like *Fermi*-LAT are used to observe gamma rays less than  $\approx 0.1$  TeV before they enter the atmosphere (Michelson et al., 2010). Alternatively, ground based observatories analyse the air shower itself to reconstruct information about the original gamma-ray. This is a method used by the High Energy Stereoscopic System (H.E.S.S.) to study TeV gamma-ray sources like HESS J1825-137.

This section will provide a brief overview of how gamma rays interact with the atmosphere and the techniques used to observe the subsequent shower of particles. Finally, there will be a description of the gamma-ray observatories whose data products were utilised in this thesis.

### 3.1 Air Showers

The presence of molecules in the atmosphere provides a target for gamma rays and cosmic-ray protons to interact and produce lower energy particles (electrons, positrons, pions). The daughter particles then go on to decay or interact with the atmosphere to produce even lower energy particles. This process cascades to form an air shower which is shown in Fig. 3.1 and Fig. 3.2.

The morphology and structure of the air shower is dependent on the atmosphere. Atmospheric depth is defined to be the attitudinal integral of atmospheric density above height  $h$  (Stanev, 2010):

$$X = \int_h^\infty \rho(h') dh' , \quad (3.1)$$

with the units of atmospheric depth being  $\text{g cm}^{-2}$ . Atmospheric depth is a proxy for the amount of material above height  $h$ . For a constant temperature, the relationship between height and atmospheric depth becomes:

$$X = X_0 \exp(-h/h_0) , \quad (3.2)$$

where  $h_0$  is the scale height of the atmosphere and  $X_0 = 1030 \text{ g cm}^{-2}$  is the atmospheric depth at sea level.

### 3.1.1 Gamma-ray Air Showers

To produce an electron-positron pair, a gamma ray must be in the vicinity of a nucleus to conserve both momentum and energy. When a gamma ray above a few GeV enters the atmosphere, the presence of atmospheric nuclei allows pair production to occur:



where the daughter electron and positron each have kinetic energy:

$$E_{e^\pm} \approx \frac{1}{2}(E_\gamma - 2m_e c^2) , \quad (3.4)$$

with  $E_\gamma$  is the energy of the original gamma ray. Hence, the original gamma ray must have a threshold energy of twice the rest mass of the electron ( $m_e c^2 = 511 \text{ keV}$ ) to undergo pair production.

Electrons and positrons interact with atmospheric nuclei through Bremsstrahlung interactions (see Section 2.3.3), resulting in the production of photons:



with a cross section,  $d\sigma_{\text{brem}}$ , described by Eq. 2.70 . The distance that an electron/-positron travels before radiating a photon through Bremsstrahlung interactions is given by (Matthews, 2005):

$$d = \lambda_r \ln 2 , \quad (3.6)$$

where the radiation length,  $\lambda_r$ , is characteristic to a material and relates to the energy loss of high-energy particles as it transverses through a medium.

Positrons can also annihilate with atmospheric electrons to produce two photons:



with each daughter photon having threshold energy  $E_{\text{thr}} \geq m_e c^2$ . If the daughter photons have energy greater than twice the rest mass of an electron (Eq. 3.4), they can undergo electron-positron production. The cross section for electron-positron production,  $\sigma_{\text{pair}}$ , can be given in terms of the cross section for Bremsstrahlung interactions,  $\sigma_{\text{br}}$ , by:

$$\sigma_{\text{pair}}(E_e, E_\gamma) = \sigma_{\text{br}}(E_e, E_\gamma) \frac{E_e^2}{E_\gamma^2} \approx \frac{7}{9} \sigma_{\text{br}}(E_e, E_\gamma) , \quad (3.8)$$

where  $k$  is the energy of the resulting photons. 2

Heitler's model of electromagnetic air showers (see Fig. 3.1) provides a method to model the development of the electromagnetic shower (Bethe and Heitler, 1934). It assumes that the radiation length for both pair production and Bremsstrahlung interactions are identical due to a similar cross section. Therefore, the atmospheric depth of the air shower after  $n$  interactions is:



Figure 3.1: Heitler's model of the formation of an air shower triggered by a gamma ray (Heitler, 1954). The gamma ray undergoes pair production to produce an electron and positron. In turn, the electron/positron undergo Bremsstrahlung interactions and/or electron-positron annihilation to produce photons. This process cascades into the air shower.

$$X = nd = n\lambda_r \ln 2 . \quad (3.9)$$

The number of particles (electrons, positrons and photons) in the air shower after  $n$  interactions is given by (Matthews, 2005):

$$N = 2^n = \exp(X/\lambda_r) , \quad (3.10)$$

with the average particle energy after  $n$  interactions being:

$$E_n = \frac{E_0}{2^n} = E_0 \exp(-X/\lambda_r) , \quad (3.11)$$

where  $E_0$  is the energy of the original gamma ray photon that triggered the air shower.

The exponential growth of the air shower continues until the daughter particles reach a critical energy  $E_c$  ( $\approx 85$  MeV in air) where ionisation losses dominate over radiative losses (Heitler, 1954). At this point, the shower has the maximum number of particles:

$$N_{\max} = 2^{n_c} = \frac{E_0}{E_c} , \quad (3.12)$$

where  $n_c$  is the number of interactions when critical energy is reached. Therefore:

$$n_c = \log_2 \frac{E_0}{E_c} = \frac{\ln \frac{E_0}{E_c}}{\ln 2} . \quad (3.13)$$

Therefore, the air shower depth after  $n_c$  interactions:

$$X_{\max} = \lambda_r \ln \frac{E_0}{E_c} . \quad (3.14)$$

The elongation rate of an air shower is defined to be the rate of change of the depth of shower maximum with energy (Matthews, 2005):

$$\Lambda = \frac{dX_{\max}}{d \log_{10} E_0} . \quad (3.15)$$

Combining Eq. 3.14 & 3.15 gives:

$$\Lambda_\gamma = 2.3\lambda_r \text{ per decade of primary energy} . \quad (3.16)$$

In air, electromagnetic air showers have elongation rate of  $85\text{g cm}^{-2}$  per decade of primary energy.

Further studies (Matthews, 2005) showed that the maximum number of electrons predicted by Heitler's model,  $N_{e, H}$  overestimates the number of particles compared to that measured by experiments. Matthews, (2005) revised the maximum number of particles,  $N_{e, M}$ , to be:

$$N_{e, M} = \frac{N_{e, H}}{10} . \quad (3.17)$$

In summary, Heitler noted that in electromagnetic cascade showers (Heitler, 1954):

1. The maximum number of particles in the cascade is proportional to the energy of the initial gamma ray  $E_{\gamma,0}$ .
2. The depth of the shower is proportional to  $\log E_0$ .
3. The shower development is independent of the atmospheric 'material' provided that atmospheric thickness is measured in cascade units and energy in units of critical energy.
4. The angular spread of an electromagnetic shower is not large as the emission of light from Bremsstrahlung interactions and pair production is at small angles assuming the initiating particle has high energy.

Overall, Heitlers model can be used to predict the basic electromagnetic air shower structure.

### 3.1.2 Cosmic-ray Air Showers

Both gamma rays and cosmic rays initiate air showers upon entering the atmosphere. Therefore, any observatory dedicated to studying gamma-rays must be able to distinguish between a gamma-ray air shower and cosmic-ray air shower.

Cosmic rays (protons or nuclei) above a few GeV undergo proton-proton collisions (see Section 2.3.2) with atmospheric nuclei and produce pions.



where the ratio of charged pions to neutral pions is approximately 2 : 1. Charged pions decay into neutrinos and muons, with muons then decaying into electrons, positrons, neutrinos and anti-neutrinos. The presence of muons in an air shower can indicate whether the shower was triggered by a gamma ray or cosmic ray. Electrons and positrons interact with the atmosphere via Bremsstrahlung and electron-positron annihilation to produce photons as discussed in Section 3.1.1. Unlike gamma-ray air showers, the original cosmic ray can go on to undergo further proton-proton collisions to increase the number of charged pions in the atmosphere. This development of cosmic-ray air showers is shown in Fig. 3.2.



Figure 3.2: The formation of an air shower triggered by a cosmic ray entering the atmosphere. The cosmic ray undergoes proton-proton interactions to produce neutral and charged pions. Neutral pions decay into two photons (which can trigger an electromagnetic air shower) while charged pions decay into muons and neutrinos. The muons decay into electrons/positrons and neutrinos. Depending on its energy, the original cosmic ray can undergo further proton-proton collision.

The decay length,  $d$ , is defined to be the distance a particle with Lorentz factor  $\gamma$  will travel before it decays (Matthews, 2005):

$$d = \beta\gamma c\tau , \quad (3.19)$$

where ( $\tau$  is the mean lifetime of the particle). The mean life time of charged pions is approximately  $2.6 \times 10^{-8}$  s, while neutral pions have a mean life of  $8.4 \times 10^{-17}$  s. This gives the decay length for neutral and charged pions to be  $d_{\pi_0} = \gamma \times 2.51 \times 10^{-6}$  cm and  $d_{\pi^\pm} = 780\gamma$  cm respectively. Compared to charged pions, neutral pions decay essentially where they were created.

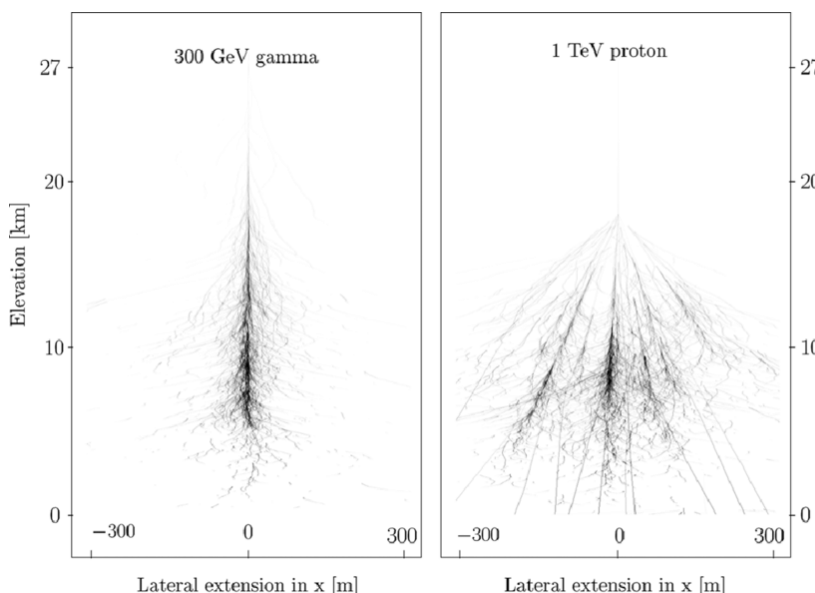


Figure 3.3: Monte Carlo simulations of an air shower triggered by a 0.3 TeV gamma-ray (left) vs an air shower triggered by a 1 TeV cosmic-ray proton (right). Image courtesy of (Aharonian et al., 2008)

After  $n$  interactions, there are  $N_{\pi_{\pm}}$  charged pions with individual energy (Matthews, 2005):

$$E_{\pi} = \frac{E_0}{(\frac{3}{2}N_{\text{ch}})^n} , \quad (3.20)$$

where  $E_0$  is the energy of the initial cosmic ray and  $N_{\text{ch}}$  is the multiplicity of charged particles produced in hadronic interactions.

Matthews, (2005) gives the number of interactions (of the initial cosmic ray) for a pion to reach critical energy,  $E_c^{\pi}$ , to be:

$$n_c = \frac{\ln(E_0/E_c^{\pi})}{\frac{3}{2}N_{\text{ch}}} = 0.85 \log_{10} \left( \frac{E_0}{E_c^{\pi}} \right) , \quad (3.21)$$

occurring when the probability of pion decay exceeds the probability that it survives to the next interaction. The original energy of the cosmic ray is now divided between  $N_{\pi}$  pions and  $N_{\text{max}}$  electromagnetic particles:

$$\begin{aligned} E_0 &= N_{\mu}E_c^{\pi} + N_e^e N_{\text{max}} \\ &\approx 0.85 \text{ GeV} (N_e + 24N_{\mu}) , \end{aligned} \quad (3.22)$$

where  $N_e = N_{\text{max}}/10$  from Eq. 3.17

The atmospheric depth where the number of air shower particles is at an maximum,  $X_{\text{max}}^p$ , is found through (Matthews, 2005):

$$X_{\text{max}}^p = X_0 + \lambda_r \ln \left( \frac{E_0}{3N_{\text{ch}}E_c^e} \right) = 470 + 58 \log_{10} (E_0/1 \text{ PeV}) \text{ g cm}^{-2} , \quad (3.23)$$

where  $X_0$  is the atmospheric depth where the shower was initiated. The atmospheric depth maximum can be compared to the atmospheric depth maximum for gamma-ray air showers via:

$$X_{\text{max}}^p = X_{\text{max}}^{\gamma} + X_0 - \gamma_r \ln 3N_{\text{ch}} . \quad (3.24)$$

This gives the elongation rate for proton initiated air showers:

$$\begin{aligned} \Lambda^p &= \Lambda^{\gamma} + \frac{d}{d \log_{10} E_0} [X - \lambda_r \ln 3N_{\text{ch}}] \\ &\approx 58 \text{ g cm}^{-2} \text{ per decade of primary energy} . \end{aligned} \quad (3.25)$$

Fig. 3.3 compares Monte Carlo simulations of air showers triggered by a 0.3 TeV gamma ray and a 1 TeV cosmic-ray proton, where the hadronic air shower is more spread out than gamma-ray air shower. Additionally, any photons produced by proton-proton interactions can trigger an electromagnetic shower within a hadronic air shower. Using this information, gamma-ray observatories can analyse the air shower to determine whether the initial particle was a gamma ray or proton.

### 3.1.3 Cherenkov Light and Cherenkov Telescopes

Particles produced in an electromagnetic air shower can travel faster than the speed of light in the atmosphere. The speed of light,  $c_n$ , in a medium with refractive index  $n$  is given by:

$$c_n = \frac{c}{n} , \quad (3.26)$$

where  $c = 3.0 \times 10^8 \text{ m s}^{-1}$  and  $n > 1$ .

A charged particle polarises the medium it is travelling through. As the particle propagates, the polarised medium oscillates back to its resting state and emits electromagnetic radiation. This is shown in Fig. 3.4, where the resulting radiation can be described by Huygen's construction of light. For a particle that is travelling with velocity less than the speed of light, the electromagnetic radiation wave-fronts will destructively interfere with each other with no net production. If the charged particle is travelling faster than the speed of light in that medium, the electromagnetic wave-fronts will constructively interfere and there is a net production of light.



Figure 3.4: Huygen's construction of a charged particle travelling at speed  $v$  in a medium of refractive index  $n$ . Cherenkov light is emitted at angle  $\theta$  when the particle is travelling faster than the speed of light in the medium

Cherenkov light is emitted in a cone in the direction of particle propagation (see Fig. 3.4). At time  $t = 0$ , a photon is emitted at angle  $\theta$  to the particle propagation. After time  $t$ , the photon has travelled distance  $ct/n$  and the particle has travelled  $\beta ct$  ( $\beta = v/c$ , with  $v$  being the velocity of the particle). Hence:

$$\begin{aligned} \cos \theta &= \frac{ct}{n} \frac{1}{\beta ct} \\ &= \frac{1}{n\beta} . \end{aligned} \quad (3.27)$$

For ultra-relativistic particles,  $\beta \rightarrow 1$  and the light is emitted at angle  $\theta \rightarrow \cos^{-1}(1/n)$ .

The threshold for particle with mass  $m$  to produce Cherenkov light occurs when it is travelling at the speed of light in a medium ( $v = c/n$ ):

$$E_{\text{thr}} = \gamma mc^2 = \frac{mc^2}{\sqrt{1 - 1/n^2}} . \quad (3.28)$$

For electrons at sea level ( $n = 1.0003$ ), the threshold energy is  $\approx 21 \text{ MeV}$ . In water,  $n = 1.33$ , the threshold energy decreases to  $1 \text{ MeV}$ . Observatories such as the Pierre Auger observatory and the High Altitude Water Cherenkov gamma-ray observatory use water tanks (which has a higher refractive index  $n = 1.33$ , hence slower speed of light than air) to produce Cherenkov light (Stanev, 2010).

The air shower forms an observable pool of Cherenkov light on the ground as shown by the left-hand panel of Fig. 3.5. At sea level, the radius of the light cone is approximately

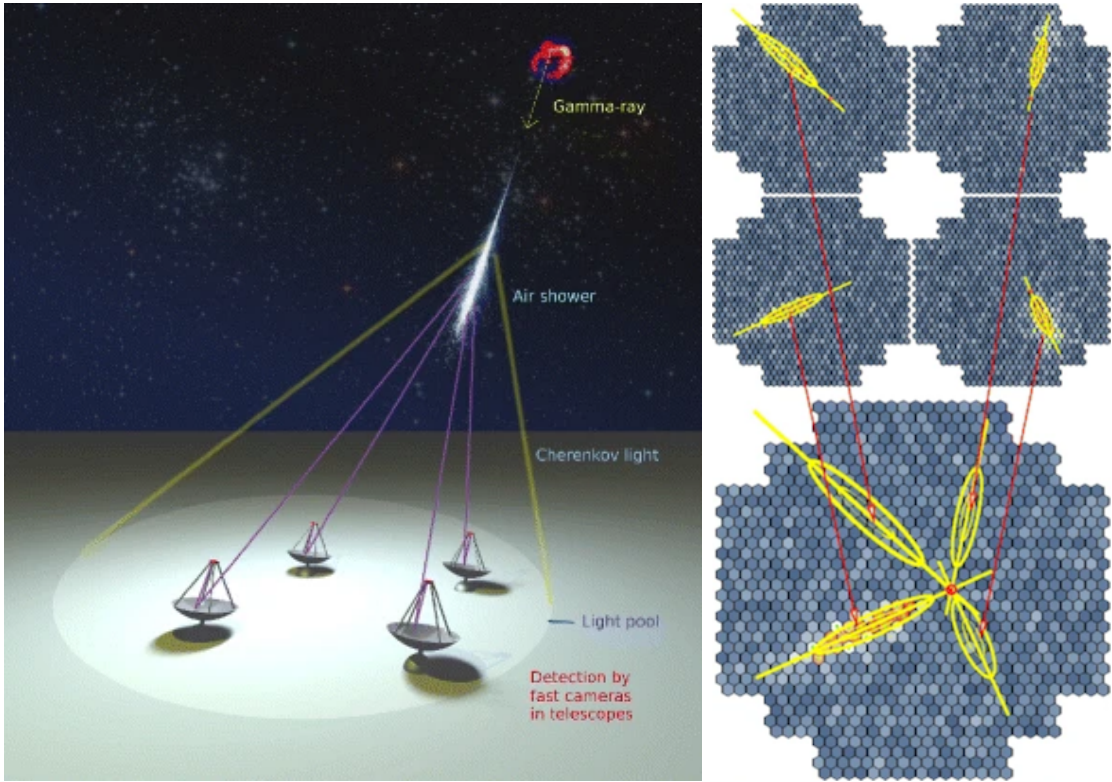


Figure 3.5: (*left*) Pool of Cherenkov light from an air shower observed by four telescopes in a stereo system. (*right*) Projection of the Cherenkov light onto one camera focal plane by the four telescopes. Images courtesy of Völk and Bernlöhr, (2009).

125 m for a primary gamma ray of energy 0.1 TeV but can extend to 1 km for energies greater than 100 TeV (Patterson and Hillas, 1983). A telescope can be placed anywhere within the light pool to detect the Cherenkov light produced from particles in an air shower. Hence, the effective collection area of the telescopes becomes the area of the light pool at the ground, which is of order  $\approx 1 \text{ km}^2$ .

The top-right hand panel of Fig. 3.5 shows how Cherenkov light is observed by single and multiple telescopes. To characterise Cherenkov light, the light is first modelled by an ellipse and then parameters such as the width, length, location & azimuthal angle to the center of the telescope is found. These parameters, known as the Hillas parameters (Hillas, 1985), can be used to determine the arrival direction, energy and type of the particle that triggered the air shower. If multiple telescopes observe the same light at different angles, the combined image (see the right hand panel of Fig. 3.5) can be reconstructed using ‘stereo’ techniques with far more precision than if one telescope was used.

## 3.2 TeV Gamma-ray Observatories

Evidence of TeV gamma rays from AGN Centaurus were reported by Grindlay et al., (1975). But TeV astronomy effectively began with the detection of TeV gamma rays from the Crab Nebula (Weekes et al., 1989). Over three decades later, TeV gamma rays from over 200 sources have been detected (Wakely and Horan, 2008). This section will describe some of the TeV gamma-ray observatories whose data products were used in this thesis.

### 3.2.1 The High Energy Stereoscopic System



Figure 3.6: The High Energy Stereoscopic System. Images from (HESS ).

The High Energy Stereoscopic System (H.E.S.S.) telescope (named after Victor Hess) is an array of telescopes located at 1800 m above sea level in Namibia (see Fig. 3.6) (HESS ). H.E.S.S. consists of five telescopes and utilises the atmospheric Cherenkov imaging technique described above to detect gamma radiation in the energy range 20 GeV to 100 TeV. A comparison of the performance of H.E.S.S. to other instruments is shown in Fig. 3.7. The angular resolution of H.E.S.S. ( $\leq 0.1^\circ$ ) allows detailed observations of gamma-ray sources, which is key in understanding the morphology of objects such as SNRs and PWNe (H.E.S.S. Collaboration et al., 2018a). HESS was constructed in two different phases; Phase 1 consisting of four 12 m telescopes and Phase 2 added one 28 m telescope at the centre of the array. Phase 1 and Phase II of H.E.S.S. commenced operations in December 2003 and July 2012 respectively.

The four 12 m telescopes of Phase I have 382 mirror segments of 0.6 m diameter mounted onto a steel frame in a Davies-Cotton optical layout (a parabolic layout where each mirror has focal length  $f$ , which is the focal length of the entire telescope (15 m)) (Bernlöhr et al., 2003). The mirrors combine to have total mirror surface area of  $107 \text{ m}^2$  and focus the Cherenkov light onto a photomultiplier camera (containing  $\approx 1000$  pixels with a  $5^\circ$  field of view. Each dish is mounted on a rotating base frame which rotates azimuthally on a rail of 13.6 m diameter. The telescopes have a peak positioning speed of  $100^\circ/\text{min}$  in both azimuth and elevation and is sensitive to gamma rays above 100 GeV. This is ideal for observing events such as gamma-ray bursts and following up activity triggered by other observatories (e.g. neutrinos from IceCube, GRBs from Swift). The four telescopes are placed in a square geometry with distances 120 m from each other.

Phase II of H.E.S.S. placed an additional 24 m telescope in the centre of phase I (Vincent, 2005). The telescope consists of 875 hexagonal mirrors of 0.9 m sides laid out in a parabolic shape with focal length of 36 m and total mirror area of  $614 \text{ m}^2$ . The Phase II telescope has azimuth and elevation speed of  $200^\circ/\text{min}$  and  $100^\circ/\text{min}$  respectively. Similar to Phase I, Phase II focuses Cherenkov light onto a photomultiplier camera consisting of  $\approx 2000$  pixels with a  $3.2^\circ$  view of the sky.



Figure 3.7: Comparison of the performance (minimum detectable flux) of different gamma-ray instruments for an observation time of 50 h. H.E.S.S., CTA south and CTA north is shown by the red, dark blue and light blue lines respectively. Image courtesy of (CTA Consortium et al., 2019).

### The H.E.S.S. Galactic Plane Survey

In 2018, H.E.S.S. released its third Galactic Plane Survey (HGPS) in TeV gamma rays that covers data from January 2004 to January 2013 totalling 2864h of observation time (H.E.S.S. Collaboration et al., 2018a). The HGPS catalogued 78 very high energy (VHE) sources compared to 10 sources in the first release (Aharonian et al., 2005a) and 22 in its second (Aharonian et al., 2006b). Of the 78 VHE sources; 3 are binary objects (composed of a massive star and a compact object), 8 are SNRs, 12 are PWN, 8 are composite objects (SNR + PWN), 11 have no known association and a further 36 are not firmly identified. H.E.S.S. Collaboration et al., (2018a) found that 47 of the HGPS sources (60%) had an associated pulsar and (39% being a PWN or a composite object (SNR + PWN). This makes PWNe the largest source class in the survey. Following the HPGS survey, H.E.S.S. Collaboration et al., (2018b) conducted a study on the population of TeV PWN to link PWN evolutionary theory to TeV observations (see Section 2.1.3 for further detail). This thesis focuses on the TeV PWN HESS J1825-137.

### 3.2.2 *Fermi*-LAT

The *Fermi* Gamma-ray Space Telescope is a space based observatory launched on the 11th of June 2008. *Fermi* has two instruments; the Large Area Telescope (LAT) and the Gamma-ray Burst Monitor (Michelson et al., 2010). *Fermi*-LAT consists of thin metal sheets that assist in the production of electron-positron pairs. The electron-positron pair then pass through microstrip detectors that can track their trajectory. Finally, the products enter a calorimeter which measures the combined energy of the electron-positron pair to determine the energy of the initial gamma ray. The Gamma-ray Burst Monitor consists of scintillators positioned on opposite sides of the spacecraft allowing different viewing angles to detect gamma-ray bursts and solar flares (Michelson et al., 2010). The performance



Figure 3.8: The H.E.S.S. Galactic plane survey superimposed onto *Planck* CO data. Image courtesy of H.E.S.S. Collaboration et al., (2018a).

characteristic of *Fermi*-LAT allows sensitivity in the energy range of 20 MeV – 300 GeV with a field of view of 2.4 sr (Michelson et al., 2010).

The equivalent *Fermi*-LAT source towards HESS J1825-137 is 4FGL J1824.5 1351e (Abdollahi et al., 2020). Principe et al., (2020) combined GeV data from *Fermi*-LAT and TeV data from H.E.S.S. to provide a broader view of the gamma-ray emission towards HESS J1825-137 from 1 GeV up to 100 TeV. They found that the size of the PWN increases at lower energies, implying that electrons from the outer edges are from an older population of electrons compared to the recently injected electrons near the powering pulsar. This is indicative of a TeV halo forming, where electrons begin to escape the PWN into the ISM and emit TeV emission via inverse Compton interactions.

### 3.2.3 LHAASO

The Large High Altitude Air Shower Observatory (LHAASO) is a gamma-ray and cosmic-ray observatory located  $\approx 4400$  m above sea level in Sichuan China (Ma et al., 2022). LHAASO consists of:

- 1.3 km<sup>2</sup> array of  $\approx 5200$  electromagnetic detectors and muon detectors that focuses on detecting gamma rays above 30 TeV and cosmic rays from 10 TeV to 100 PeV (Aharonian et al., 2021b).
- A water Cherenkov array sensitive to gamma rays between 100 GeV and 30 TeV and has total detection area of  $7.8 \times 10^4$  m<sup>2</sup>. This array monitors galactic gamma-ray sources, gamma-ray bursts and AGNs (LHAASO collaboration, 2021).



Figure 3.9: The LHAASO (*left*) and HAWC (*right*) observatories. Images courtesy of Ma et al., (2022) and Abeysekara et al., (2023)

- 18 Cherenkov telescopes that aims to measure the cosmic ray energy spectrum and composition between 10 TeV and 1 EeV (Aharonian et al., 2021a).
- An upcoming electron-neutron detector array to study the cosmic ray spectrum and composition above 1 PeV (Ma et al., 2022).

LHAASO has detected significant gamma-ray emission above 100 TeV from 12 Galactic sources including LHAASO 1825-1326 (LHAASO equivalent of HESS J1825-137 / HESS J1826-130, see Fig. 2.8) (Cao et al., 2021). In 2021, LHAASO revealed the detection of gamma rays up to 1.1 PeV from the Crab Nebula, implying the existence of a 2.3 PeV electron (The LHAASO Collaboration et al., 2021)

### 3.2.4 HAWC

The High Altitude Water Cherenkov Observatory (HAWC) is a gamma-ray and cosmic-ray observatory located in Puebla, Mexico. The primary detector of HAWC consists of 300 water tanks arranged in a  $22\,000 \text{ m}^2$  area at an altitude of  $\approx 4100 \text{ m}$  above sea level (Abeysekara et al., 2023). The high refractive index of water ( $n = 1.33$ ) lowers the cosmic-ray/gamma-ray energy threshold to produce Cherenkov light which is then observed by four photomultiplier tubes.

HAWC has detected over 100 sources of VHE gamma rays, which are summarised in the third HAWC catalogue (Albert et al., 2020). Abeysekara et al., (2020) revealed 9 gamma-ray sources with emission above 56 TeV, with three of these sources having significant detection above 100TeV. This includes the equivalent HESS J1825-137 / HESS J1826-130: eHWC J1825-134.

### 3.2.5 The Cherenkov Telescope Array

The Cherenkov Telescope Array (CTA) is the next generation ground-based telescope array that will observe gamma rays from 10 GeV up to 300 TeV. It will be the largest ground-based telescope that can observe the night sky with sensitivity up to 10 times greater than current instruments (see Fig. 3.7). CTA will have two arrays in both the Southern (Chile) and Northern hemisphere (Canary Islands) to allow access to the majority of the night sky. CTA LST-1 at CTA-north begun data collection in 2022 **ASK SABRINA FOR REFERENCE AS I CANNOT FIND IT.**

CTA will be an array of three different sized telescopes (see Fig. 3.10): Small-Sized Telescopes (sensitive to energies  $> 1 \text{ TeV}$ ) with a mirror diameter and field of view of 4 m



Figure 3.10: Telescopes for the Cherenkov Telescope Array. From left to right: the Small-Sized Telescope, two of the proposed Middle-Sized Telescope and the Large-Size Telescope. Image courtesy of CTA () .

and  $\approx 0^\circ$  respectively, Medium-Sized Telescopes (sensitive to energies between 80 GeV and 50 TeV) with a mirror diameter and field of view of 11.5 m and  $\approx 7.5^\circ$  respectively and the Large-Sized Telescope (sensitive to the lowest energy gamma-rays) with a mirror diameter and field of view of  $\approx 23$  m and  $\approx 4.3^\circ$  respectively (CTA ; CTA Consortium et al., 2019).

PWN transitioning from their second to their third stage of evolution (see Section 2.1.2) are too faint and/or extended for their emission to be detected by current instruments such as H.E.S.S.. The increased sensitivity of CTA (see Fig. 3.7) will be able observe these previously undetectable TeV PWN, providing more insight into the evolution of PWN.

# Chapter 4

## Interstellar Medium towards HESS J1825-137 and HESS J1826-130

The interstellar medium (ISM) is the gas existing in between stars and other astrophysical objects in the Galaxy. The ISM includes atomic and molecular gas, dust, plasma and cosmic rays and accounts for 10 – 15% of the total mass in the Galactic disc (Ferrière, 2001). By number, the chemical composition of the ISM is 90.8% hydrogen, 9.1% helium and 0.12% heavier elements (Ferrière, 2001). By mass hydrogen makes up 70.4% of the ISM with the remainder being 28.1% Helium and 1.5% heavier elements. As cosmic rays and gamma rays leave their place of birth, they must traverse the ISM before being observed at Earth.

As discussed in Section 2.1.5, HESS J1825-137 lies at a distance of 4.0 kpc (Aharonian et al., 2006a). Fig. 4.1 shows carbon monoxide (CO) gas lying in range 3.5 – 4.5 kpc towards HESS J1825-137 and HESS J1826-130, where CO is used as a trace for molecular hydrogen (see Section 4.2.1). The ISM gas towards this region will influence the transport of cosmic rays escaping the PWN (and SNR) associated with HESS J1825-137 and the subsequent gamma-ray emission from this region. Therefore the ISM must be considered in any study towards this region. This chapter will discuss properties of the ISM as well as the observatories whose data products were used in this thesis.



Figure 4.1:  $^{13}\text{CO}(1 - 0)$  (top) and  $^{12}\text{CO}(1 - 0)$  (bottom) integrated intensity between velocity range 40 – 60  $\text{km s}^{-1}$  (equivalent to 3.5 – 4.5 kpc) towards HESS J1825-137. HESS TeV gamma-ray emission contours are shown by the solid and dashed black contours. Image courtesy of (Voisin et al., 2016)

## 4.1 Detecting the interstellar medium

The ISM gas towards HESS J1825-137 influences the rate at which cosmic rays propagate and their cooling time (see Section 2.3). Radiation theory describes how particles (photons and cosmic rays) interact with a medium during propagation (Draine, 2011). As photons travel through the ISM before detection at Earth, it is important to characterise how the interstellar gas affects observations.

### 4.1.1 Specific Intensity, Specific Flux and Bolometric flux

Firstly, this section will define fundamental concepts.

Let a telescope with detecting area  $dA$  observe photons (in frequency range  $\nu + d\nu$  and energy range  $E + dE$ ) from a source within solid angle  $d\Omega$  at orientation  $\theta$  in time  $dt$  (see Fig. 4.2).



Figure 4.2: A basic illustration of a telescope with area  $dA$  observing a cloud of ISM gas with solid angle  $d\Omega$  at orientation  $\theta$ .

The amount of photons arriving within solid angle  $d\Omega$  is described by the specific intensity:

$$I_\nu(\hat{\Omega}) = \frac{dE}{dA dt d\nu d\Omega} \quad [\text{W m}^{-2} \text{Hz}^{-1} \text{sr}^{-1}] . \quad (4.1)$$

The net specific flux,  $F_\nu$ , is obtained by integrating the specific intensity over the entire source:

$$F_\nu = \oint I_\nu(\hat{\Omega}) \cos \theta d\Omega \quad [\text{W m}^{-2} \text{Hz}^{-1}] . \quad (4.2)$$

A common unit for the specific flux in the radio domain is the Jansky (Jy) where  $1 \text{ Jy} = 10^{-26} \text{ W m}^{-2} \text{Hz}^{-1} = 10^{-23} \text{ erg cm}^{-2} \text{s}^{-1} \text{Hz}^{-1}$ . If the specific intensity is isotropic ( $I_\nu(\hat{\Omega}) = I_\nu$ ) then  $\oint \cos \theta d\Omega = 0$  and the specific flux is zero. If the telescope is pointed towards the source ( $\cos \theta = 1$ ) and the source is uniformly bright ( $I_\nu(\hat{\Omega}) = I_\nu$ ), then the specific flux is simply:

$$F_\nu = I_\nu \Delta \Omega . \quad (4.3)$$

The bolometric flux,  $F$ , is the specific flux integrated over all frequencies:

$$F = \int F_\nu d\nu \quad [\text{W m}^{-2}] , \quad (4.4)$$

and is a measure of the total amount of photons emitted by a source.

### 4.1.2 Radiative Transfer

Let a cloud with thickness  $ds = c dt$  (volume  $dV = dA c dt$ ) and particle number density  $n$  be illuminated by a background source with specific intensity  $I_\nu$  on area  $dA$  (see Fig. 4.3).



Figure 4.3: A cloud of thickness  $ds$  is illuminated by a background source with intensity  $I_\nu(s)$ . Photons of frequency  $\nu$  are emitted and re-emitted by particles (dark circles) within the cloud, changing the intensity by  $dI_\nu$

The cloud contains  $n dV$  particles with each particle having an absorption cross section  $\sigma_\nu$  for radiation of frequency  $\nu$ . The total absorption area of the cloud can be described by  $n ds dA \sigma_\nu$ , giving the fraction of photons absorbed to be:

$$\begin{aligned} f_{\text{absorbed}} &= n ds dA \sigma_\nu / dA \\ &= n ds \sigma . \end{aligned} \quad (4.5)$$

Therefore the change in intensity due to absorption is:

$$\begin{aligned} dI_{\nu, \text{absorbed}} &= -\frac{n dV \sigma_\nu}{dA} \\ &= -\alpha_\nu I_\nu ds , \end{aligned} \quad (4.6)$$

where  $\alpha_\nu = n \sigma_\nu [\text{m}^{-1}]$  is the absorption coefficient. The absorption mean free path is the distance a photon will travel in the cloud before absorption and is given by:

$$\ell_\nu = \alpha_\nu^{-1} . \quad (4.7)$$

If the cloud in Fig. 4.3 has emission coefficient  $j_\nu [\text{W m}^{-3} \text{Hz}^{-1} \text{sr}^{-1}]$  (i.e. the power emitted at frequency  $\nu$  by an infinitesimal volume  $dV$ ), the specific intensity emitted by the cloud is:

$$\begin{aligned} dI_{\nu, \text{emitted}} &= j_\nu ds \\ \therefore I_{\nu, \text{emitted}} &= \int j_\nu ds . \end{aligned} \quad (4.8)$$

Giving the total change in intensity in the cloud to be:

$$\begin{aligned} \frac{dI_\nu}{ds} &= -\alpha(s) I_\nu(s) + j_\nu(s) \\ \frac{dI_\nu}{\alpha_\nu ds} &= -I_\nu(s) + \frac{j_\nu(s)}{\alpha_\nu(s)} \\ \frac{dI_\nu}{d\tau} &= -I_\nu(\tau_\nu) + S(\tau_\nu) , \end{aligned} \quad (4.9)$$

where  $\tau_\nu$  is the optical depth defined by:

$$d\tau_\nu = \alpha_\nu ds , \quad (4.10)$$

and  $S_\nu(\tau_\nu) = j_\nu(s)/\alpha_\nu(s)$  is the source function of the cloud. Eq. 4.9 has solution:

$$I_\nu(\tau_\nu) = \exp(-\tau_\nu) \left[ I_\nu(0) + \int_0^{\tau_\nu} \exp(\tau'_\nu) S_\nu(\tau'_\nu) d\tau'_\nu \right] . \quad (4.11)$$

If there is no emission from the cloud,  $S_\nu(\tau_\nu) = j_\nu(s) = 0$ , then the specific intensity can be described by:

$$I_\nu(\tau_\nu) = I_\nu(0) \exp(-\tau_\nu) . \quad (4.12)$$

i.e. the specific intensity of the background source after absorption by the cloud. If the emission/absorption of the cloud is uniform,  $S_\nu(\tau_\nu) = S_\nu$ , Eq. 4.11 becomes:

$$\begin{aligned} I_\nu(\tau_\nu) &= I_\nu(0) \exp(-\tau_\nu) + S_\nu(1 - \exp(-\tau_\nu)) \\ &= S_\nu + \exp(-\tau_\nu)[I_\nu(0) - S_\nu] . \end{aligned} \quad (4.13)$$

If optically thick,  $\tau_\nu \gg 1$ :

$$I_\nu(\tau_\nu) \approx S_\nu . \quad (4.14)$$

This is when a medium is opaque and only photons emitted by the cloud are observed. If optically thin,  $\tau \ll 1$ , then the exponential in Eq. 4.13 can be approximated by  $\exp(-\tau_\nu) \approx 1 - \tau_\nu$  and the observed specific intensity becomes:

$$I_\nu(\tau_\nu) = I_\nu(0)(1 - \tau_\nu) + S_\nu \tau_\nu . \quad (4.15)$$

### 4.1.3 Black Bodies

Thermal radiation is the emitted radiation due to the random motion/kinetic energy (i.e. temperature) of its particles. Thermal sources such as stars, CMB, interstellar dust can be described by an object emitting radiation with frequency  $\nu$  at temperature  $T$ . A black body is an idealised object that absorbs all incoming radiation. A black body at temperature  $T$  emits radiation at an intensity described by Planck's distribution:

$$B_\nu(T) = \frac{2h\nu^3/c^2}{\exp(h\nu/kT) - 1} \quad [\text{W sr}^{-1} \text{ m}^{-2} \text{ Hz}^{-1}] , \quad (4.16)$$

where  $h$  is Planck's constant and  $k$  is Boltzmann's constant. The integrated intensity over all frequencies from a black body is given by the Stefan-Boltzman Law:

$$F = \sigma T^4 \quad [\text{W m}^{-2}] , \quad (4.17)$$

with  $\sigma$  being the Stefan–Boltzmann constant. Objects in thermal equilibrium emit radiation in a manner that is dependent on their temperature. For an ‘ideal’ black body to be in thermal equilibrium with its surroundings, the incoming intensity ( $I(0) = B_\nu$ ) and emitted intensity ( $I(\tau) = B_\nu$ ) are equal. Eq. 4.13 becomes:

$$B_\nu(T) = S_\nu(T) + \exp(-\tau_\nu)[B(T) - S_\nu(T)] . \quad (4.18)$$

This is only true for all  $\tau$  when:

$$\therefore S_\nu(T) = B_\nu(T) = \frac{j_\nu(T)}{\alpha_\nu(T)} . \quad (4.19)$$

Eq. 4.19 is known as Kirchoff's law of radiation. Hence, the emission of a black body can be described by:

$$I_\nu(\tau_\nu) = I_\nu(0) \exp(-\tau_\nu) + B_\nu(T)[1 - \exp(-\tau_\nu)] . \quad (4.20)$$

For an optically thick medium ( $\tau \gg 1$ ) then:

$$I_\nu(\tau_\nu) \approx B_\nu(T) , \quad (4.21)$$

and the medium can be approximated as a black body. Molecular tracers such as CO (see Section 4.2.1) emit radiation in the radio band. At these low frequencies ( $h\nu \ll kT$  and  $\exp(h\nu/kT) \approx 1 + h\nu/kT$ ), the intensity of a black body can be approximated by:

$$B_\nu(T) = \frac{2\nu^2 k T}{c^2} . \quad (4.22)$$

In radio astronomy, brightness temperature ( $T_B$ ) is often used to measure intensity where  $B_\nu(T_B) \equiv I_\nu$ :

$$T_B(\nu) = \frac{c^2}{2\nu^2 k} I_\nu . \quad (4.23)$$

Brightness temperature is the temperature that an ideal black body in thermal equilibrium would have in order to emit intensity  $I_\nu$ . For example, brightness temperature can be used to describe molecular clouds with temperatures  $\approx 10$  K for frequencies  $\ll 208$  GHz (Longair, 2011).

#### 4.1.4 Spectral Line Excitation and Emission

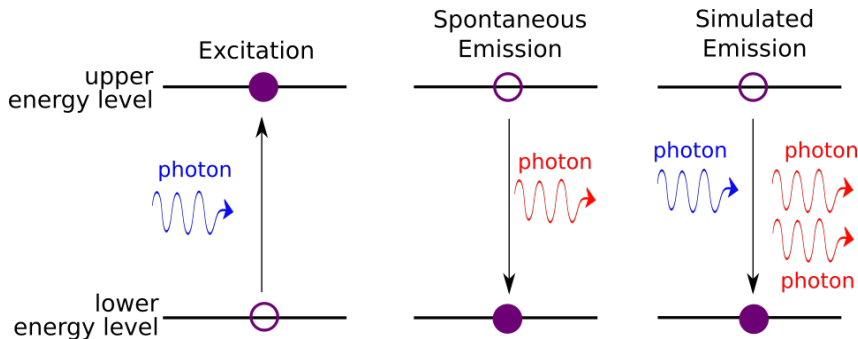


Figure 4.4: (left) Excitation of an electron from a low to higher energy level due to absorption of energy from a photon. (middle) Spontaneous emission of a photon with energy equal to energy difference between energy levels. (right) Simulated emission of a photon with same wavelength and direction as incident photon.

Atoms populate their electrons in orbitals, from low to high energy levels. The stable state (or ground state) of an atom occurs when the electrons occupy their lowest energy level. The absorption of a photon can raise the energy level of an atom to a higher one (see left panel of Fig. 4.4). This is known as excitation. An atom can exist in this excited state for a short period of time until it decays to a lower energy level and emits a photon with energy equal to the energy difference between the initial and final energy level (see middle panel of Fig. 4.4). This is known as spontaneous emission. The Einstein coefficient,  $A_{if}$ , gives the probability per unit time for spontaneous emission from state  $i$  to state  $f$  and releasing photon of frequency  $\nu_{if}$ . If the number density of atoms in state  $i$  is  $n_i$ , then the emission coefficient is given by:

$$j_\nu = \frac{n_i h \nu_{if} A_{if}}{4\pi} \Phi(\nu) . \quad (4.24)$$

For example, H $\alpha$  emission occurs when the electron in an excited hydrogen atom decays from the third to second energy level. As a result H $\alpha$  emission is used as a tracer for ionised gas. In its neutral state, a hydrogen atom consists of one electron-proton pair with their spins either parallel or anti-parallel. The hydrogen atom may spontaneously switch the spin of its electron from parallel to anti-parallel to the proton spin and release radiation with a wavelength of 21 cm known as the HI line. This HI line can be used to probe neutral hydrogen gas in the Galaxy and beyond.

Simulated emission occurs when an external photon interacts with an excited atom causing an emission of a photon with the same wavelength, polarisation and direction as the initial photon (see Fig. 4.4).

## 4.2 Probing the interstellar medium

### 4.2.1 Molecular Tracers

H<sub>2</sub> is the most abundant molecule in the Galaxy, consisting of two bound hydrogen atoms. Molecular hydrogen has 14 vibration energy levels that require high temperatures ( $> 5000$  K) for excitation (Draine, 2011). However, observed molecular clouds have temperatures  $\approx 10 - 20$  K (Ferrière, 2001) and the transition rate to higher energy levels are quite low. Moreover, the symmetry of H<sub>2</sub> molecules makes dipole radiation ‘forbidden’ while electric quadrupole radiation is possible with very low probability (Draine, 2011).

The two nuclei in H<sub>2</sub> molecules rotate around their centre of mass with angular momentum components  $J_x$ ,  $J_y$  and  $J_z$  (Zettilli, 2001) and total rotational energy:

$$E_{\text{rot}} = \frac{J_x^2}{2I_x} + \frac{J_y^2}{2I_y} + \frac{J_z^2}{2I_z} , \quad (4.25)$$

where  $I_i$  is the moment of inertia in the  $i$ th axis ( $i = x, y, z$ ). For linear rotors (e.g. H<sub>2</sub>, CO)  $I_x \ll I_y = I_z$  where  $I_x$  can be treated as zero (*Modern Physical Chemistry A Molecular Approach* 2000). Eq. 4.25 becomes:

$$E_{\text{rot}} = \frac{J^2}{2I} , \quad (4.26)$$

where the eigenvalue of  $J^2$  is  $j(j+1)\hbar^2$  (Zettilli, 2001). Hence:

$$E_{\text{rot}} = \frac{\hbar^2}{2I} j(j+1) , \quad (4.27)$$

with  $\hbar = h/(2\pi)$  and  $j = 0, 1, 2\dots$ . For a H<sub>2</sub> molecule absorbing/emitting a photon (with energy  $E_\gamma$ ) that causes a change in energy level, the difference in energy levels is given by:

$$E_\gamma = \Delta E_{\text{rot}} = \frac{j\hbar^2}{I} . \quad (4.28)$$

For molecular hydrogen, temperatures greater than 100 K are required for rotational energy excitation. Hence, molecules within the majority of quiescent H<sub>2</sub> clouds exist in their vibrational and rotational ground state.

After  $\text{H}_2$ , the second most abundant molecule is CO, following a CO/ $\text{H}_2$  abundance ratio of  $10^{-4}$  in molecular clouds (Lacy et al., 1994). The transition between the ground and first rotational energy level ( $J = 1 - 0$ ) for CO requires much lower temperatures  $\approx 5 \text{ K}$ , corresponding to photons being emitted at frequency 115 GHz ( $\lambda = 2.6 \text{ mm}$ ) (Wilson, 2013). Therefore, carbon monoxide can be used as a tracer for molecular hydrogen (see (Bolatto et al., 2013)).

High-frequency radio telescopes such as Nanten (see Section 4.2.6) observe the intensity of molecular CO in units of brightness temperature (see Eq. 4.23). To interpret the amount of gas towards a particular region, the CO( $1 - 0$ ) brightness intensity is converted to a column density ( $\text{cm}^{-2}$ ) of molecular hydrogen through the conversion factor  $X_{\text{CO}}$ :

$$N_{\text{H}_2} = X_{\text{CO}} W_{\text{CO}} , \quad (4.29)$$

where  $W_{\text{CO}}$  is the integrated intensity in units kilom/s. The conversion factor is often assumed to be constant ( $X_{\text{CO}} = 1.5 \times 10^{20} \text{ cm}^{-2} \text{ K}^{-1} \text{ km}^{-2} \text{ s}$ ) across the Galactic plane, but it is known to vary with galactocentric radius (Strong et al., 2004). The number density  $n_H$  and mass  $M_H$  of hydrogen in a cloud with column density  $N_{\text{H}_2}$  are respectively:

$$\begin{aligned} n_H &= \frac{\mu N_{\text{H}_2}}{\Delta z} \\ M_H &= n_H m_p V , \end{aligned} \quad (4.30)$$

$\Delta z$  is the width of the cloud along the line of sight,  $V$  is the volume of the cloud and  $m_p$  is the mass of the proton. The weight factor,  $\mu$ , of a gas cloud is:

$$\mu = \sum_Z n A_r , \quad (4.31)$$

where  $\sum_Z$  sums over the molecules present in the cloud,  $n$  is the number of atoms present in the molecule ( $n = 2$  for molecular hydrogen) and  $A_r$  is the atomic weight ( $A_r \approx 1$  for hydrogen and  $A_r \approx 4$  for helium). For a gas cloud with 20% Helium component, the weight factor is 2.8.

## 4.2.2 Doppler Shift

Section 4.2.1 discussed how atomic and molecular gas emit photons with wavelengths dependent on their atomic structure. However, the bulk movement of gas clouds around the Galactic Center (GC) will shift the frequency of photons due to the Doppler effect. The shift in frequency is described by:

$$\nu = \frac{c + V_{\text{obs}}}{c + V} \nu_0 , \quad (4.32)$$

where  $\nu$  is the observed frequency,  $\nu_0$  is the emitted frequency,  $V$  is the velocity of the gas cloud and  $V_{\text{obs}}$  is the velocity of the observer. Therefore, a shift in frequency can be represented as a velocity in respect to a rest frame:

$$V_{\text{LSR}} = c \frac{(\nu_0 - \nu)}{\nu_0} . \quad (4.33)$$

The typical rest frame used is the local standard of rest (LSR), taken at the point coincident with the Sun orbiting around the GC in a perfect circular orbit.

### 4.2.3 Galactic Rotation Curve

Matter rotates around the GC with an average tangential speed of  $\Theta_0 \approx 220 \text{ km s}^{-1}$ . The Galactic rotation curve is an empirical model (see Fig. 4.5) that relates the galactocentric radius (distance to the GC) of an object to its observational velocity. Using HI



Figure 4.5: (*Left*) Rotation of the Galaxy around the GC (dark blue circle) with the yellow circle as the Sun, the blue arrow is the tangential velocity of the green objects (e.g. gas cloud) and the blue arrows are their velocities projected along the line of sight to the Sun. (*Right*) Geometry of an object at Galactic longitude  $\ell$ , Galactic latitude  $b$  and distance  $d$  from the Sun.

clouds, Brand and Blitz, (1993) found that the measured velocity of a cloud,  $V_{\text{LSR}}$ , can be transformed into circular rotation velocity,  $\Theta_0$  via:

$$V_{\text{LSR}} = \left( \frac{\Theta R_\odot}{R} - \Theta_\odot \right) \sin \ell \cos b , \quad (4.34)$$

where  $\ell$  and  $b$  are the Galactic coordinates of the cloud,  $R$  and  $\Theta$  are the galactocentric distance and circular rotation velocity of the cloud respectively and  $R_\odot$  is the galactocentric distance of the Sun. The circular rotation velocity is related to the galactocentric distance by:

$$\frac{\Theta}{\Theta_\odot} = a_1 \left( \frac{R}{R_\odot} \right)^{a_2} + a_3 , \quad (4.35)$$

where  $a_1 = 1.00767$ ,  $a_2 = 0.0394$  and  $a_3 = 0.00712$  are the values found by Brand and Blitz, (1993). For a cloud with circular rotation velocity  $V_{\text{LSR}}$  at coordinate  $\ell$  and  $b$ , Eq. 4.34 and Eq. 4.35 can be solved numerically to find  $R$  and  $\Theta$ . Using simple trigonometry (see Fig. 4.5), the distance to the GC for an object at distance  $d$  and coordinates  $(\ell, b)$  is given by:



Figure 4.6: (Left) Four spherical gas clouds located 4 kpc from the Earth at distances  $d$  along the line of sight (z-axis runs in/out of page) from a source of electrons (red cross). (Right) Subsequent gamma-ray flux 40 kyr after electron injection commences.

$$R^2 = d^2 \cos^2 b + R_\odot^2 - 2dR_\odot \cos b \cos \ell , \quad (4.36)$$

which gives a near and far distance to the cloud (see Fig. 4.5). In general, the near distance is taken to be the solution; a source further away is more likely to have its emission being obstructed by closer gas. Moreover, a distant source will appear dimmer than a nearby source due to intensity following the inverse square law ( $I \propto d^{-2}$ ).

Other Galactic rotation curves include Clemens, (1985), who analysed the Massachusetts-Stony Brook Galactic plane CO survey (Sanders et al., 1985). Persic et al., (1996) provided a ‘universal rotation curve’ which includes contributions from a stellar disk and a dark halo. Alternatively Reid et al., (2014) describes the Galactic rotation curve as a polynomial:

$$\begin{aligned} \Theta(R) &= a_{p1} + a_{p2}\rho + a_{p3}\rho^3 \\ \rho &= \frac{R}{R_0} - 1 , \end{aligned} \quad (4.37)$$

with  $a_{p1} = [241 \pm 9] \text{ km s}^{-1}$ ,  $a_{p2} = 0.5 \pm 3.7$  and  $a_{p3} = -15.1 \pm 8.4$ .

The velocity in Eq. 4.34 describes the circular rotation velocity of an object around the Galaxy. However, the velocity measured at Earth is the combined velocity due to Galactic rotation and local individual gas motion (e.g. due to stellar winds, SNR shock fronts). Brand and Blitz, (1993) noted that residuals of modelled gas with respect to the Galactic rotation curve can be as large as  $40 \text{ km s}^{-1}$  with the average being around  $12.8 \text{ km s}^{-1}$ . This is significant compared to the Nanten observatory velocity resolution of  $1 \text{ km s}^{-1}$  (see Section 4.2.6), whose data products were used in this thesis. The uncertainty in the individual velocity of the gas will lead to large uncertainties in distances (hundreds of parsecs) to gas clouds.

The large uncertainties in distances to gas clouds (see Section 4.2.3) leads to a caveat in modelling the gas and magnetic field distribution (see next section) around a cosmic ray source. For example, consider a crude estimation in which the cosmic ray intensity is described by an inverse square law  $I \propto d^{-2}$  where  $d$  is the distance from the accelerator.

The cosmic ray flux decreases with distance from a source, decreasing the subsequent gamma ray energy flux from non-thermal emission (see Section 2.3). This can be seen in Fig. 4.6, where four spherical gas clouds of number density  $600 \text{ cm}^{-3}$  ( $B \approx 25 \mu\text{G}$ ) are located at different distances along the line of sight (z-axis) from a continuous source of electrons. The gamma-ray flux through IC interactions at 40 kyr (suggested age of PWN HESS J1925-137, Van Etten and Romani, (2011)) decreases with increasing distance from the accelerator. Therefore, large uncertainties in distances to gas clouds will influence the modelled multiwavelength emission towards an accelerator.

#### 4.2.4 Magnetic fields in molecular clouds

The Zeeman effect (the splitting of spectral lines in the presence of a static magnetic field) can be used to measure the magnetic field strength in a medium. Crutcher et al., (2010) studied a population of quiescent clouds and related the magnetic strength a cloud's its number density  $n$  through:

$$B_{\text{gas}}(n) = \begin{cases} B_0 & , n < n_0 \\ B_0 \left(\frac{n}{n_0}\right)^{\alpha} & , n > n_0 \end{cases}, \quad (4.38)$$

where clouds with a density above  $n_0 = 300 \text{ cm}^{-3}$  have an enhanced magnetic field described by a power-law regime with  $B_0 = 10 \mu\text{G}$  and  $\alpha = 0.65$ .

Cosmic rays propagating through the ISM scatter off magnetic field turbulence and the overall motion is described by a random walk/diffusion (see Section 2.2.2), where the rate of diffusion is related to the strength of the magnetic field. From Eq. 2.31 and Eq. 4.38, the rate that cosmic rays propagate through molecular clouds is anti-correlated with its density. i.e. cosmic rays travel through dense molecular clouds at a lower rate than less-dense clouds. Similarly, magnetic field turbulence in molecular clouds influences the rate of synchrotron energy loss (see Eq. 2.53). Cosmic ray electrons in dense molecular clouds will experience a higher rate of synchrotron (and Bremsstrahlung, see Eq. 2.72) interactions than less-dense clouds due to the enhanced magnetic field. Consequently, this decreases the ‘available’ energy for IC interactions (see Eq. 2.64).

#### 4.2.5 H $\alpha$ emission

Atomic hydrogen in clouds can be ionised by UV light from background stars to form HII regions, while shocks (SNRs), X-rays and cosmic rays leads to the ionisation of molecular hydrogen (Draine, 2011). Recombination of HII atoms and electrons may result in the the emission of light in the H $\alpha$  band (corresponding to a decay from the third to the second energy level). Hence H $\alpha$  emission can be used as a tracer for ionised hydrogen gas (HII gas). Shocks associated with SNRs ionise hydrogen gas, leading to H $\alpha$  rim-like features like those towards HESS J1825-137 (see Fig. 4.7). Both structures are located  $\approx 120 \text{ pc}$  from PSR J1826-1334 which is consistent with the predicted SNR radius ( $\approx 130 \text{ pc}$ ) as suggested by Jager and Djannati-Ataï, (2009).

Ionised gas towards HESS J1825-137 acts as a target for cosmic rays escaping from the PWN/SNR to undergo hadronic/leptonic interactions and emit gamma radiation. The following describes two different methods to trace the ionised hydrogen within molecular clouds.



Figure 4.7:  $\text{H}\alpha$  intensity towards HESS J1825-137. The dashed and dotted lines represent two  $\text{H}\alpha$  rim-like features associated with the progenitor SNR of HESS J1825-137. Image courtesy of (Voisin et al., 2016)

## Method A

For a spherical shell of gas located at distance  $d$  from the Earth with thickness  $d\ell$ , the volume of the shell is given by:

$$dV = 2\pi d^2 d\ell , \quad (4.39)$$

where photons emitted by the gas travel at the speed of light, hence  $d\ell = c dt$ . The total number of photons emitted in the shell in time  $dt$  is related to the luminosity,  $L$ , via:

$$dN = L dt , \quad (4.40)$$

where the luminosity of the region of interest with solid angle  $\omega$  is:

$$L \quad [\text{photon/s}] = \frac{d^2}{10^{-10}} \Omega I , \quad (4.41)$$

with  $I$  being the measured  $\text{H}\alpha$  in Rayleigh units ( $= 10^{10} \text{ ph/m}^2/\text{s/column}$ ). Assuming atoms are not re-excited by an external source, the density of photons emitted by ionised gas  $u_{\text{ph}}$  is approximately equal to the ionised gas density  $n_{\text{ion}}$ :

$$n_{\text{ion}} \approx u_{\text{ph}} = \frac{dN}{dV} = \frac{L}{4\pi d^2 c} . \quad (4.42)$$

## Method B

For photons of frequency  $\nu$ , the photon intensity ( $I_\nu$ ) is related to the luminosity ( $L$ ) through:

$$I_\nu = L \frac{E_\nu}{\nu} = hL , \quad (4.43)$$

where  $h$  is Planck's constant. For a cloud with thickness  $s$ , the emission coefficient is given by:

$$j_\nu = \frac{I_\nu}{s} , \quad (4.44)$$

assuming that the emission coefficient is constant throughout the gas. Hence, the density of atoms in the  $i$ th state emitting photons at frequency  $\nu$  via spontaneous emission:

$$n_i = \frac{j_\nu \Omega_{\text{Earth}}}{E_\nu A \phi(\nu)} , \quad (4.45)$$

where  $A$  is the Einstein coefficient,  $\Omega_{\text{earth}}$  is the solid angle of Earth projected at source lying at distance  $d$  and  $\phi(\nu)$  is the spectral line shape normalised by:

$$\int \phi(\nu) = 1 . \quad (4.46)$$

Assuming that hydrogen atoms in the  $n = 3$  state emit mainly  $H\alpha$  light;  $\phi = 0$  in all frequencies except when  $\nu = \nu_{H\alpha}$ .

#### 4.2.6 Nanten2 Observatory



Figure 4.8: Nanten2 telescope. Image courtesy of Fukui et al., (2006).

Nanten2 (Japanese for ‘Southern Sky’) is an upgrade to the 4m Nanten telescope originally located in Las Campanas before its relocation to the Atacama desert in Chile in 2004 (Fukui et al., 2006). Nanten2 is located at altitude 4800 m and consists of 33 adjustable aluminum panels on a light-weight carbon fiber back structure. Nanten2 is sensitive to atomic and molecular spectral lines 100 – 880 Hz and has angular resolution up to 2'6 beam size (Mizuno et al., 2001), allowing detailed observations of gas structures. Nanten2 has conducted multiple CO surveys of regions such as the Large Magnetic Cloud (Kawamura et al., 2009) and the Galactic plane (Mizuno and Fukui, 2004) covering velocity range  $-300 \text{ km s}^{-1}$  to  $300 \text{ km s}^{-1}$  with a velocity resolution up to  $1.0 \text{ km s}^{-1}$ .

Voisin et al., (2016) conducted an ISM gas study towards PWN HESS J1825-137 and HESS J1826-130 utilising Nanten2 data. They found that the majority of gas towards this region is located in the velocity range  $45 - 60 \text{ km s}^{-1}$  ( $3.8 - 4.5 \text{ kpc}$ ) which is equivalent to the dispersion measure distance of the associated pulsar PSR J1826-134. Voisin et al., (2016) noted six clouds of interest, named R1-R6, whose parameters are summarised in Table 4.1. Cloud R1 was noted to show enhanced turbulence possibly due to the associated SNR shock or the formation of high-mass stars.

Table 4.1: Derived parameters for clouds R1-R6 towards HESS J1825-137 and HESS J1826-130 utilising Nanten2 CO(J=1-0) from Voisin et al., (2016)

Cloud	RA (h)	DEC ( $^{\circ}$ )	Radii ('')	$n_H$ (cm $^{-3}$ )	$M_H$ ( $M_{\odot}$ )
R1	18.421	-13.282	405 $\times$ 405	960	$1.2 \times 10^5$
R2	18.420	-13.125	135 $\times$ 270	1200	$1.3 \times 10^4$
R3	18.429	-13.178	64 $\times$ 64	1600	$3.3 \times 10^3$
R4	18.422	-12.832	175 $\times$ 280	930	$1.6 \times 10^4$
R5	18.449	-13.336	150 $\times$ 270	680	$9.5 \times 10^3$
R6	18.385	-14.049	460 $\times$ 460	430	$7.6 \times 10^4$

# Chapter 5

## Time evolution of cosmic ray particles from an accelerator

Cosmic Rays (electrons and protons) are accelerated by sources such as PWNe and SNRS. Then cosmic rays then escape the acceleration regions and subsequently propagate through the interstellar medium, losing energy through various processes such as radiative cooling, adiabatic expansion and ionisation as discussed in Section 2.3. By modelling the transport of cosmic ray particles from an accelerator, the subsequent gamma-ray distribution can be predicted (see Section 2.3) and compared to observations.

This section first discusses how the energy distribution of cosmic rays evolve in time due to radiation losses and predict the subsequent gamma-ray emission. This will then be expanded to include the escape of cosmic rays out of the region of interest due to diffusion (see Section 2.2.2). Finally, this section describes the numerical code developed by Voisin, (2017), which can be used for systems where the cosmic ray energy distribution and the gamma ray SED cannot be solved analytically.

This code was applied to investigate the origin of the GeV gamma-ray emission to the south of HESS J1825-137. Proposed sources included the impulsive SNR and continuous PWN associated with HESS J1825-137 and the impulsive SNR and continuous compact object binary associated with LS 5039. The results of this study were published in the Monthly Notices of the Royal Astronomical Society and is shown in Chapter 6.

### 5.1 Radiation losses

First consider cosmic rays being injected by a homogeneous source into a region of interest at rate  $S(\gamma, t)$  and escaping at rate  $v_{\text{esc}}$ . The time evolution of the cosmic-ray energy density distribution,  $n(\gamma, t)$ , can be described by (Melrose, 1980):

$$\frac{\partial n(\gamma, t)}{\partial t} = \frac{\partial}{\partial \gamma} [\dot{\gamma}(\gamma)n(\gamma, t)] - v_{\text{esc}}(\gamma)n(\gamma, t) + S(\gamma, t) , \quad (5.1)$$

where cosmic rays with Lorentz Factor  $\gamma$  continuously lose energy at rate  $\frac{dy}{dt} = \dot{\gamma}$  and have probability  $v_{\text{esc}} dt$  of escaping the system in time  $dt$ . Physically,  $\dot{\gamma}(\gamma)n(\gamma, t)$  is the number of cosmic rays per unit time that cool at Lorentz factor  $\gamma$  for a cosmic ray density  $n$ . The following will describe the solution of Eq. 5.1 using Laplace transformations.

Laplace transformations are used to reduce differential equations conveniently into an algebraic equation. The Laplace Transform for the function  $f(t)$  is given by:

$$\bar{f}(q) = \int_0^\infty e^{-qt} f(t) dt . \quad (5.2)$$

Similarly, the Laplace transformation for  $f'(t) = \frac{df}{dt}$ :

$$\bar{f}'(q) = q\bar{f}(q) - f(0) . \quad (5.3)$$

Hence, the Laplace transformation of Eq. 5.1:

$$\begin{aligned} q\bar{n}(\gamma, q) - n(\gamma, 0) &= \frac{\partial}{\partial \gamma} [\dot{\gamma}(\gamma)\bar{n}(\gamma, q)] - v_{\text{esc}}(\gamma)\bar{n}(\gamma, q) + \bar{S}(\gamma, q) \\ -\bar{S}(\gamma, q) - n(\gamma, 0) &= \frac{\partial}{\partial \gamma} [\dot{\gamma}\bar{n}(\gamma, q)] - [q + v_{\text{esc}}(\gamma)]\bar{n}(\gamma, q) . \end{aligned} \quad (5.4)$$

The variable  $Q(\gamma, q) = \dot{\gamma}\bar{n}(\gamma, q)$  is defined such that Eq. 5.4 becomes:

$$-\bar{S}(\gamma, q) - n(\gamma, 0) = \frac{\partial}{\partial \gamma} Q(\gamma, q) - [q + v_{\text{esc}}(\gamma)] \frac{Q(\gamma, q)}{\dot{\gamma}} , \quad (5.5)$$

$Q(\gamma, q)$  can be described as the number of cosmic rays per unit time that cool from Lorentz factor  $\gamma$ . The differential equation describing the time evolution of the cosmic-ray energy density distribution has been reduced to a first order linear differential equation of form:

$$b(x) = \frac{dy}{dx} + a(x)y , \quad (5.6)$$

which has solution:

$$y(x) = e^{-A(x)} \int_{x'=x} e^{A(x')} b(x') dx' , \quad (5.7)$$

where  $A(x) = \int_{x''=x}^x a(x'') dx''$ . Therefore, the solution of Eq. 5.5 is given by:

$$Q(\gamma, q) = e^{\int_{\gamma''=\gamma}^{\gamma'} d\gamma'' [q + v_{\text{esc}}]/\dot{\gamma}} \int_{\gamma'=\gamma}^{\gamma'} e^{-\int_{\gamma''=\gamma'}^{\gamma''} d\gamma'' [q + v_{\text{esc}}]/\dot{\gamma}} [\bar{S}(\gamma', q) + n(\gamma', 0)] d\gamma' . \quad (5.8)$$

Following Melrose, (1980), the time required for a cosmic ray to cool from Lorentz factor  $\gamma'$  to  $\gamma$  is given by:

$$\begin{aligned} \tau(\gamma', \gamma) &= \int_{\gamma''=\gamma'}^{\gamma} d\gamma'' \frac{1}{\dot{\gamma}(\gamma'')} - \int_{\gamma''=\gamma}^{\gamma'} d\gamma'' \frac{1}{\dot{\gamma}(\gamma'')} \\ &= \int_{\gamma}^{\gamma'} d\gamma'' \frac{1}{\dot{\gamma}(\gamma'')} , \end{aligned} \quad (5.9)$$

where  $\gamma_0$  is the original Lorentz factor (at  $t = 0$ ) of a cosmic ray before cooling to Lorentz factor  $\gamma$ , i.e.  $\tau(\gamma_0, \gamma) = t$ . The term  $\lambda(\gamma', \gamma)$  is defined such that  $1 - \exp[-\lambda(\gamma', \gamma)]$  is the probability that the cosmic ray escapes the region of interest while cooling from Lorentz factor  $\gamma'$  to  $\gamma$ :

$$\begin{aligned} \lambda(\gamma', \gamma) &= \int_{\gamma''=\gamma'}^{\gamma} d\gamma'' \frac{v_{\text{esc}}(\gamma'')}{\dot{\gamma}(\gamma'')} - \int_{\gamma''=\gamma}^{\gamma'} d\gamma'' \frac{v_{\text{esc}}(\gamma'')}{\dot{\gamma}(\gamma'')} \\ &= \int_{\gamma}^{\gamma'} d\gamma'' \frac{v_{\text{esc}}(\gamma'')}{\dot{\gamma}(\gamma'')} . \end{aligned} \quad (5.10)$$

Therefore, Eq. 5.8 has solution:

$$\begin{aligned} Q(\gamma, q) &= \int_{\gamma}^{\infty} e^{-[q\tau(\gamma', \gamma) + \lambda(\gamma', \gamma)]} \{ \bar{S}(\gamma', q) + n(\gamma', 0) \} d\gamma' \\ \bar{n}(\gamma, q) &= \frac{1}{\dot{\gamma}} \int_{\gamma}^{\infty} e^{-\lambda(\gamma', \gamma)} \left\{ e^{-q\tau(\gamma', \gamma)} \bar{S}(\gamma', s) + e^{-q\tau(\gamma', \gamma)} n(\gamma', 0) \right\} d\gamma' . \end{aligned} \quad (5.11)$$

The following inverse Laplace transformations can be used to obtain the cosmic ray energy density distribution  $n(\gamma, t)$  from Eq. 5.11:

$$\begin{aligned} e^{-cq} \bar{f}(q) &\longleftrightarrow H(t - c)f(t) \\ e^{-cq} &\longleftrightarrow \delta(t - c) , \end{aligned} \quad (5.12)$$

with  $H$  is the Heaviside step function and  $\delta$  is the Dirac delta function. Therefore, Eq. 5.1 has solution:

$$\begin{aligned} n(\gamma, t) &= \frac{1}{\dot{\gamma}} \int_{\gamma}^{\infty} e^{-\lambda(\gamma', \gamma)} \{ H(t - \tau(\gamma', \gamma)) S(\gamma', t - \tau(\gamma', \gamma)) + \delta(t - \tau(\gamma', \gamma)) n(\gamma', 0) \} d\gamma' \\ &= \frac{1}{\dot{\gamma}} \int_{\gamma}^{\gamma_0} e^{-\lambda(\gamma', \gamma)} S(\gamma', t - \tau(\gamma', \gamma)) d\gamma' + \frac{\dot{\gamma}_0}{\dot{\gamma}} e^{-\lambda(\gamma_0, \gamma)} n(\gamma_0, 0) , \end{aligned} \quad (5.13)$$

where  $\gamma_0$  is the original Lorentz factor (at  $t = 0$ ) of a cosmic ray before cooling to Lorentz factor  $\gamma$ , i.e.  $\tau(\gamma_0, \gamma) = t$ . Eq. 5.13 describes the cosmic ray energy density distribution at time  $t$  with Lorentz factor  $\gamma$ . In order to solve Eq. 5.13 analytically, impulsive and continuous accelerator sources will be treated separately.

### 5.1.1 Impulsive source of cosmic rays

An impulsive source is a source of cosmic rays (and/or electrons) that inject material into the ISM at one point in time instantaneously or over a time period much less than the observation time. Examples of impulsive sources include supernovae, SNRs or gamma-ray bursts. The source term of an impulsive source can be described by  $S(\gamma, t > 0) = 0$ . Assuming that cosmic rays do not escape the system ( $\lambda = 0$ ), Eq. 5.13 becomes:

$$n(\gamma, t) = \frac{\dot{\gamma}_0}{\dot{\gamma}} n(\gamma_0, 0) \exp(-\lambda(\gamma_0, \gamma)) . \quad (5.14)$$

The cosmic ray flux at Earth tends to follow a power law spectrum (see Section 2.2.3), suggesting that sources inject cosmic rays with a power law energy distribution. Hence, it will be assumed that injected particles can be described by an exponential cutoff power law spectrum:

$$\begin{aligned} n(\gamma_0, 0) &= \tilde{A} E^{-\Gamma} \exp\left(-\frac{E}{E_c}\right) = \tilde{A} \left(\gamma_0 mc^2\right)^{-\Gamma} \exp\left(-\frac{\gamma_0 mc^2}{\gamma_c mc^2}\right) \\ &= A \gamma_0^{-\Gamma} \exp\left(-\frac{\gamma_0}{\gamma_c}\right) , \end{aligned} \quad (5.15)$$

where  $\Gamma$  is the spectral index,  $A = \tilde{A}(mc^2)^{-\Gamma}$  is the normalisation factor and  $E_c$  and  $\gamma_c$  are the cutoff energy and cutoff Lorentz factor respectively.

## Hadronic Cosmic Ray Source

Hadronic cosmic rays lose their energies through proton-proton interactions with the ISM (see Section 2.3.2). The energy loss rate of hadronic cosmic rays with Lorentz factor  $\gamma$  is approximated by Aharonian and Atoyan, (1996):

$$\dot{\gamma} = -\frac{\gamma}{\tau_{pp}} , \quad (5.16)$$

where  $\tau_{pp}$  is the p-p cooling time (Eq. 2.42). The cooling time is inversely proportional to the p-p cross section,  $\sigma_{pp}$ , where the p-p cross section is weakly dependent on the proton energy (see Eq. 2.41). The solution to Eq. 5.16 is:

$$\gamma = \gamma_0 \exp(-t/\tau_{pp}) . \quad (5.17)$$

The initial cosmic ray energy distribution can be rewritten in terms of  $\gamma$ :

$$n_p(\gamma_0, 0) = A\gamma^{-\Gamma} \exp\left(-\frac{\Gamma t}{\tau_{pp}}\right) \exp\left(\frac{-\gamma \exp(t/\tau_{pp})}{\gamma_c}\right) . \quad (5.18)$$

As  $\dot{\gamma}_0 = -\gamma_0/\tau_{pp}$ :

$$\frac{\dot{\gamma}_0}{\dot{\gamma}} = \frac{\gamma_0}{\gamma} = \exp(t/\tau_{pp}) . \quad (5.19)$$

Eq. 5.14 and Eq. 5.18 can be combined to find the energy density distribution of cosmic rays for an impulsive source injecting protons with an exponential cutoff power law spectrum:

$$n_p(\gamma, t) = A\gamma^{-\Gamma} \exp\left(-\frac{(\Gamma - 1)t}{\tau_{pp}} - \frac{\gamma \exp(t/\tau_{pp})}{\gamma_c}\right) . \quad (5.20)$$

The top panel of Fig. 5.1 shows the evolution of a hadronic cosmic ray energy density distribution and subsequent gamma-ray SED for an initial power law spectrum ( $\Gamma = 2.2$ ) and an exponential cutoff power law spectrum ( $\Gamma = 2.2$ ,  $E_c = 100$  TeV). As the age of the system increases beyond the proton cooling time (i.e.  $t > \tau_{pp} = 5.3 \times 10^5$  yr), the cosmic-ray density and subsequent gamma-ray emission decreases (see Section 2.3.2).

## Leptonic Cosmic Ray Source

Assuming synchrotron losses are dominant (valid for high-energy electrons and/or regions of high magnetic field strength, see Eq. 2.79), the leptonic cooling rate is given by:

$$\dot{\gamma} = -b_s \gamma^2 , \quad (5.21)$$

where  $b_s = 1.292 \times 10^{-15} (B/\text{mG})^2 \text{ s}^{-1}$  is the synchrotron loss term for electrons. The solution for Eq. 5.21 is:

$$\gamma_0 = \frac{\gamma}{1 - \gamma b_s t} , \quad (5.22)$$

giving the initial electron distribution in terms of Lorentz factor  $\gamma$ :

$$n_e(\gamma_0, 0) = A\gamma^{-\Gamma} (1 - \gamma b_s t)^\Gamma \exp\left(-\frac{\gamma}{\gamma_c(1 - \gamma b_s t)}\right) . \quad (5.23)$$

From Eq. 5.22 it can be seen that at any time  $t$ , there exists a critical Lorentz factor:



Figure 5.1: Evolution of the cosmic ray energy density distribution (*top*) and subsequent gamma-ray SED (*bottom*) for an impulsive source injecting protons following a power law spectrum ( $\propto E^{-\Gamma}$ , red) and an exponential cutoff power law spectrum ( $\propto E^{-\Gamma} \exp(-E/E_c)$ , black) as given by Eq. 5.20.  $W_p$  is the total energy of cosmic ray protons injected at  $t = 0.1q$

$$\gamma_{\text{cr}} = \frac{1}{b_s t} , \quad (5.24)$$

where electrons with  $\gamma_{\text{cr}}$  have an initial Lorentz factor  $\gamma_0 \rightarrow \infty$ . An impulsive system at time  $t$  cannot have electrons exceeding this critical Lorentz factor.

As  $\dot{\gamma}_0 = -b_s \gamma^2$ :

$$\frac{\dot{\gamma}_0}{\dot{\gamma}} = \left( \frac{\gamma_0}{\gamma} \right)^2 , \quad (5.25)$$

Eq. 5.14 and Eq. 5.23 can be combined to find the cosmic-ray energy density distribution for electrons with Lorentz factor  $\gamma$ :

$$n_e(\gamma, t) = A \gamma^{-\Gamma} (1 - \gamma b_s t)^{\Gamma-2} \exp\left(-\frac{\gamma}{\gamma_c(1 - \gamma b_s t)}\right) . \quad (5.26)$$

Fig. 5.2 shows the energy density distribution evolution of electrons and the subsequent gamma-ray emission for an impulsive source with an initial power law and exponential cutoff power law spectrum. As the system ages, the critical Lorentz factor (see Eq. 5.24) decreases and the energy density distribution can be described by an exponential cutoff power regardless of the distribution at times  $t = 0$  yr. The peak in the subsequent synchrotron and inverse Compton emission shifts to lower energies as the system evolves in time.

### 5.1.2 Continuous source of cosmic rays

A continuous source is a source that injects cosmic rays into the ISM at a constant rate over a significant time frame. For simplicity, it will be assumed that source has a constant injection luminosity; i.e. no outbursts or ‘dormant’ stages. Examples of continuous sources include pulsars and massive stellar clusters which typically inject cosmic rays for over  $10^5$  yr. At  $t = 0$  yr the initial cosmic ray density,  $n(\gamma_0, 0)$ , is zero. Assuming that no cosmic rays escape the system ( $\lambda = 0$ ), Eq. 5.11 becomes:

$$n(\gamma, t) = \frac{1}{\dot{\gamma}(\gamma)} \int_\gamma^{\gamma_0} S(\gamma', t - \tau(\gamma', \gamma)) d\gamma' , \quad (5.27)$$

and it will be assumed that the electron energy distribution of accelerators such as PWNe follow a power law (e.g. (Torres et al., 2014)). Hence, the source term in Eq. 5.27 will follow:

$$S(\gamma, t) = A \gamma^{-\Gamma} . \quad (5.28)$$

#### Hadronic Cosmic Ray Source

Combining Eq. 5.16, Eq. 5.17, Eq. 5.27 & Eq. 5.28 gives the proton energy density distribution at Lorentz factor  $\gamma$ :



Figure 5.2: Evolution of the cosmic ray energy density distribution (*top*) and subsequent gamma-ray SED (*bottom*) for an impulsive source injecting electrons following a power law spectrum (red) and an exponential cutoff power law spectrum (black) as given by Eq. 5.26. The critical Lorentz factor (Eq. 5.24) at different ages are shown by the vertical blue-dashed lines.

$$\begin{aligned}
n_p(\gamma, t) &= \frac{A\tau_{pp}}{\gamma} \int_\gamma^{\gamma_0} \gamma^{-\Gamma} d\gamma' \\
&= \frac{A\tau_{pp}}{\gamma(\Gamma - 1)} [\gamma^{1-\Gamma} - \gamma_0^{1-\Gamma}] \\
&= \frac{A\tau_{pp}}{\gamma(\Gamma - 1)} \left[ \gamma^{1-\Gamma} - (\gamma \exp(t/\tau_{pp}))^{1-\Gamma} \right] \\
&= \frac{A\tau_{pp}\gamma^\Gamma - 1}{\gamma(\Gamma - 1)} \left[ 1 - \exp\left(-\frac{t(\Gamma - 1)}{\tau_{pp}}\right) \right] \\
&= \frac{\tau_{pp}A\gamma^{-\Gamma}}{\Gamma - 1} \left[ 1 - \exp\left(-\frac{t(\Gamma - 1)}{\tau_{pp}}\right) \right].
\end{aligned} \tag{5.29}$$

At  $t = 0$ , the cosmic ray energy density distribution is initially zero. As the system ages ( $t \gg \tau_{pp}$ ), a steady state occurs when the energy loss through p-p interactions is balanced by the energy injected by the source (see Fig. 5.3). The steady state ( $t \gg \tau_{pp}$ ) has an energy spectrum:

$$n_p(\gamma, t \gg \tau_{pp}) = \frac{\tau_{pp}A\gamma^{-\Gamma}}{1 - \Gamma}. \tag{5.30}$$

Fig. 5.3 shows the evolution of the cosmic-ray and subsequent gamma-ray spectra for a system that continuously injects protons into a system with proton-proton cooling time of  $5.7 \times 10^5$  yr.

### Leptonic Cosmic Ray Source

Again, synchrotron radiation is assumed to be the dominant cause of electron energy loss. From Eq. 5.22 & Eq. 5.24, electrons with Lorentz factor greater than the critical Lorentz factor ( $\gamma \geq \gamma_{cr}$ ) must be treated separately:

$$n_e(\gamma) = \begin{cases} \frac{1}{\dot{\gamma}(\gamma)} \int_\gamma^{\gamma_0} S(\gamma', t - \tau(\gamma', \gamma)) d\gamma' & \gamma < \gamma_{cr} \\ \frac{1}{\dot{\gamma}(\gamma)} \int_\gamma^\infty S(\gamma', t - \tau(\gamma', \gamma)) d\gamma' & \gamma \geq \gamma_{cr} \end{cases}. \tag{5.31}$$

For  $\gamma < \gamma_{cr}$ , combining Eq. 5.21, Eq. 5.22, Eq. 5.28 & Eq. 5.31:

$$\begin{aligned}
n_e(\gamma < \gamma_{cr}) &= \frac{A}{b_s \gamma^2(\Gamma - 1)} [\gamma^{1-\Gamma} - \gamma_0^{1-\Gamma}] \\
&= \frac{A}{b_s \gamma^2(\Gamma - 1)} \left[ \gamma^{1-\Gamma} - \frac{\gamma^{1-\Gamma}}{(1 - \gamma b_s t)^{1-\Gamma}} \right] \\
&= \frac{A\gamma^{-\Gamma}\gamma}{b_s \gamma^2(\Gamma - 1)} \left[ 1 - \frac{1}{(1 - \gamma b_s t)^{1-\Gamma}} \right] \\
&= \frac{A\gamma^{-\Gamma}}{b_s \gamma(\Gamma - 1)} [1 - (1 - \gamma b_s t)^{\Gamma-1}].
\end{aligned} \tag{5.32}$$

For  $\gamma \geq \gamma_{cr}$ :

$$\begin{aligned}
n_e(\gamma \geq \gamma_{cr}) &= \frac{A}{b_s \gamma^2(1 - \Gamma)} (\infty^{1-\Gamma} - \gamma^{1-\Gamma}) \\
&= \frac{A\gamma^{-\Gamma}}{b_s \gamma(\Gamma - 1)}.
\end{aligned} \tag{5.33}$$

Therefore:



Figure 5.3: Evolution of the cosmic ray energy density distribution (top) and subsequent gamma-ray spectrum (bottom) for a continuous source injecting protons following a power law spectrum as given by Eq. 5.29. The steady state ( $t \gg \tau_{pp}$ , see Eq. 5.30) is represented by the solid red line.  $L_p$  is the energy of cosmic rays injected per second into the system.

$$n_e(\gamma) = \frac{A\gamma^{-\Gamma}}{b_s\gamma(\Gamma-1)} \begin{cases} [1 - (1 - \gamma b_s t)^{\Gamma-1}] & \gamma < \gamma_{\text{cr}} \\ 1 & \gamma \geq \gamma_{\text{cr}} \end{cases}. \quad (5.34)$$

A steady state is reached when:

$$t \equiv \tau = (\gamma b_s)^{-1} = \tau_{\text{sync}}, \quad (5.35)$$

where  $\tau_{\text{sync}}$  is the cooling time of electrons through synchrotron emission. The evolution of the electron spectra and subsequent gamma-ray spectra is shown in Fig. 5.4. Unlike protons, where the cooling time  $\tau_{pp}$  is dependent only on the medium number density, the cooling time for electrons through synchrotron radiation is inversely proportional to their energy. Therefore, high-energy electrons reach a steady state before lower energy electrons.

## 5.2 Transport of Cosmic Rays

Eq. 5.20, Eq. 5.26, Eq. 5.29 and Eq. 5.34 describe the evolution of the spectral energy density distribution of cosmic rays at the location of the source. However, cosmic rays propagate from their place of birth into the ISM through diffusion (see Section 2.2.2). This section will describe how the cosmic ray energy density distribution spatially and temporally evolves as a function of distance  $r$  from the accelerator.

### 5.2.1 Propagation of Cosmic Rays

We will take the simple example of an impulsive cosmic ray source injecting particles with power law spectrum ( $n(\gamma, r=0, t=0) = A\gamma^{-\Gamma}$ ) into the centre of a uniform cloud at  $t=0$ . The cosmic rays are then allowed to propagate outwards. Atoyan et al., (1995) gives the Green's function solution of Eq. 5.13 at a distance  $r$  from an impulsive source:

$$n(\gamma, r, t) = \frac{\dot{\gamma}_0}{\dot{\gamma}} \frac{n(\gamma, 0, 0)}{\pi^{\frac{3}{2}} R_{\text{diff}}(\gamma, t, B)^3} \exp\left(-\frac{r^2}{R_{\text{diff}}(\gamma, t, B)^2}\right) \quad (5.36a)$$

$$R_{\text{diff}}(\gamma, t, B) = \sqrt{4 \int_{\gamma}^{\gamma_0} \frac{D(\gamma', B)}{\dot{\gamma}'} d\gamma'}, \quad (5.36b)$$

where  $R_{\text{diff}}(\gamma, t)$  represents the distance of which cosmic rays with Lorentz factor  $\gamma$  propagate after time  $t$ , i.e. ‘diffusion distance’ and  $D(\gamma, B)$  represents the diffusion coefficient for cosmic rays in a magnetic field strength  $B$  (see section (reference diffusion section in chapter 1)).

#### Hadronic Cosmic Ray Source

Combining Eq. 5.16 and Eq. 5.36b gives the evolution of the diffusion radius at distance  $r$  from the accelerator:



Figure 5.4: Evolution of the cosmic ray energy density distribution (*top*) and subsequent gamma-ray SED (*bottom*) for a continuous source injecting electrons following a power law spectrum as given by Eq. 5.34. The steady state of electrons ( $t \gg \tau \approx \tau_{\text{sync}}$ , see Eq. 5.35) is represented by the dash-dot line.  $L_e$  is the energy of electrons injected per second into the system.

$$\begin{aligned}
R_{\text{diff}}(\gamma, t, B) &= \sqrt{4\tau_{pp}\chi D_0 \left(\frac{B}{3 \mu\text{G}}\right)^{-\delta} \int_\gamma^{\gamma_0} \gamma'^{\delta-1} d\gamma'} \\
&= \sqrt{4\tau_{pp}\chi D_0 \left(\frac{B}{3 \mu\text{G}}\right)^{-\delta} \{\gamma_0^\delta - \gamma^\delta\}} \\
&= \sqrt{4\tau_{pp}\chi D_0 \left(\frac{B}{3 \mu\text{G}}\right)^{-\delta} \{\gamma^\delta \exp(\gamma t/\tau_{pp}) - \gamma^\delta\}} \\
&= \sqrt{4D(\gamma, B)t \frac{\left(\exp\left(\frac{\delta t}{\tau_{pp}}\right) - 1\right)}{\delta t/\tau_{pp}}} .
\end{aligned} \tag{5.37}$$

The time evolution of the cosmic ray density distribution can be found by combining Eq. 5.16, Eq. 5.18 and Eq. 5.36a:

$$n_p(\gamma, r, t) = \frac{A\gamma^{-\Gamma}}{\pi^{\frac{3}{2}} R_{\text{diff}}(\gamma, t, B)^3} \exp\left(-\frac{(\Gamma-1)t}{\tau_{pp}} - \frac{r^2}{R_{\text{diff}}(\gamma, t, B)^2}\right). \tag{5.38}$$

The top panel of Fig. 5.5 shows the hadronic cosmic-ray energy density distribution at different distances  $r$  from an impulsive accelerator 10 kyr after injecting cosmic rays with spectrum  $n(\gamma_0, 0) = A\gamma^{-\Gamma}$  in a medium with number density and magnetic field  $n = 100 \text{ cm}^{-3}$  and  $B = 10 \mu\text{G}$  respectively. A diffusion suppression coefficient of  $\chi = 0.01$  was chosen to demonstrate the transport of cosmic rays in molecular clouds (see Section 2.2.2). Eq. 5.37 and Fig. 5.5 shows that higher energy protons are able to diffuse further from the source than their lower energy counterparts. For distances far from the source, only the highest energy protons (e.g.  $E \gtrsim 30 \text{ TeV}$  for a distance of 20 pc) are able to reach this region for a given time. Hence, for distances greater than the diffusion length ( $r > R_{\text{diff}}$ ), the proton energy spectra is steeper than the initial injected spectra. For distances close to the source, high-energy protons escape this region faster than low energy protons (e.g. a 1 TeV and a 100 TeV proton takes  $\approx 14$  kyr and  $\approx 1.4$  kyr respectively to travel 5 pc). Therefore, for distances within the diffusion length ( $r < R_{\text{diff}}$ ), the cosmic energy density distribution is shallower than the injected spectrum.

A continuous source can be treated as a series of impulsive injectors and Eq. 5.13 must be solved numerically. However, for a case when  $t \ll \tau_{pp}$ , the cosmic ray energy density distribution can be described by (Aharonian and Atoyan, 1996):

$$\begin{aligned}
n_p(E, R, t) &= \frac{AE^{-\Gamma}}{4\pi D(E, B)r} \operatorname{erfc}\left(\frac{r}{R_{\text{diff}}(\gamma, t, B)}\right) \\
\operatorname{erfc}(z) &= \frac{2}{\sqrt{\pi}} \int_z^\infty \exp(-x^2) dx .
\end{aligned} \tag{5.39}$$

The bottom panel of Fig. 5.5 shows the cosmic ray energy density distribution at different distances  $r$  from a continuous accelerator of protons. For distances close to the source ( $R \ll R_{\text{diff}}$ ), the cosmic ray energy spectrum is simply:

$$n_p(E, R, t) = \frac{AE^{-\Gamma}}{4\pi D(E, B)r} . \tag{5.40}$$

As  $D \propto \gamma^\delta$  (see Eq. 2.31), the cosmic ray energy spectrum can be described by a power law with index  $\Gamma + \delta$ . The higher index (compared to the injected spectrum) mathematically describes high-energy cosmic rays escaping at a faster rate compared to low energy protons.



Figure 5.5: The cosmic ray energy density distribution for an impulsive (top panel) and continuous (bottom panel) source of protons after 10 kyr as described by Eq. 5.38 and Eq. 5.39 respectively. The solid blue line shows the shape of the injected proton energy distribution ( $\propto E^{-\Gamma}$ ).

. For reference, the diffusion distance (Eq. 5.37) is represented by the dashed-dotted line.

### Leptonic Cosmic Ray Source

For an accelerator injecting electrons, combining Eq. 2.31, Eq. 5.21 and Eq. 5.36b gives the diffusion radius for electrons:

$$\begin{aligned}
 R_{\text{diff}}(\gamma, t, B) &= \sqrt{4b_s^{-1}\chi D_0 \left(\frac{B}{3 \text{ pG}}\right)^{-\delta} \int_{\gamma}^{\gamma_0} \gamma'^{\delta-2} d\gamma'} \\
 &= \sqrt{\frac{4}{b_s(\delta-1)}\chi D_0 \left(\frac{B}{3 \text{ pG}}\right)^{-\delta} \{\gamma_0^{\delta-1} - \gamma^{\delta-1}\}} \\
 &= \sqrt{\frac{4}{b_s(\delta-1)}\chi D_0 \left(\frac{B}{3 \text{ pG}}\right)^{-\delta} \{\gamma^{\delta-1}(1 - \gamma b_s t)^{\delta-1} - \gamma^{\delta-1}\}} \\
 &= \sqrt{\frac{4D(\gamma, B)}{b_s \gamma(1-\delta)} [1 - (1 - \gamma b_s t)^{1-\delta}]}.
 \end{aligned} \tag{5.41}$$

The leptonic energy density distribution for an impulsive injector is found by combining Eq. 5.21, Eq. 5.36a and Eq. 5.23:

$$n_e(\gamma, r, t) = \frac{(1 - \gamma b_s t)^{\Gamma-2} n_0 \gamma^{-\Gamma}}{\pi^{3/2} R_{\text{diff}}(\gamma, t, B)^3} \exp\left(-\frac{r^2}{R_{\text{diff}}(\gamma, t, B)^2}\right). \tag{5.42}$$

The top panel of Fig. 5.6 describes the leptonic energy density distribution at a distance  $r$  from an impulsive injector 10 kyr after injecting electrons with power law spectrum  $(n(\gamma, r = 0, t = 0) = A\gamma^{-\Gamma})$  into a medium with number density  $1 \text{ cm}^{-3}$  and magnetic field  $B = 10 \text{ pG}$ . As with protons, high-energy electrons are able to diffuse to further than lower energy electrons. Therefore, for distances greater than the diffusion length ( $r > R_{\text{diff}}$ ), the electron energy spectra is steeper than the injected spectra. For distances close to the source ( $r < R_{\text{diff}}$ ), the electron energy spectra is shallower than the injected spectra. Unlike protons, a maximum electron energy can be seen corresponding to the critical Lorentz factor described by Eq. 5.24.

For a continuous source of electrons, Eq. 5.13 must be solved numerically. However, for a source injecting electrons constantly with a simple power law (and assuming synchrotron losses are dominant), Atoyan et al., (1995) gives the electron energy spectrum as:

$$\begin{aligned}
 n_e(E, R, t) &= \frac{n_0 E^{-\Gamma}}{4\pi D(E, B)r} \operatorname{erfc}\left(\frac{r}{2\sqrt{D(E, B)t_\gamma}}\right) \\
 t_\gamma &= \min\left(t, \frac{1}{b_s \gamma}\right).
 \end{aligned} \tag{5.43}$$

Similarly to protons, for distances close to the source ( $R \ll R_{\text{diff}}$ ), the electron energy spectrum is:

$$n_e(E, R, t) = \frac{AE^{-\Gamma}}{4\pi D(E, B)r}, \tag{5.44}$$

where  $n_e \propto \gamma^{-(\Gamma+\delta)}$ .



Figure 5.6: The cosmic ray energy density distribution for an impulsive source (*top*) and continuous source (*bottom*) of electrons following a power law (solid blue line) after  $t = 10$  kyr as described by Eq. 5.42 and Eq. 5.43 respectively. For reference, the diffusion distance is represented by the dashed-dotted line and the critical energy ( $\gamma_{\text{cr}} \approx 13$  TeV) is shown by the blue vertical dashed line.

## 5.3 Modelling the energy density distribution of cosmic rays

Section 5.1 and Section 5.2 assumed simple scenarios in order to solve Eq. 5.13. Such scenarios included the type of accelerator (impulsive or continuous) and whether the time of interest is less than the cooling time of the particle (e.g. Eq. 5.39 and Eq. 5.43). It was also assumed that no particles escape the system (i.e.  $v_{\text{esc}} = 0$  in Eq. 5.1). For scenarios that do not make these assumptions, Eq. 5.13 must be solved analytically. A Riemann sum can be used to approximate the integral in Eq. 5.13 with:

$$n(\gamma, t) = \frac{1}{\dot{\gamma}(\gamma)} \sum_{\gamma'=\gamma}^{\gamma_0} e^{-\lambda(\gamma', \gamma)} S(\gamma') \Delta\gamma' + \frac{\dot{\gamma}_0}{\dot{\gamma}} n(\gamma_0, 0) e^{-\lambda(\gamma_0, \gamma)} , \quad (5.45)$$

where  $\sum_{\gamma'=\gamma}^{\gamma_0}$  sums the function  $e^{-\lambda(\gamma', \gamma)} S(\gamma')$  over Lorentz factor  $\gamma' = \gamma \rightarrow \gamma_0$  in intervals of width  $\Delta\gamma'$ . The radiation loss rate  $\dot{\gamma}$  for cosmic ray protons and electrons is calculated via Eq. 2.42 and Eq. 2.79 respectively. This section will describe the software **Newsedprod** which analytically solves Eq. 5.13.

### 5.3.1 Newsedprod

**Newsedprod** is a software originally developed by (Voisin, 2017) that injects cosmic rays into a uniform region of ISM (constant number density and magnetic field) with injection luminosity  $W$  [ergs/s] (continuous source) or energy budget  $L$  [erg] (impulsive source). The energy spectrum of cosmic ray protons and electrons can be described by:

$$J(E) = N_0 J'(E) \quad [\text{TeV}^{-1} \text{cm}^{-3}] , \quad (5.46)$$

where  $A$  is the normalisation constant and  $J'(E)$  is the ‘denormalised’ energy spectrum. The denormalised energy spectrum follows either:

- power-law,  $J'(E) = E^{-\Gamma}$
- exponential cutoff power-law,  $J'(E) = E^{-\Gamma} \exp(-E/E_c)$ , where  $E_c$  is the cutoff energy
- broken power-law,  $J'(E) = (E/E_{\text{break}})^{-\Gamma_i}$ , where  $\Gamma_i = \Gamma_1$  for  $E \leq E_{\text{break}}$  and  $\Gamma_i = \Gamma_2$  otherwise

For an accelerator injecting cosmic rays (protons or electrons) with Lorentz factor between  $\gamma_{\min}$  and  $\gamma_{\max}$ , the total amount of energy injected into the system must equate to the injection luminosity/energy budget:

$$N_0 = \frac{L \text{ or } W\Delta t}{\int_{\gamma_{\min}}^{\gamma_{\max}} E J'(E) dE} , \quad (5.47)$$

where  $W\Delta t$  represents the total energy injected into the system in time interval  $\Delta t$ .

After injection, cosmic rays radiate their energy and cool to lower Lorentz factors as described in Section 2.3.  $\gamma_1$  and  $\gamma_2$  are defined to be the Lorentz factors at time  $t$  that correspond to the minimum,  $\gamma_{\min}$ , and maximum,  $\gamma_{\max}$ , Lorentz factor at  $t = 0$  before cooling:



Figure 5.7: Comparison of Newsedprod (solid lines) and results by Manolakou et al., (2007) (dots) where electrons between Lorentz factors  $\gamma_{\min} = 10^2$  and  $\gamma_{\max} = 10^9$  are injected with power law spectrum ( $\Gamma = 2.0$ ) into a medium with number density and magnetic field  $n = 1 \text{ cm}^{-3}$  and  $B = 10 \mu\text{G}$  respectively. Electrons are not allowed to escape the cloud ( $v_{\text{esc}} = 0$ ). (top) Time evolution of electrons against a soft photon field of temperature  $T = 30000 \text{ K}$  and energy density  $u_0 = 500 \text{ eV cm}^{-3}$ . The positions of  $\gamma_1$  (see Eq. 5.48) are shown by the solid vertical blue lines. (bottom) The age of the system is kept constant at  $10^6 \text{ yr}$  while the energy density of the photon field is allowed to vary. note that the variation at lower Lorentz factors is due to different values of  $\gamma_{\min}$  chosen by Manolakou et al., (2007).

$$\begin{aligned}\tau(\gamma_{\max}, \gamma_1) &= t \\ \tau(\gamma_{\min}, \gamma_2) &= t ,\end{aligned}\tag{5.48}$$

where  $\tau$  is the cooling time described in Eq. 5.9. Electrons with Lorentz factor  $\gamma < \gamma_1$  represent the ‘uncooled’ part of the spectrum and the energy density distribution follows the initial injected electron spectra ( $\Gamma = 2.0$ ). Electrons above  $\gamma_1$  have reached a steady state where radiative losses are balanced by the injected electrons. To reduce computation time, Eq. 5.45 can be split into three different regimes:

$$n(\gamma, t) = \frac{1}{\dot{\gamma}(\gamma)} \sum_{\gamma'=\gamma_\ell}^{\gamma_u} e^{-\lambda(\gamma', \gamma)} S(\gamma') \Delta\gamma' ,\tag{5.49}$$

where  $\gamma_\ell$  and  $\gamma_u$  are the lower and upper Lorentz factors given by:

$$(\gamma_\ell, \gamma_u) = \begin{cases} (\gamma_{\min}, \gamma_0), & \gamma_2 < \gamma \leq \gamma_{\min} \\ (\gamma, \gamma_0), & \gamma_{\min} < \gamma \leq \gamma_1 \\ (\gamma, \gamma_{\max}), & \gamma_1 < \gamma \leq \gamma_{\max} \end{cases} ,\tag{5.50}$$

for  $\gamma_{\min} < \gamma_1$  and:

$$(\gamma_\ell, \gamma_u) = \begin{cases} (\gamma_{\min}, \gamma_0), & \gamma_2 < \gamma \leq \gamma_1 \\ (\gamma_{\min}, \gamma_{\max}), & \gamma_1 < \gamma \leq \gamma_{\min} \\ (\gamma, \gamma_{\max}), & \gamma_{\min} < \gamma \leq \gamma_{\max} \end{cases} ,\tag{5.51}$$

for  $\gamma_{\min} > \gamma_1$ .

Fig. 5.7 shows the comparison of the electron energy density distribution predicted by `Newsedprod` to the results published by Manolakou et al., (2007). Assuming that there is no escape, i.e. ( $v_{\text{esc}} = 0$ ), electrons are continuously injected with an exponential cutoff power law spectrum ( $\Gamma^{2.0}$ ) into a uniform cloud with number density  $n = 1 \text{ cm}^{-3}$  and magnetic field  $B = 10 \mu\text{G}$ . The top panel of Fig. 5.7 shows the time evolution of electrons against a soft photon field with temperature and energy density  $T = 30000 \text{ K}$  and  $u_0 = 500 \text{ eV cm}^{-3}$  (in line with the parameters chosen by Manolakou et al., (2007)) at times  $10^5$  ( $\gamma_1 = 2.5 \times 10^6$ ),  $8 \times 10^5$  ( $\gamma_1 = 5 \times 10^4$ ),  $2 \times 10^6 \text{ yr}$  ( $\gamma_1 = 1.6 \times 10^3$ ). Synchrotron losses are dominant for electrons with Lorentz factor  $\gamma > \gamma_s = 6 \times 10^5$  (see reference non thermal section). The bottom panel of Fig. 5.7 investigates how the change in the photon field energy density affects the electron energy density distribution at time  $10^6 \text{ yr}$ . Synchrotron losses are dominant for  $\gamma > \gamma_s = 3.8 \times 10^5$  ( $u_0 = 250 \text{ eV cm}^{-3}$ ) and  $\gamma > \gamma_s = 1.8 \times 10^6$  ( $u_0 = 2500 \text{ eV cm}^{-3}$ ). Manolakou et al., (2007) injects electrons between  $\gamma_{\min} = 10^4$  and  $\gamma_{\max} = 10^9$  while `Newsedprod` injects electrons between  $\gamma_{\min} = 10^{-2}$  and  $\gamma_{\max} = 10^9$ . The threshold Lorentz factor seen in the Manolakou et al., (2007) corresponds to  $\gamma = 10^4$  at  $t = 0$  after being cooled, i.e.  $\gamma_1$ .

Fig. 5.8 shows the subsequent inverse-Compton and synchrotron photon emission of a continuous source of electrons for different scenarios. The top-left panel of Fig. 5.8 shows the evolution of the spectral energy density distribution at times  $10^3$ ,  $10^4$ ,  $10^5$  and  $10^6$  years. The IC and synchrotron emission originally peaks at high energies and then migrates to lower energies at later ages, representing the steady state of cooled low-energy electrons. The highest energy photons of the IC and synchrotron spectra rapidly reaches a steady state due to the relatively short lifetime of high-energy electrons (e.g. a 100 TeV



Figure 5.8: The multiwavelength SED results from Newsedprod for different scenarios of a continuous source. Unless otherwise stated, the input parameters are shown in the bottom-right panel ( $L$  =energy injection luminosity,  $t$  =age of system,  $d$  =distance to the cloud from Earth,  $n$  =density of ISM,  $B$  =background magnetic field,  $\Gamma$  =spectra of injected electrons,  $T$  and  $u_0$  are the temperature and energy density of the background CMB field.)

electron has cooling time  $\tau \approx 10^3$  yr). The top-right panel of Fig. 5.8 shows how the magnetic field affects the IC and synchrotron flux ratio (where we find  $f_{\text{IC}}(E)/f_{\text{sync}}(E) \propto 1/B^2$ , see Eq. 2.81). As the magnetic field increases, synchrotron losses start to dominate and less energy is channelled into inverse Compton emission  $f_{\text{IC}}(E)/f_{\text{sync}}(E) \rightarrow 0$ . However, the peak in synchrotron emission eventually plateaus due to the finite amount of electrons injected into the system up to a given age. Hence, lower energy electrons begin to accumulate in the region. The bottom-left hand panel of Fig. 5.8 shows that introducing a cutoff in the injected electron spectrum shifts the IC and synchrotron emission to lower energies as well as decreasing the overall flux. Both examples shown in Fig. 5.8 assume that electrons do not escape the system.

### 5.3.2 Including particle escape in Newsedprod



Figure 5.9: An accelerator inside a uniform region of ISM with number density  $n$  and magnetic field  $B$ . After injection, cosmic rays scatter off magnetic field turbulence resulting in net diffusion from the accelerator. The probability that a cosmic ray escapes the region while cooling from Lorentz factor  $\gamma' \rightarrow \gamma$  is  $1 - \exp(-\lambda(\gamma', \gamma))$  (see Eq. 5.10)

Cosmic rays scatter off magnetic field turbulence, randomising their direction (see Section 2.2.2). The net transport of cosmic rays can be described by diffusion. After time  $t$ , the 3D distance that approximately 68% of cosmic rays have ‘diffused’ from the accelerator is given by:

$$R_{68\%} = 6(\gamma, B)Dt , \quad (5.52)$$

where  $D$  is the diffusion coefficient described in Eq. 2.31 (Aharonian and Atoyan, 1996). Therefore, cosmic rays can escape the system as shown in Fig. 5.9. For a spherical region with radius  $R$ , the escape rate (particles/s) is defined to be:

$$\nu_{\text{esc}}(\gamma) = \frac{6D(\gamma, B)}{R^2} , \quad (5.53)$$

where the diffusion coefficient ( $D(\gamma, B) \propto \gamma^\delta$ ) can lie within three different regimes describing the rate of diffusion (Bohm:  $\delta = 1$ , Kraichnan:  $\delta = 1/2$  and Kolmogorov  $\delta = 1/3$ ) (see Section 2.2.2). For Bohm diffusion ( $\delta = 1$ ), the diffusion coefficient is related to its gyro-radius ( $r_g$ ) through:

$$D(\gamma, B) = \frac{r_g c}{3} = \frac{\gamma m_e c}{e B} . \quad (5.54)$$

Combining Eq. 2.31 and Eq. 5.53 gives:

$$\nu_{\text{esc}} = \frac{6\chi_0 D_0}{R^2(B/3)^\delta} \gamma^\delta \equiv b_{\text{esc}} \gamma^\delta. \quad (5.55)$$



Figure 5.10: Comparison of `Newsedprod` (solid lines) to results by Manolakou et al., (2007) where electrons are allowed to escape the system at rate  $\nu_{\text{esc}} = b_{\text{esc}}\gamma$  (see Eq. 5.55), i.e. Bohm diffusion regime. Electrons are injected with a power-law spectrum  $\Gamma = 2.0$ . The position of  $\gamma_1$  is represented by the vertical dotted line.

For simplicity, synchrotron losses will be assumed to be dominant ( $\dot{\gamma} = b_s \gamma^2$ ). Therefore, the probability that a cosmic ray escapes the region whilst cooling from  $\gamma'$  to  $\gamma$  is given by:

$$\begin{aligned} \lambda(\gamma, \gamma') &= \frac{b_{\text{esc}}}{b_s} \int_\gamma^{\gamma'} d\gamma'' \gamma^{\delta-2} \\ &= b_{\text{es}} \begin{cases} \ln(\gamma'/\gamma), & \delta = 1 \\ \frac{1}{\delta-1} (\gamma'^{\delta-1} - \gamma^{\delta-1}), & \text{otherwise} \end{cases}, \end{aligned} \quad (5.56)$$

with  $b_{\text{es}} \equiv b_{\text{esc}}/b_s$ . For Bohm diffusion ( $\delta = 1$ ), the probability of escape for an electron then becomes:

$$\begin{aligned} p_{\text{esc}} &= 1 - \exp(-b_{\text{es}} \ln(\gamma'/\gamma)) \\ &= 1 - \left( \frac{\gamma'}{\gamma} \right)^{b_{\text{es}}}. \end{aligned} \quad (5.57)$$

Fig. 5.10 shows the comparison of the electron energy density distribution of `Newsedprod` to the results by Manolakou et al., (2007) for different values of  $b_{\text{es}}$  assuming Bohm diffusion ( $\delta = 1$ ). There is negligible escape when  $b_{\text{es}} = 0.1$ , but escape losses become significant when  $b_{\text{es}} = 100$  and  $1000$ . Electrons with Lorentz factor  $\gamma_1$ , the maximum Lorentz factor that electrons injected at  $t = 0$  can take, is the least affected by escape losses. Electrons with Lorentz factor  $> \gamma_1$  represent the population of electrons injected after  $t = 0$ . As the Lorentz factor increases beyond  $\gamma_1$ , electrons rapidly escape the region and only recently injected electrons contribute to the energy spectrum. Below  $\gamma_1$ , the electron cooling rate rapidly decreases and the probability that an electron escapes before cooling increases.

### 5.3.3 Investigation of magnetic field turbulence regimes

The rate at which cosmic rays escape a sphere of radius  $R$  depends on the diffusion properties which, in turn, depend on the power spectrum of the magnetic field turbulence (see Eq. 2.31). Using `Newsedprod`, the effects of the different magnetic field regimes (Kolmogrov  $\delta = \frac{1}{3}$ , Kraichan  $\delta = 0.5$  and Bohm  $\delta = 1$ ) on the electron energy spectra and subsequent SED can be seen in Fig. 5.11 and Fig. 5.12 for an impulsive and continuous electron accelerator respectively.

For both accelerators types, as the power spectrum of the magnetic field turbulence ( $\delta$ ) increases, the rate of diffusion increases for electrons  $> E_{\text{cr}}$  and decreases for electrons  $< E_{\text{cr}}$  where  $E_{\text{cr}}$  is the crossover energy corresponding to  $D = \chi D_0$  (see Eq. 2.31):

$$E_{\text{cr}} = \frac{B}{3 \mu\text{G}} \quad [\text{GeV}] . \quad (5.58)$$

For a magnetic field of  $10 \mu\text{G}$ , the cross over energy is  $0.3 \text{ GeV}$  as seen in the top panel of Fig. 5.11. As the magnetic field increases, the crossover energy migrates to higher energies as seen in the left hand panels of Fig. 5.12. The subsequent IC and synchrotron SED then follows the electron energy density distribution as shown in the bottom panel of Fig. 5.11 and right hand panels of Fig. 5.12 (see Section 2.3.3).

Electrons will cool to a lower energy before escaping the system when their cooling time ( $\tau$ ) is less than the time it takes for a particle to diffuse distance  $R$  (see Eq. 5.52). Therefore for a continuous source, electrons with high energy reach a steady state where radiative losses and escape losses are balanced by the injected electrons (e.g.  $E \gtrsim 10 \text{ TeV}$  for  $B = 50 \mu\text{G}$ )

### 5.3.4 Applications of `Newsedprod`

In summary, `Newsedprod` numerically solves the energy density distribution of cosmic rays (protons and electrons) for an accelerator (impulsive or continuous) injecting cosmic rays into a region of constant number density, magnetic field and photon field (e.g. CMB, infrared fields and optical photons). `Newsedprod` can then be tuned (e.g. changing the injected spectra or age of the system) to sources such as SNRe and SNRs to compare the predicted SED to observations from instruments such as HE.S.S. and *Fermi*-LAT (see Section 3.2). Observatories such as Nanten (see Section 4.2.6) can be used to obtain information about the number density of hydrogen towards the object of interest and estimate the magnetic field strength through Crutcher's relation (see Eq. 4.38 and Crutcher et al., (2010)). Once the model 'matches' the observed emission from the source, the input parameter space can be examined to see if the model is reasonable or not.



Figure 5.11: Variation of the electron energy density distribution (*top*) and subsequent synchrotron and inverse Compton SED (*bottom*) for an impulsive source of electrons escaping a cloud with radius 10 pc in the different diffusion regimes ( $\delta$ ). Kolmogorov regime:  $\delta = \frac{1}{3}$ , Kraichnan regime:  $\delta = 0.5$  and Bohm regime:  $\delta = 1$ . Electrons are injected following a power law spectrum with  $\Gamma = 2$ . The black line represents a situation where there is no escape of electrons.



$$\begin{array}{lll} L = 10^{36} \text{ ergs/s} & n = 1 \text{ cm}^{-3} & \Gamma = 2.0 \\ t = 10^4 \text{ yrs} & D_0 = 10^{27} \text{ cm}^2 \text{s}^{-1} & T = 2.72 \text{ K} \\ d = 4 \text{ kpc} & \chi = 1 & u_0 = 0.26 \text{ eV/cm}^{-3} \end{array}$$

Figure 5.12: Variation of the electron energy density distribution (*left*) and subsequent synchrotron and inverse Compton SED (*right*) for a continuous source of electrons escaping a cloud with radius 10 pc in the different diffusion regimes ( $\delta$ ). Kolmogorov regime:  $\delta = \frac{1}{3}$ , Kraichnan regime:  $\delta = 0.5$  and Bohm regime:  $\delta = 1$ . A magnetic field of  $10 \mu\text{G}$  (*top*),  $50 \mu\text{G}$  (*middle*) and  $100 \mu\text{G}$  (*bottom*) was utilised. The black line represents a situation where there is no escape of electrons.

Chapter 6 applies `Newsedprod` to a region south of the PWNe HESS J1825-137 in order to determine the origin of cosmic rays resulting in the GeV emission seen towards this region. It was postulated that either an accelerator associated with HESS J1825-137 (PWN or the progenitor SNR) or with nearby binary system LS 5039 (accretion onto associated compact object or progenitor SNR) powered the GeV emission. Using `Newsedprod`, it was found that neither source provided sufficient energetics to account for this emission, but did not rule out a combination of both sources.

# Chapter 6

## Explaining the extended GeV gamma-ray emission adjacent to HESS J1825-137

# Statement of Authorship

Title of Paper	Explaining the extended GeV gamma-ray emission adjacent to HESS J1825-137		
Publication Status	<input checked="" type="checkbox"/> Published	<input type="checkbox"/> Accepted for Publication	
	<input type="checkbox"/> Submitted for Publication	<input type="checkbox"/> Unpublished and Unsubmitted work written in manuscript style	

## Principal Author

Name of Principal Author (Candidate)	Tiffany Collins		
Contribution to the Paper	-Nanten 12CO gas analysis, ISM and multiwavelength interpretation writing Paper		
Overall percentage (%)			
Certification:	This paper reports on original research I conducted during the period of my Higher Degree by Research candidature and is not subject to any obligations or contractual agreements with a third party that would constrain its inclusion in this thesis. I am the primary author of this paper.		
Signature	yt Collins	Date	22/05/23

## Co-Author Contributions

By signing the Statement of Authorship, each author certifies that:

- i. the candidate's stated contribution to the publication is accurate (as detailed above);
- ii. permission is granted for the candidate to include the publication in the thesis; and
- iii. the sum of all co-author contributions is equal to 100% less the candidate's stated contribution.

Name of Co-Author	Gavin Rowell		
Contribution to the Paper	Parkes observations Multiwavelength interpretation Review		
Signature	/ Av	Date	12/12/22

Name of Co-Author	Alison Mitchell		
Contribution to the Paper	High energy observation Review		
Signature	Alison Mitchell	Date	12/12/22

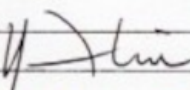
Please cut and paste additional co-author panels here as required.

### Co-Author Contributions

By signing the Statement of Authorship, each author certifies that:

- i. the candidate's stated contribution to the publication is accurate (as detailed above);
- ii. permission is granted for the candidate to include the publication in the thesis; and
- iii. the sum of all co-author contributions is equal to 100% less the candidate's stated contribution.

Name of Co-Author	Fabien Vobisn		
Contribution to the Paper	Background code 4%		
Signature		Date	15/05/23

Name of Co-Author	Yasuo Fukui		
Contribution to the Paper	Nonten COCI-O data 1%		
Signature		Date	18-May 2023

Name of Co-Author	Hirotoshi Sano		
Contribution to the Paper	Nonten COCI-O data 1%		
Signature		Date	01-05-2023

Name of Co-Author	Rami Alsulami		
Contribution to the Paper	High energy interpretation 1%		
Signature		Date	12-12-2022

Name of Co-Author	Sabrina Einecke		
Contribution to the Paper	Review 3%		
Signature		Date	12-12-2022

Name of Co-Author			
Contribution to the Paper			
Signature		Date	

Please cut and paste additional co-author panels here as required.



## Explaining the extended GeV gamma-ray emission adjacent to HESS J1825-137

T. Collins<sup>1,2</sup>★ G. Rowell,<sup>1</sup> A. M. W. Mitchell<sup>1,2</sup> F. Voisin,<sup>1</sup> Y. Fukui,<sup>3</sup> H. Sano,<sup>3</sup> R. Alsulami<sup>1,4</sup> and S. Einecke<sup>1</sup>

<sup>1</sup>School of Physical Sciences, University of Adelaide, Adelaide 5005, Australia

<sup>2</sup>Department of Physics, ETH Zurich, CH-8093 Zürich, Switzerland

<sup>3</sup>Department of Physics, University of Nagoya, Furo-cho, Chikusa-ku, Nagoya 464-8601, Japan

<sup>4</sup>Astronomy Department, Faculty of Science, King Abdulaziz University, Jeddah 460-0011, Saudi Arabia

Accepted 2021 April 7. Received 2021 April 6; in original form 2020 December 10

### ABSTRACT

HESS J1825-137 is one of the most powerful and luminous TeV gamma-ray pulsar wind nebulae (PWN). To the south of HESS J1825-137, *Fermi*-LAT observation revealed a new region of GeV gamma-ray emission with three apparent peaks (termed here, GeV-ABC). This study presents interstellar medium (ISM) data and spectral energy distribution (SED) modelling towards the GeV emission to understand the underlying particle acceleration. We considered several particle accelerator scenarios – the PWN associated with HESS J1825-137, the progenitor SNR also associated with HESS J1825-137, plus the gamma-ray binary system LS 5039. It was found that the progenitor SNR of HESS J1825-137 has insufficient energetics to account for all GeV emission. GeV-ABC may be a reflection of an earlier epoch in the history of the PWN associated with HESS 1825-137, assuming fast diffusion perhaps including advection. LS 5039 cannot meet the required energetics to be the source of particle acceleration. A combination of HESS J1825-137 and LS 5039 could be plausible sources.

**Key words:** ISM: clouds – cosmic rays – ISM: individual (HESS J1825-137) – ISM: individual (LS 5039) – ISM: supernova remnants – gamma rays: ISM.

### 1 INTRODUCTION

HESS J1825-137 is a luminous pulsar wind nebula (PWN) powered by the pulsar PSR J1826-1334 with spin-down power of  $\dot{E} = 2.8 \times 10^{36}$  erg s<sup>-1</sup> and characteristic age of 21.4 kyr (Manchester et al. 2005; Aharonian et al. 2006). To the south of HESS J1825-137 a new region of GeV gamma-ray emission was revealed by Araya, Mitchell & Parsons (2019) using *Fermi*-LAT data (see Fig. 1). Araya et al. (2019) also suggested that this new region of GeV emission may be either an extension of HESS J1825-137 or unrelated to the system. If related to HESS J1825-137, the gamma-rays may be resultant from high energy particles from the PWN (in the form of electrons and positrons) or from the progenitor supernova remnant (SNR) linked to HESS J1825-137. If unrelated to HESS J1825-137 another source of high energy particles must exist towards this region. Araya et al. (2019) conducted spectral analysis in range 10–250 GeV and fitted the spectra observed from this new region to a power-law ( $\frac{dN}{dE} \propto E^{-\Gamma}$ ) with index  $\Gamma = 1.92 \pm 0.07_{\text{stat}} \pm 0.05_{\text{sys}}$ . Fig. 3 from Araya et al. (2019) shows a TS map towards this region with three distinct peaks. We label the three GeV features GeV-A, GeV-B, and GeV-C and are located at positions RA: 18<sup>h</sup>29<sup>m</sup>36.0<sup>s</sup>, Dec: -14°23'41.6", RA: 18<sup>h</sup>30<sup>m</sup>10.6<sup>s</sup>, Dec: -15°19'03.4", and RA: 18<sup>h</sup>30<sup>m</sup>21.4<sup>s</sup>, Dec: -16°00'40.3", respectively. Hereafter, the extended region of GeV

emission will be referred to as GeV-ABC for simplicity. Fig. 1 shows the locations of GeV-ABC relative to HESS J1825-137.

A TeV halo may be associated with HESS J1825-137 (Liu & Yan 2020). TeV haloes occur when electrons and positrons escape the PWN through diffusion and interact with the ambient interstellar medium producing surrounding TeV emission forming a ‘halo’. The equivalent HAWC observatory source, eHWC J1825-134, has detected an extension of 0.36° above 56 TeV HAWC Collaboration (2019). The extension around HESS J1825-137 can be seen to decrease with energy as shown by *Fermi*-LAT data Principe et al. (2019). It is possible that GeV-ABC may be an extension of the TeV emission around HESS J1825-137

A H $\alpha$  rim like structure has been noted 120 pc to the south-east of the pulsar from PSR J1826-1334 (Voisin et al. 2016). This structure may be associated with the progenitor supernova remnant (SNR) that is linked to PSR J1826-1334. The H $\alpha$  region overlays the *Fermi*-LAT GeV emission.

Another potential accelerator also towards GeV-ABC is the gamma-ray binary system LS 5039, comprising a compact object and a massive O-type star

This study presents gas analysis (CO, H $\text{I}$ , and H $\alpha$ ) towards the new region of *Fermi*-LAT GeV emission. To identify the origin of the GeV emission, spectral energy distribution (SED) modelling of the gamma-ray emission is performed assuming hadronic or leptonic particle populations accelerated by continuous or impulsive particle injectors.

\* E-mail: tiffany.collins@adelaide.edu.au



**Figure 1.** *Fermi*-LAT count map above 10 GeV (Araya et al. 2019) towards HESS J1825-137 overlaid by black HESS significance contours at  $1\sigma$ ,  $2\sigma$ , and  $3\sigma$  (H. E. S. S. Collaboration 2018).

## 2 GAS MORPHOLOGY TOWARDS GEV-ABC

PSR J1826-1334 and LS-5039, located within the vicinity towards GeV-ABC, are possible particle accelerators to produce the GeV emission as seen by *Fermi*-LAT. PSR J1826-1334 has measured dispersion distance of  $3.9 \pm 0.4$  kpc (Taylor & Cordes 1993) while the binary system LS-5039 distance is estimated to be  $2.54 \pm 0.04$  kpc (Casares et al. 2005). For these two reasons ISM data in the velocity range of 15–30 and 40–60 km s $^{-1}$  corresponding to distances 1.6–2.8 and 3.5–4.5 kpc, respectively, will be examined (Brand & Blitz 1993).

### 2.1 CO data

Using the Nanten 12CO(1-0) survey data, the molecular hydrogen column density will be traced using conversion factor  $N_{H_2} = X_{CO} W_{12CO}$ . The  $X_{CO}$  factor is assumed to be constant  $\approx 1.5 \times 10^{20}$  cm $^{-2}$  K $^{-1}$  km $^{-1}$  s (Strong et al. 2004), over the galactic plane but may vary with Galactocentric radius.

The top panel in Fig. 2 shows the 12CO(1-0) integrated intensity between 15 and 30 km s $^{-1}$ . Regions of clumpy gas are noted to the north-east of HESS J1825-137 as noted by Voisin et al. (2016). Towards GeV-B, a region of denser gas is noticed which does not appear in the 40–60 km s $^{-1}$  range as shown in the bottom panel of Fig. 2. In both velocity ranges the region towards GeV-ABC has relatively little gas compared to the Galactic plane. The distance to these clouds is determined from the galactic rotation curve. Individual gas motion may give a false interpretation of the velocity range. In Brand & Blitz (1993), it was noticed that residuals of the modelled versus observed Galactic rotation curve can be as great as 40 km s $^{-1}$  with the average being around 12.8 km s $^{-1}$ .

The mass of a cloud with average column density  $N_{H_2}$  and cloud area A can be calculated by

$$M_H = 2.8N_{H_2}A \frac{m_p}{m_\odot} M_\odot, \quad (1)$$

where  $M_H = 2.8M_{H_2}$  includes a 20 per cent He component. The cloud areas used can be seen in Fig. 2. The number density can then



**Figure 2.** Nanten 12CO(1-0) integrated intensity in velocity ranges 15–30 km s $^{-1}$  (top) and 40–60 km s $^{-1}$  (bottom). The green contours represent GeV emission as seen by *Fermi*-LAT at  $1\sigma$  to  $7\sigma$ . The new regions of GeV emission, GeV-A, Gev-B, and Gev-C, are shown by black markers. The Nanten beam size, shown in bottom left, is 2.6 arcmin (Mizuno & Fukui 2004).

be obtained through:

$$n_H = \frac{M_H}{4/3\pi R^3 m_p} \text{ cm}^{-3}, \quad (2)$$

where  $R$  represents the radius of cloud area considered. The results of these calculations are given in Table A1 with cloud areas shown in Fig. 2. The size and shape of object B is chosen to contain dense gas seen in the 15–30 km s $^{-1}$  velocity ranges, while objects A and C were chosen to be the same size but independent of object B. The clumps seen towards Gev-B in the top panel of Fig. 2 is an order of magnitude denser compared to the ISM towards Gev-A and Gev-C.

### 2.2 H I data

The Galactic All Sky Survey of atomic Hydrogen (HI) data set will be used to trace atomic hydrogen towards new region of GeV gamma-ray activity (McClure-Griffiths et al. 2009).

The integrated column density in the velocity of ranges of interest can be seen in Fig. 3. In the 40–60 km s $^{-1}$  range



**Figure 3.** Parkes H1 integrated column density (from GASS) in velocity ranges  $15-30 \text{ km s}^{-1}$  (top) and  $40-60 \text{ km s}^{-1}$  (bottom) (McClure-Griffiths et al. 2009). The regions that were analysed here can be seen in white (HESS J1825-137) and black (new GeV regions). The Parkes beam size, shown in bottom left, is 15 arcmin (see Table A2 for results).

towards the region around GeV-ABC, the H1 column density is relatively low compared to the Galactic plane. The area towards the new GeV emission has slightly greater H1 density in the  $15-30 \text{ km s}^{-1}$  velocity range compared to the  $40-60 \text{ km s}^{-1}$  velocity range.

The calculated H1 parameters for different regions towards HESS J1825-137 and the new emission of GeV gamma rays can be seen in Table A2. Atomic hydrogen, compared to molecular hydrogen, is less abundant. The total ISM parameters are shown in Table 1. The contribution of atomic hydrogen compared to molecular hydrogen is minimal (approximately 10 per cent) to the total density of hydrogen gas.

### 2.3 H $\alpha$ data

An intensity map of H $\alpha$  emission towards HESS J1825-137 and surrounding regions can be seen in Fig. 4 from the full width at half-maximum (FWHM) survey (Finkbeiner 2003). The H $\alpha$  rims detected by Stupar et al. (2008) and Voisin et al. (2016) can clearly be seen and are located  $\approx 120 \text{ pc}$  from PSR J1826-1334 if it lies

**Table 1.** Total ISM densities for HESS J1825-137 and new GeV emission regions GeV-A, GeV-B, and GeV-C.

$15-30 \text{ km s}^{-1}$	Object	$M_H (\text{M}_\odot)$	$n_H (\text{cm}^{-3})$
$40-60 \text{ km s}^{-1}$	HESS J1825-137	$1.18 \times 10^5$	40.1
	GeV-A	$4.56 \times 10^3$	7.2
	GeV-B	$1.38 \times 10^5$	79.8
	GeV-C	$2.30 \times 10^3$	3.6
	Object	$M_H (\text{M}_\odot)$	$n_H (\text{cm}^{-3})$
	HESS J1825-137	$5.22 \times 10^5$	178
	GeV-A	$8.93 \times 10^3$	14
	GeV-B	$1.26 \times 10^4$	7.3
	GeV-C	$3.11 \times 10^2$	0.5



**Figure 4.** H $\alpha$  emission from the FWHM survey towards HESS J1825-137 and surrounding regions (Finkbeiner 2003). HESS J1825-137 can be seen by  $\sigma = 1, 2$ , and 3 purple TeV contours with PSR J1826-1334 represented by the dark green cross and LS-5039 by the yellow dot lying to the lower right with yellow radio jets described by Paredes et al. (2002). GeV regions GeV-A, GeV-B, and GeV-C can be seen as green neon crosses. The H $\alpha$  rims noted by Stupar, Parker & Filipovic (2008) and Voisin et al. (2016) are shown by pink dots. A closer look at the region contained within yellow box is shown in Fig. 5.

at the same distance (3.9 kpc) as the pulsar. From hydrodynamical simulations, the supernova remnant radius is, at least, four times the radius of this PWN (van der Swaluw & Wu 2001); this suggests an SNR radius of 140 pc as calculated by Voisin et al. (2016) agreeing with the rim of ionized gas seen in Fig. 4 and predictions made by de Jager & Djannati-Ataï (2009).

Overlaying combined molecular and H1 contours on to the H $\alpha$  map, (see Fig. 5), it can be seen that the CO(1-0) cloud in the  $15-30 \text{ km s}^{-1}$  range noted in Section 2.1 overlaps a region of reduced H $\alpha$  emission. This may indicate that the cloud is in the foreground or that the CO(1-0) cloud is surrounded by H $\alpha$  gas.

Two different methods were utilized to calculate the density of ionized hydrogen towards the regions of interest. The details of these calculations are provided in appendix B. The results of both methods are shown in Table A3. Method A assumes that the density of photons is approximately equal to the density of ionized gas, assuming that atoms are not re-excited by an external source. Method B considers basic radiation transfer. It is expected that the ratio of ionized to neutral hydrogen atoms is  $\approx 10^{-6}$  which agrees with both methods (Draine 2011). Therefore ionized hydrogen does not significantly contribute to the total density of the ISM.



**Figure 5.** Zoomed in H $\alpha$  intensity overlayed with Nanten 12CO(1-0) in the 15–30 km s $^{-1}$  (red) and 40–60 km s $^{-1}$  (blue) range. The H $\alpha$  rims are indicated by the pink dots. Note that this corresponds to the yellow box in Fig. 4. The dense CO cloud in the 15–30 km s $^{-1}$  velocity range towards GeV-B can be seen to anticorrelate with the H $\alpha$  emission.

### 3 PARTICLE TRANSPORT

After having mapped out the ISM, we can now consider the diffusive transport of high energy particles. In this study, the SED modelling assumes that the high energy particles are able to enter GeV-ABC in sufficient number and energy range to produce the GeV gamma radiation. This section will look into the validity of this assumption assuming a purely diffusive scenario and looking at the cooling time of particles and how it affects the particle transport.

Once high energy particles are emitted by the PWN (or progenitor SNR), they must traverse the interstellar medium before entering the region towards GeV-ABC. In a purely diffusive scenario, the distance that particles of energy  $E$  diffuse into the ISM in time  $t$  is estimated by

$$R(E, t) = \sqrt{2D(E, B)t} \quad [\text{cm}], \quad (3)$$

where

$$D(E, B) = \chi D_0 \sqrt{\frac{E/\text{TeV}}{B/3 \mu\text{G}}} \quad [\text{cm}^2 \text{s}^{-1}] \quad (4)$$

$D_0 = 1 \times 10^{29} \text{ cm}^2 \text{s}^{-1}$  is the galactic diffusion coefficient at 1 TeV and  $\chi$  takes values of around 0.01 (with variation) (Berezinskii et al. 1990; Gabici, Aharonian & Blasi 2007). As particles traverse the ISM they suffer energy losses through IC, bremsstrahlung, and synchrotron radiation. The cooling time for bremsstrahlung,  $t_{\text{brem}}$ , inverse Compton,  $t_{\text{IC}}$ , and synchrotron,  $t_{\text{sync}}$ , loss processes is given by

$$t_{\text{brem}} \approx \frac{4 \times 10^7}{n \text{ cm}^{-3}} \quad \text{yr} \quad (5a)$$

$$t_{\text{IC}} \approx \begin{cases} 3 \times 10^5 U^{-1} (\frac{E}{\text{TeV}})^{-1} \text{ yr} & \text{Thompson Regime} \\ 3.1 \times 10^5 U^{-1} (\frac{E}{\text{TeV}})^{-1} f_{\text{KN}}^{-1} \text{ yr} & \text{KN Regime} \end{cases} \quad (5b)$$

$$t_{\text{sync}} \approx 12 \times 10^6 \left(\frac{B}{\mu\text{G}}\right)^{-2} \left(\frac{E}{\text{TeV}}\right)^{-1} \text{ yr}, \quad (5c)$$



**Figure 6.** Transport time for particles to traverse from PSR 1826-1336 to GeV-B versus cooling time of synchrotron and IC processes. The ambient density of the ISM is assumed to be  $n = 1 \text{ cm}^{-3}$ . The black horizontal solid and dashed lines show the two possible ages of PSR J1826-1334 ( $t = 21.4 \text{ yr}$  and  $t = 40 \text{ yr}$ , respectively), the dotted blue line shows the cooling time through synchrotron losses at 1  $\mu\text{G}$  while the two red dashed lines is through IC losses in the Thompson and Klein Nishina regime. The solid lines with varying  $\chi$  values shows the values necessary for particles with that energy to reach GeV-B in the available time through ISM with magnetic field  $B = 1 \mu\text{G}$ . The inferred minimum and maximum electron energy,  $E_{e,\min}$  and  $E_{e,\max}$ , emitted by the pulsar wind nebula is shown by the vertical solid lines.

where  $U = 0.26 \text{ eV cm}^{-3}$  is the energy density of the cosmic microwave background and  $f_{\text{KN}}$  is the Klein Nishina (KN) suppression factor given by Moderski et al. (2005):

$$f_{\text{KN}} = \left(1 + 40 \frac{E}{\text{TeV}} kT_{\text{cv}}\right)^{-1.5} \quad (6)$$

for an electron with energy  $E$  interacting with photon field with temperature  $T$  (with  $kT$  in units of eV). If the density of the ISM is  $n = 1$ , the time it takes for particles of varying energies to be emitted by the PWN and travel to GeV-B ( $\approx 70 \text{ pc}$ ) and the cooling time is shown in Fig. 6. The intersection of the diffusion time and the age of PSR J1826-1334 represents the minimum particle energy that can reach GeV-B. Naturally if the pulsar is older, more lower energy particles can reach GeV-B. The maximum energy of electrons able to reach GeV-B is found through the intersection of the diffusion line and the IC cooling time (the quickest process where electrons lose most of their energy).

In IC processes, the final energy of the photon,  $E_{\Gamma, \text{TeV}}$ , is related to initial electron energy,  $E_{e, \text{TeV}}$  and initial photon energy  $E_{i, \text{eV}}$  through:

$$E_{\Gamma, \text{TeV}} = E_{e, \text{TeV}} \frac{h}{(1 + h^{4/5})^{5/4}}, \quad (7)$$

where  $h \approx 31.5 E_{e, \text{TeV}} E_{i, \text{eV}}$  (Hinton & Hofmann 2009). Photons up to 54 TeV has been observed towards HESS J1825-137 (H. E. S. S. Collaboration 2019). Assuming IC interactions with the cosmic microwave background are responsible for this emission, this is equivalent to an electron with maximum energy of 96 TeV. Similarly photons as low as 1.26 GeV has been observed by *Fermi*-LAT (Principe et al. 2020), which is equivalent to minimum electron energy of 0.25 TeV. This electron energy range is shown by the vertical lines in Fig. 6. This further limits how many electrons are able to diffuse to GeV-B.

The region around the PWN can harbour a strong magnetic field strength compared to the surrounding ISM. Equation (5c) outlines the cooling time for the synchrotron processes as a function of electron energy and magnetic field (as shown by Fig. 6). Consequently, electrons in the zone around the pulsar wind nebula will experience stronger synchrotron losses compared to what is shown in Fig. 6.

#### 4 SED MODELLING OF THE GAMMA-RAY EMISSION

Two main pathways are possible for the production of GeV gamma radiation. In a hadronic scenario, proton-proton interactions with the ISM leading to the production of neutral pions which, in turn, decay into gamma radiation. Leptonic scenarios include synchrotron emission associated with the magnetic field pervading in the ISM, inverse-Compton emission with the cosmic microwave background and bremsstrahlung interactions with the ISM.

Two types of particle accelerators will be considered; continuous and impulsive accelerators. Continuous accelerators constantly inject particles into the interstellar medium throughout their lifetime. For this study, it will be assumed that particles will be injected at a constant energy rate. Continuous accelerators may include pulsars and stellar clusters, for example. On the other hand, an impulsive accelerator, such as a supernova remnant, injected particles in one big burst in the past.

The particles that are injected are then free to undergo interactions producing radio to gamma-ray emission. The following section will describe potential particle accelerators that may result in the GeV gamma radiation as seen by *Fermi*-LAT. The model utilized in this study takes the initial particle spectrum and then lets the system evolve over the age of the particle accelerator. After the allocated time has passed, the final particle spectrum is calculated and the gamma-ray spectrum is extracted. For further explanation of the process utilized in this study, please refer to Appendix C.

The ISM density of the region to be modelled will utilize the data calculated in Section 2. In turn the magnetic field strength, which affects the production of synchrotron radiation, is related to the density of ISM through the relation (Crutcher 1999):

$$B(n_H) = 100 \sqrt{\frac{n_H}{10^4 \text{ cm}^{-3}}} \mu\text{G}. \quad (8)$$

Note that the updated version of this relation provides a slightly higher magnetic field estimation (Crutcher et al. 2010). Crutcher's relation computes the maximum magnetic field in a molecular cloud, allowing estimations calculated using Crutcher (1999) to be acceptable for this study.

##### 4.1 Potential particle accelerators

###### 4.1.1 HESS J1825-137 (PWN – Continuous)

As shown in Fig. 2, it appears the Fermi GeV-ABC might be an extension of HESS J1825-137.

A part of the spin-down power of HESS J1825-137,  $2.8 \times 10^{36}$  erg s $^{-1}$ , is channelled into accelerating particles that propagate out of the system. It was found that the major axis of gamma-emission is to the south-west of the pulsar towards GeV-ABC (H. E. S. S. Collaboration 2019). The asymmetry in the gamma-ray emission may indicate an asymmetry in the particle emission by the PWN. The PWN would be a continuous source of high energy electrons towards the new region of GeV *Fermi*-LAT emission.

###### 4.1.2 HESS J1825-137 Progenitor (SNR – Impulsive)

Here we assume the progenitor SNR is an impulsive accelerator where the bulk of the cosmic rays escape the system very early and travel ahead of the SNR. Cosmic rays of energies  $E$  escape the SNR in time  $\chi$ :

$$\chi(E) = t_{\text{Sedov}} \left( \frac{E}{E_{\max}} \right)^{-1/\delta}, \quad (9)$$

where  $t_{\text{Sedov}} = 200$  yr is the onset of the Sedov Phase of an SNR,  $\delta = 2.48$  is a parameter describing the energy-dependent release of cosmic rays and  $E_{\max} = 500$  TeV is the maximum possible cosmic ray proton energy (Gabici, Aharonian & Casanova 2009). The TeV cosmic rays responsible for the emission of gamma-rays towards GeV-ABC have an escape time of  $\sim 2$  kyr. This is negligible compared to age of the pulsar (21.4 kyr). The size of the SNR during the Sedov phase can be determined through (Reynolds 2008):

$$R = 0.31 E_{51}^{1/5} (\mu_1 / 1.4)^{-1/5} n^{-1/5} t_{\text{yr}}^{2/5} \text{ pc}, \quad (10)$$

where  $E_{51}$  is the kinetic energy of the SNR in units of  $10^{51}$  erg,  $\mu_1$  is the mean mass per particle, and  $n$  is the background ISM density. If we assume  $E_{51} = 1$ ,  $n = 1 \text{ cm}^{-3}$ , and  $\mu = 1.41$ ; at age 2 kyr, the SNR will have a radius of  $\sim 7$  pc. The TeV cosmic rays will escape the SNR at this radius and diffuse ahead of the SNR to GeV-ABC. Therefore the SNR progenitor associated with HESS J1825-137, as noted by Stupar et al. (2008) and Voisin et al. (2016), can be approximated as an impulsive source of high energy particles. Additionally, it is generally believed that 10–30 per cent of the  $10^{51}$  erg of kinetic energy released in a supernova is channelled into accelerated high energy particles by the subsequent supernova remnant.

The distance to the PWN and SNR associated with HESS J1825-137 will be assumed to be 3.9 kpc (Taylor & Cordes 1993). For this reason ISM parameters in the  $40$ – $60$  km s $^{-1}$  velocity range (see Table. 1) will be used in the SED modelling of GeV-A, GeV-B, and GeV-C. Due to the anticorrelation of CO(1-0) to H $\alpha$  emission as seen in Fig. 5, the dense gas towards GeV-B in the  $15$ – $30$  km s $^{-1}$  velocity will also be considered as a target for high energy particles to emit radiation. Due to individual gas motion compared to the Galactic rotation curve (Brand & Blitz 1993), this region of dense gas may be located at the same distance as HESS J1825-137.

###### 4.1.3 LS 5039 (accretion powered – Continuous)

LS 5039 is a microquasar and X-ray binary system (Motch et al. 1997). LS 5039 contains an O type star in orbit around an unknown compact object with mass  $\approx 3.7 M_{\odot}$  (Ptuskin & Zirakashvili 2005). This high mass is greater than standard neutron star masses leading to the possibility of the compact object being a black hole. The high mass of the compact object suggests that the progenitor was born in the binary system with a mass greater than the O-type star ( $M_O = 22.9 M_{\odot}$ ). The age of LS 5039 is unknown; the lifetime of an O-type star is of the order of a few million years, giving an upper limit to the age of the system. The minimum and maximum plausible ages, of  $1 \times 10^3$  and  $1 \times 10^6$  yr, respectively, will be considered in the modelling (Moldón et al. 2012). Moldón et al. (2012) aimed to find the galactic trajectory of LS 5039 to determine its birthplace. Depending on where LS 5039 was born, Moldón et al. (2012) gives the age of the system to be between 0.1 and 1.2 Myr. Therefore an age of  $10^5$  yr will also be considered in the SED modelling of this paper. In modelling the SED, these ages reflect the time when high energy particles enter GeV-ABC. Assuming diffusion is the particle transport method as in section 3, the transportation time of



**Figure 7.** Spectral energy distribution of GeV-ABC as revealed by Araya et al. (2019) is shown in blue. The flux points of HESS J1825-137 are represented by red. H. E. S. S. Collaboration (2019). *Fermi*-LAT data towards HESS J1825-137 (Principle et al. 2020) shown in green can be seen to follow the HESS data points as noticed by H. E. S. S. Collaboration (2019).

high energy particles between LS 5039 and GeV-ABC ( $\approx 10^4$  yr) is negligible compared to the age of LS 5039.

After formation, the compact object associated with LS 5039 continuously accretes matter from its star companion allowing particles to be accelerated in a relativistic radio jet. This may be a continuous accelerator of particles to form the new GeV region as seen by *Fermi*-LAT. Radio jets described by Paredes et al. (2002) can be seen in Fig. 4. The average accretion luminosity of LS 5039 was calculated by Casares et al. (2005) to be  $L_{\text{acc}} = 8 \times 10^{35}$  erg s $^{-1}$ . The luminosity released in the vicinity of LS 5039 is given by:  $L_{\text{radio}, 0.1-100 \text{ GHz}} \approx 1.3 \times 10^{31}$  erg s $^{-1}$  (Marti, Paredes & Ribo 1998),  $L_{\text{x-ray}, 3-30 \text{ keV}} = 0.5 - 5 \times 10^{34}$  erg s $^{-1}$  (Bosch-Ramon et al. 2005) and  $L_{>100 \text{ GeV}} = 2.7 \times 10^{35}$  erg s $^{-1}$  (Casares et al. 2005). Therefore, Casares et al. (2005) concluded that approximately one-third of the accretion luminosity is channelled into the relativistic jets. The remaining  $5.5 \times 10^{35}$  erg s $^{-1}$  can be channelled into GeV-ABC. Given the distance estimate to LS 5039 of 2.5 kpc, the ISM within the 15–30 km s $^{-1}$  regime will be considered. It has been noticed that the radio jets are persistent with variability on day, week, and year time-scales (Marcote et al. 2015).

#### 4.1.4 LS 5039 progenitor (SNR – impulsive)

Whether the compact object within LS 5039 is a black hole or neutron star, the compact object is the result of a star gone supernova. By this logic an impulsive source of high energy particles occurred sometime in the past. At the time of writing, no clear SNR has been linked to LS 5039. If LS 5039 has age of order  $10^5$  yr, any SNR will be too old to be detected.

#### 4.2 Spectral energy distribution

The spectral analysis conducted by Araya et al. (2019) towards GeV-ABC is shown in Fig. 7. They found that a simple power-law ( $\frac{dN}{dE} \propto E^{-\Gamma}$ ) best describes the spectrum with spectral index of  $\Gamma = 1.92 \pm 0.07_{\text{stat}} \pm 0.05_{\text{sys}}$  and integrated flux of  $\phi_0 = (1.46 \pm 0.11_{\text{stat}} \pm 0.13_{\text{sys}}) \times 10^{-9}$  photons cm $^{-2}$  s $^{-1}$ .

In the study by Araya et al. (2019), individual peaks GeV-A, B, and C were found to have spectral indices  $\Gamma_A = 1.78 \pm 0.25_{\text{stat}}$ ,  $\Gamma_B = 1.7 \pm 0.4_{\text{stat}}$ , and  $\Gamma_C = 1.43 \pm 0.23_{\text{stat}}$ , respectively. The

extended GeV emission observed by *Fermi*-LAT will be modelled by approximating the spectra of GeV-ABC as coming from three sources corresponding to the peaks observed by Araya et al. (2019). By integrating the flux over all energy ranges for all three peaks and normalizing to the spectra of GeV-ABC, the amount each peak contributes to the total flux can be determined. This assumes that the entirety of the GeV emission originates from the three peaks. As seen by fig. 3 from Araya et al. (2019) GeV A, B, and C contains the majority of the GeV emission. It was found that GeV-A, GeV-B, and GeV-C, contributed 37 per cent, 34 per cent, and 29 per cent of the total GeV flux, respectively. For each peak in the GeV gamma-ray emission region, SEDs based on different particles accelerators (e.g. PWN HESS J1825-137 and LS 5039) will be modelled and fit by eye to the data. Input parameters will also be varied to provide a range where the model matches the data. The *ROSAT* X-ray upper limit towards GeV-ABC was calculated using the *ROSAT* X-Ray background tool (Sabot & Snowden 2019).

Input parameters of the SED modelling towards the new region of GeV emission can be seen in Tables 2 and 3 and Tables 4 and 5 for HESS J1825-137 and LS 5039 being the source of high energy particles, respectively.

An example fit to the SED is shown in Fig. 8. It is assumed that both hadronic and leptonic particles followed an exponential cutoff power-law injection spectra ( $\frac{dN}{dE} \propto E^{-\Gamma} \exp(-E/E_c)$ ). It is important to note that the energy budget/injection luminosity,  $W$  or  $W_i$ , that is inferred reflects the energy budget for each individual peak (GeV-A, GeV-B, and GeV-C) and not the total energy budget/injection luminosity for the combination of all three regions.

Assuming constant cosmic ray density within a supernova remnant, the inferred energy ( $W_{\text{SNR}}$ ) of the SNR can be calculated. The filling factor,  $f_f$ , is defined to be the ratio of the area of GeV-A, B, or C to the projected area of the SNR. The inferred energy of the SNR is then given by

$$W_{\text{SNR}} = \frac{W}{f_f}. \quad (11)$$

#### 4.2.1 HESS J1825-137 progenitor

A clear SNR rim can be seen in Fig. 4 connected to HESS J1825-137. The projected area of the SNR, with radius of 140 pc, is assumed to be  $\approx 64 \times 10^3$  pc $^2$ . Note that the denser regions to the north of HESS J1825-137 shown in Figs 2 and 3 may dampen the northern expansion of the SNR associated with HESS J1825-137. This will affect the filling factor geometrically and in turn affect the inferred energy of the SNR as shown in equation (11). If no particles have escaped, it is expected that  $10^{50}$  erg of energy remains within the SNR. As the SNR is definitely well into its Sedov phase, some cosmic rays will have escaped the system, lowering the remaining energy within the SNR.

For an individual model to be successful, it must allow sufficient energetics within all three clouds simultaneously. If the particle energetics impacting one cloud is too large, the model will be rejected. For this reason when looking at Tables 2 and 3, to determine if individual impulsive models were successful, the maximum energy budget/injection luminosity will be compared to theoretical energetics.

#### 4.2.2 LS 5039 progenitor

No clear SNR rim has been associated with LS 5039. If the age of LS 5039 is greater than  $10^5$  yr the SNR will have already dispersed into the projected area of SNR and will assume a minimum radius

**Table 2.** SED model parameters matching the observed emission of GeV-A, B, and C for a hadronic scenario. The particle accelerators considered are the impulsive progenitor SNR associated with PSR 1826-1334 and the continuous accelerator associated with the pulsar wind nebula, HESS J1825-137. High energy particles are assumed to be injected with a power-law spectra with an exponential cutoff:  $\frac{dN}{dE} \propto E^{-\Gamma} \exp[E/E_c]$ .

Accelerator PSR 1826-1334 or SNR	Peak	$n_H$ (cm $^{-3}$ )	${}^1 W$ or ${}^2 \dot{W}$	Hadronic			${}^3 W_{SNR}$ or ${}^4 \dot{W}_{tot}$
				$\Gamma$	$E_C$ (TeV)		
Impulsive (SNR) $t = 21 \times 10^3$ yr	A	14	$1.0 \times 10^{50}$	erg	2.0	50	$6.0 \times 10^{51}$
	<b>B</b>	<b>79.8</b>	<b><math>1.5 \times 10^{49}</math></b>	—	<b>2.0</b>	<b>50</b>	<b><math>4.7 \times 10^{50}</math></b>
	B	7.0	$1.5 \times 10^{50}$	—	2.0	50	$4.7 \times 10^{51}$
	C	1.0	$1.2 \times 10^{51}$	—	2.0	50	$7.3 \times 10^{52}$
Impulsive (SNR) $t = 40 \times 10^3$ yr	A	14	$1.0 \times 10^{50}$	erg	2.0	50	$6.1 \times 10^{51}$
	<b>B</b>	<b>79.8</b>	<b><math>1.5 \times 10^{49}</math></b>	—	<b>2.0</b>	<b>50</b>	<b><math>4.7 \times 10^{50}</math></b>
	B	7.0	$1.5 \times 10^{50}$	—	2.0	50	$4.7 \times 10^{51}$
	C	1.0	$1.1 \times 10^{51}$	—	2.0	50	$6.7 \times 10^{52}$
Continuous (PWN) $t = 21 \times 10^3$ yr	A	14	$1.2 \times 10^{38}$	erg s $^{-1}$	2.0	50	—
	B	79.8	$2.0 \times 10^{37}$	—	2.0	50	—
	B	7.0	$2.2 \times 10^{38}$	—	2.0	50	—
	C	1.0	$1.7 \times 10^{39}$	—	2.0	50	$1.8-2.0 \times 10^{39}$
Continuous (PWN) $t = 40 \times 10^3$ yr	A	14	$8.0 \times 10^{37}$	erg s $^{-1}$	2.0	50	—
	B	79.8	$1.25 \times 10^{37}$	—	2.0	50	—
	B	7.0	$1.25 \times 10^{38}$	—	2.0	50	—
	C	1.0	$8.5 \times 10^{38}$	—	2.0	50	$0.9-1.0 \times 10^{39}$

Notes.  ${}^1 W$ : Energy budget of high energy particles within individual clouds (see Fig. 2).

${}^2 \dot{W}$ : Particle injection luminosity of high energy particles into individual clouds.

${}^3 W_{SNR}$ : Injected energy budget of high energy particles within progenitor SNR (see equation 11).

${}^4 \dot{W}_{tot}$ : Total injection luminosity of all three regions by PWN.

Plausible scenarios are shown in bold.

Matching scenarios have systematic variation of up to 56 per cent in energy budget  $W$  or luminosity  $\dot{W}$ , 12 per cent in the spectral index  $\Gamma$  and 12 per cent in the cutoff energy  $E_c$  (see the text and Fig. 8).

Downloaded from https://academic.oup.com/mnras/article/504/2/1840/6219862 by Acquisition Dept.(Journals) user on 30 August 2021

**Table 3.** Same as Table 2 but parameters in a leptonic origin.

Accelerator PSR 1826-1334 or SNR	Peak	$n_H$ (cm $^{-3}$ )	$W$ or $\dot{W}$	Leptonic			$W_{SNR}$ or $\dot{W}_{tot}$
				$\Gamma$	$E_C$ (TeV)		
Impulsive (SNR) $t = 21 \times 10^3$ yr	A	14	$1.2 \times 10^{49}$	erg	2.0	10	$7.3 \times 10^{50}$
	<b>B</b>	<b>79.8</b>	<b><math>9.0 \times 10^{48}</math></b>	—	2.0	30	$2.8 \times 10^{50}$
	B	7.0	$8.0 \times 10^{48}$	—	2.0	30	$2.5 \times 10^{50}$
	C	1.0	$7.0 \times 10^{48}$	—	2.0	10	$4.3 \times 10^{50}$
Impulsive (SNR) $t = 40 \times 10^3$ yr	A	14	$1.4 \times 10^{49}$	erg	2.0	10	$8.5 \times 10^{50}$
	<b>B</b>	<b>79.8</b>	<b><math>6.0 \times 10^{48}</math></b>	—	1.0	50	$1.9 \times 10^{50}$
	B	7.0	$3.0 \times 10^{48}$	—	1.5	50	$9.4 \times 10^{49}$
	C	1.0	$7.6 \times 10^{48}$	—	2.0	50	$4.6 \times 10^{50}$
Continuous (PWN) $t = 21 \times 10^3$ yr	<b>A</b>	<b>14</b>	<b><math>1.5 \times 10^{37}</math></b>	erg s $^{-1}$	<b>2.0</b>	<b>10</b>	—
	<b>B</b>	<b>79.8</b>	<b><math>1.5 \times 10^{37}</math></b>	—	<b>2.0</b>	<b>10</b>	—
	<b>B</b>	<b>7.0</b>	<b><math>1.5 \times 10^{37}</math></b>	—	<b>2.0</b>	<b>10</b>	—
	C	1.0	<b><math>1.0 \times 10^{37}</math></b>	—	<b>2.0</b>	<b>10</b>	<b><math>4.0 \times 10^{37}</math></b>
Continuous (PWN) $t = 40 \times 10^3$ yr	A	14	$1.0 \times 10^{37}$	erg s $^{-1}$	2.0	10	—
	<b>B</b>	<b>79.8</b>	$2.6 \times 10^{36}$	—	1.7	<b>10</b>	—
	B	7.0	$1.6 \times 10^{36}$	—	1.7	10	—
	C	1.0	$6.0 \times 10^{36}$	—	2.0	10	$1.8-1.9 \times 10^{37}$

of  $\approx 80$  pc to completely encompass GeV-ABC as seen by *Fermi*-LAT. Equation (11) is then used to estimate the total energy of high energy particles remaining in the progenitor SNR of LS 5039. The assumed minimum radius of SNR will lead to an underestimation of the inferred energy of the SNR associated with LS 5039.

## 5 DISCUSSION

In this section, we will discuss the results of the SED modelling and consider the possible accelerator scenarios.

### 5.1 Accelerator related to HESS J1825-137

First, we will examine the plausibility of an accelerator related to HESS J1825-137. The two sources of high energy particles are the progenitor SNR and PWN.

#### 5.1.1 A progenitor SNR (impulsive)

The progenitor SNR linked to HESS J1825-137 is an impulsive accelerator; releasing  $\approx 10^{50}$  erg of cosmic rays (with electrons

**Table 4.** Model parameters matching the observed emission of GeV-A, B, and C for a hadronic scenario. The particle accelerators considered are the progenitor SNR associated with LS 5039 (impulsive) or the accretion of matter by the companion star on to LS 5039 (continuous). Example SED best fit is shown in Fig. 8.  $W$  or  $\dot{W}$  represents the energy budget. To see the regions used, refer to Fig. 3. The spectra of injected particles is represented by an exponential cut-off power-law spectrum:  $\frac{dN}{dE} \propto E^{-\Gamma} \exp[-E/E_c]$ .

Accelerator LS 5039 or SNR	Peak	$n_H$ (cm $^{-3}$ )	$W$ or $\dot{W}$	Hadronic			${}^5 W_{\text{SNR}}$ or ${}^6 \dot{W}_{\text{total}}$
				$\Gamma$	$E_C$ (TeV)		
Impulsive (SNR) $t = 1 \times 10^3$ yr	A	7.0	$8.0 \times 10^{49}$	erg	2.0	50	$3.9 \times 10^{51}$
	B	79.8	$6.0 \times 10^{48}$	–	2.0	50	$1.5 \times 10^{50}$
	C	3.6	$1.0 \times 10^{50}$	–	2.0	50	$4.9 \times 10^{51}$
Impulsive (SNR) $t = 1 \times 10^5$ yr	A	7.0	$1.0 \times 10^{50}$	erg	2.0	50	$4.9 \times 10^{51}$
	B	79.8	$8.0 \times 10^{48}$	–	2.0	50	$2.0 \times 10^{50}$
	C	3.6	$1.5 \times 10^{50}$	–	2.0	50	$7.4 \times 10^{51}$
Impulsive (SNR) $t = 1 \times 10^6$ yr	A	7.0	$3.0 \times 10^{51}$	erg	1.0	50	$1.5 \times 10^{53}$
	B	79.8	$4.0 \times 10^{49}$	–	1.5	50	$1.0 \times 10^{51}$
	C	3.6	$4.0 \times 10^{51}$	–	1.0	50	$2.0 \times 10^{53}$
Continuous (accretion) $t = 1 \times 10^3$ yr	A	7.0	$2.3 \times 10^{39}$	erg s $^{-1}$	2.0	50	–
	B	79.8	$2.0 \times 10^{38}$	–	2.0	50	–
	C	3.6	$4.5 \times 10^{39}$	–	2.0	50	$7.0 \times 10^{39}$
Continuous (accretion) $t = 1 \times 10^5$ yr	A	7.0	$2.8 \times 10^{37}$	erg s $^{-1}$	2.0	50	–
	B	79.8	$2.0 \times 10^{36}$	–	2.0	50	–
	C	3.6	$4.0 \times 10^{37}$	–	2.0	50	$7.0 \times 10^{37}$
Continuous (accretion) $t = 1 \times 10^6$ yr	A	7.0	$2.5 \times 10^{36}$	erg s $^{-1}$	2.0	50	–
	B	79.8	$3.5 \times 10^{35}$	–	2.0	50	–
	C	3.6	$4.0 \times 10^{36}$	–	2.0	50	$6.9 \times 10^{36}$

Notes.  ${}^5 W_{\text{SNR}}$ : Inferred energy budget of high energy particles inside progenitor SNR related to LS 5039.

${}^6 \dot{W}_{\text{total}}$ : The total injection luminosity into all three clouds.

Plausible scenarios are shown in bold.

Matching scenarios have systematic variation of up to 56 per cent in energy budget  $W$  or luminosity  $\dot{W}$ , 12 per cent in the spectral index  $\Gamma$  and 12 per cent in the cutoff energy  $E_c$  (see the text and Fig. 8).

**Table 5.** Same as Table 4 but parameters in a leptonic scenario for gamma-ray emission.

Accelerator LS 5039 or SNR	Peak	$n_H$ (cm $^{-3}$ )	$W$ or $\dot{W}$	Leptonic			$W_{\text{SNR}}$ or $\dot{W}_{\text{total}}$
				$\Gamma$	$E_C$ (TeV)		
Impulsive (SNR) $t = 1 \times 10^3$ yr	A	7.0	$4.0 \times 10^{48}$	erg	2.0	10	$2.0 \times 10^{50}$
	B	79.8	$2.5 \times 10^{48}$	–	2.0	10	$6.4 \times 10^{49}$
	C	3.6	$3.0 \times 10^{48}$	–	2.0	10	$1.5 \times 10^{50}$
Impulsive (SNR) $t = 1 \times 10^5$ yr	A	7.0	$5.0 \times 10^{48}$	erg	1.7	50	$2.5 \times 10^{50}$
	B	79.8	$2.0 \times 10^{49}$	–	1.0	10	$5.1 \times 10^{50}$
	C	3.6	$5.0 \times 10^{48}$	–	2.0	10	$2.5 \times 10^{50}$
Impulsive (SNR) $t = 1 \times 10^6$ yr	A	7.0	$3.0 \times 10^{50}$	erg	1.7	100	$1.5 \times 10^{52}$
	B	79.8	–	–	–	–	–
	C	3.6	$2.0 \times 10^{50}$	–	2.0	10	$9.9 \times 10^{51}$
Continuous (accretion) $t = 1 \times 10^3$ yr	A	7.0	$1.0 \times 10^{38}$	erg s $^{-1}$	2.0	10	–
	B	79.8	$8.5 \times 10^{37}$	–	2.0	10	–
	C	3.6	$5.0 \times 10^{38}$	–	2.0	10	$6.9 \times 10^{38}$
Continuous (accretion) $t = 1 \times 10^5$ yr	A	7.0	$3.5 \times 10^{35}$	erg s $^{-1}$	1.7	10	–
	B	79.8	$9.0 \times 10^{35}$	–	2.0	10	–
	C	3.6	$2.0 \times 10^{35}$	–	1.5	10	$1.5 \times 10^{36}$
Continuous (accretion) $t = 1 \times 10^6$ yr	A	<b>7.0</b>	<b><math>2.0 \times 10^{35}</math></b>	erg s $^{-1}$	<b>1.7</b>	<b>10</b>	–
	B	<b>79.8</b>	<b><math>7.5 \times 10^{35}</math></b>	–	<b>1.8</b>	<b>30</b>	–
	C	<b>3.6</b>	<b><math>9.0 \times 10^{34}</math></b>	–	<b>1.5</b>	<b>10</b>	<b><math>1.0 \times 10^{36}</math></b>

making up  $\approx 10^{48}$  erg) into the surrounding environment. The SNR expands and cosmic rays will escape from the system, decreasing the total energy of particles trapped inside the SNR. From SED modelling, the energy budget in regions GeV-A, B, and C required to reproduce the SED of GeV  $\gamma$ -rays was obtained.

The total SNR cosmic ray energy budget,  $W_{\text{SNR}}$ , is estimated by equation (11).

To reproduce the SED of any of GeV-A, B, or C requires the hadronic SNR energy budget to range between  $5 \times 10^{50}$  and  $730 \times 10^{50}$  erg, as shown in Table 2. It is possible that



**Figure 8.** SED example for GeV-B with impulsive hadronic SED (left-hand panel) and continuous leptonic SED (right-hand panel). This assumes that HESS J1825-137 (at age 40 kyr) is the source of acceleration. The upper data points represent the total SED as measured by *Fermi*-LAT. The lower data points is 34.0 per cent of this spectra due to source being only GeV-B. The green arrow is the *ROSAT* X-ray upper limit towards GeV-ABC. The blue, pink, and yellow shaded regions represent the systematic variation of energy budget ( $W$ ) or injection luminosity ( $\dot{W}$ ), cutoff energy and spectral index, respectively. See Tables 2 and 3 for input parameters.

HESS J1825-137 may be a possible hypernova candidate: supernova with kinetic energy greater than  $10^{52}$  erg (Nomoto et al. 2004). This is equivalent to a supernova releasing  $10^{51}$  erg of cosmic rays. A plausible scenario requires for all three GeV regions to simultaneously explain the gamma-ray spectrum. For both ages ( $t = 21$  and 40 kyr), only GeV-B has reasonable energetics assuming a higher ISM density; therefore a pure hadronic progenitor SNR scenario must be rejected unless a hypernova scenario is considered.

Hydrogen volume density is not constant across GeV-A, B, and C. Equation (C13) shows that the spectra of gamma-rays from proton–proton interactions is proportional to the density of the target material. Assuming that the high density cloud observed in the  $15\text{--}30 \text{ km s}^{-1}$  velocity range lies at the same distance as HESS J1825-137 then GeV-B should appear brighter in gamma-rays compared to GeV-A and C assuming that the cosmic ray energy density over all three regions are constant. This is not the case, therefore the cosmic ray energy density in cloud A and C must be 7 and 80 times greater, respectively, than the energy density in cloud B. As discussed in section 4.1.2, particles escape the SNR at age  $\sim 2$  kyr when it has a radius of  $\sim 7$  pc and diffuse to GeV-ABC. By the time the particles have diffused the remaining distance to GeV-ABC ( $\approx 130$  pc) any local anisotropy at the GeV-ABC position will likely have been lost. Therefore an impulsive hadronic scenario cannot explain why GeV-A, B, and C have the same brightness.

A pure impulsive leptonic energy budget requires, at least,  $10^{50}$  erg of electrons within the SNR. Therefore, a pure impulsive leptonic model of HESS J1825-137 being the accelerator of high energy particles resulting in the GeV gamma-radiation as observed by *Fermi*-LAT is rejected.

A leptonic–hadronic impulsive scenario requires leptonic interactions to produce 1 per cent of the GeV gamma-rays as seen by *Fermi*-LAT to reduce the total SNR leptonic energy budget to  $10^{48}$  erg. This leaves 99 per cent of gamma-rays to be the result of hadronic interactions from SNR with energy budget of  $5\text{--}720 \times 10^{50}$  erg. Therefore an impulsive scenario considering a combination of hadronic and leptonic interactions producing the observed GeV gamma-rays can be rejected.

### 5.1.2 PWN (continuous)

We will now examine the pulsar wind nebula as the source of high energy particles.

The spin-down power of the pulsar powering PWN HESS J1825-137 is of the order of  $10^{36}$  erg s $^{-1}$ . The spin-down power of the pulsar is not constant over time; Aharonian et al. (2006) has suggested that the high gamma-ray luminosity may indicate that the spin-down power was far greater in the past.

From Table 2 a hadronic continuous scenario requires injection luminosities of  $1.8 \times 10^{39}$  and  $9.4 \times 10^{38}$  erg s $^{-1}$  for ages 21 and 40 kyr, respectively. This far exceeds the spin-down power of PSR J1826-1334, rejecting this scenario. Considering a leptonic continuous scenario for ages of 21 and 40 kyr, all three GeV regions require a total of  $\approx 10^{37}$  erg s $^{-1}$  in injection luminosity. If the spin-down power of PSR J1826-1334 was greater in the past as suggested by Aharonian et al. (2006), GeV-ABC may be a reflection of an earlier epoch in the PWN history. The original spin-down power,  $\dot{E}_0$  of the pulsar is linked to the present spin-down power  $E(t)$  through:

$$\dot{E}(t) = \dot{E}_0 \left(1 + \frac{t}{\tau_0}\right)^{-\frac{n+1}{n-1}}, \quad (12)$$

where  $n$  is the braking index of the pulsar and  $\tau_0$  is the initial spin-down time-scale (Pacini & Salvati 1973). The spin-down time-scale can be determined from

$$\tau_0 = \frac{P_0}{(n-1)|\dot{P}_0|}. \quad (13)$$

Taking the assumption from Principe et al. (2020) that  $\dot{P}_0 = 15$  ms and assuming  $\dot{P} = \dot{P}_0$  with a braking index of 3, the original spin-down power of PSR J1826-1334,  $\dot{E}_0$ , was in the order of  $10^{39}$  erg s $^{-1}$ . This exceeds the injection luminosity for a leptonic scenario with the PWN as the accelerator of high energy particles. Electrons injected into the PWN by the pulsar are transported by a combination of advection and diffusion. At the edge of the PWN, it can be assumed that the electrons escape isotropically. Consequently, the GeV gamma-ray emission towards GeV-ABC is expected to follow the photon fields through IC interactions. As the CMB photon field is constant, only the IR photon field would affect the morphology of

gamma-ray emission. As seen in Fig. 10 the peaks in the GeV gamma-ray emission do not correspond to the IR field. Under this scenario, a preferential direction would be required for the advection/diffusion of electrons from the PWN.

Fig. 6 shows diffusive particle transport of electrons travelling a distance of 140 pc in ambient density of  $n = 1 \text{ cm}^{-3}$  versus the cooling of synchrotron and IC processes. This is equivalent to the distance that electrons travel after being emitted by the pulsar to reach GeV-B. The vertical lines represent the equivalent minimum and maximum electron energy seen by *Fermi*-LAT and H.E.S.S., respectively. Fast diffusion ( $\chi = 1.0$ ) is required for electrons in this energy range to reach GeV-B within the age of PWN.

The High Altitude Water Cherenkov Observatory (HAWC) has observed  $\gamma$ -rays greater than 100 TeV (HAWC Collaboration 2019) suggesting that  $E_{e,\max}$  is greater than shown in Fig. 6. The maximum electron able to reach GeV-B is determined by the intersection of diffusion time and the cooling time, i.e. where all electrons have lost their energy through leptonic interactions. On the other hand, the minimum electron energy is represented by the intersection of diffusion time and the age of the pulsar. It can be concluded that for slow diffusion ( $\chi = 0.01$ ) no electrons are able to reach GeV-B; while for fast diffusion, electrons greater than  $\approx 10 \text{ TeV}$  can travel to GeV-B in time. This is reaching the cut-off energy required to reproduce the SED of leptonic process as seen in Table 3.

A more powerful pulsar can convert more of its spin-down power into electron energy, allowing a greater proportion of higher energy electrons. This, in turn, allows more electrons to reach GeV-ABC in time to emit GeV radiation. Therefore, unless advection or fast diffusion is considered or the PWN is powerful, electrons are unable to reach GeV-ABC from PSR J1826-1334 without significant energy losses.

## 5.2 LS 5039 as a particle accelerator

We will now discuss the possibility of LS 5039 as the accelerator for high energy particles resulting in gamma-rays observed towards GeV-ABC.

### 5.2.1 Progenitor SNR (impulsive)

From Table 4, if GeV-ABC is the result of hadronic interactions from an impulsive progenitor SNR, no age of LS 5039 can simultaneously explain the GeV emission as total energy budgets exceed  $10^{50} \text{ erg}$ . Due to the denser cloud towards GeV-B as seen in Fig. 2 for all three clouds to be explained by the same source of high energy particles, the cosmic ray density must be approximately a factor of 10 larger in GeV-B than GeV-A and GeV-C. It can be concluded that an impulsive hadronic source of cosmic rays from LS 5039 cannot simultaneously explain the GeV regions observed by Araya et al. (2019). Similarly an impulsive leptonic source for any age of LS 5039 cannot explain any of the GeV emission from GeV-ABC due to energy budgets exceeding  $10^{49} \text{ erg}$  as shown in Table 5.

### 5.2.2 Accretion powered (continuous)

Microquasars such as LS 5039 are considered to be candidates for particle acceleration up to gamma-ray energies (Aharonian et al. 2005). The average accretion luminosity of LS 5039 is  $8.0 \times 10^{35} \text{ erg s}^{-1}$  (Casares et al. 2005). Approximately one-third of accreted energy is radiated in the relativistic jet (Casares et al. 2005). The remaining  $5.3 \times 10^{35} \text{ erg}$  is assumed to be channelled into

GeV-ABC through a jet. It is unknown whether this jet is hadronic or leptonic in origin. This jet is a continuous source of particles into the region towards GeV-ABC. While the jet generally points in the direction of GeV-B (see Fig. 4), the precession of the jet may allow electrons to be channelled into GeV-A and GeV-C. Particles may also diffuse from the jet escaping into the necessary regions.

A hadronic scenario requires a total injection luminosity into GeV-ABC of  $10^{39} - 10^{36} \text{ erg s}^{-1}$  for an age range of  $10^3 - 10^6 \text{ yr}$ . All ages require total injection luminosity greater than the accretion luminosity can provide; rejecting a hadronic accretion powered scenario.

On the other hand, a leptonic scenario requires a total injection luminosity into GeV-ABC of  $10^{38} - 10^{36} \text{ erg s}^{-1}$  for an age range of  $10^3 - 10^6 \text{ yr}$ . The younger ages of  $10^3$  and  $10^5 \text{ yr}$  can be rejected. All scenarios can vary systematically up to 56 per cent in injection luminosity, an age of  $10^6 \text{ yr}$  can provide the energetics required to reproduce the gamma-rays as seen by *Fermi*-LAT. But this age is greater than the age of  $\approx 10^5 \text{ yr}$  predicted by Moldón et al. (2012). Therefore a leptonic scenario with a continuous jet powered by the accretion onto a compact object in LS 5039 can be rejected.

Using the calculated hydrogen densities towards the regions of interest in LS 5039 in the  $40 - 60 \text{ km s}^{-1}$  range rather than the  $15 - 30 \text{ km s}^{-1}$  range will not alter the results due to values being within a factor of 10 of each other.

In summary, it is unlikely that LS 5039 is the source of the new region of GeV gamma-ray emission.

## 5.3 Combination of LS 5039 and HESS J1825-137

The new region of GeV gamma-rays may be a line-of-sight combination of HESS J1825-137 and LS 5039. As discussed in Sections 5.1 and 5.2 a hadronic scenario requires cosmic ray energy density to be ten times higher in GeV-A and GeV-C compared to GeV-B assuming the dense gas observed in the velocity range  $15 - 30 \text{ km s}^{-1}$  in Fig. 2 lies at the same distance as HESS J1825-137. Note in the case of HESS J1825-137, it assumes the dense gas observed in  $15 - 30 \text{ km s}^{-1}$  range in Fig. 2 lies at the same distance as HESS J1825-137. If the GeV gamma-ray emission from GeV-A and GeV-C is unrelated to emission from GeV-B, this issue will be negated.

As seen in Fig. 4, the region around GeV-ABC contains several astrophysical environments; a H $\alpha$  region believed to be associated with the SNR linked to HESS J1825-137 and a relativistic jet from LS 5039. Even though HESS J1825-137 and LS 5039 are at different distances (3.9 and 2.5 kpc, respectively), the combination of these two processes may explain the spectra observed by *Fermi*-LAT.

Peaks GeV-B and GeV-C have similar spectral indices,  $\Gamma = 1.7 \pm 0.4$  and  $\Gamma = 1.78 \pm 0.25$ , respectively, indicating a common origin scenario, whilst GeV-A has a marginally harder spectra with  $\Gamma = 1.43 \pm 0.23$ . GeV-A is positioned the closest to both HESS J1825-137 and LS 5039. As shown by equations (3) and (4), high energy particles are able to travel further distances than lower energy particles in the same time. Clouds closer to the source of high energy particles are expected to have a softer spectrum than clouds lying further from the source for both continuous and impulsive sources (Aharonian & Atoyan 1996). This is the opposite to what is observed in GeV-ABC.

## 5.4 Particle accelerators unrelated to HESS J1825-137 and LS 5039

Towards GeV-ABC, there are four known supernova remnants; these are SNR G017.4-02.3, SNR G018.9-01.1, SNR G016.2-02.7, and SNR G017.8-02.6 (see Fig. 9). From equation (5c), the cooling



**Figure 9.** *Fermi*-LAT count map above 10 GeV (Araya et al. 2019) towards HESS J1825-137 is shown with alternative accelerators for high energy particles towards HESS J1825-137 and GeV-ABC. The red circles describe H II regions where star formation may occur as given by the WISE catalogue (Anderson 2014). The black circles show the location of other SNR towards the region of interest as described in Section 5.4. The dark purple stars represent pulsars PSR J1826-1334 and PSR J1826-1256 (Manchester et al. 2005). The water maser, G016.8689-02.1552, can be seen as a dark blue dot nearby GeV-B (Urquhart et al. 2011).

time of electrons resulting in synchrotron emission is proportional to the energy; as the supernova remnant ages, higher energy electrons escape from the system or lose their energy decreasing the emitted photon energy. Therefore, as a supernova remnant ages, the amount of X-ray emission detected decreases. Three of the four supernova remnants have no current X-ray detection, indicating that these SNRs are old (at least in the later stages of the Sedov–Taylor phase). They are therefore unlikely to be a source of high energy particle acceleration, resulting in the production of GeV gamma-rays. The remaining supernova remnant, SNR G18.9-1.1, has a partial X-ray shell (Harris et al. 2004). Based on radio measurements by Harris et al. (2004), it is located 2 or 15.1 kpc away. More recent research indicates a distance of  $2.1 \pm 0.4$  kpc and age of 3700 yr (Ranasinghe, Leahy & Tian 2019). As mentioned by Araya et al. (2019), if GeV-ABC is the result of a combination of SNRs, *Fermi*-LAT images will show distinct sources above 10 GeV with the given *Fermi*-LAT resolution. Star forming regions have also been suggested as an accelerator of cosmic rays. See Fig. 9 to see location of star forming regions, SNRs, and pulsars towards HESS J1825-137 and GeV-ABC. The presence of water maser G016.8689-02.1552, as shown in Fig. 9, highly suggests star formation towards this region (Urquhart et al. 2011). This is supported by data from the MSX satellite; data reveals infra-red emission towards GeV-B and GeV-C in the 8.26  $\mu$ m band (see Fig. 10).

## 6 CONCLUSIONS

This study presented spectral models of a region of GeV gamma-ray emission to the south of HESS J1825-137 revealed by *Fermi*-LAT. Different accelerators were proposed to be an origin for high energy particles that created this new region of gamma-rays; the PWN



**Figure 10.** Infrared emission in the 8.26  $\mu$ m band towards GeV-ABC (Egan, Price & Kraemer 2003). Overlayed are the HESS significance contours towards HESS J1825-137 at 1 $\sigma$ , 2 $\sigma$ , and 3 $\sigma$  (H. E. S. S. Collaboration 2018).

(continuous) and SNR (impulsive) associated with HESS J1825-137, and the binary system and microquasar LS 5039 (continuous) as well as the associated progenitor SNR (impulsive). We found that the progenitor SNR related to HESS J1825-137 is unlikely to be the sole source of high energy particles due to the energetics needed to replicate the SED is greater than what the system can provide. For example, an impulsive SNR releases approximately  $10^{50}$  erg of cosmic rays (with 1 per cent of energy channelled into electrons), whereas the SED model of the progenitor SNR of HESS J1825-137 is required to provide either  $10^{52}$  erg of protons or  $10^{50}$  erg of electrons to replicate the SED. A continuous acceleration scenario from the PWN (powered by the pulsar) into GeV-ABC requires particle injection luminosity to be of the order of  $10^{39}$  erg s $^{-1}$  and  $10^{37}$  erg s $^{-1}$  for hadronic and leptonic particles, respectively. GeV-ABC may be a reflection of an earlier epoch in the PWN history, where the pulsar was more powerful. Therefore, the PWN may be a possible accelerator for high energy electrons resulting in this new region of gamma-ray emission, assuming fast diffusion perhaps including advection towards this region. Moreover, it is unlikely that leptonic inverse-Compton emission into this region will produce the localized features such as GeV-ABC. LS 5039 at any age cannot solely explain the GeV emission from GeV-ABC with required injection luminosity  $> 10^{36}$  erg s $^{-1}$  compared to the  $10^{35}$  erg s $^{-1}$  accretion luminosity of LS 5039 (Casares et al. 2005). However a combination of emission from both HESS J1825-137 and LS 5039 could be the cause of the gamma rays.

## ACKNOWLEDGEMENTS

This research has made use of the NASA’s Astrophysics Data System and the SIMBAD data base, operated at CDS, Strasbourg, France. TC acknowledges support through the provision of Australian Government Research Training Program Scholarship.

## DATA AVAILABILITY

No new data were generated or analysed in support of this research.

## REFERENCES

- Aharonian F. A., Atoyan A. M., 1996, *A&A*, 309, 917  
 Aharonian F. et al., 2005, *Science*, 309, 746  
 Aharonian F. et al., 2006, *A&A*, 460, 365  
 Anderson L. D., 2014, American Astronomical Society Meeting Abstracts, Vol. 223, p. 312  
 Araya M., Mitchell A. M. W., Parsons R. D., 2019, *MNRAS*, 485, 1001  
 Berezhinskii V. S., Bulanov S. V., Dogiel V. A., Ptuskin V. S., 1990, *Astrophysics of Cosmic Rays*, North Holland, Netherlands.  
 Blumenthal G. R., Gould R. J., 1970, *Rev. Mod. Phys.*, 42, 237  
 Bosch-Ramon V., Paredes J. M., Ribó M., Miller J. M., Reig P., Martí J., 2005, *ApJ*, 628, 388  
 Brand J., Blitz L., 1993, *A&A*, 275, 67  
 Casares J., Ribó M., Ribas I., Paredes J. M., Martí J., Herrero A., 2005, *MNRAS*, 364, 899  
 Crutcher R. M., 1999, *ApJ*, 520, 706  
 Crutcher R. M., Wandelt B., Heiles C., Falgarone E., Troland T. H., 2010, *ApJ*, 725, 466  
 de Jager O. C., Djannati-Atai A., 2009, in Becker W., eds, *Implications of HESS Observations of Pulsar Wind Nebulae*. Springer, Berlin, Heidelberg, p. 451  
 Draine B. T., 2011, *Physics of the Interstellar and Intergalactic Medium*, Princeton University Press, New Jersey.  
 Egan M. P., Price S. D., Kraemer K. E., 2003, American Astronomical Society Meeting Abstracts, 57  
 Finkbeiner D. P., 2003, *ApJS*, 146, 407  
 Gabici S., Aharonian F. A., Blasi P., 2007, *Ap&SS*, 309, 365  
 Gabici S., Aharonian F. A., Casanova S., 2009, *MNRAS*, 396, 1629  
 H. E. S. S. Collaboration, 2018, *A&A*, 612, A1  
 H. E. S. S. Collaboration, 2019, *A&A*, 621, A116  
 Harris I. M., Slane P. O., Hughes J. P., Plucinsky P. P., 2004, *ApJ*, 603, 152  
 HAWC Collaboration, 2019, Multiple Galactic Sources with Emission Above 56 TeV Detected by HAWC, preprint ([arXiv:1909.08609](https://arxiv.org/abs/1909.08609))  
 Hinton J. A., Hofmann W., 2009, *ARA&A*, 47, 523  
 Liu R.-Y., Yan H., 2020, *MNRAS*, 494, 2618  
 Manchester R. N., Hobbs G. B., Teoh A., Hobbs M., 2005, *AJ*, 129, 1993  
 Manolakou K., Horns D., Kirk J. G., 2007, *aap*, 474, 689  
 Marcote B., Ribó M., Paredes J. M., Ishwara-Chandra C. H., 2015, *MNRAS*, 451, 59  
 Martí J., Paredes J. M., Ribo M., 1998, *A&A*, 338, L71  
 McClure-Griffiths N. M. et al., 2009, *ApJS*, 181, 398  
 Mizuno A., Fukui Y., 2004, in Clemens Dan, Shah Ronak Y., Brainerd T., eds, *Physical properties of molecular clouds as revealed by NANTEX CO survey: from the galactic center to the galactic warp*, Astronomical Society of the Pacific Conference Series, p. 59  
 Moderski R., Sikora M., Coppi P. S., Aharonian F., 2005, *MNRAS*, 363, 954  
 Moldón J., Ribó M., Paredes J. M., Brisken W., Dhawan V., Kramer M., Lyne A. G., Stappers B. W., 2012, *A&A*, 543, A26  
 Motch C., Haberl F., Dennerl K., Pakull M., Janot-Pacheco E., 1997, *A&A*, 323, 853  
 Nomoto K., Maeda K., Mazzali P. A., Umeda H., Deng J., Iwamoto K., 2004, in Shore S., eds, *Hypernovae and Other Black-Hole-Forming Supernovae*, Springer Nature, Switzerland, p. 277  
 Pacini F., Salvati M., 1973, *ApJ*, 186, 249  
 Paredes J. M., Ribó M., Ros E., Martí J., Massi M., 2002, *A&A*, 393, L99  
 Principe G., Mitchell A., Hinton J., Parson D., Caroff S., Hahn J., Funk S., 2019, in 36th International Cosmic Ray Conference (ICRC2019), Madison, p. 595  
 Principe G., Mitchell A. M. W., Caroff S., Hinton J. A., Parsons R. D., Funk S., 2020, *A&A*, 640, A76  
 Ptuskin V. S., Zirakashvili V. N., 2005, *A&A*, 429, 755  
 Ranasinghe S., Leahy D., Tian W. W., 2019, preprint ([arXiv:1910.05407](https://arxiv.org/abs/1910.05407))  
 Reynolds S. P., 2008, *ARA&A*, 46, 89  
 Sabol E. J., Snowden S. L., 2019, *sxrbg: ROSAT X-Ray Background Tool*, Astrophysics Source Code Library,
- Strong A. W., Moskalenko I. V., Reimer O., Digel S., Diehl R., 2004, *A&A*, 422, L47  
 Stupar M., Parker Q. A., Filipovic M. D., 2008, *MNRAS*, 390, 1037  
 Taylor J. H., Cordes J. M., 1993, *ApJ*, 411, 674  
 Urquhart J. S. et al., 2011, *MNRAS*, 418, 1689  
 van der Swaluw E., Wu Y., 2001, *ApJ*, 555, L49  
 Voisin F., Rowell G., Burton M. G., Walsh A., Fukui Y., Aharonian F., 2016, *MNRAS*, 458, 2813

## APPENDIX A: ISM PARAMETERS

**Table A1.** Calculated molecular parameters for HESS J1825-137 and the new GeV emission regions GeV-A, GeV-B, GeV-C as shown in Fig. 2.  $M_H$  and  $n_H$  describes the average mass and density, respectively, over the new GeV regions.

15–30 km s <sup>-1</sup>	Region	$M_H$ (M <sub>⊙</sub> )	$n_H$ (cm <sup>-3</sup> )
HESS J1825-137	GeV-A	$1.14 \times 10^5$	39
	GeV-B	$3.67 \times 10^3$	5
	GeV-C	$1.36 \times 10^5$	79
		$1.53 \times 10^3$	2
40–60 km s <sup>-1</sup>	Region	$M_H$ (M <sub>⊙</sub> )	$n_H$ (cm <sup>-3</sup> )
	HESS J1825-137	$5.18 \times 10^5$	176
	GeV-A	$8.49 \times 10^3$	13
	GeV-B	$1.21 \times 10^4$	7
	GeV-C		No ISM values

**Table A2.** Calculated H<sub>i</sub> densities for HESS J1825-137 and the new GeV emission regions GeV-A, GeV-B, and GeV-C.

15–30 km s <sup>-1</sup>	Object	$M_H$ (M <sub>⊙</sub> )	$n_H$ (cm <sup>-3</sup> )
HESS J1825-137	GeV-A	$3.53 \times 10^3$	1.2
	GeV-B	$8.91 \times 10^2$	1.4
	GeV-C	$1.51 \times 10^3$	0.9
		$7.70 \times 10^2$	1.2
40–60 km s <sup>-1</sup>	Object	$M_H$ (M <sub>⊙</sub> )	$n_H$ (cm <sup>-3</sup> )
	HESS J1825-137	$4.29 \times 10^3$	1.5
	GeV-A	$4.36 \times 10^2$	0.7
	GeV-B	$5.06 \times 10^2$	0.3
	GeV-C	$3.11 \times 10^2$	0.5

**Table A3.** Calculated H<sub>α</sub> densities for HESS J1825-137 and new GeV emission regions.

Object	Method A (cm <sup>-3</sup> )	Method B (cm <sup>-3</sup> )
HESS J1825-137	$8.88 \times 10^{-6}$	$4.12 \times 10^{-6}$
GeV-A	$1.12 \times 10^{-6}$	$2.40 \times 10^{-6}$
GeV-B	$6.49 \times 10^{-6}$	$5.13 \times 10^{-6}$
GeV-C	$2.45 \times 10^{-6}$	$5.23 \times 10^{-6}$

## APPENDIX B: H $\alpha$ DENSITY CALCULATION METHOD

### B1 Method A

Method A assumes that the density of photons in the region of interest is approximately equal to the density of ionized gas  $n \approx u_{\text{ph}}$ . This assumes that atoms are not being re-excited by an external source. Considering a spherical shell located at distance  $d$  from the source with thickness  $d\ell$ ; the volume of the shell is given by  $dV = 4\pi d^2 \times d\ell$ . Photons emitted by the source travel at the speed of light, therefore  $d\ell = c d\tau$ . The number of photons emitted by the source in time  $d\tau$  is related to the luminosity  $L$  through  $dN = L d\tau$ . Using the original approximation, the density of ionized hydrogen in a region of interest:

$$n \approx u_{\text{ph}} = \frac{dN}{dV} = \frac{L}{4\pi d^2 c}. \quad (\text{B1})$$

Let the region of interest have solid angle  $\Omega$  and lying at distance  $d$ . The luminosity of the region is given by

$$L [\text{photon s}^{-1}] = \frac{d^2}{10^{-10}} \Omega I, \quad (\text{B2})$$

where  $I$  is the measured H  $\alpha$  intensity in Rayleigh units.

### B2 Method B

Method B considers basic radiation transfer. The density of atoms in the  $i$ th excited state emit photons at frequency  $\nu$  through spontaneous emission is related to the emission coefficient by

$$n_i = \frac{j_\nu \Omega_{\text{Earth}}}{E_\nu A \phi(\nu)}, \quad (\text{B3})$$

where  $A$  is the Einstein coefficient,  $\Omega_{\text{earth}}$  is the solid angle of Earth projected at source lying at distance  $d$ , and  $\phi(\nu)$  is the spectral line shape normalized by

$$\int \phi(\nu) = 1. \quad (\text{B4})$$

Assuming that hydrogen atoms in the  $n = 3$  state emit mainly H  $\alpha$  light;  $\phi = 0$  in all frequencies except when  $\nu = \nu_{H\alpha}$ . The photon radiance  $L_{\text{rad}}$  is related to the intensity  $I$  in Rayleigh's through:

$$L_{\text{rad}} [\text{photons m}^{-2} \text{s}^{-1} \text{sr}^{-1}] = \frac{L}{4\pi d^2}. \quad (\text{B5})$$

The photon intensity can be found utilizing  $I_\nu = L \frac{E_\nu}{\nu} = hL$  where  $h$  is Planck's constant. Let  $s$  be the thickness of gas in the line of sight and assuming the emission coefficient is constant, the emission coefficient and intensity are related by

$$j_\nu = \frac{I_\nu}{s}. \quad (\text{B6})$$

This can be used in combination with equation (B3) to obtain the photon density.

## APPENDIX C: SED MODEL

The SED modelling code includes various astrophysical processes; included proton–proton interactions:



Inverse Compton interactions:



Bremsstrahlung interactions with a nucleus with proton number  $Z$ :



and synchrotron interactions:



The evolution of the cosmic ray energy distribution with Lorentz factor  $\gamma$  at time  $t$  is given by

$$\frac{\partial n(\gamma, t)}{\partial t} = \frac{\partial}{\partial \gamma} [\dot{\gamma}(\gamma)n(\gamma, t)] + S(\gamma, t), \quad (\text{C6})$$

where  $S(\gamma, t)$  is the source term,  $\dot{\gamma}(\gamma)$  represents the energy loss rate of a particle with Lorentz factor  $\gamma$ . The analytical solution of equation (C6) is

$$n(\gamma, t) = \frac{1}{\gamma} \int_{\gamma_0}^{\gamma_0} S(\gamma'', t - \tau(\gamma'')) d\gamma'' + \frac{\dot{\gamma}_0}{\gamma} n(\gamma_0, 0), \quad (\text{C7})$$

where  $\tau$  is a variable describing the time for a cosmic ray with initial Lorentz factor  $\gamma'$  to evolve to factor  $\gamma$ :

$$\tau(\gamma', \gamma) = \int_{\gamma'}^{\gamma} \frac{d\gamma''}{\dot{\gamma}(\gamma'')} \quad (\text{C8})$$

and  $\gamma_0$  is the initial Lorentz factor. The code solves equation (C7) considering hadronic and leptonic interactions and then extracts the SED. The model allows the user to choose whether the case is leptonic, hadronic, or a mixture. Similarly the user can choose if the model is continuous (constant cosmic ray input, e.g. a PWN) or impulsive (releases all the cosmic rays at once, e.g. a SNR). Other parameters such as the age and distance from the source, density, and magnetic field of background material, the total energy, and spectral distribution of cosmic rays and background photon field energy distribution can be changed depending on the source.

To find the SED at time  $t$ , for each lorentz factor  $\gamma$  the lorentz factor at earlier time,  $\gamma_0$  is derived. In the case of an impulsive source  $\gamma_0$  is simply  $\gamma$  at  $t = 0$ . The total cooling rate is given by Manolakou, Horns & Kirk (2007):

$$\dot{\gamma}(\gamma) = \begin{cases} b_s \gamma^2 + b_c (3 \ln \gamma + 18.8) \\ + 5.3 b_b + \sum_{i=i}^l b_{i\text{C}}^l \gamma^2 F_{\text{KN}}^l(\gamma), & \text{for leptonic cases} \\ \frac{1}{n_H c \sigma_{\text{pp}}(\gamma)}, & \text{for hadronic cases} \end{cases}, \quad (\text{C9})$$

where

(i)  $b_s = 1.292 \times 10^{-15} (B/10^3 \mu\text{g})^2 \text{s}^{-1}$  is a synchrotron loss constant.

(ii)  $b_c = 1.491 \times 10^{-14} (n_H/1\text{cm}^{-3})$  is the Coulomb loss constant.

(iii)  $b_b = 1.37 \times 10^{-16} (n_H/1\text{cm}^{-3}) \text{s}^{-1}$  is the bremsstrahlung loss constant.

(iv)  $b_{i\text{C}} = 5.204 \times 10^{-20} (u_0^i/\text{eV}) \text{s}^{-1}$  is a IC loss constant with the energy density of photons given by  $u_0$ .

(v)  $\sum_{i=i}^l$  sums over all radiation fields contributing to the Inverse-Compton gamma-ray flux.

(vi)  $n_H$  is the density of the ambient hydrogen gas.

(vii)  $\sigma_{\text{pp}}(\gamma)$  is the cross-section for proton–proton interactions.

To obtain  $\gamma_0$ , the following two steps are repeated until  $t = t_{\text{age}}$ :

(i) derive  $\Delta t = d\gamma/\dot{\gamma}(\gamma)$

(ii) Increment  $\gamma$  by  $d\gamma$ 

with automatic adjustment of the  $d\gamma$  step. Another parameter in the code is ‘escape’. If this parameter is activated, once a particle escapes the system, it is no longer considered. The final synchrotron flux is given by

$$P(v) = \frac{\sqrt{3}e^3 B}{mc^2} \frac{v}{v_c} \int_{\frac{v}{v_c}}^{\infty} K_{\frac{5}{3}}(x) dx, \quad (C10)$$

where  $e$  and  $m$  are the charge and mass of an electron, respectively,  $v$  is the frequency of the gamma-ray,  $v_c$  is the critical frequency of the emission, and  $K_{\frac{5}{3}}$  is the modified Bessel Function. The final Inverse-Compton flux radiated by a single electron with energy  $\epsilon$  is given by

$$\frac{dN}{dE_\gamma} = \frac{3}{4} \sigma_T c \int \frac{n(\epsilon)d\epsilon}{\epsilon} F_{KN}(E_e, E_\gamma, \epsilon), \quad (C11)$$

where  $\sigma_T$  is the Thompson cross-section and  $F_{KN}$  is the Klein-Nishina cross-section. The final bremsstrahlung Flux is given by

$$\frac{dN}{dE_\gamma} = nc \int d\sigma(E_e, E_\gamma, Z) dE_e, \quad (C12)$$

where  $Z$  is the atomic number of the target material and  $d\sigma$  is defined in Blumenthal & Gould (1970). Finally proton–proton interactions produce a flux of

$$\frac{dN}{dE_\gamma} = nc \int_{E_p=E_\gamma}^{\infty} A_{\max}(T_p) F(E_\gamma, T_p) dE_p, \quad (C13)$$

where  $n$  is the density of protons,  $A_{\max}(T_p)$  is the pion production

cross-section,  $T_p$  is the kinetic energy of the proton, and  $F(E_\gamma, T_p)$  is the spectra of gamma-rays emitted for a single proton of energy  $E_p$ .

## APPENDIX D: OTHER SPECTRAL ENERGY DISTRIBUTION PLOTS



**Figure D1.** SED example for GeV-A with continuous hadronic SED (left-hand panel) and continuous leptonic SED (right-hand panel). This assumes that LS 5039 (at age  $10^5$  yr) is the source of acceleration. The upper data points represent the total SED as measured by *Fermi*-Lat. The lower data points is 36.9 per cent of this spectra due to source being only GeV-A. The green cross is the *ROSAT* X-ray upper limit towards GeV-ABC. The blue, pink, and yellow shaded regions represent the systematic variation of energy budget ( $W$ ) or injection luminosity ( $\dot{W}$ ), cutoff energy and spectral index, respectively. See Tables 4 and 5 for input parameters.

This paper has been typeset from a TeX/LaTeX file prepared by the author.

# Chapter 7

## Modelling the 3D environment around Pulsar Wind Nebulae

Chapter 5 discussed how radiative and escape losses affect the energy density distribution of cosmic rays and the subsequent photon SED in a gas with constant density and magnetic field. The SED towards the extended GeV gamma-ray region to the south of HESS J1825-137 was then modelled to determine the origin of cosmic rays towards this region. This is summarised in chapter Chapter 6.

However, astrophysical environments are not uniform. For example, observatories such as Nanten (see Section 4.2.6) and Mopra (Braiding et al., 2018) have conducted surveys of molecular and atomic gas across the Galactic plane and identified numerous structures of dense gas. Non-uniform soft photon fields such as IR and UV fields driven by star formation also provide seed photons for inverse Compton interactions, affecting the subsequent gamma-ray morphology. As discussed in Section 2.2.2, the magnetic field varies on a local (< pc) and Galactic scales > 100 pc. In the case of PWNe, the magnetic field varies with distance to the pulsar (Reynolds et al., 2012), affecting the properties of cosmic ray propagation out of this region (see Eq. 2.31).

This chapter will first discuss the transport equation that governs the time and spatial evolution of cosmic ray and electron energy density distribution as they escape into a non-uniform environment. The chapter will then move on to describe how numerical techniques are applied to solve the transport equation. These numerical techniques are then applied to PWN HESS J1825-137, the results of which can be seen in Chapter 8.

### 7.1 The Transport Equation

Section 5.1 described the solution of the cosmic-ray energy density distribution for a simple scenario of cosmic rays being injected into a homogeneous source. However, the environment around pulsars is not uniform. The evolution of the cosmic ray (including high-energy electrons) energy density distribution,  $n$ , for a non-uniform environment can be described by a Fokker-Planck equation (Skilling, 1975; Cesarsky and Volk, 1978):

$$\frac{\partial n}{\partial t} = -\nabla \cdot (n\mathbf{v}_A) - \nabla \left( \bar{D} \cdot \nabla n \right) + \frac{\partial}{\partial \gamma} (\dot{\gamma} n) - \frac{\partial}{\partial \gamma} \left( \frac{\gamma}{3} (\nabla \cdot \mathbf{v}_A) n \right) \\ + \frac{\partial}{\partial \gamma} \left( \gamma^2 D_{\gamma\gamma} \frac{\partial}{\partial \gamma} \left( \frac{n}{\gamma^2} \right) \right) + S(\gamma, \mathbf{r}, t) , \quad (7.1)$$

where the first term in Eq. 7.1 describes the evolution of cosmic rays due to a co-moving fluid with velocity  $\mathbf{v}_A$ . The second term considers the diffusion of cosmic rays where

$\overline{\overline{D}}$  is a second rate tensor describing the rate of diffusion in 3D. The third and fourth term represents losses due to radiative processes (see chapter Section 2.3) and adiabatic expansion respectively. The fifth term describes diffusion as a result of the re-acceleration of cosmic rays due to stochastic process. Finally,  $S(\gamma, \mathbf{r}, t)$ , is the source term of high-energy cosmic rays.

As discussed in Section 2.2.2, over small distances (less than the gyro-radius  $r_g$ ), cosmic rays propagate through the ISM via ballistic motion. Over large distances, cosmic rays scatter off magnetic field turbulence and the overall propagation can be described by diffusion (Prosekin et al., 2015). Neglecting adiabatic losses, bulk motion and re-acceleration of cosmic rays, Eq. 7.1 can be simplified to:

$$\begin{aligned} \frac{\partial n}{\partial t} &= -\nabla(D(\mathbf{r}, \gamma) \cdot \nabla n) + \frac{\partial}{\partial \gamma}(\dot{\gamma}n) + S(\gamma, \mathbf{r}, t) \\ &= \left(\frac{\partial n}{\partial t}\right)_{\text{diffusion}} + \left(\frac{\partial n}{\partial t}\right)_{\text{radiative}} + \left(\frac{\partial n}{\partial t}\right)_{\text{source term}}, \end{aligned} \quad (7.2)$$

where the time evolution of the cosmic ray distribution is described by the sum of the evolution due to diffusion, radiative cooling and a cosmic ray source term. Note that Eq. 7.2 is similar to Eq. 5.1, where the ‘escape term’ has been replaced with an expression describing the losses due to diffusion. For a simple case of isotropic diffusion ( $\overline{\overline{D}} = D$  and  $\nabla D = 0$ ), the diffusion term in Eq. 7.2 becomes:

$$\begin{aligned} \left(\frac{\partial n}{\partial t}\right)_{\text{diffusion}} &= -\nabla(D(\mathbf{r}, \gamma) \cdot \nabla n) \\ &= -\nabla D \cdot \nabla n - D\nabla^2 n \\ &= -D\nabla^2 n, \end{aligned} \quad (7.3)$$

Eq. 7.2 can only be solved analytically for simple scenarios (e.g. an impulsive accelerator of electrons in a medium of constant density and magnetic field, see Atoyan et al., (1995)). These assumptions cannot be applied to accelerators like PWNe that evolve within complex environments (see Section 2.1). Therefore, numerical methods must be applied in order to solve Eq. 7.2.

### 7.1.1 Particle Transport literature review

Numerical solutions of Eq. 7.1 can be applied to many different scenarios in order to obtain an understanding of astrophysical phenomena. For example, **GALPROP** is a publicly available software package that describes the propagation of cosmic rays within the Galaxy (Porter et al., 2022). It combines models of the cosmic-ray source distribution, interstellar gas, radiation fields and magnetic fields in order to solve the transport equation. **GALPROP** then normalises the modelled cosmic ray spectrum to observations at Earth in order to predict the diffuse gamma-ray emission. Other examples of software that solve the transport equation on a Galactic scale include **DRAGON** (Evoli et al., 2017) and **PICARD** (Kissmann, 2014). **CRPTIC** is a recent software package that simulates the propagation through complex ISM with propagation properties depending on the state of the gas (Krumholz et al., 2022). **CRPTIC** has been used to investigate how ISM parameters (e.g. sonic Mach number, Alfvén Mach number) affect the transport of cosmic rays (Sampson et al., 2023).

### 7.1.2 Numerical Solution of the Transport Equation

GALPROP, DRAGON and PICARD solve the transport equation on a Galactic scale ( $> 100$  pc). To understand the detailed nature and evolution of cosmic rays that escape their place of origin (e.g. PWN), the transport equation must be solved on smaller scales ( $\gtrsim$  pc). To do this, finite difference techniques will be utilised to solve Eq. 7.2. There are other techniques used to solve differential equations (e.g. method of lines, finite volume method), however finite difference techniques are one of the most commonly used and the simplest to apply. Similarly, finite difference techniques describe a range of techniques with the simplest being the forward difference, backward difference and central difference (see Appendix C). More complex techniques include the Euler method and Crank-Nicolson method require the solution of linear equations, which can be computationally intensive. Therefore, a combination of the simpler techniques will be considered in this thesis. As the transport equation will be applied to the PWN HESS J1825-137 in Chapter 8, only the transport of electrons will be considered. However, these techniques also apply to the transport of cosmic ray protons.

Finite difference techniques obtain numerical solutions to differential equations (e.g. transport equation) by approximating derivatives with finite differences found through a Taylor series expansion (see Appendix C). To solve Eq. 7.2 numerically, a region of interest is subdivided into a grid of voxels (a 3D pixel) of size  $\Delta x \Delta y \Delta z$  as shown in Fig. 7.1. The change in the electron energy distribution for a voxel at position  $x$ ,  $y$  and  $z$  due to diffusion from surrounding voxels in time interval  $\Delta t$  is then described by:

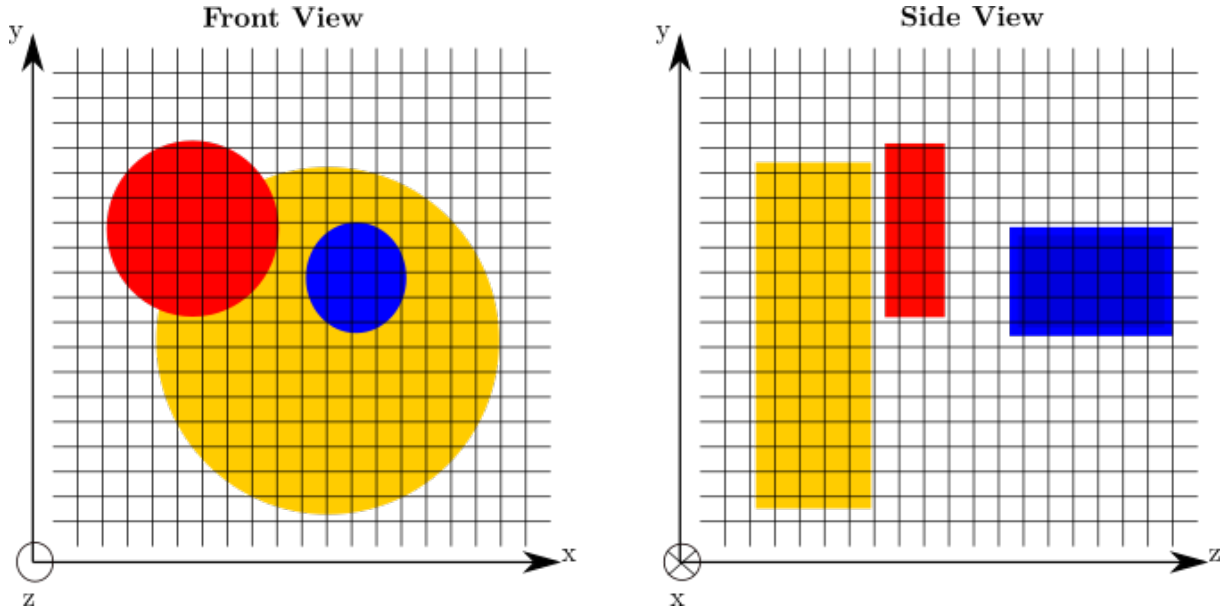


Figure 7.1: Front (left) and side (right) view of an example region of interest showing three clouds of different densities and sizes. To numerically solve the transport equation, the region of interest is split into a 3D grid of voxels.

$$\left( \frac{\partial n}{\partial t} \right)_{\text{diffusion}} \Big|_{x, y, z}^{\gamma} = \sum_{\{i=x, y, z\}} \left[ \mathbf{D}^* \left| \begin{array}{c} \gamma \\ t - \Delta t \\ i + \Delta i / 2 \end{array} \right. \left( n \left| \begin{array}{c} \gamma \\ t - \Delta t \\ -n \end{array} \right. \right|_i^{\gamma_0} \right. \right. \\ \left. \left. + \mathbf{D}^* \left| \begin{array}{c} \gamma \\ t - \Delta t \\ i - \Delta i / 2 \end{array} \right. \left( n \left| \begin{array}{c} \gamma \\ t - \Delta t \\ -n \end{array} \right. \right|_i^{\gamma} \right) \right] , \quad (7.4)$$

where

$$\mathbf{D}^* \left| \frac{\gamma}{t - \Delta t} \right|_{i \pm \Delta i/2} = \chi D_0 \left( \frac{\gamma m_e}{1 \text{ TeV}} \right)^\delta \left( \frac{B_i + B_{i+1}}{2 \times 3 \mu\text{G}} \right)^{-\delta} \frac{\Delta t}{\Delta i^2}, \quad (7.5)$$

is the dimensionless diffusion factor that considers the average magnetic field between voxel  $i$  and  $i \pm 1$  (see Eq. 2.31). See Fig. 7.2 for a graphical description of Eq. 7.5.

Errors in finite difference methods arise due to the discretization of the grid and approximating partial derivatives with truncated partial derivatives (see Section C.1), leading to the discrepancy between the numerical and analytical solution. Finite difference methods are said to be ‘stable’ when the numerical solution converges to the analytical solution. Von Neumann stability analysis treats the numerical error of finite difference techniques as a time-dependent Fourier expansion and determines the condition when the error at  $t = t + 1$  is less or equal to the error at  $t = t$  (see Section C.1.1). That is, Von Neumann stability analysis determines whether any errors due to numerical techniques are magnified in further iterations. Using Von Neumann stability analysis, Eq. 7.4 is stable when:

$$D \frac{\Delta t}{\Delta x^2} \leq \frac{1}{2}. \quad (7.6)$$

i.e. finite difference techniques can be applied to the transport equation when the diffusion coefficient,  $D$ , is less than or equal to half of the ‘maximum’ diffusion coefficient (see Eq. 2.31) implied by the voxel size and time step. Therefore, the maximum displacement of electrons across one time step is less than one voxel. If this condition is not met, electrons are transported across more than voxel. As Eq. 7.4 only considers neighbouring voxels, there will be a net loss of electrons in the 3D grid.

### 7.1.3 Multizone

**Multizone** is a software originally developed by Voisin, (2017) that tracks the transport and cooling of electrons in a 3D grid by applying finite difference techniques to solve Eq. 7.4. Fig. 7.3 shows the method that **Multizone** uses to solve Eq. 7.4.

1. The region of interest is divided into a grid of voxels of size  $\Delta x \Delta y \Delta z$  of varying ISM number density and magnetic field. For simplicity,  $\Delta x = \Delta y = \Delta z$ . The ISM number density of each voxel can be obtained from observations of atomic and molecular gas from surveys such as Nanten (see Section 4.2.6). Similarly, the magnetic field of each voxel is estimated via Crutcher’s relationship (see Eq. 4.38) or assigned a value based on a specific magnetic field model (e.g. magnetic field of a PWN).
2. From Eq. 2.31, the rate at which an electron propagates via diffusion is proportional to its energy ( $D \propto E^\delta$ ). The 3D grid is therefore subdivided into three resolutions based on the electron energy for computational efficiency. The highest energy electrons are tracked using the grid with the lowest resolution while the slower low energy electrons are tracked on the high resolution grid. The medium and high resolution voxels have size  $2\Delta x 2\Delta y 2\Delta z$  and  $4\Delta x 4\Delta y 4\Delta z$  respectively (see Fig. 7.4). In the context of this thesis, the high energy resolution considers electrons with energy



Figure 7.2: The electron energy distribution in each voxel will be calculated by tracking the flux in (red) and out (green) of neighbouring cells.

$< 0.02$  TeV, the medium energy resolution considers electrons between 0.02–15 TeV and the lowest resolution considers electrons greater than 15 TeV.

3. To ensure that the electron distribution stays positive ( $n \geq 0$ ) and the position of the maximum value of  $\mathbf{D} = D\Delta t/\Delta x^2$  remains constant across time:



Figure 7.3: A flow-chart description of the steps **Multizone** uses to calculate the electron energy distribution and subsequent SED by numerically solving the transport equation.



Figure 7.4: A 2D representation of the three 3D grid resolutions used to numerically solve Eq. 7.4. Voxels with high number density or magnetic field are shown in red.

$$n_{\max}(1 - 6\mathbf{D}) \geq n_{\max}\mathbf{D} \quad (7.7a)$$

$$\mathbf{D}_{\max} \leq \frac{1}{7}, \quad (7.7b)$$

where the factor six in Eq. 7.7a comes from the three degrees of freedom. Hence the time step becomes:

$$\Delta t = \frac{\Delta x^2}{\mathbf{D}_{\max}}, \quad (7.8)$$

where  $\mathbf{D}_{\max}$  is the maximum value of  $\mathbf{D}$  across the 3D grid. Note that Eq. 7.8 satisfies the condition where the finite difference method is stable (Eq. 7.6).

4. At  $t = 0$ , electrons are injected into a region of size  $4\Delta x 4\Delta y 4\Delta z$  centered on position  $(x_s, y_s, z_s)$ . This ensures that electrons are injected into the same region regardless of their energy. For an impulsive accelerator injecting electrons with injection luminosity  $L$  ( $\text{erg s}^{-1}$ ) with spectra  $J'(E)$  (the ‘de-nominalised spectra following, e.g. a power law  $E^{-\Gamma}$ ), the total energy of electrons injected into the  $4\Delta x 4\Delta y 4\Delta z$  cube in time interval  $\Delta t$  is:

$$E_{\text{tot}} = \frac{L}{\int_{E_{\min}}^{E_{\max}} E J'(E) dE} \Delta t, \quad (7.9)$$

where  $E_{\min}$  and  $E_{\max}$  are the minimum and maximum electron energy injected into the grid respectively.

5. For every time step:

- 5a. The energy loss of electrons from the previous time step is calculated. As `Multizone` treats continuous injectors as a series of impulsive injections, the electron energy distribution due to radiative losses during time  $\Delta t$  is:

$$n(\gamma, t) = \frac{\dot{\gamma}_0}{\dot{\gamma}} n(\gamma_0, t - \Delta t), \quad (7.10)$$

where  $\gamma_0$  is the Lorentz factor of the electron at  $t = t - \Delta t$  before cooling to Lorentz factor  $\gamma$  (see Eq. 5.9).

- 5b. For each voxel, the electron energy distribution at time  $t$  is found by incrementing the electron energy distribution from step 5a. with the net transfer of electrons from neighbouring voxels with (see Eq. 7.4).
- 5c. Electrons are injected into the grid with total energy given by Eq. 7.9. The current electron energy distribution becomes the ‘old’ electron energy distribution for the next time step.
6. When the desired age is reached (e.g. the estimated age of HESS J1825-137 is 21 – 40 kyr), the subsequent photon SED emitted by each voxel is calculated and summed along the line of sight. The photon SED and electron energy distribution are then written as FITS cubes for further analysis.

#### 7.1.4 Analytical Solution: Diffusion-only

The numerical solution (`Multizone`) will now be compared to a diffusion-only scenario (no radiative losses) for an impulsive accelerator injecting electrons at  $x = y = z = t = 0$ . The analytical solution of Eq. 7.2 for a diffusion-only scenario (Eq. 5.36b when  $t \ll \gamma/\dot{\gamma} = \tau$ ) is:



Figure 7.5: Distribution of electrons injected into a 3D grid at  $x = y = z = t = 0$  and subjected to diffusion. (*Top*) The number density distribution taken at slice  $z = (0 \pm 1) \text{ pc}$  and time 40 kyr. The black and yellow dashed circles represent the 2D variance radius ( $R_{\text{var}}$ ) and the radius containing  $1\sigma = 68\%$  of electrons ( $R_\sigma$ ) in the 2D slice respectively. (*Bottom*) Comparing the numerical solution (lines) and analytical solution (dots, see Eq. 7.11) at  $t = 20$  and 40 kyr along  $y = (0 \pm 1) \text{ pc}$  (dashed horizontal line in the bottom panel).

$$n(E, t, r) = n_0 \left( \frac{1}{4\pi D t} \right)^{\frac{3}{2}} \exp \left( -\frac{r^2}{4Dt} \right), \quad (7.11)$$

where  $r^2 = x^2 + y^2 + z^2$ .

Fig. 7.5 compares the numerical and analytical solution for model parameters applicable to the region towards HESS 1825-137 (see Chapter 8). Electrons are injected into a uniform ISM with a magnetic field taking the Galactic average of  $3 \mu\text{G}$  (Schlickeiser, 2002) and diffusion suppression factor  $\chi = 0.1$ . A time step of 8 yr and voxel width of  $\Delta x = \Delta y = \Delta z = 2 \text{ pc}$  was chosen such that the finite difference method is stable for electrons  $\lesssim 600 \text{ TeV}$  (see Eq. 7.6). The bottom panels of Fig. 7.5 show the number density

distribution taken at slice  $z = (0 \pm 1)$  pc for electron energies 0.1 and 10 TeV and age  $t = 40$  kyr. Note that the radius containing  $1\sigma = 68\%$  of electrons ( $R_\sigma$ ) in the 2D slice is equivalent to the 2D variance radiance ( $R_{\text{var}} = \sqrt{4Dt}$ ) for both energies. Similarly, the top panels show that the numerical solution is able to closely match the analytical solution for a slice taken at  $y = z = (0 \pm 1)$  pc.

The variance of the 68% containment radius of Eq. 7.11 is given by (see Appendix D):

$$\text{Var}(r) = 6Dt . \quad (7.12)$$

i.e. 68% of electrons are contained within 3D radius of  $R_{\text{var}} = \sqrt{6Dt}$ . The 2D variance radius for a slice in the 3D grid (e.g.  $z = (0 \pm 1)$  pc) is given by:

$$\text{Var}(r) = \sqrt{4Dt} . \quad (7.13)$$

### 7.1.5 Diffusion and Radiative Energy Losses: Analytical and Numerical Solution Comparison

Next, finite difference techniques will be used to predict the electron number density for a diffusive scenario including radiative energy losses for a constant ISM and magnetic field (see Section 2.3.3).

An impulsive accelerator will inject electrons with spectra  $= AE^{-\Gamma}$  into a volume of size  $4 \text{ pc} \times 4 \text{ pc} \times 4 \text{ pc}$  at  $t = 0$ . The analytical solution can be found by convolving the Green's solution of the transport equation (see Eq. 5.42) with the radius of the electron injector  $R_{\text{source}}$ :

$$n(x, y, z, \gamma, t) = \iiint_{x, y, z=-\infty}^{\infty} n_{\text{green}}(\mathbf{r} - \mathbf{s}_r) R_{\text{source}}(\mathbf{s}_r) d\mathbf{s}_r , \quad (7.14)$$

where:

$$R_{\text{source}}(\mathbf{s}_r) = \begin{cases} 1, & -2 \text{ pc} \leq s_r \leq 2 \text{ pc} \\ 0, & \text{otherwise} \end{cases} , \quad (7.15)$$

and

$$\begin{aligned} n_{\text{green}}(\gamma, r, t) &= \frac{(1 - \gamma b_s t)^{\Gamma-2} A \gamma^{-\Gamma}}{\pi^{\frac{3}{2}} R_{\text{diff}}(\gamma, t, B)^3} \exp\left(-\frac{r^2}{R_{\text{diff}}(\gamma, t, B)^2}\right) \\ &= \frac{n_0}{\pi^{\frac{3}{2}} R_{\text{diff}}(\gamma, t, B)^3} \exp\left(-\frac{r^2}{R_{\text{diff}}(\gamma, t, B)^2}\right) \\ &\quad \boxed{R_{\text{diff}} = \sqrt{\frac{4D(\gamma, B)}{b_s \gamma (1-\delta)} [1 - (1 - \gamma b_s t)^{1-\delta}]}} , \end{aligned} \quad (7.16)$$

where  $A$ ,  $b_s$ , ect. are defined in Section 5.1. As with Section 7.1.4, electrons will be injected into a uniform ISM (i.e constant density  $n_0$  and magnetic field  $B$ ). Combining Eq. 7.14, Eq. 7.15 and Eq. 7.16:

$$n_{\text{exact}}(x, y, z, \gamma, t) = \int_{x=-2}^2 \int_{y=-2}^2 \int_{z=-2}^2 \frac{n_0}{64\pi^{\frac{3}{2}} R_{\text{diff}}^3} \prod_{i=x,y,z} \exp\left(-\frac{(i - s_i)^2}{R_{\text{diff}}^2}\right) ds_i , \quad (7.17)$$

where  $i = x, y, z$ . Using a change of variables:

$$u_i = \frac{i - s_i}{R_{\text{diff}}} \quad (7.18)$$

$$\therefore ds_i = -R_{\text{diff}} du_i .$$

Eq. 7.17 becomes:

$$n_{\text{exact}}(x, y, z, \gamma, t) = \frac{n_0}{64\pi^{\frac{3}{2}}} \prod_{i=x,y,z} \int_{\frac{i-2}{R_{\text{diff}}}}^{\frac{i+2}{R_{\text{diff}}}} \exp(-u_i^2) du_i . \quad (7.19)$$

From the definition of the error function:

$$\text{erf}(a) = \frac{2}{\sqrt{\pi}} \int_0^a \exp(-t^2) dt . \quad (7.20)$$

The analytical solution can be simplified to:

$$n_{\text{exact}}(x, y, z, \gamma, t) = \frac{n_0}{64\pi^{\frac{3}{2}}} \prod_{i=x,y,z} \int_{\frac{i-2}{R_{\text{diff}}}}^0 \exp(-u_i^2) + \int_0^{\frac{i+2}{R_{\text{diff}}}} \exp(-u_i^2) \quad (7.21)$$

$$= \frac{n_0}{512} \prod_{i=x,y,z} \text{erf}\left(\frac{i+2}{R_{\text{diff}}}\right) - \text{erf}\left(\frac{i-2}{R_{\text{diff}}}\right) .$$

Fig. 7.6 shows the time it takes for the numerical solution of the electron energy distribution to ‘converge’ to the analytical solution (Eq. 7.21) for a situation with the same parameters as Fig. 7.5 but including energy losses due to synchrotron radiation. It can be noted that the numerical solution tends to under-predict the analytical solution before converging, where the convergence time is proportional to the distance from the source (top-panel), diffusion suppression factor (middle-panel) and inversely proportional to the energy (bottom panel). The blue dashed line in the middle panel shows the numerical solution for  $\chi = 0.01$  with a finer time and spatial resolution. The convergence time for the fine ( $dx = 0.2$  pc,  $dt = 0.08$  yr) and coarse ( $dx = 2$  pc,  $dt = 8$  yr) resolution are  $\approx 0.4$  kyr and  $\approx 12.8$  kyr respectively. Note that the numerical solution starts to diverge after 30 kyr for  $\chi = 0.1$  and electron energy of 10 TeV (middle-panel). Divergence occurs when the variance radius  $R_{\text{var}} = \sqrt{6Dt}$  is approximately half the width of the grid, i.e. the time it takes electrons to reach the simulated boundary. For the aforementioned example, this occurs at approximately 10 kyr. Therefore, the numerical solution must employ a grid size larger than the diffusion variance radius.

Fig. 7.7 compares the analytical solution of the electron energy distribution (Eq. 7.21) and the energy distribution predicted by the numerical solution for ages 20 kyr and 40 kyr with the same parameters as per Fig. 7.5. The numerical solution is able to match the critical energies (the maximum energy of electron due to energy losses, see Eq. 5.24) of  $\approx 70$  TeV and  $\approx 35$  TeV after 20 kyr and 40 kyr respectively. The 20 kyr and 40 kyr numerical solution at a distance of 5 pc from the accelerator follows the analytical solution. However, the numerical solution under-predicts the electron energy distribution for energies  $\lesssim 0.1$  TeV at a distance of 10 pc and 15 pc. In these cases, the  $d = 10$  pc and  $d = 15$  pc numerical solutions for electrons with energies  $\lesssim 0.1$  TeV have not yet ‘converged’ to the analytical solution. However, these electrons will interact with the CMB via IC interactions to produce photons with energies less than 100 MeV (see Eq. 2.67) which lies at the lower end of *Fermi*-LAT’s sensitivity and flux points extracted from HESS J1825-137 (see Fig. 2.7). A finer grid resolution and time step would be needed



Figure 7.6: Evolution of the impulsive electron energy density distribution for the analytical solution (filled dots) and numerical solution (solid lines) with the same parameters to Fig. 7.5. The top panel shows the evolution at distance 5 pc and 10 pc from the source. The middle panel compares the evolution for a situation where  $\chi = 0.01$  and  $\chi = 0.1$ . The blue dashed line represents the numerical solution for  $\chi = 0.01$  with a time and spatial resolution of  $dt = 0.08$  yr and  $dx = 0.2$  pc respectively. The bottom panel compares the evolution for electrons with energy  $E = 0.1$  TeV and 10 TeV.

for the numerical solution to predict the analytical solution at these energies as seen in Fig. 7.6. However, this is left to future work as the focus of this thesis is on TeV electron energies.

## 7.2 Advection

Section 7.1 only considered a simple case of isotropic diffusion, where the diffusion tensor in Eq. 7.1 becomes a scalar ( $\overline{\overline{D}} = D$ ). In this case, the overall net motion of the electron population is zero, i.e. the average position of the electrons does not change (see Fig. 7.5). However, this is not always the case. Consider an impulsive injector of cosmic rays moving at velocity  $v$  in the laboratory frame (see the example in Fig. 7.8). The average position of cosmic rays remains constant in the reference frame of the injector. While in laboratory



Figure 7.7: Energy distribution of electrons 20 kyr (*top*) and 40 kyr (*bottom*) after an impulsive accelerator injects electrons into a system with the same parameters as Fig. 7.5. The electron energy distribution of electrons is taken 5 pc (red), 10 pc (green) and 15 pc (blue) from the accelerator with the analytical and numerical solutions being represented by the circles and solid lines respectively. The vertical black dotted lines represents the critical energy  $E_{cr}$  of electrons (see Eq. 5.24).

frame, the average position of cosmic rays changes with time where the overall bulk particle flow is defined as advection.

Anisotropic diffusion describes a situation where cosmic rays have a preferential direction of diffusion. This can be due to the presence of strong magnetic field lines, inhibiting transport perpendicular to the magnetic field (see Malkov et al., (2013); Nava and Gabici, (2013); Lazarian et al., (2023)) or some asymmetric force as typically seen in PWN. If diffusion is anisotropic then the second term in Eq. 7.1 becomes:

$$\left(\frac{\partial n}{\partial t}\right)_{\text{diff}} = \nabla \cdot (\overline{D} \cdot \nabla n) = \nabla \overline{D} \cdot \nabla n + \overline{D} \cdot \nabla^2 n . \quad (7.22)$$

Note that Eq. 7.22 is similar to the transport equation that considers both advection and isotropic diffusion:

$$\left(\frac{\partial n}{\partial t}\right)_{\text{diff+adv}} = \nabla \cdot (n \mathbf{v}_A) + D \nabla^2 n . \quad (7.23)$$

i.e. anisotropic diffusion can be approximated by diffusion isotropic diffusion with an advective component (as in the case of Fig. 7.8).

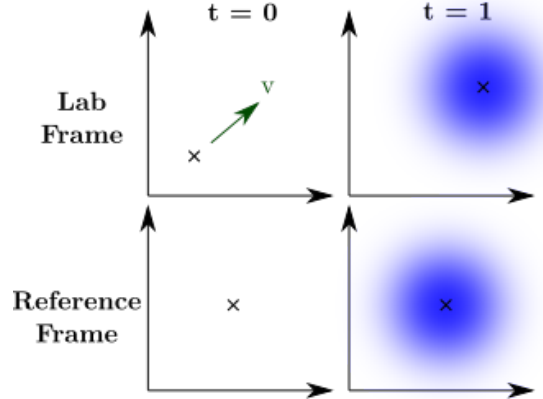


Figure 7.8: Advection of electrons in the lab frame due to impulsive injector (cross) moving at velocity  $v$  in lab frame.

Several astrophysical environments show a preferential direction of particle transport. For example, the geometry of SNRs and the surrounding medium can affect the transport of protons out of the system and the subsequent shape of the SNR (e.g. Meyer et al., (2015); Griffeth Stone et al., (2021)). Such SNRs include the young SNR G1.9+0.3, SNR G296.5+10.0 and the Cygnus loop nebula. Advection may be of particular importance to PWNe. For example the asymmetric gamma-ray morphology towards PWN HESS J1825-137 (H.E.S.S. Collaboration et al., 2019) implies a bulk motion of particles towards lower Galactic longitudes with total velocity ( $v = v_{\text{adv}} + v_{\text{diff}}$ ) of  $0.01c$  (H.E.S.S. Collaboration et al., 2019). In general, it has been proposed that advection dominates the particle transport close to the pulsar, while diffusion dominates the outer reaches of the nebula (Giacinti et al., 2020; Recchia et al., 2021). This section will describe the finite difference techniques used to solve Eq. 7.1 that includes a bulk advective transport of electrons.

### 7.2.1 Numerical Solution

The advective component of Eq. 7.1 is:

$$\left( \frac{\partial n}{\partial t} \right)_{\text{advection}} = -\nabla \cdot (nv_A) , \quad (7.24)$$

where  $v_A$  is the velocity of the bulk flow. Taking the simple case where  $v_A$  is constant over time and both energetically and spatially independent, Eq. 7.24 becomes:

$$\left( \frac{\partial n}{\partial t} \right)_{\text{advection}} = -v_A \nabla n . \quad (7.25)$$

For a scenario considering advection and isotropic diffusion, diffusion is the dominant particle transport process for higher energy particles (when  $R_{\text{diff}} > v_a t$ ) and advection dominating at lower energies ( $R_{\text{diff}} < v_a t$ ). For the 3D grid described in Section 7.1.2, the advective change in the electron energy distribution due to the surrounding voxels in time  $\Delta t$  is described by (see Eq. C.26):

$$\left( \frac{\partial n}{\partial t} \right)_{\text{advection}} \Big|_{x, y, z}^t = -v \frac{\Delta t}{\Delta x} \sum_{\{i=x, y, z\}} \begin{cases} \left( n_{i+\Delta i}^t - n_i^t \right), & v_i < 0 \\ \left( n_i^t - n_{i-\Delta i}^t \right), & v_i > 0 \end{cases} , \quad (7.26)$$

where the forward difference method (i.e. using cells  $i$  and  $i + \Delta i$  to approximate the derivative) is used when  $v_i < 0$  and the backward difference method (i.e. using cells  $i$  and  $i - \Delta i$ ) is used when  $v_i > 0$ .

Using Von Neumann stability analysis (see Eq. C.32), Eq. 7.26 is stable when:

$$\Delta t \leq \frac{\Delta x}{|v|} . \quad (7.27)$$

i.e. the distance travelled by a cosmic ray in one time step must be less than the size of one voxel.

### 7.2.2 Analytical Solution

Consider 1D advection, the analytical solution to Eq. 7.24 is simply:

$$n(x, t) = n(x - vt, t = 0) . \quad (7.28)$$

i.e. by assuming  $v_A$  is constant, advection is simply a translation in space. However, the discretization of space can lead to dispersion in the numerical solution. If  $\Delta t = \Delta x/v$ , electrons are translated exactly one voxel for each time step as shown in the upper panels of Fig. 7.9. But when  $\Delta t < \Delta x/v$ , electrons are transported less than the voxel width and the numerical solution effectively begins to ‘disperse’ particles as shown in the lower panels of Fig. 7.9.



Figure 7.9: The application of finite difference methods for an initial distribution following distribution ( $n(-0.5 \leq x < 0.5) = 4$ ) at  $t = 0$  with velocity  $v = 1$ . The voxel width ( $\Delta x = 1$ ) remains constant while the time steps are 1 (top) and 0.5 (bottom).

To understand the origins of the dispersion, consider Eq. 7.25 where the time derivative is replaced by the forward difference (see Eq. C.5a) and the space derivative has been replaced by the backwards derivative (i.e. when  $v > 0$ ):

$$\begin{aligned} \frac{n_i^{t+\Delta t} - n_i^t}{\Delta t} &= -\frac{v}{\Delta i} (n_i^t - n_{i-\Delta i}^t) \\ \frac{1}{2\Delta t} (n_i^{t+\Delta t} + n_i^{t+\Delta t} - n_i^{t-\Delta t} + n_i^{t-\Delta t} - 2n_i^t) &= -\frac{v}{2\Delta i} (2n_i^t - n_{i-\Delta i}^t - n_{i-\Delta i}^t - n_{i+\Delta i}^t + n_{i+\Delta i}^t) \\ \frac{1}{2\Delta t} ([n_i^{t+\Delta t} - n_i^{t-\Delta t}] + [n_i^{t+\Delta t} + n_i^{t-\Delta t} - 2n_i^t]) &= -\frac{v}{2\Delta i} ([n_{i+\Delta i}^t - n_{i-\Delta i}^t] - [n_{i+\Delta i}^t + n_{i-\Delta i}^t - 2n_i^t]) . \end{aligned} \quad (7.29)$$

Similarly, if the spatial derivative Eq. 7.29 is approximated by the backward difference (when  $v < 0$ ):

$$\begin{aligned} \frac{n_i^{t+\Delta t} - n_i^t}{\Delta t} &= -\frac{v}{\Delta i} (n_{i+\Delta i}^t - n_i^t) \\ \frac{1}{2\Delta t} ([n_i^{t+\Delta t} - n_i^{t-\Delta t}] + [n_i^{t+\Delta t} + n_i^{t-\Delta t} - 2n_i^t]) &= -\frac{v}{2\Delta i} ([n_{i+\Delta i}^t - n_{i-\Delta i}^t] + [n_{i+\Delta i}^t + n_{i-\Delta i}^t - 2n_i^t]) . \end{aligned} \quad (7.30)$$

In the continuous limit:

$$n_i^{t+\Delta t} - n_i^{t-\Delta t} = 2 \lim_{\Delta t \rightarrow 0} \Delta t \frac{\partial n}{\partial t} \Big|_i \quad (7.31a)$$

$$n_{i+\Delta i}^t - n_{i-\Delta i}^t = 2 \lim_{\Delta i \rightarrow 0} \Delta i \frac{\partial n}{\partial i} \Big|_i \quad (7.31b)$$

$$n_i^{t+\Delta t} + n_i^{t-\Delta t} - 2n_i^t = \lim_{\Delta t \rightarrow 0} \Delta t^2 \frac{\partial^2 n}{\partial t^2} \Big|_i \quad (7.31c)$$

$$n_{i+\Delta i}^t + n_{i-\Delta i}^t - 2n_i^t = \lim_{\Delta i \rightarrow 0} \Delta i^2 \frac{\partial^2 n}{\partial i^2} \Big|_i , \quad (7.31d)$$

and Eq. 7.29 and Eq. 7.30 become:

$$\frac{\partial n}{\partial t} + v \frac{\partial n}{\partial x} = \frac{v \Delta x}{2} \frac{\partial^2 n}{\partial x^2} \mp \frac{\Delta t}{2} \frac{\partial^2 n}{\partial t^2} . \quad (7.32)$$

By taking the time derivative of Eq. 7.25:

$$\frac{\partial^2 n}{\partial t^2} = -v \frac{\partial}{\partial t} \left[ \frac{\partial n}{\partial x} \right] = -v \frac{\partial}{\partial x} \left[ \frac{\partial n}{\partial t} \right] = v^2 \frac{\partial^2 n}{\partial x^2} , \quad (7.33)$$

and placing it into Eq. 7.32:

$$\begin{aligned} \frac{\partial n}{\partial t} + v \frac{\partial n}{\partial x} &= \frac{v \Delta x}{2} \frac{\partial^2 n}{\partial x^2} \mp \frac{v^2 \Delta t}{2} \frac{\partial^2 n}{\partial x^2} \\ &= \frac{v \Delta x}{2} \left( 1 \mp v \frac{\Delta t}{\Delta x} \right) \frac{\partial^2 n}{\partial x^2} \\ &= D' \frac{\partial^2 n}{\partial x^2} , \end{aligned} \quad (7.34)$$

where:

$$D' = \frac{v \Delta x}{2} \left( 1 \mp v \frac{\Delta t}{\Delta x} \right) , \quad (7.35)$$

represents the introduced dispersive component. Now consider a 1D scenario that includes both advection and diffusion in this mathematical form:

$$\frac{\partial n}{\partial t} + v \frac{\partial n}{\partial x} = -(D - D') \frac{\partial^2 n}{\partial x^2} . \quad (7.36)$$

When  $D' \ll D$ , dispersion can be considered negligible compared to diffusion.

Any application of advection to HESS J1825-137 in this thesis will consider the same parameters as used in Fig. 7.5 ( $\Delta x = 2$  pc,  $\Delta t = 8$  yr,  $\chi = 0.1$ ,  $D_0 = 3 \times 10^{27}$  cm $^2$ s $^{-1}$  and  $B = 3$  pG) with an additional advective velocity of  $0.002c$  (see Chapter 8). Therefore, dispersion is negligible compared to diffusion for electrons with energy  $\gg 10^{-3}$  TeV. The resultant photon from a  $10^{-3}$  TeV electron interacting with the CMB via inverse Compton interactions will have energy  $\approx 10^{-8}$  TeV. Consequently, the dispersion due to the application of finite difference techniques to advection is negligible to the electron and gamma-ray energy range considered in this thesis.

This dispersion effect can be seen in the top panel of Fig. 7.10, where electrons are injected at  $x = 0$  and are transported only through advection at speed  $v = 0.002c$ . After



Figure 7.10: Advection and diffusion of the electron number density with velocity  $v = 0.002c$  with identical parameters as per Fig. 7.5. (top) Dispersion of electrons for an advection-only scenario. (middle) A comparison of the 1D diffusive variance radius ( $R = \sqrt{2Dt}$ ) and the radius containing 68% of electrons after advection ( $R_\sigma$ ) for an advection-only, diffusion only and diffusion + advection scenarios at different ages of the system. (bottom) The numerical (solid lines) and analytical (dots) electron number density distribution at  $t = 40 \text{ kyr}$  for electron energies  $E = 0.1$  and  $10 \text{ TeV}$ .

40 kyr, electrons have dispersed with the mean position centred on the voxel corresponding to  $d = vt$  with a dispersive radius  $R_\sigma \approx 5 \text{ pc}$  containing 68% of electrons. The middle panel of Fig. 7.10 compares the 1D diffusive variance radius ( $R = \sqrt{2Dt}$ ) with  $R_\sigma$  for an advection-only scenario, diffusion-only scenario and a diffusion + advection scenario. For electrons within the energy range of interest,  $R_{\sigma, \text{adv}}$  is negligible compared to  $R_{\sigma, \text{diff}}$ . Thus  $R_{\sigma, \text{diff+adv}}$  follows the 1D diffusive variance radius. Finally, the bottom panel of Fig. 7.10 compares the numerical solution of diffusion + advection scenario with the analytical solution:

$$n_{\text{diff+adv}}(E, t, x, v) = n_{\text{diff}}(E, t, x - vt) , \quad (7.37)$$

for energies  $E = 0.1$  and  $10 \text{ TeV}$  and age  $t = 40 \text{ kyr}$ .

Finite difference methods will now be applied to 2D advection with parameters similar to Fig. 7.5 ( $\Delta x = 2 \text{ pc}$ ,  $\Delta t = 8 \text{ yr}$ ,  $\chi = 0.1$ ,  $D_0 = 3 \times 10^{27} \text{ cm}^2 \text{s}^{-1}$  and  $B = 3 \mu\text{G}$ ) and an advective component  $v = [0.002c, 0.002c]$  as applied to HESS J1825-137. Following Eq. 7.37, the analytical solution for diffusion + advection is:

$$n_{\text{diff+adv}}(E, t, \mathbf{r}, \mathbf{v}) = n_{\text{diff}}(E, t, \mathbf{r} - \mathbf{v}t) , \quad (7.38)$$

where  $\mathbf{r} = [x, y, z = 50]$ . The numerical solution is able to match adequately the analytical solution as shown in the top panels of Fig. 7.11.



Figure 7.11: Electron injection into a 2D grid at  $x = y = t = 0$  and experiencing diffusion and advection with  $v = [0.002c, 0.002c]$ . (Top) The number density distribution after 40 kyr. The black and yellow dashed circles represent the 2D variance radius ( $R_{\text{var}}$ ) and the radius containing  $1\sigma = 68\%$  of electrons ( $R_\sigma$ ) respectively. The red circle describes the  $R_\sigma$  containment radius for an advection-only scenario. Finally, the red cross represents the electron source position at  $x = y = 0$  (Bottom) Comparing the numerical solution (lines) and analytical solution (dots, see Eq. 7.38) at  $t = 20$  and 40 kyr along  $y = (vt \pm 1) \text{ pc}$  (dashed horizontal line in the bottom panel). The vertical grey line shows the electron source position at  $x = 0$ .

### 7.3 Summary and Application

In summary, `Multizone` uses finite difference techniques to numerically solve the transport equation in order to predict the electron energy distribution around an accelerator. Isotropic diffusion and spatially independent advection were considered as the main methods of transport. The conditions under which `Multizone` can match the analytical solution were shown and noted that the dispersive effects due to numerical techniques were negligible for the parameters considered here.

Finite difference methods can be used to predict the electron number density in 3D due to advection, where the third dimension is the distance along the line of sight. As discussed in Appendix A, the reverse shock of the associated SNR is influenced by the surrounding ISM, where the time the reverse shock takes to form depends on the amount of ISM gas (Vink, 2020). The reverse shock, in turn, influences the morphology of the PWN and the preferential direction of electron flow. Figure 2. in Chapter 6 shows the presence of dense gas clouds to the north of PSR 1826-1334 in velocity range  $40 - 60 \text{ km s}^{-1}$  ( $3.5 - 4.5 \text{ kpc}$ ). Therefore, the reverse shock will first form to the Galactic north of H.E.S.S. J1825-137 and travel southwards to influence the PWN. Electrons will then be preferentially transported to the Galactic south, resulting the asymmetric gamma-ray morphology seen towards HESS J1825-137. Therefore for simplicity, any modelling of HESS J1825-137 in this thesis will assume a bulk flow of electrons to the Galactic south and zero bulk flow in the line of sight.

**Multizone** will be combined with Nanten data (see Section 4.2.6) and magnetic field models to predict the electron energy distribution around HESS J1825-137 due to pulsar PSR 1826-1334 and the subsequent multi-wavelength morphology. The contamination of nearby TeV gamma-ray source HESS J1826-130 (see Section 2.1.5) due to HESS J1825-137 will be investigated. This is summarised in Chapter 8.

# Chapter 8

## A 3D Diffusive and Advective Model of Electron Transport Applied to the Pulsar Wind Nebula HESS J1825-137

## Statement of Authorship

Title of Paper	A 3D Diffusive and Advection Model of electron Transport Applied to the Pulsar Wind Nebula HESS J1825-131		
Publication Status	<input type="checkbox"/> Published	<input type="checkbox"/> Accepted for Publication	<input checked="" type="checkbox"/> Submitted for Publication
Publication Details	Submitted to MNRAS		

### Principal Author

Name of Principal Author (Candidate)	Tiffany Collins		
Contribution to the Paper	Nanten 10co gas analysis & interpretation Multiwavelength interpretation  writing		
Overall percentage (%)	65%		
Certification:	This paper reports on original research I conducted during the period of my Higher Degree by Research candidature and is not subject to any obligations or contractual agreements with a third party that would constrain its inclusion in this thesis. I am the primary author of this paper.		
Signature	Lyf Collins	Date	22/05/23

### Co-Author Contributions

By signing the Statement of Authorship, each author certifies that:

- i. the candidate's stated contribution to the publication is accurate (as detailed above);
- ii. permission is granted for the candidate to include the publication in the thesis; and
- iii. the sum of all co-author contributions is equal to 100% less the candidate's stated contribution.

Name of Co-Author	Gavin Rowell		
Contribution to the Paper	ISM Interpretation, Multiwavelength interpretation  Review		
Signature	/m	Date	12/12/22

Name of Co-Author	Fabien Voisin		
Contribution to the Paper	Background Code Advice  Review		
Signature	Vorit	Date	15/05/23

Please cut and paste additional co-author panels here as required.

### Co-Author Contributions

By signing the Statement of Authorship, each author certifies that:

- i. the candidate's stated contribution to the publication is accurate (as detailed above);
- ii. permission is granted for the candidate to include the publication in the thesis; and
- iii. the sum of all co-author contributions is equal to 100% less the candidate's stated contribution.

Name of Co-Author	Sabrina Einecke		
Contribution to the Paper	Review 9%		
Signature	Einecke	Date	12-12-2022

Name of Co-Author	Yasuo Fukui		
Contribution to the Paper	Nonten (co1-o) data 1%		
Signature	Fukui	Date	18-May 2023

Name of Co-Author	Hirotoshi Sano		
Contribution to the Paper	Nonten (co1-o) data 1 %		
Signature	Sano	Date	01-05-2023

Name of Co-Author			
Contribution to the Paper			
Signature		Date	

Contribution to the Paper			
Signature		Date	

Name of Co-Author			
Contribution to the Paper			
Signature		Date	

Please cut and paste additional co-author panels here as required.

# A 3D Diffusive and Advective Model of Electron Transport Applied to the Pulsar Wind Nebula HESS J1825-137

T. Collins,<sup>1</sup>★, G. Rowell<sup>1</sup>, F. Voisin<sup>1</sup>, S. Einecke<sup>1</sup>, Y. Fukui<sup>2</sup> and H. Sano<sup>3</sup>

<sup>1</sup>School of Physical Sciences, University of Adelaide, Adelaide 5005, Australia

<sup>2</sup>Department of Physics, University of Nagoya, Furo-cho, Chikusa-ku, Nagoya, 464-8601, Japan

<sup>3</sup>Faculty of Engineering, Gifu University, Yanagido 1-1, Gifu, 501-1193, Japan

Accepted XXX. Received YYY; in original form ZZZ

## ABSTRACT

HESS J1825-137 is one of the most powerful and luminous TeV gamma-ray pulsar wind nebulae (PWNe), making it an excellent laboratory to study particle transportation around pulsars. We present a model of the (diffusive and advective) transport and radiative losses of electrons from the pulsar powering HESS J1825-137 (PSR 1826-1334) using interstellar medium gas (ISM) data, soft photon fields and a spatially varying magnetic field due to the pulsar. Assuming a characteristic age of 21 kyr, PSR 1826-1334 is unable to meet the energy requirements to match the observed X-ray and gamma-ray emission. An older age of 40 kyr requiring 14% of the pulsar's spin-down power and advective flow with a velocity of  $v = 0.002 c$  towards lower Galactic longitudes is able to produce an asymmetric gamma-ray morphology and the multi-wavelength spectral energy distribution towards HESS J1825-137. In addition, a turbulent ISM with magnetic field of  $B = 20 \mu\text{G}$  to  $60 \mu\text{G}$  to the north of HESS J1825-137 (as suggested by ISM observations) is required to prevent significant gamma-ray contamination towards the northern TeV source HESS J1826-130.

**Key words:** cosmic rays - ISM: evolution - gamma-rays: general - X-rays: general - ISM individual (HESS J1825-137) - pulsars: individual (PSR J1826-1334)

## 1 INTRODUCTION

HESS J1825-137 is a luminous pulsar wind nebula (PWN) powered by pulsar PSR 1826-1334 with spin-down power  $\dot{E} = 2.8 \times 10^{36} \text{ erg s}^{-1}$  and characteristic age  $\tau_c = P/2\dot{P} = 21.4 \text{ kyr}$  (Aharonian et al. 2005b; Manchester et al. 2005). The distance to PSR J1826-130 has been estimated to lie at a distance of  $\approx 4.0 \text{ kpc}$  based on dispersion measurements (Taylor & Cordes 1993; Cordes & Lazio 2002). The TeV gamma-ray emission from HESS J1825-137 has characteristic ( $1/e$ ) extension of  $0.66^\circ \pm 0.03^\circ \text{ stat} \pm 0.04^\circ \text{ sys}$ , implying a radius of  $\approx 46 \text{ pc}$  based on a distance of  $4.0 \text{ kpc}$  (H.E.S.S. Collaboration et al. 2019). Owing to its brightness in TeV gamma rays, HESS J1825-137 is an ideal laboratory to study relativistic particle transportation in and around middle-aged PWNe. Several studies (e.g. Porth et al. (2016), Giacinti et al. (2020)) suggest that both diffusive and advective transport mechanisms are required to explain the extended gamma-ray morphology towards PWNe.

Situated  $0.7^\circ$  north of HESS J1825-137 (see Figure 1), HESS J1826-130 is a TeV gamma-ray source and possible accelerator of cosmic rays up to PeV energies (HAWC Collaboration et al. 2019; Cao et al. 2021). Due to its close proxim-

ity to HESS J1825-137, HESS J1826-130 was originally considered an extension of HESS J1825-137 until it revealed it was a separate source of gamma rays (H.E.S.S. Collaboration et al. 2018a; Aharonian et al. 2005a). Two supernova remnants (SNRs) (SNR G018.1-0.1 and SNR G018.6-0.2) lie in the vicinity of HESS J1826-137 (Odegard 1986; Brogan et al. 2006). However, their offset positions and small angular diameters make it unlikely that they are connected to the gamma-ray emission (H.E.S.S. Collaboration et al. 2020). The Eel PWN (PWN G18.5-0.4) and PSR J1826-1256 are associated with HESS J1826-130 based on spatial coincidence (H.E.S.S. Collaboration et al. 2018a). PSR J1826-1256 has a spin-down power of  $3.6 \times 10^{36} \text{ erg s}^{-1}$  and characteristic age of 14 kyr, well within the range of pulsar properties associated with TeV PWNe (Manchester et al. 2005; H.E.S.S. Collaboration et al. 2018b).

Araya et al. (2019) revealed GeV gamma-ray emission  $\sim 2.5^\circ$  to the Galactic south of HESS J1825-137. The same study postulated that the GeV emission from this region originates from cosmic rays accelerated by the SNR or PWN associated with HESS J1825-137 or a star forming region such as the Cygnus Cocoon. Spectral energy distribution (SED) modelling towards the GeV region suggests that the emission may be reflective of an earlier epoch of the PWN or a combination of HESS J1925-137 and nearby compact object LS 5039 (Collins et al. 2021).

\* E-mail: tiffany.collins@adelaide.edu.au

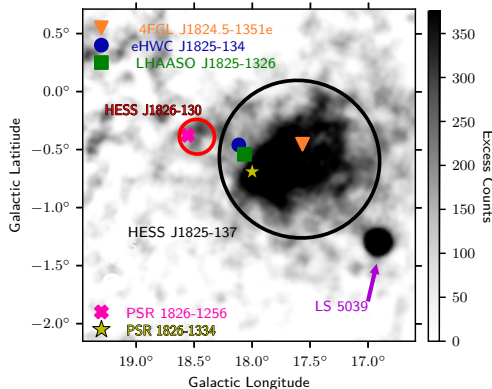


**Figure 1.** HESS excess count map towards HESS J1825-137 (H.E.S.S. Collaboration et al. 2019) overlayed by the regions used to extract the gamma-ray spectra towards HESS J1825-137 (black) and HESS J1826-130 (red). The positions of PSR J1826-1256 and PSR J1826-1334 are shown together with 4FGL J1824.5-1351e (radius= 0.75°), eHWC J1825-134 (radius= 0.36°) and LHAASO J1825-1326 (radius= 0.3°).

The PWN associated with HESS J1825-137 is expanding within the progenitor SNR. A large H $\alpha$  rim-like structure discovered by Stupar et al. (2008) is present towards the south of HESS J1825-137. Voisin et al. (2016) postulated a connection between this rim and another southern H $\alpha$  rim to the progenitor SNR of HESS J1825-137. Both structures lie  $\approx 1.7^\circ$  away from PSR 1826-1334 ( $\approx 120$  pc for a distance of 4 kpc), which is consistent with the predicted SNR radius of  $\approx 130$  pc as suggested by de Jager & Djannati-Atai (2009).

The evolution of the cosmic-ray energy distribution can be described by the Fokker-Planck equation for particle transport (e.g. (Skilling 1975; Cesarsky & Volk 1978)). Henceforth, this equation will be called the transport equation for simplicity. Analytical solutions of the transport equation can be found for specific cases, e.g. an impulsive source in a homogeneous environment (Blumenthal & Gould 1970; Atoyan et al. 1995; Aharonian & Atoyan 1996), however, it must be solved numerically for more complex systems, e.g. continuous source where cosmic-ray propagation and radiative losses vary strongly with position.

Many models of HESS J1825-137 and other environments assume an homogeneous nebula; where high-energy electrons electrons are injected into a symmetric sphere of constant density and magnetic field (e.g. H.E.S.S. Collaboration et al. (2019); Principe et al. (2020)). For example, the work conducted by Van Etten & Romani (2011) treated the transport of electrons from the powering pulsar as a series of uniform, spherical ‘bubbles’ and projected the gamma-ray SED onto a 2D plane. But the asymmetric gamma-ray morphology towards HESS J1825-137 noted by H.E.S.S. Collaboration et al. (2019) suggests a similarly irregular particle density and/or magnetic field around the pulsar.

Our study in this paper numerically solves the transport equation over a 3D Cartesian grid based on Voisin (2017). The spatially-dependent hydrogen number density and magnetic field for each voxel (a 3D pixel) in the grid follows observations of the ISM. The transport of high-energy electrons from PSR J1826-1334 is modelled in order to reproduce the X-ray and gamma-ray morphology, SED and radial profiles towards HESS J1825-137.

## 2 PARTICLE TRANSPORT AND RADIATIVE LOSSES

Upon the release of cosmic rays from an accelerator, such as a SNR or PWN, particles are transported throughout the ISM and experience radiative losses. The number distribution evolution of particles (cosmic-ray protons and electrons),  $n = n(\gamma, \mathbf{r}, t)$ , with Lorentz factor  $\gamma$  in neutral ISM containing inhomogeneous magnetic fields can be described by (e.g. Skilling (1975); Cesarsky & Volk (1978)):

$$\frac{\partial n}{\partial t} = -\nabla \cdot (n \mathbf{v}_A) - \nabla \left( \bar{\overline{D}} \cdot \nabla n \right) + \frac{\partial}{\partial \gamma} (\dot{\gamma} n) - \frac{1}{3} \frac{\partial}{\partial \gamma} (\gamma (\nabla \cdot \mathbf{v}_A)) n \\ + \frac{\partial}{\partial \gamma} \left( \gamma^2 D_{\gamma\gamma} \frac{\partial}{\partial \gamma} \left( \frac{n}{\gamma^2} \right) \right) + S(\gamma, \mathbf{r}, t) \quad (1)$$

The first term in Equation 1 describes the evolution of cosmic-ray density due to advection as a co-moving fluid with velocity  $\mathbf{v}_A = \mathbf{v}_A(\gamma, \mathbf{r}, t)$ . The second term considers the spatial diffusion of cosmic rays as a second rank tensor ( $\bar{\overline{D}} = \bar{\overline{D}}(\gamma, \mathbf{r}, t)$ ); allowing preferential direction of transport. The third term considers losses due to radiative processes and adiabatic expansion. The fourth term represents diffusion resulting from re-acceleration of cosmic rays due to stochastic processes with  $D_{\gamma\gamma}$  being the acceleration rate (e.g. Tsytovich (1966)). Finally  $S(\gamma, \mathbf{r}, t)$  is the cosmic ray source/injection function.

To numerically solve Equation 1, the region of interest was divided into a grid of voxels of with dimensions  $\Delta x \Delta y \Delta z$ . Figure F1 shows a 2D representation of this grid. Finite difference techniques were used to transfer electrons in and out of each cell over time step  $\Delta t$  to model the transport. The following discussion describes how the implemented model treats individual terms in Equation 1.

### 2.1 Diffusion

Over distances smaller than the gyro-radius,  $r_g$ , electrons propagate through the ISM via ballistic motion. In a medium with randomised magnetic turbulence ( $\delta B$ ), electrons scatter and the motion switches to a diffusive regime for distances larger than the gyro-radius (e.g. Prosekin et al. (2015)). For a simple case of isotropic diffusion, the diffusion tensor in Equation 1 becomes a scalar;  $\bar{\overline{D}} \rightarrow D(E, B)$ , where  $E$  is the energy of the cosmic ray and  $B$  is the magnetic field.

Suppression of cosmic-ray diffusion is to be expected towards PWNe and SNRs where magnetic field turbulence is enhanced and the diffusion coefficient,  $D(E, B)$ , can be parameterized by (e.g. Gabici et al. (2007)):

$$D(E, B) = \chi D_0 \left( \frac{E/\text{TeV}}{B/3 \mu\text{G}} \right)^\delta \quad [\text{cm}^2 \text{s}^{-1}] \quad (2)$$

where  $D_0 = 3 \times 10^{27} \text{ cm}^2 \text{s}^{-1}$  is the average Galactic diffusion coefficient at 1 GeV,  $\delta = 0.5$  (in the Kraichnan regime) and the diffusion suppression factor  $\chi$  takes values  $\leq 1$  (Berezinskii et al. 1990). Gabici et al. (2007) found that highly suppressed diffusion ( $\chi \sim 0.01$ ) in molecular clouds can significantly effect the shape of the observed gamma-ray spectrum. The diffusion suppression factor is poorly constrained, but is demonstrated by studies towards SNR W28. Li & Chen (2010), Giuliani et al. (2010) and Gabici et al. (2010) found  $\chi = 0.1, 0.01$  and  $0.06$  respectively. Similarly, Protheroe et al. (2008) showed that the suppression factor towards the star forming region Sgr B2 takes values  $< 0.02$  based on the

radio synchrotron flux. Modelling by H.E.S.S. Collaboration et al. (2019) suggests that towards HESS J1825-137 the Galactic diffusion coefficient takes a value of  $D_0 = 1.4 \times 10^{29} \text{ cm}^2 \text{ s}^{-1}$  at 1 TeV.

The diffusive component of Equation 1 can be described using finite difference techniques:

$$n_{\text{diff}} \Big|_{x,y,z} \frac{\gamma}{t + \Delta t} = \sum_{\{i=x,y,z\}} \left[ \mathcal{D} \left| \begin{array}{c} \gamma \\ i + \Delta i / 2 \end{array} \right. \left( \begin{array}{c} \gamma \\ n \Big| \begin{array}{c} \gamma \\ t - \Delta t \\ i + \Delta i \end{array} \end{array} \right. - n \Big| \begin{array}{c} \gamma \\ t \end{array} \right) \right. \\ \left. + \mathcal{D} \left| \begin{array}{c} \gamma \\ i + \Delta i / 2 \end{array} \right. \left( \begin{array}{c} \gamma \\ n \Big| \begin{array}{c} \gamma \\ t \\ i - \Delta i \end{array} \end{array} \right. - n \Big| \begin{array}{c} \gamma \\ t \end{array} \right) \right] \quad (3)$$

where electrons from the current time step,  $n(\gamma, t)$ , are first allowed to radiatively cool and are then incremented with the net transfer of electrons from the surrounding voxels.  $\gamma_0$  describes the Lorentz factor at time  $t$  before electrons cool to factor  $\gamma$  at time  $t + \Delta t$  and  $\mathcal{D} = D(\gamma, B)\Delta t/\Delta x^2$  is a dimensionless diffusion factor with  $D(\gamma, B)$  being the diffusion coefficient from Equation 2.

By solving Equation 1 for simple isotropic diffusion and accounting for radiative losses in the environment around accelerators, the electron energy distribution in each voxel of the 3D grid is tracked until the age of the system is reached. The subsequent multi-wavelength photon SED, radial profiles and morphology can then be predicted for the regions of interest.

The implemented model tracks the particle motion from voxel to voxel in a 3D grid. As a result, each time step must ensure that electrons travel a maximum displacement less than the size of the voxel. By knowing that  $n > 0$  and for Lorentz Factor  $\gamma$ , the  $x, y, z$  position of the maximum value of  $\mathcal{D}$  remains constant over time:

$$n_{\text{max}}(1 - 6\mathcal{D}) \geq n_{\text{max}}\mathcal{D} \quad (4a)$$

$$\mathcal{D} \leq \frac{1}{7} \quad (4b)$$

where the factor of 6 in Equation 4a comes about from the Cartesian configuration. The time step is dependent on the voxel size  $\Delta t = \Delta x = \Delta y = \Delta z$ :

$$\Delta t = \frac{\Delta i^2}{\mathcal{D}_{\text{max}}} \quad (5)$$

where  $\mathcal{D}_{\text{max}}$  is the maximum value of  $\mathcal{D}$  across the 3D grid.

## 2.2 Advection

The advective component of Equation 1 is given by:

$$\left( \frac{\partial n}{\partial t} \right)_{\text{adv}} = -\nabla \cdot (n \mathbf{v}_A) \quad (6)$$

where  $\mathbf{v}_A$  is the velocity due to the bulk flow of electrons. For simplicity,  $\mathbf{v}_A$  was assumed to be spatially and energy independent across the 3D Cartesian grid. Using the finite difference method as described in subsection 2.1, Equation 6 could be solved numerically via:

$$\left( \frac{\partial n}{\partial t} \right)_{\text{adv}} \Big|_{x,y,z} \frac{\gamma}{t + \Delta t} = -v \frac{\Delta t}{\Delta x} \left\{ \begin{array}{l} \left( n_{i+\Delta i}^t - n_i^t \right), \quad v_i < 0 \\ \left( n_i^t - n_{i-\Delta i}^t \right), \quad v_i > 0 \end{array} \right. \quad (7)$$

where  $v_i$  is the component of advective velocity in the  $x, y$  and  $z$  direction. Equation 7 uses the forward difference method to approximate the derivative in Equation 6 when  $v_i < 0$  and the backward difference method when  $v_i > 0$ . Note that isotropic diffusion with an advective velocity can be approximated as anisotropic diffusion.

For Equation 7 to numerically model the transport of electrons due to advection, the time step must be chosen so that an electron does not travel across more than one voxel in time  $\Delta t$ :

$$\Delta t \geq |v| \Delta t \quad (8)$$

## 2.3 Radiation Losses

High-energy electrons interact with the ISM via inverse Compton interactions on ambient photons, via Bremsstrahlung with interstellar gas and via synchrotron interactions against magnetic fields (see Appendix A). The evolution of the electron number density with Lorentz factor  $\gamma$  due to radiative losses is given by:

$$\frac{\partial n}{\partial t} = \frac{\partial}{\partial \gamma} (\dot{\gamma} n) \quad (9)$$

where the cooling rate,  $\dot{\gamma}(\gamma)$ , is given by Manolakou et al. (2007):

$$\dot{\gamma}(\gamma) = b_s \gamma^2 + b_c (3 \ln \gamma + 18.8) + 5.3 b_b + \sum_{i=1}^4 b_{IC}^i \gamma^2 F_{KN}^i(\gamma) \quad (10)$$

for the case of ionisation or Bremsstrahlung losses in neutral hydrogen. Here,  $i$  sums over all radiation fields (CMB, Infra-red and optical photons),  $b_s, b_c, b_b$  and  $b_{IC}$  are the coefficients for synchrotron losses, Coulomb losses, Bremsstrahlung losses and inverse Compton losses respectively and  $F_{KN}$  is the Klein-Nishina cross section (see Equation A6). The general solution to Equation 9 is:

$$n(\gamma, t + \Delta t) = \frac{\dot{\gamma}_0}{\dot{\gamma}} n(\gamma_0, t) \quad (11)$$

with  $n(\gamma_0, t)$  being the initial energy distribution with Lorentz factor  $\gamma_0$  at time  $t = t$ .

## 2.4 Adiabatic expansion and re-acceleration of electrons

For an energy independent advective velocity  $\mathbf{v}_A$ , losses due to adiabatic expansion is given by:

$$\frac{\partial n}{\partial t} = -\frac{1}{3} (\nabla \cdot \mathbf{v}_A) n \quad (12)$$

Due to the assumption that advection is spatially independent, adiabatic losses were not considered. Moreover, studies such as Tanaka & Takahara (2010) and Porth et al. (2016) that considered spherically symmetric advection concluded that adiabatic losses are dominant over radiation losses for low energy electron ( $< 10$  TeV). Therefore, losses due to adiabatic expansion are not considered here but are left for future work.

The termination shock (TS) of pulsars have been proposed as sites for re-acceleration of electrons through diffusive shock acceleration (DSA). The source term in Equation 2 treats the injected electron spectrum as the spectra obtained after re-acceleration due to the TS by ensuring the voxel size  $\Delta x \Delta y \Delta z$  is larger than the radius of the TS ( $r_{\text{ts}} = 0.1$  pc). Furthermore, magnetohydrodynamics



**Figure 2.** (top) Nanten  $^{12}\text{CO}$ (1-0) integrated intensity in the velocity range  $40 - 60 \text{ km s}^{-1}$  corresponding to  $3.5 - 4.5 \text{ kpc}$  overlaid by green H.E.S.S. contours (at 4, 5, 6, 7, 8 and  $9\sigma$ ). The yellow circle represents the X-ray region A as defined in Uchiyama et al. (2009). The region used to obtain the gamma-ray spectra towards HESS J1825-137 and HESS J1826-130 are shown in black and red respectively. (bottom) The voxels in black are set to a density of  $0.5 \text{ cm}^{-3}$  to represent the bubble that has been swept out by the stellar wind from the progenitor star. Molecular clouds R1-R5 from Voisin et al. (2016) are shown in yellow with the position of PSR J1826-1256 indicated by the red star.

models (e.g. Lemoine & Pelletier (2010); Sironi et al. (2015)) suggest that DSA at the TS is too suppressed for electron acceleration up to energies responsible for the TeV emission seen towards PWN. Hence, the re-acceleration of electrons (fifth term in Equation 2) will not be concluded.

### 3 APPLICATION TO HESS J1825-137

The modelling described in section 2 was then applied to the PWN HESS J1825-137.

#### 3.1 The environment towards HESS J1825-137

##### 3.1.1 Gas morphology, Magnetic Field and Soft Photon Fields

Our model tracked the particle transport over a 3D grid of interstellar medium (ISM) gas with each voxel containing a value for the ISM gas density. Using the Nanten  $^{12}\text{CO}$ (1-0) survey (Mizuno & Fukui

**Table 1.** Parameters describing molecular hydrogen/ISM gas towards HESS J1825-137 and HESS J1826-130 (see Figure 2) using Nanten  $^{12}\text{CO}$ (1-0) data.

Object	$M_H (M_\odot)$	$n_H (\text{cm}^{-3})$	Radius (arcmin)
HESS J1825-137	$1.86 \times 10^6$	170	42
HESS J1826-130	$3.13 \times 10^4$	195	10

2004), the total column density of molecular hydrogen,  $N_{H_2}$ , was traced towards the region of interest using

$$N_{H_2} = X_{12\text{CO}} W_{12\text{CO}} \quad (13)$$

where  $W_{12\text{CO}}$  is the integrated intensity of the gas.  $X_{12\text{CO}} = 1.5 \times 10^{20} \text{ cm}^{-2} \text{ K}^{-1} \text{ km}^{-1} \text{ s}$  is assumed to be constant over the Galactic plane but may vary with galactocentric radius (Strong et al. 2004). The locality of HESS J1825-137 allows the assumption of a constant  $X_{12\text{CO}}$  towards the region of interest. PSR 1826-1334 has a dispersion measure distance of  $3.9 \pm 0.4 \text{ kpc}$  (Taylor & Cordes 1993), thus ISM data in the velocity range of  $40 - 60 \text{ km s}^{-1}$  was considered (Voisin et al. 2016). This is equivalent to distances of  $3.5 \text{ kpc}$  to  $4.5 \text{ kpc}$  as given by the Galactic rotation model (Brand & Blitz 1993). Atomic hydrogen in the same velocity range contributes less than 1% to the total column density towards HESS J1825-137 and was not considered (Voisin et al. 2016; Collins et al. 2021).

Each voxel in the 3D grid (see Figure F1) has a volume of  $\Delta x \Delta y \Delta z$  where  $\Delta z$  is the voxel length in the line of sight. For the purposes of this study, we utilised a  $200 \text{ pc} \times 200 \text{ pc} \times 200 \text{ pc}$  grid consisting of voxels of size  $2 \text{ pc} \times 2 \text{ pc} \times 2 \text{ pc}$ . Assuming that all the gas in the  $40 - 60 \text{ km s}^{-1}$  velocity range lies within the 3D grid, Equation 14 calculated the density in each cubic voxel. The Nanten telescope has a velocity resolution of  $1 \text{ km s}^{-1}$  (Mizuno & Fukui 2004), therefore we assumed that density along the line of sight in the 3D grid is constant for simplicity. The number density of gas within a voxel with average column density of  $N_{H_2}$ , area  $A = \Delta x \Delta y$  and volume  $V = \Delta x \Delta y \Delta z$  was calculated by:

$$n_H = \frac{N_{H_2}}{\Delta z} [\text{cm}^{-3}] \quad (14)$$

$N_{H_2} = 2.8 N_{H_2}$  considers a 20% He component. The mass of gas in each voxel is:

$$M_H = n_H V m_p \quad (15)$$

where  $m_p$  is the mass of a proton.

Figure 2 shows Nanten  $^{12}\text{CO}$ (1-0) integrated intensity in the  $40 - 60 \text{ km s}^{-1}$  range. The average molecular number densities towards HESS J1825-137 and HESS J1826-130 are given in Table 1

Stellar winds from the progenitor star of PSR J1826-1334 will push out gas in the nearby vicinity (Castor et al. 1975). The subsequent supernova explosion creates a ‘bubble’ of hot dense gas around a low-density interior. A region of low density gas in the  $40 - 60 \text{ km s}^{-1}$  velocity range can be seen towards the centre of the TeV emission in Figure 2. To include this, any voxels lying within the extent of the PWN volume (a sphere centered on the pulsar with radius  $0.5^\circ$ ) was set to a density of  $0.5 \text{ cm}^{-3}$  based on the average densities expected within massive stellar wind bubbles (Weaver et al. 1977).

Turbulent motion in interstellar medium results in an amplification of magnetic field, suppressing the diffusion of electrons as they travel through the ISM as given by Equation 2. Figure 6 of Voisin et al.



**Figure 3.** A 2D representation of the magnetic field due to the PWN with the pulsar centred on the origin. The magnetic field is related to the distance from pulsar through Equation 16. Overlaid are the green H.E.S.S. contours at 4, 5, 6, 7, 8 and 9  $\sigma$ .

(2016) shows a three coloured image of the CS(1-0) and NH<sub>3</sub> integrated intensity between 40–60 km s<sup>-1</sup> and the H62 $\alpha$  integrated intensity between 45–65 km s<sup>-1</sup> towards the cloud defined as R1 (see Figure 2 for the position of clouds R1-R5 from Voisin et al. (2016)). Located between HESS J1825-137 and HESS J1826-130, cloud R1 is highly turbulent with minimum magnetic field strength of 21  $\mu$ G as given by Crutcher's relation (see Equation B1). Given the likely physical proximity of this turbulent ISM to HESS J1825-137, cloud R1 may act as a barrier for electrons escaping into HESS J1826-130 from PSR 1826-1334 (Voisin et al. 2016).

Following Van Etten & Romani (2011), the magnetic field due to the PWN was assumed to follow a time-independent power-law with a decreasing magnetic field strength varying with distance  $r$  from the pulsar:

$$B_{\text{PWN}}(r) = B_0 \left( \frac{r}{r_{\text{ts}}} \right)^{-\beta} \quad (16)$$

where  $r_{\text{ts}} = 0.03$  pc is the radius of the termination shock, and  $B_0$  and  $\beta$  are free parameters chosen to match the X-ray and gamma-ray spectra of HESS J1825-137. Van Etten & Romani (2011) suggests  $\beta = -0.69$  for an age of 40 kyr. Note that Van Etten & Romani (2011) considers an additional dependence on the spin-down energy of the pulsar which is not considered in this study for simplicity.

Crutcher's relation (see Equation B1) suggests that the magnetic field contribution of gas with number density  $\leq 300$  cm<sup>-3</sup> is 10  $\mu$ G. As PWNe are expected to evolve inside a low dense bubble formed by stellar winds from the progenitor, only the magnetic field due to the pulsar will initially be considered.

The photon fields around HESS J1825-137 are estimated utilising the radiation field model described by Popescu et al. (2017); the Far-infrared field (FIR) with temperature  $T = 40$ K and energy density  $U = 1$  eV cm<sup>-3</sup>, near infra-red field (NIR) with temperature  $T = 500$  K and energy density 0.4 eV cm<sup>-3</sup> and optical light with temperature  $T = 3500$ K and energy density of  $U = 1.9$  eV cm<sup>-3</sup> (these are similar to the values utilised by Van Etten & Romani (2011), who assumed a FIR field of  $U = 1$  eV cm<sup>-3</sup> with  $T = 32$  K and optical field of  $U = 4$  eV cm<sup>-3</sup> with  $T = 2500$  K).

### 3.1.2 Evolution of electron injection

Cosmic rays (and high energy electrons) injected into the 3D grid at the position of PSR J1826-1334 ( $\ell = 18.0^\circ$  and  $b = -0.69^\circ$ ) and follow an exponential cutoff power-law:

$$S(E, t) = A \left( \frac{E}{1 \text{ TeV}} \right)^{-\Gamma} \exp \left( -\frac{E}{E_c} \right) \quad (17)$$

where  $E_c$  is the cutoff energy and  $A$  is the normalisation factor. For PWN, we assume that point-like particle injection is powered by the spin-down power,  $\dot{E}$ , of the associated pulsar:

$$\dot{E}(t) = \int S(E, t) dE \quad (18)$$

At time  $t$  the spin-down power of the pulsar is given by (see Appendix D):

$$\dot{E}(t) = \dot{E}(t_{\text{age}}) \left[ 1 + (n - 1) \frac{\dot{P}(t - t_{\text{age}})}{P} \right]^{-\Gamma_n} \quad (19)$$

where  $n$  is the braking index of the pulsar with  $\Gamma_n = (n + 1)/(n - 1)$  and  $\dot{E}(t_{\text{age}})$ ,  $P$  and  $\dot{P}$  are the spin-down power, period and spin-down period of the pulsar at the current age  $t_{\text{age}}$ .

## 3.2 Results

As the **Multizone** model allows variation over numerous parameters (e.g. electron injection spectra, ISM parameters, etc.), a single-zone model was utilised to gain insight into HESS J1825-137 before more complex modelling. Single zone modelling takes a region of uniform number density and magnetic field to model the multi-wavelength SED. The results of the single-zone modelling is shown in Appendix C. For an age of 21 kyr, the single-zone model required electrons to follow an exponential cutoff power-law with spectral index  $\Gamma = 2.1$  and cutoff  $E_c = 40$  TeV to match the gamma-ray SED while an older age of 40 kyr required index of  $\Gamma = 2.1$  and cutoff  $E_c = 50$  TeV.

### 3.2.1 Model 1 - Isotropic Diffusion

PWNe are formed by winds generated by a pulsar. By the time electrons reach the termination shock of the pulsar ( $\approx 0.1$  pc), multiple scattering events have randomised the direction of motion. Hence, this study first considered a simple model of isotropic diffusion.

Based on the results of the single-zone model, **Multizone** was used to model the electron energy density towards HESS J1825-137. Electrons were injected by PSR J1826-1334 according to an exponential cutoff power-law spectra ( $\frac{dN}{dE} \propto E^{-\Gamma} \exp(E/E_c)$ ) and then transported by methods described in section 2. The time step used for the finite difference technique is  $\approx 7$  yr. These electrons interact with the soft photon and magnetic fields to produce gamma rays (see Appendix A). Two different ages of 21 kyr and 40 kyr were considered following Van Etten & Romani (2011).

Figure 4 and Figure 5 shows the modelled gamma-ray morphology in different energy bands, the multiwavelength SED and the 1–9 keV X-ray and 0.1–91 TeV gamma-ray radial profiles for the 21 and 40 kyr models respectively as well as corresponding model inputs. To compare the modelled gamma-ray radial profile to observations, a collection area of 0.25 km<sup>2</sup> was used (Benbow 2005) for an observation time of 387 hr as utilised by H.E.S.S. Collaboration

## 6 T. Collins et al.

et al. (2019). Similarly a collection area of  $0.029 \text{ m}^2$  was utilised to compare the modelled X-ray profile to the observed Suzaku radial profile shown in Figure 4 from Uchiyama et al. (2009). Figure 6 shows the modelled SED towards HESS J1826-130 due to electrons escaping from HESS J1825-137 for the 40 kyr model.

Both ages predicted that the gamma-ray morphology towards HESS J1825-137 is symmetric around the powering pulsar with some gamma-ray contribution  $< 1 \text{ TeV}$  via Bremsstrahlung radiation toward the region between HESS J1825-137 and HESS J1826-130 (see Figure 4 and Figure 5). The 40 kyr gamma-ray emission between  $1 - 10 \text{ TeV}$  extends further from the pulsar than the 21 kyr emission. Both ages predicted a steep radial profile for X-rays between  $1 - 9 \text{ keV}$  (see the left lower-middle right panels of Figure 4 and Figure 5). The 21 kyr model was able to replicate the HESS radial profile for gamma rays between  $0.133 - 91 \text{ TeV}$  (see the right lower-middle panel of Figure 4) while the 40 kyr model over-predicted the gamma-ray emission for distances  $> 0.5^\circ$  from the pulsar (see the lower-middle right panel of Figure 5).

The 21 kyr modelled gamma-ray SED was able to match observations with a slight over-prediction ( $\sim 94\%$ ) of the HESS data between  $1 - 10 \text{ TeV}$  as seen in the single-zone models (see Figure C1). While able to predict the normalisation of X-rays produced by synchrotron emission, the model was unable to replicate the slope of the observed Suzaku SED. The 40 kyr SED was able to predict both the X-ray and gamma-ray SED with a similar over-prediction in  $1 - 10 \text{ TeV}$  photons as seen in the 21 kyr model. A slight ‘bump’ is present in the SED for photons around  $50 - 100 \text{ TeV}$  for both ages.

The 21 kyr model required electrons with spectral index  $\Gamma = 2.0$  and cutoff  $40 \text{ TeV}$  to be injected into the ISM with injection luminosity  $3.0 \times 10^{37} \text{ erg s}^{-1}$ . This exceeds the spin-down power of PSR 1826-1334 by a factor of 10. The 40 kyr model had an electron injection luminosity of  $4.0 \times 10^{35} \text{ erg s}^{-1}$  ( $\approx 14\% \text{ of } \dot{E}_{\text{PSR}}$ ) with spectral index and cutoff of 1.9 and  $500 \text{ TeV}$  respectively. Consequently, in our model we will only consider an age of 40 kyr.

The observed gamma-ray contamination of HESS J1826-130 by HESS J1827-137 was estimated by H.E.S.S. Collaboration et al. (2020) to be  $\approx 40\%$  for photon energies below  $1.5 \text{ TeV}$  and  $20\%$  above  $1.5 \text{ TeV}$ . The modelled SED towards HESS J1826-130 can therefore be used to further constrain the model. The SED towards HESS J1826-130 is extracted from the red source region shown in Figure 2 and is defined in § 3.2 of H.E.S.S. Collaboration et al. (2020). The gamma-ray SED towards HESS J1826-130 due to HESS J1825-137 at age 40 kyr is shown in Figure 6 together with the spectrum of HESS J1826-130 and equivalent *Fermi*-LAT source 4FGL J1826.1-1256. The residuals are given by:

$$\text{Residual} = \frac{f_{\text{J1826}} - f_{\text{model}}}{f_{\text{J1826}}} \quad (20)$$

where  $f_i = E^2 \frac{dN_i}{dE}$  ( $i = \text{J1826 or model}$ ) for the SED observed towards HESS J1826-130 and the predicted SED from the model. For photons below  $2 \text{ TeV}$ , the SED towards HESS J1826-130 as a result of HESS J1825-137 exceeds observations. In the model, too many low energy electrons have escaped into the region towards HESS J1826-130 before losing their energy to radiative losses. It is clear that further refinement of the model is required to accurately describe the region surrounding HESS J1825-137.

### 3.2.2 Model 2 - Isotropic Diffusion + Advection

The gamma-ray morphology in Figure 5 shows that Model 1 40 kyr (isotropic diffusion) did not predict the extended TeV gamma-ray morphology towards HESS J1825-137 at lower Galactic longitudes (see blue the arrow in the upper-middle left panel of Figure 5). H.E.S.S. Collaboration et al. (2019) suggested that particle transport within the PWN is a combination of diffusion and an additional advective flow of electrons with a total flow velocity of  $0.01c$ . Thus, Model 2 introduced an advective flow.

The modelled flux, radial profiles and gamma-ray morphology for Model 2 40 kyr with an advective flow of  $v = 0.002$  are shown in Figure 7. A comparison between different advection speeds ( $v = 0.001c$ ,  $v = 0.002c$  and  $v = 0.003c$ ) is shown in Figure F5.

For further comparison of the morphology towards HESS J1825-137, slices were taken across the model maps and compared to the HESS data. The results and the region used to take the slices are shown in Figure 8. An advective velocity of  $0.002c$  was chosen so that the peak in the modelled gamma-ray morphology in energy range  $E < 1 \text{ TeV}$  and  $1 \text{ TeV} < E < 10 \text{ TeV}$  corresponds to the HESS data (see the left-upper panel of Figure F5).

While an additional advective flow lowered the gamma-ray SED towards HESS J1826-130 for energies less than  $2 \text{ TeV}$ , the emission still exceeds H.E.S.S. observations.

### 3.2.3 Model 3 - Isotropic Diffusion + Advection + Magnetic Field towards HESS J1826-130

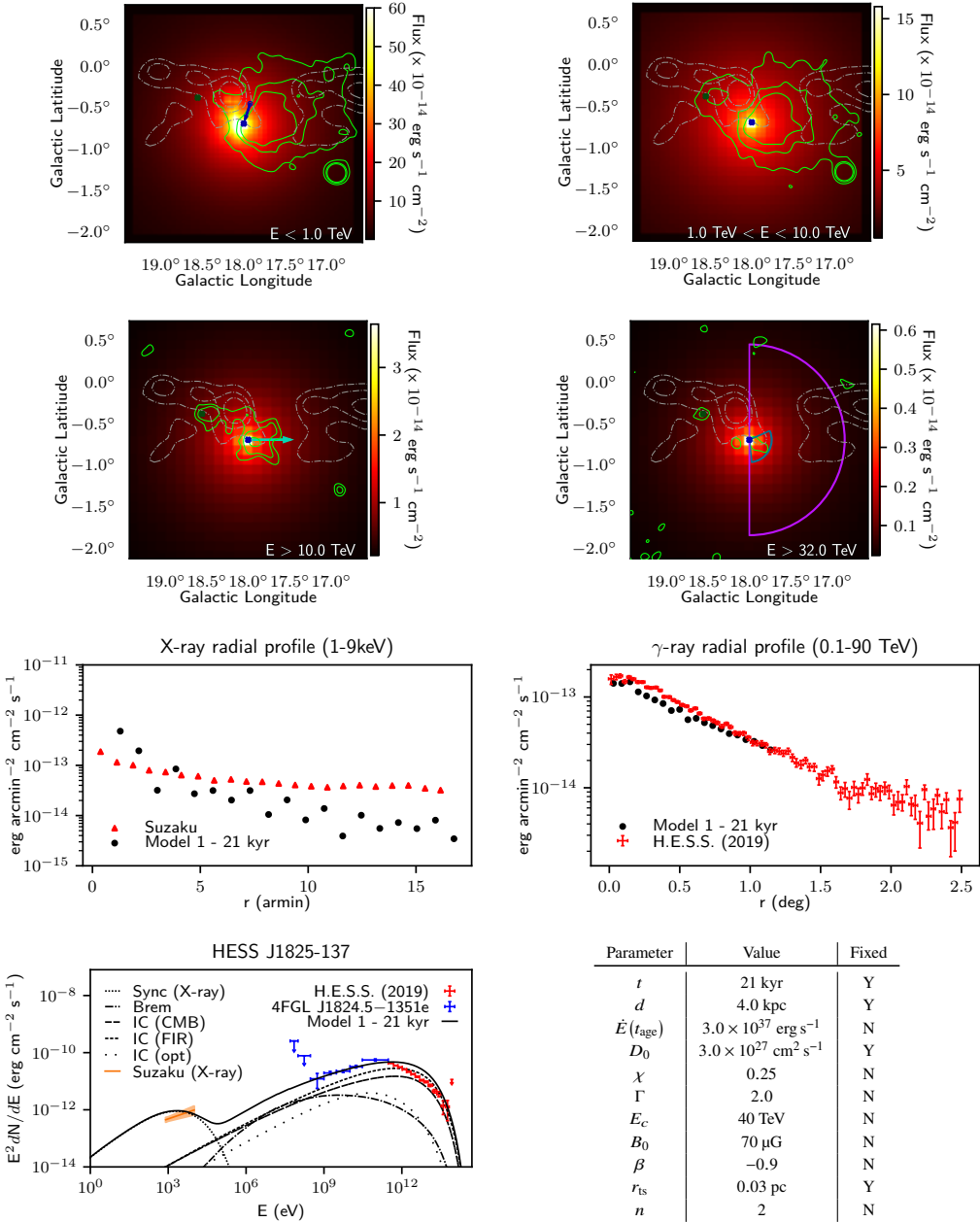
As discussed in § 3.1.1, the turbulent molecular gas between HESS J1825-137 and HESS J1826-130 can act as a barrier for electrons escaping from the PWN. As clouds R1-R5 are positioned in an approximate semi-circle around PSR J1826-1256 (see Figure 2), Model 3 considered a shell of dense gas centred on HESS J1826-130 with inner and outer radii  $0.17^\circ$  and  $0.33^\circ$  respectively with an advective velocity of  $v_A = 0.002c$ .

Figure 9 shows the SED, radial profiles and gamma-ray slices of HESS J1825-137 and HESS J1826-130 for Model 3 with magnetic field strengths of  $B = 20, 60$  and  $100 \mu\text{G}$ . A comparison between the 40 kyr Model 1, isotropic diffusion + magnetic field of  $60 \mu\text{G}$  (Model 3\*) and Model 3  $60 \mu\text{G}$  is shown in Figure 10 as well as the gamma-ray morphology for Model 3. All models have the same parameters as Model 1 40 kyr that is detailed in the table of Figure 5.

## 3.3 Discussion

### 3.3.1 Model 1 - Isotropic Diffusion

The 21 kyr and 40 kyr models were unable to reproduce both the X-ray and gamma-ray radial profiles. For example, the diffusion suppression coefficient,  $\chi$ , could be increased to compensate for the steep X-ray radial profile for the 21 kyr model. Electrons would then escape the PWN at a higher rate and the gamma-ray radial profile will flatten. This can be seen in the 40 kyr model, which assumes a lower value of  $\chi$  than the 21 kyr model. The shallow 40 kyr gamma-ray radial profile indicates that lower energy electrons have started to accumulate near the pulsar, while high-energy electrons rapidly lose their energy through radiative cooling and do not escape far from the pulsar. This is demonstrated in the upper right panel in Figure 5 where the gamma-ray flux below  $10 \text{ TeV}$  is relatively constant over the grid while the flux above  $10 \text{ TeV}$  is constrained to the pulsar. This accumulation is not as apparent in the 40 kyr X-ray radial profile



**Figure 4.** 21 kyr Model 1 - Isotropic diffusion. (*Top & Middle Upper*) Modelled gamma-ray morphology towards HESS J1825-137 in different energy band overlaid by green HESS significance contours (5, 10 and 15 $\sigma$  for  $E < 10 \text{ TeV}$  and 3, 5 and 10 $\sigma$  for  $E > 10 \text{ TeV}$ ) and grey 40, 50 and 60 $\sigma$  Nanten  $^{12}\text{CO}$  integrated intensity contours. PSR 1826-134 and PSR 1826-1256 are shown by the dark blue and green crosses respectively. The direction of advection flow as discussed by H.E.S.S. Collaboration et al. (2019) is shown by the light blue arrow for  $E > 10 \text{ TeV}$ . The current proper motion direction of PSR 1826-1334 is indicated by the dark blue arrow for  $E < 1 \text{ TeV}$  with its projected birth place shown by the empty blue circle (based on age 21 kyr). The regions used to obtain the X-ray and gamma radial profiles are shown as the dark blue and purple wedges respectively in the  $E > 32 \text{ TeV}$ . *Middle Lower - Left* 1 – 9 keV X-ray radial profile in comparison to Suzaku (Uchiyama et al. 2009). *Middle Lower - Right* 0.1 – 90 TeV gamma-ray radial profile compared to red HESS observations (H.E.S.S. Collaboration et al. 2019). *Bottom - Left* Modelled SED towards HESS J1825-137 compared against the orange Suzaku X-ray spectral fit, 4FGL J1824.5-135e flux points (blue) and HESS J1825-137 SED (red). *Bottom - Right* Corresponding model parameters. MNRAS **000**, 1–20 (2022)



**Figure 5.** 40 kyr Model 1 - Isotropic diffusion. Same panel layout as in Figure 4. The projected birth place based on age 40 kyr is shown by the empty blue circle.

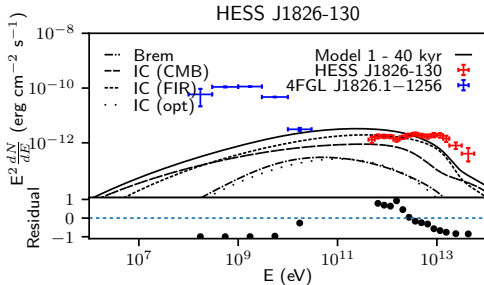


**Figure 6.** Total SED (solid black line) towards HESS J1826-130 (using the region encapsulated by the red circle in Figure 2) from electrons accelerated by PSR 1826-1256 by the 40 kyr Model 1. The GeV and TeV gamma-ray flux points towards HESS J1826-130 are represented by blue and red respectively. The bottom panel shows the residuals of the model as given by Equation 20

and the SED as the regions used in extracting X-ray spectra and radial profile are smaller than the regions used for the gamma-ray analysis (see Figure 2 and upper-middle right panel of Figure 4). The accumulation of lower-energy electrons is also a reflected as a bump in the TeV gamma-ray SED. The bump occurs when synchrotron losses start to dominate at electron energies  $> 9$  TeV, resulting in inverse Compton radiation  $> 6$  TeV (Manolakou et al. 2007; Hinton & Hofmann 2009). This bump is not present for a slightly younger age of 36 kyr as the 40 kyr) as shown in Figure F2. The higher energy TeV emission at age 36 kyr matches the 40 kyr emission while the GeV and lower energy TeV emission is weaker for 36 kyr.

The 21 kyr model required an electron injection luminosity of  $3.0 \times 10^{37}$  erg s $^{-1}$ , exceeding the spin-down power of PSR 1826-1334 ( $\dot{E} = 2.8 \times 10^{36}$  erg s $^{-1}$ ). A higher braking index results in a greater quantity of electrons at earlier times (see Equation 19), reducing the current spin-down power of the pulsar. This results in an accumulation of electrons at lower energy, consequently increasing the gamma-ray flux for photons with energies  $< 1$  TeV (see Figure F3). Similarly the accumulation of electrons increases the X-ray flux for lower photon energies ( $E < 1$  keV). This suggests that the age of HESS J1825-137 lies between 21 kyr and 40 kyr. The 40 kyr magnetic field profile takes values of  $B_0 = 450$   $\mu$ G and  $\beta = -0.7$  (see Equation 16) in comparison to  $B_0 = 400$   $\mu$ G and  $\beta = -0.69$  used in (Van Etten & Romani 2011). Van Etten & Romani (2011) considered an evolving magnetic field  $B \propto \dot{E}(t)$  where the magnetic field takes larger values at earlier times. This could explain the larger  $B_0$  normalisation used in our modelling.

### 3.3.2 Model 2 - Isotropic Diffusion + Advection

An advective component of  $0.002c$  towards lower Galactic longitudes was included into Model 2.

The SED and X-ray radial profile with an advective transportation component remains unchanged to Model 1 40 kyr (as shown in the lower-middle and lower-left panels of Figure 7. Electrons rapidly escape the small ( $r = 0.05^\circ$ ) X-ray region, hence the subsequent X-ray SED and radial profile depends more on the injected electron spectra rather than the method of transport. On the other hand, for both Model 1 and Model 2, the majority of electrons remain within the large ( $0.7^\circ$ ) HESS region leaving the gamma-ray

SED unchanged. However, the electrons in Model 2 have migrated further from the pulsar while remaining within the HESS region. Subsequently, the gamma-ray profile for Model 2 is flatter than Model 1 (lower-middle right panel of Figure 7).

Figure F4 shows the distance that electrons are transported before losing their energy to radiation. It can be seen that advection is the dominant particle transport method for electron energies less than 10 TeV, resulting in IC emission below 1 TeV. Diffusion is dominant for electrons above 10 TeV. However, these high-energy electrons do not travel far from their birthplace before losing their energy to radiative cooling.

The peak in the uncorrelated excess slices is offset from the position of the pulsar as described by H.E.S.S. Collaboration et al. (2019). Our model assumes that the position of the pulsar does not change over its lifetime. However, any kick velocity gained by the pulsar during the progenitor supernova will shift the source of electrons over time. Old, low-energy electrons will then appear to originate in a position offset to the current position of the pulsar while young, high-energy electrons appear to originate at the pulsar (Principe et al. 2020). The direction of proper motion of PSR 1826-1334 is shown by the cyan arrow in the left upper-middle panel of Figure 4, Figure 5 and Figure 7 and lies parallel to the region used to construct the slice morphology in Figure 8. At all energies, the gamma-ray slices for Model 1 appears symmetric around the pulsar position and shows no preferential direction of transportation. However, the HESS uncorrelated excess data indicates that electrons are preferentially transported to lower Galactic longitudes. With the addition of an advective flow of  $0.002c$ , the peak in the 40 kyr gamma-ray slices for photons less than 1 TeV is now offset from the pulsar and follows the shape of the uncorrelated excess. For the  $1 \text{ TeV} < E < 10 \text{ TeV}$  energy band, both Model 1 and Model 2 show a flatter slice profile compared to HESS observations. Electrons resulting from this emission appear to be contained near their birthplace before escaping into the nebula.

Our model assumes that the diffusion index,  $\chi$ , lies within the Kraichnan regime ( $\delta = 0.3 - 0.6$ ) with the index being fixed at  $\delta = 0.5$ . The top-right panel of Figure 8 shows that the modelled gamma-ray slice morphology is broader than that observed by HESS, suggesting that electrons are constrained within the PWN. This suggests that the diffusion index inside the PWN may be somewhat less than the  $\delta = 0.5$  value we assumed, and perhaps to the lower bound for the Kraichnan regime.

By assuming that diffusion was isotropic in (as used in Equation 1), any preferential direction for particle transport was a result of ISM irregularities or advective flow. The highly asymmetric morphology towards HESS J1825-137 could be explained if diffusion is anisotropic with preferential diffusion towards lower Galactic longitudes. However, an anisotropic diffusion model can be approximated by an isotropic diffusion + advection model (Model 2).

### 3.3.3 Model 3 - Isotropic Diffusion + Advection + Magnetic Field towards HESS J1826-130

Here, a spherical shell of increased magnetic field strength around HESS J1826-130 was considered to replicate the turbulent gas towards cloud R1 from Voisin et al. (2016).

The bottom-right panel of Figure 8 shows that cloud R1 lies within the area used to determine the gamma-ray SED of HESS J1825-137. The ratio of synchrotron to inverse Compton flux is proportional to the magnetic field (Aharonian et al. 1997). Hence, as the magnetic field around HESS J1826-130 increases, electrons lose more energy through synchrotron losses and the inverse Compton

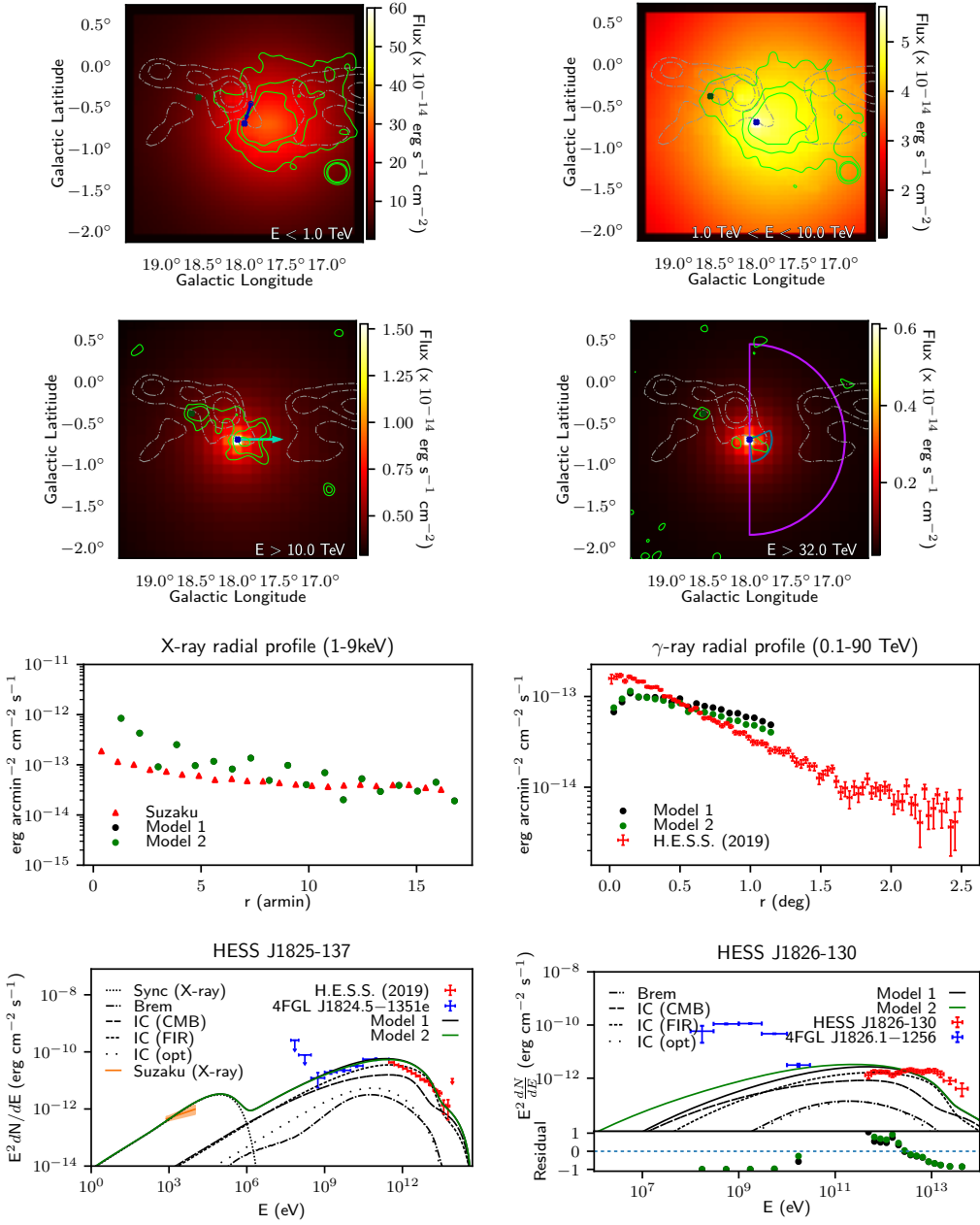


**Figure 7.** 40 kyr Model 2 - isotropic diffusion + advection ( $v = 0.002c$ ) with the same panel layout as in Figure 4. The total multi-wavelength SED and radial profiles for the diffusion + advection model is shown in green while the original diffusion model is shown in black.



**Figure 8.** Slices taken along Galactic longitude with Model 1 (isotropic diffusion (black)) and Model 2 (isotropic diffusion + advection (green)) models at 40 kyr for energy bands  $E < 1 \text{ TeV}$  (top left),  $1 < E < 10 \text{ TeV}$  (top right) and  $E > 10 \text{ TeV}$  (bottom left) vs the H.E.S.S data (H.E.S.S. Collaboration et al. 2019). The peak of Model 2 slices are normalised to the Model 1 slices. (bottom left) Nanten  $^{12}\text{CO}(1-0)$  gas towards HESS J1825-137 in the  $40 - 60 \text{ km s}^{-1}$  velocity band. The region used to take the slice profile is indicated by the black rectangle and the position of PSR 1826-1334 is marked by the orange cross.

ton flux decreases at equivalent gamma-ray energies. This can be seen in the SED for HESS J1825-137 in the lower-middle right panel of Figure 9. This has the effect of improving the match (from 94% to 44% over-prediction) to HESS observations between  $1 - 10 \text{ TeV}$  compared to Model 1 and Model 2 as shown in the bottom-middle-left panel of Figure 10.

The gamma-ray slice profiles are shown in the top and top-middle panels of Figure 9. As the magnetic field around HESS J1826-130 increases, gamma-ray emission less than  $1 < \text{TeV}$  and  $> 10 \text{ TeV}$  remains unchanged at lower longitudes, with a decrease at higher longitudes. Between  $1 \text{ TeV} < E < 10 \text{ TeV}$ , the gamma-ray slice profile drops off at a shallower rate compared to the HESS data at lower Galactic magnitudes. However the gamma-ray emission at higher longitudes, representing the area towards HESS J1826-130, increases proportionally with the magnetic field.

Additionally, the bottom-left panel of Figure 9 indicates that increasing the magnetic field strength around HESS J1826-130 lowers the contamination of HESS J1826-130 by the PWN associated with HESS J1825-137 for energies  $< 2 \text{ TeV}$ . Regions of high magnetic field strength experience a slower rate of diffusion (see Equation 2) and high synchrotron losses. Hence regions of high magnetic field tend to ‘block’ cosmic rays from passing through. The model implies that a minimum magnetic field strength of  $60 \mu\text{G}$  is required to successfully lower the contamination of HESS J1826-130 according to H.E.S.S. observations. The bottom-right panel of Figure 9 shows the

multi-wavelength spectral distribution towards HESS J1826-130. An upper-limit to the X-ray emission towards HESS J1826-130 can be obtained using HEARSAC’s X-Ray background tool utilising ROSAT data (Sabol & Snowden 2019). The estimated synchrotron flux towards HESS J1826-130 combined with the ROSAT X-ray upper limit (obtained from the same region used to extract the SED of HESS J1826-130) implies a maximum magnetic field strength of  $\approx 20 \mu\text{G}$  around HESS J1826-130. This constraint violation suggests that the model is not fully encapsulating the transport of particle between PSR 1826-1334 and HESS 1826-130.

### 3.4 Future Work

Presently, `Multizone` only considers isotropic diffusion and does not account for diffusion parallel and perpendicular to the magnetic field (Drury 1983; Lazarian et al. 2023). The magnetic fields of PWNe are believed to be toroidal in nature (Schmidt et al. 1979; Kothes et al. 2006), hence diffusion is expected to be suppressed perpendicular to the magnetic axis of the pulsar. Additionally, the recent detection of TeV halos (Abeysekara et al. 2017) implies that the region surrounding the PWN experiences a higher diffusion suppression compared to the average Galactic diffusion coefficient (Schroer et al. 2023). While current models of particle transport suggest that advection dominates particle transport within the PWN and diffusion dominates at the edges, this could be described by two dif-



**Figure 9.** Model 3 - 40 kyr + advection + magnetic field of 20  $\mu\text{G}$  (black), 60  $\mu\text{G}$  (green) and 100  $\mu\text{G}$  (purple) around HESS J1826-130.

ferent regions of diffusion suppression. Model 2 and 3 in this study considered spatially-independent advection towards lower Galactic longitudes to explain the asymmetric TeV gamma-ray morphology towards HESS J1825-137. As a result, losses due to adiabatic expansion were neglected. Any future modelling of PWN with Multi-

zone will investigate the effects of spatially-dependent anisotropic diffusion and an azimuthal and radial dependent advective velocity on the gamma-ray morphology and SED. This can then be applied to model the formation of the TeV halo around HESS J1825-137 (Principe et al. 2020).



**Figure 10.** Comparison of the 40 kyr isotropic diffusion - Model 1 (black), isotropic diffusion + magnetic field of 60  $\mu\text{G}$  - Model 3\* (green) and the isotropic diffusion + advection + magnetic field of 60  $\mu\text{G}$  - Model 3. The morphology plots towards HESS J1825-137 for model 3 are shown in the top and upper middle panels.

The transverse velocity of PSR J1826-1334 ( $\approx 400 \text{ km s}^{-1}$ ) implies that the position of the pulsar has shifted approximately 9 pc and 16 pc for ages 21 kyr and 40 kyr respectively (Manchester et al. 2005). Multizone assumed that the position of the pulsar is constant over time which would not be the case for a voxel size of 2 pc. The implementation of a time-dependent source position would not affect the X-ray radial profile and SED due to the small extraction region and the pulsar's magnetic field (see Figure 3). However, the gamma-ray SED would remain unchanged as a result of the large HESS extraction region. Future work will investigate the affects of an evolving source position on the gamma-ray radial profile and morphology of HESS J1825-137. Similarly, the application of Multizone to SNRs would require cosmic rays to be injected by an expanding shell to model diffusive shock acceleration by the expanding SNR.

Multizone is not limited to HESS J1825-137 and can be used to model the transport of cosmic rays (electrons and protons) from other PWN and cosmic ray sources.

flux with the ROSAT X-ray upper limit towards HESS J1826-130, we were able to constrain the magnetic field shell to have maximum strength of  $20 \mu\text{G}$ . This constraint violation suggests that further modelling of the turbulent gas is needed to fully disentangle the particle transport towards HESS J1825-137.

## ACKNOWLEDGEMENTS

T. Collins acknowledges support through the provision of Australian Government Research Training Program Scholarship. The Nanten project is based on a mutual agreement between Nagoya University and the Carnegie Institution of Washington (CIW). We greatly appreciate the hospitality of all the staff members of the Las Campanas Observatory of CIW. We are thankful to many Japanese public donors and companies who contributed to the realization of the project.

This research has made use of the NASA's Astrophysics Data System and the SIMBAD data base, operated at CDS, Strasbourg, France.

## 4 SUMMARY

By modelling the transport of electrons across a 3D Cartesian grid of varying ISM density and magnetic field, we are able to predict the multi-wavelength emission and morphology towards HESS J1825-137. Three models were considered; isotropic diffusion (Model 1), isotropic diffusion + advection (Model 2) and isotropic diffusion + advection + magnetic field towards HESS J1826-130 (Model 3). The best fit 21 kyr and 40 kyr Model 1 consisted of a pulsar injecting electrons into the surrounding medium with injection luminosity of  $3.0 \times 10^{37} \text{ erg s}^{-1}$  and  $4.0 \times 10^{35} \text{ erg s}^{-1}$  respectively. This represents 1000% and 14% of the present spin-down power of the pulsar associated HESS J1825-137, indicating that the true age of the system is older than what the characteristic age suggests. While able to reproduce the multi-wavelength SED, neither model was able to perfectly reproduce the gamma-ray morphological profile described in H.E.S.S. Collaboration et al. (2019) for photons with energies  $1 \text{ TeV} < E < 10 \text{ TeV}$ . However, the morphological profile could be matched for gamma-rays with energies  $< 1 \text{ TeV}$  (with an offset of  $0.3^\circ$  towards higher Galactic longitudes compared to the HESS data) and energies  $> 10 \text{ TeV}$ .

Applying an advective bulk flow (with velocity  $v = 0.002 c$ ) of electrons towards lower Galactic longitudes did not alter the photon SED predicted by Model 1. By taking slices along the predicted flux maps, we were able to compare in detail the gamma-ray morphology towards HESS J1825-137. Model 2 40 kyr is able to reproduce the slice profile shape for photons  $< 1 \text{ TeV}$  and  $> 10 \text{ TeV}$ , however photons with energies  $1 < E < 10 \text{ TeV}$  experience a shallower drop-off compared to the uncorrelated HESS excess slices as revealed by H.E.S.S. Collaboration et al. (2019). This suggests that the parent electrons are constrained within the PWN before escaping into the interstellar medium to form a TeV halo.

As the gamma-ray emission associated with PSR 1826-1334 cannot exceed the observed emission towards HESS J1826-130, HESS J1826-130 can be used to constrain the model. Model 1 and Model 2 were found to over-predict the SED of HESS J1826-130 for photons  $< 1.5 \text{ TeV}$ . By placing a shell of increased magnetic field strength of at least  $60 \mu\text{G}$  around HESS J1826-130, representing the turbulent gas between the two HESS sources (Voisin et al. 2016), the contamination was successfully lowered below the levels closer to those estimated by HESS By combining the modelled synchrotron

## DATA AVAILABILITY

No new data were generated or analysed in support of this research.

## REFERENCES

- Abeysekara A. U., et al., 2017, Science, 358, 911
- Aharonian F. A., Atoyan A. M., 1996, A&A, 309, 917
- Aharonian F. A., Atoyan A. M., Kifune T., 1997, MNRAS, 291, 162
- Aharonian F., et al., 2005a, Science, 307, 1938
- Aharonian F. A., et al., 2005b, A&A, 442, L25
- Araya M., Mitchell A. M. W., Parsons R. D., 2019, MNRAS, 485, 1001
- Atoyan A. M., Aharonian F. A., Völk H. J., 1995, Phys. Rev. D, 52, 3265
- Benbow W., 2005, in Aharonian F. A., Völk H. J., Horns D., eds, American Institute of Physics Conference Series Vol. 745, High Energy Gamma-Ray Astronomy, pp 611–616, doi:10.1063/1.1878471
- Berezhinskii V. S., Bulanov S. V., Dogiel V. A., Ptuskin V. S., 1990, Astrophysics of cosmic rays. John Wiley & Sons, Inc.
- Blumenthal G. R., Gould R. J., 1970, Reviews of Modern Physics, 42, 237
- Brand J., Blitz L., 1993, A&A, 275, 67
- Brogan C. L., Gelfand J. D., Gaensler B. M., Kassim N. E., Lazio T. J. W., 2006, ApJ, 639, L25
- Cao Z., et al., 2021, Nature, 594, 33
- Castor J., McCray R., Weaver R., 1975, ApJ, 200, L107
- Cesarsky C. J., Volk H. J., 1978, A&A, 70, 367
- Collins T., Rowell G., Mitchell A. M. W., Voisin F., Fukui Y., Sano H., Alsulami R., Einecke S., 2021, MNRAS,
- Cordes J. M., Lazio T. J. W., 2002, arXiv e-prints, pp astro-ph/0207156
- Crutcher R. M., Wandelt B., Heiles C., Falgarone E., Troland T. H., 2010, ApJ, 725, 466
- Drury L. O., 1983, Reports on Progress in Physics, 46, 973
- Gabici S., Aharonian F. A., Blasi P., 2007, Ap&SS, 309, 365
- Gabici S., Casanova S., Aharonian F. A., Rowell G., 2010, in Boissier S., Heydari-Malayeri M., Samadi R., Valls-Gabaud D., eds, SF2A-2010: Proceedings of the Annual meeting of the French Society of Astronomy and Astrophysics, p. 313 (arXiv:1009.5291)
- Giacinti G., Mitchell A. M. W., López-Coto R., Joshi V., Parsons R. D., Hinton J. A., 2020, A&A, 636, A113
- Giuliani A., et al., 2010, A&A, 516, L11
- HAWC Collaboration et al., 2019, arXiv e-prints, p. arXiv:1909.08609
- H.E.S.S. Collaboration et al., 2018a, A&A, 612, A1
- H.E.S.S. Collaboration et al., 2018b, A&A, 612, A2
- H.E.S.S. Collaboration et al., 2019, A&A, 621, A116
- H.E.S.S. Collaboration et al., 2020, A&A, 644, A112

- 714 Hinton J. A., Hofmann W., 2009, ARA&A, 47, 523  
 715 Kothes R., Reich W., Uyaniker B., 2006, ApJ, 638, 225  
 716 Lazarian A., Xu S., Hu Y., 2023, Frontiers in Astronomy and Space Sciences,  
 717 10, 1154760  
 718 Lemoine M., Pelletier G., 2010, MNRAS, 402, 321  
 719 Li H., Chen Y., 2010, MNRAS, 409, L35  
 720 Manchester R. N., Hobbs G. B., Teoh A., Hobbs M., 2005, AJ, 129, 1993  
 721 Manolakou K., Horns D., Kirk J. G., 2007, A&A, 474, 689  
 722 Mizuno A., Fukui Y., 2004, in Clemens D., Shah R., Brainerd T., eds,  
 723 Astronomical Society of the Pacific Conference Series Vol. 317, Milky  
 724 Way Surveys: The Structure and Evolution of our Galaxy, p. 59  
 725 Odegard N., 1986, AJ, 92, 1372  
 726 Popescu C. C., Yang R., Tuffs R. J., Natale G., Rushton M., Aharonian F.,  
 727 2017, MNRAS, 470, 2539  
 728 Porth O., Vorster M. J., Lyutikov M., Engelbrecht N. E., 2016, MNRAS,  
 729 460, 4135  
 730 Principe G., Mitchell A. M. W., Caroff S., Hinton J. A., Parsons R. D., Funk  
 731 S., 2020, A&A, 640, A76  
 732 Prosekin A. Y., Kelner S. R., Aharonian F. A., 2015, Phys. Rev. D, 92,  
 733 083003  
 734 Protheroe R. J., Ott J., Ekers R. D., Jones D. I., Crocker R. M., 2008,  
 735 MNRAS, 390, 683  
 736 Sabol E. J., Snowden S. L., 2019, sxbg: ROSAT X-Ray Back-  
 737 ground Tool, Astrophysics Source Code Library, record ascl:1904.001  
 738 (ascl:1904.001)  
 739 Sano H., et al., 2017, ApJ, 843, 61  
 740 Schmidt G. D., Angel J. R. P., Beaver E. A., 1979, ApJ, 227, 106  
 741 Schroer B., Evoli C., Blasi P., 2023, arXiv e-prints, p. arXiv:2305.08019  
 742 Sironi L., Keshet U., Lemoine M., 2015, Space Sci. Rev., 191, 519  
 743 Skilling J., 1975, MNRAS, 172, 557  
 744 Strong A. W., Moskalenko I. V., Reimer O., Digel S., Diehl R., 2004, A&A,  
 745 422, L47  
 746 Stupar M., Parker Q. A., Filipović M. D., 2008, MNRAS, 390, 1037  
 747 Tanaka S. J., Takahara F., 2010, ApJ, 715, 1248  
 748 Taylor J. H., Cordes J. M., 1993, ApJ, 411, 674  
 749 Tsytovich V. N., 1966, Soviet Physics Uspekhi, 9, 370  
 750 Uchiyama H., Matsumoto H., Tsuru T. G., Koyama K., Bamba A., 2009,  
 751 PASJ, 61, S189  
 752 Van Etten A., Romani R. W., 2011, ApJ, 742, 62  
 753 Voisin F., 2017, Environment Studies of Pulsar Wind Nebulae and Their  
 754 Interactions with the Interstellar Medium  
 755 Voisin F., Rowell G., Burton M. G., Walsh A., Fukui Y., Aharonian F., 2016,  
 756 MNRAS, 458, 2813  
 757 Weaver R., McCray R., Castor J., Shapiro P., Moore R., 1977, ApJ, 218, 377  
 758 de Jager O. C., Djannati-Atai A., 2009, in Becker W., ed., Astrophysics  
 759 and Space Science Library Vol. 357, Astrophysics and Space Science  
 760 Library, p. 451 (arXiv:0803.0116), doi:10.1007/978-3-540-76965-  
 761 1\_17  
 762 **APPENDIX A: NON-THERMAL EMISSION**  
 763 This section will provide an overview of leptonic interactions and  
 764 the subsequent photon emission via Synchrotron, Bremsstrahlung  
 765 and inverse Compton Processes.  
 766  
 767 Synchrotron interactions occur when an electron interacts with back-  
 768 ground magnetic fields. The resulting SED emission from a single  
 769 electron with Lorentz factor  $\gamma$  with pitch angle  $\alpha$  to the magnetic  
 770 field  $B$  is given by:  
 771  
 772 
$$P(\nu) = \frac{\sqrt{3}e^3B}{mc^2} \frac{\nu}{\nu_c} \int_{\frac{\nu}{\nu_c}}^{\infty} K_{\frac{5}{3}}(x) dx \quad (\text{A1})$$
  
 773 where  $e$  and  $m$  are the charge and mass of an electron respectively,  
 774  
 775  $K_{\frac{5}{3}}$  is the modified Bessel Function,  $\nu$  is the frequency of the gamma  
 776 ray and  $\nu_c$  is the critical frequency of the emission:  
 777  

$$\nu_c = \gamma^2 \frac{3eB \sin \alpha}{4\pi mc} \quad (\text{A2})$$
  
 778 The inverse Compton gamma-ray SED from an electron with energy  
 779  $E_e$  scattering off a target photon with energy in range  $(\epsilon + d\epsilon)$  and  
 780 number density  $n(\epsilon)$  can be found using:  

$$\frac{dN}{dE_\gamma} = \frac{3\sigma_T mc^3}{4\gamma} \int_{E_\gamma/4\gamma^2}^{E_\gamma} \frac{n(\epsilon) d\epsilon}{\epsilon} f(q, \Gamma) \quad (\text{A3})$$
  

$$f(q, \Gamma) = 2q \ln q + (1 + 2q)(1 - q) + \frac{1}{2} \frac{(\Gamma q)^2}{1 + \Gamma q} (1 - q) \quad (\text{A4})$$
  

$$q = \frac{E_\gamma}{\Gamma(E_e - E_\gamma)}, \quad \Gamma = \frac{4\epsilon\gamma}{m_e c^2} \quad (\text{A5})$$
  
 781 where  $\sigma_T = (3/8\pi)r_0^2$  is the Thompson cross section,  $r_0$  is the  
 782 classical electron radius and  $F_{KN}$  takes account the full Klein-  
 783 Nishina cross section for Inverse Compton scattering (Manolakou  
 784 et al. 2007):  

$$F_{KN} = \frac{1}{u_0} \int_0^\infty f(\gamma, \epsilon) u_\epsilon d\epsilon, \quad f(\gamma, \epsilon) = (1 + 4\gamma\epsilon)^{-\frac{3}{2}} \quad (\text{A6})$$
  
 785 For a Planckian distribution of photon energies,  $F_{KN}$  can be approx-  
 786 imated by:  

$$F_{KN} = (1 + 4\gamma\epsilon_{\text{eff}})^{-3/2}, \quad \epsilon_{\text{eff}} = \frac{2.8kT}{m_e c^2} \quad (\text{A7})$$
  
 787 Finally, the gamma-ray SED from Bremsstrahlung interactions is  
 788 given by:  

$$\frac{dN}{dE_\gamma} = nc \int d\sigma (E_e, E_\gamma, Z) dE_e \quad (\text{A8})$$
  
 789 where  $Z$  is the atomic number of the target material and  $d\sigma$  is the  
 790 bremsstrahlung differential cross section as defined in Blumenthal  
 791 & Gould (1970).  
 792 The coefficients for leptonic losses in Equation 10 are:  

$$- b_s = 1.292 \times 10^{-15} (B/10^3 \mu\text{G})^2 \text{ s}^{-1}$$
 is the synchrotron loss  
 793 coefficient  

$$- b_c = 1.491 \times 10^{-14} (n_H/1\text{cm}^{-3})$$
 is the Coulomb loss coeffi-  
 794 cient  

$$- b_b = 1.37 \times 10^{-16} (n_H/1\text{cm}^{-3}) \text{ s}^{-1}$$
 is the Bremsstrahlung loss  
 795 coefficient  

$$- b_{IC} = 5.204 \times 10^{-20} (u_0/\text{eV}) \text{ s}^{-1}$$
 is the IC loss coefficient with  
 796 the energy density of photons given by  $u_0$   

$$- n_H$$
 is the density of the ambient hydrogen gas

The diffusion radius for electrons (Atoyan et al. 1995):

$$R_{\text{diff}} = \sqrt{\frac{4D(\gamma)}{b_s \gamma (1 - \delta)} \left[ 1 - (1 - \gamma b_s t)^{1-\delta} \right]} \quad (\text{A9})$$

800 **APPENDIX B: MAGNETIC FIELD DUE TO TURBULENT  
801 ISM GAS**

802 The magnetic field due to the ISM gas with number density  $n$  is  
803 given through Crutcher's relation (Crutcher et al. 2010):

$$804 B_{\text{gas}}(n) = \begin{cases} B_{0,\text{gas}}, & n < 300 \text{ cm}^{-3} \\ B_{0,\text{gas}}(n/300 \text{ cm}^{-3})^{\alpha}, & n > 300 \text{ cm}^{-3} \end{cases} \quad (\text{B1})$$

where  $B_{0,\text{gas}} = 10 \mu\text{G}$  and  $\alpha = 0.65$ .

805 **APPENDIX C: SINGLE-ZONE MODELLING**

806 Here we considered a 'single-zone' model, where single-zone mod-  
807 elling takes a region of constant number density and magnetic field  
808 and injects electrons into the centre (Sano et al. 2017; Collins et al.  
809 2021). The final electron energy distribution in the region is found  
810 by solving Equation 1 by only considering radiative losses. The  
811 subsequent gamma-ray energy distribution is then estimated. While  
812 unable to encapsulate the complexity towards HESS J1825-137, a  
813 general insight of the system was gained before more detailed mod-  
814 elling of the morphology and time evolution.

815 **C1 Method**

816 The Suzaku X-ray and HESS gamma-ray SED was extracted using  
817 two different areas by H.E.S.S. Collaboration et al. (2019) and  
818 Uchiyama et al. (2009) with radii  $r \approx 0.7$  and  $0.025$  respectively.  
819 Both regions were centered on the pulsar position. Consequently,  
820 the X-ray and gamma-ray emission must be modelled separately  
821 utilising single zone modelling.

822 Supernovae tend to leave a bubble of low-density gas in the  
823 interstellar medium. Within the extent of the PWN, the density of  
824 both regions was set to  $0.5 \text{ cm}^{-3}$ . A diffusion coefficient of  $1.0 \times$   
825  $10^{29} \text{ cm}^2 \text{s}^{-1}$  was utilised, as proposed by H.E.S.S. Collaboration  
826 et al. (2019). Electrons were injected into the ISM at a constant rate  
827  $\dot{E}$  and followed a power-law spectrum with an exponential cutoff:  
828  $\frac{dN}{dE} \propto E^{-\Gamma} \cdot \exp(E/E_c)$ , where  $\Gamma$  is the spectral index and  $E_c$  is  
829 the cutoff energy. Two different ages were modelled, 21 kyr based  
830 on the characteristic age of the pulsar and 40 kyr based on previous  
831 modelling (Van Etten & Romani 2011).

832 The HESS region adopted a uniform magnetic field of  $5 \mu\text{G}$  as  
833 suggested by Principe et al. (2020) from comparing the estimated  
834 synchrotron emission to the Suzaku X-ray emission. Subsequently,  
835 it was assumed that the smaller X-ray region has a higher magnetic  
836 field strength than the HESS region due to the proximity of the  
837 pulsar and was left as a free parameter.

838 The fits to the SED towards HESS J1825-137 as well as the  
839 input parameters can be seen in Figure C1.

840 **C2 Discussion**

841 Figure C1 shows the modelled SED with corresponding parame-  
842 ters to the gamma and X-ray spectra towards HESS J1825-137 .  
843 The majority of gamma rays in this model are predicted to come  
844 from inverse Compton interactions from the infrared and CMB  
845 photon fields. An electron injection luminosity of  $2 \times 10^{38}$  and  
846  $1 \times 10^{38} \text{ erg s}^{-1}$  is needed to match the gamma-ray spectra at ages  
847 21 and 40 kyr respectively. This is a factor ten times greater than  
848 the spin-down power of PSR 1826-1334 ( $\dot{E} = 2.8 \times 10^{36} \text{ erg s}^{-1}$ ).  
849



Parameter	$t = 21 \text{ kyr}$		$t = 40 \text{ kyr}$		units
	HESS	Suzaku	HESS	Suzaku	
$\dot{E}$	$2 \times 10^{38}$	$8 \times 10^{35}$	$1 \times 10^{38}$	$4 \times 10^{35}$	$\text{erg s}^{-1}$
$d$	4	4	4	4	$\text{kpc}^{\circ}$
$r$	0.70	0.025	0.70	0.025	
$n$	0.5	0.5	0.5	0.5	$\text{cm}^{-3}$
$B$	5	40	5	40	$\mu\text{G}$
$D_0$	$1 \times 10^{29}$	$1 \times 10^{29}$	$1 \times 10^{29}$	$1 \times 10^{29}$	$\text{cm}^2 \text{s}^{-1}$
$\chi$	0.25	0.25	0.1	0.1	
$\Gamma$	2.1	1.9	2.1	1.9	
$E_c$	40	1000	50	1000	$\text{TeV}$

Figure C1. SED for leptonic interactions towards HESS J1825-137 using single-zone modelling. The X-ray and gamma-ray spectra are fitted separately due to the different coverage areas of HESS and Suzaku. The orange line shows the Suzaku match of X-rays between 1–9 keV towards the pulsar associated with HESS J1825-137 (Uchiyama et al. 2009). Blue data points represent the spectrum from the *Fermi*-LAT 4FGL source catalogue towards HESS J1825-137 while the red data shows the H.E.S.S. energy flux towards HESS J1825-137 (H.E.S.S. Collaboration et al. 2019). The top and bottom panels are at ages 21 kyr and 40 kyr respectively. The corresponding model parameters is shown in the table.

The single-zone model assumes a time-independent injection luminosity, whereas the spin-down power of the pulsar decreases over time. The spin-down power of PSR 1826-1334 could have been as high as  $10^{39} \text{ erg s}^{-1}$  at a pulsar age of 1 kyr (see § 3.1.2). Therefore the modeled injection luminosities represents the average electron injection luminosity over the age of the pulsar.

The X-ray emission towards PSR 1826-1334 can be predicted with an injection luminosity of  $8 \times 10^{35} \text{ erg s}^{-1}$  and  $4 \times 10^{35} \text{ erg s}^{-1}$  for the 21 and 40 kyr model respectively. The single-zone model can reasonably predict both the X-ray and gamma-ray SED, yet the X-ray and gamma-ray photon models require different injection spectra for both ages of the system. The single-zone model assumes constant density and magnetic field strength across the region of interest. However, the magnetic field structures towards PWNe have been suggested to be toroidal in nature but the viewing angle results in magnetic fields appearing radially dependent or tangled (Kothes et al. 2006). If the dense clouds towards HESS J1826-130, as seen in Figure 2, lie at the same distance as the pulsar, diffusion will be suppressed towards this region with electrons losing their energy to bremsstrahlung losses. As previously mentioned, the spin-down power of the pulsar decreases over time which has an effect on the

870 injection luminosity of electrons in the ISM. While the single-zone  
 871 model is able to predict the X-ray and gamma-ray SED towards  
 872 HESS J1825-137, it is unable to encapsulate the complexity of the  
 873 PWN.

#### 874 APPENDIX D: DERIVATION OF PULSAR SPIN-DOWN 875 POWER

876 Assuming there is no accretion of matter onto the pulsar, as the  
 877 pulsar ages the angular frequency  $\Omega$  evolves according to:

$$878 \quad \dot{\Omega} = -k\Omega^n \quad (D1)$$

879 where  $n$  is the braking index of the pulsar and  $k$  is just a constant.  
 880 Angular frequency is related to the period of the pulsar through  
 881  $\Omega = 2\pi P^{-1}$ , giving:

$$882 \quad \dot{\Omega} = -\frac{2\pi}{P^2} \dot{P} \quad (D2)$$

883 combining with Equation D1:

$$884 \quad P^{n-2} \dot{P} = (2\pi)^{n-1} k = \text{constant} \quad (D3)$$

$$885 \quad \therefore \dot{P}_0 P_0^{n-2} = \dot{P}(t) P^{n-2}(t) = \dot{P}_{\text{age}} P_{\text{age}}^{n-2} \quad (D4)$$

886 where  $P_0 = P(0)$  and  $P_{\text{age}} = P(t_{\text{age}})$ . Integrating Equation D3 from  
 887 time  $t$  to the current age of the pulsar  $t_{\text{age}}$ :

$$888 \quad \int_t^{t_{\text{age}}} P^{n-2} \frac{dp}{dt} dt = \int_t^{t_{\text{age}}} (2\pi)^{n-1} k dt \quad (D5)$$

$$889 \quad \int_{P(t)}^{P_{\text{age}}} P^{n-2} dP = \int_t^{t_{\text{age}}} (2\pi)^{n-1} k dt \quad (D6)$$

890 Assuming  $n \geq 2$ :

$$891 \quad P^{n-1}(t) = -(n-1) \left[ (2\pi)^{n-1} k \right] (t_{\text{age}} - t) + P_{\text{age}}^{n-1} \quad (D7)$$

892 Utilising Equation D4:

$$893 \quad P(t) = P_{\text{age}} \left[ 1 - (n-1) \frac{\dot{P}_{\text{age}}}{P_{\text{age}}} (t_{\text{age}} - t) \right]^{n-1} \quad (D8)$$

894 The rotational energy of pulsar,  $E_{\text{rot}}$  is related to its angular frequency:

$$895 \quad E_{\text{rot}} = \frac{1}{2} mr^2 \Omega_{\text{age}}^2 = \frac{1}{2} mr^2 \frac{(2\pi)^2}{P_{\text{age}}^2} \quad (D9)$$

896 where  $m$  and  $r$  are the mass and radius of the pulsar respectively.  
 897 Therefore the spin-down of the pulsar can be described by

$$898 \quad \dot{E}(t) = \frac{1}{2} mr^2 (2\pi)^2 (-2) \frac{\dot{P}(t)}{P^3(t)} \quad (D10)$$

899 leading to:

$$900 \quad \dot{E}(t) = \dot{E}_{\text{age}} \left( \frac{P_{\text{age}}}{P(t)} \right)^{n+1} \quad (D11)$$

901 Combing Equation D8 and Equation D11:

$$902 \quad \dot{E}(t) = \dot{E}(t_{\text{age}}) \left[ 1 + (n-1) \frac{\dot{P}(t - t_{\text{age}})}{P} \right]^{-\Gamma_n} \quad (D12)$$

903 where:

$$904 \quad \Gamma_n = \frac{n+1}{n-1} \quad (D13)$$

905 Note that a caveat to Equation D12 is that:

$$906 \quad n \leq 1 - \frac{P}{\dot{P}(t - t_{\text{age}})} \quad (D14)$$

907 Therefore for an age of 21 kyr, PSR J18226-130 requires that  $n \leq 3.03$  and for an age of 40 kyr,  $n \leq 2.07$ .

#### 908 APPENDIX E: SYSTEMATIC VARIATION OF 909 MULTIZONE PARAMETERS

910 Figure E1 and Figure E2 shows the 10% and 20% systematic variation  
 911 of the free parameters,  $\dot{E}$ ,  $\chi$ ,  $\gamma$ ,  $E_c$ ,  $B_0$  and  $\beta$  for the 21 kyr  
 912 and 40 kyr models. These figures show that the spectral index of  
 913 injection electrons,  $\Gamma$ , exerts the most influence on the SED and  
 914 radial profiles than  $\chi$ ,  $B_0$  and  $\beta$ . The X-ray SED and radial profiles  
 915 are more sensitive on the parameters than the gamma-ray emission.  
 916 This is a result of the smaller region used to extract the X-ray and  
 917 SED (see Figure 2 and Figure 4).

918 The modelled X-ray radial profiles for the 21 and 40 kyr models  
 919 are steeper than observations (Uchiyama et al. 2009) indicating  
 920 that the model over-predicts the synchrotron emission closer to  
 921 PSR 1826-1334. This may be corrected by decreasing the rate at  
 922 which the magnetic field drops off with distance from the pulsar  
 923 ( $\beta$ ), allowing electrons to escape the PWN at a faster rate. The outer  
 924 edges of the PWN experiences greater synchrotron losses at the cost  
 925 of TeV gamma-ray emission from IC interactions, flattening out the  
 926 gamma-ray radial profile. This is demonstrated in the 10 and 20%  
 927 variation of  $\beta$  shown in the top row of Figure E1 and Figure E2.  
 928 Alternatively, decreasing the overall magnetic field strength,  $B_0$ ,  
 929 decreases synchrotron losses towards HESS J1825-137 at the cost  
 930 of increasing the gamma-ray to X-ray flux ratio. With flux being  
 931 dependent on the observational area, any changes to the gamma-ray  
 932 and X-ray ratio will be more prominent in the X-ray SED as shown  
 933 in Figure E1 and Figure E2.

934 To better fit the X-ray radial profile, the diffusion suppression  
 935 coefficient towards HESS J1825-137 could be increased to allow  
 936 electrons to escape further from the pulsar before losing their energy  
 937 to synchrotron radiation. High-energy electrons rapidly lose their  
 938 energy to radiative losses and remain close to the pulsar, hence the  
 939 gamma-ray radial profile will flatten as shown in Figure E1 and  
 940 Figure E2. As the region used to extract the X-ray data is small  
 941 ( $< 2pc$ ) compared to the HESS region ( $\approx 49$  pc), electrons quickly  
 942 escape the X-ray region while remaining in the HESS region. Thus  
 943 the X-ray SED far more sensitive to the value of  $\chi$  than the gamma-  
 944 ray SED.

945 Both the radial profiles and SED are very sensitive to the in-  
 946 jected electron spectral index,  $\Gamma$ , as seen in Figure E1 and Figure E2.  
 947 If  $\beta$ ,  $B_0$  or  $\chi$  was altered to fit the observed Suzaku X-ray radial  
 948 profile, the predicted SED from the model will no longer fit to the  
 949 data. In turn, the spectral index can be modified to refit the modelled  
 950 SED. Consequently, the X-ray radial profile will no longer match  
 951 the Suzaku observations.



**Figure E1.** 21 kyr Model 1 as in Figure 4 but with 10% (grey shaded band) and 20% (pink shaded band) variation in parameters.

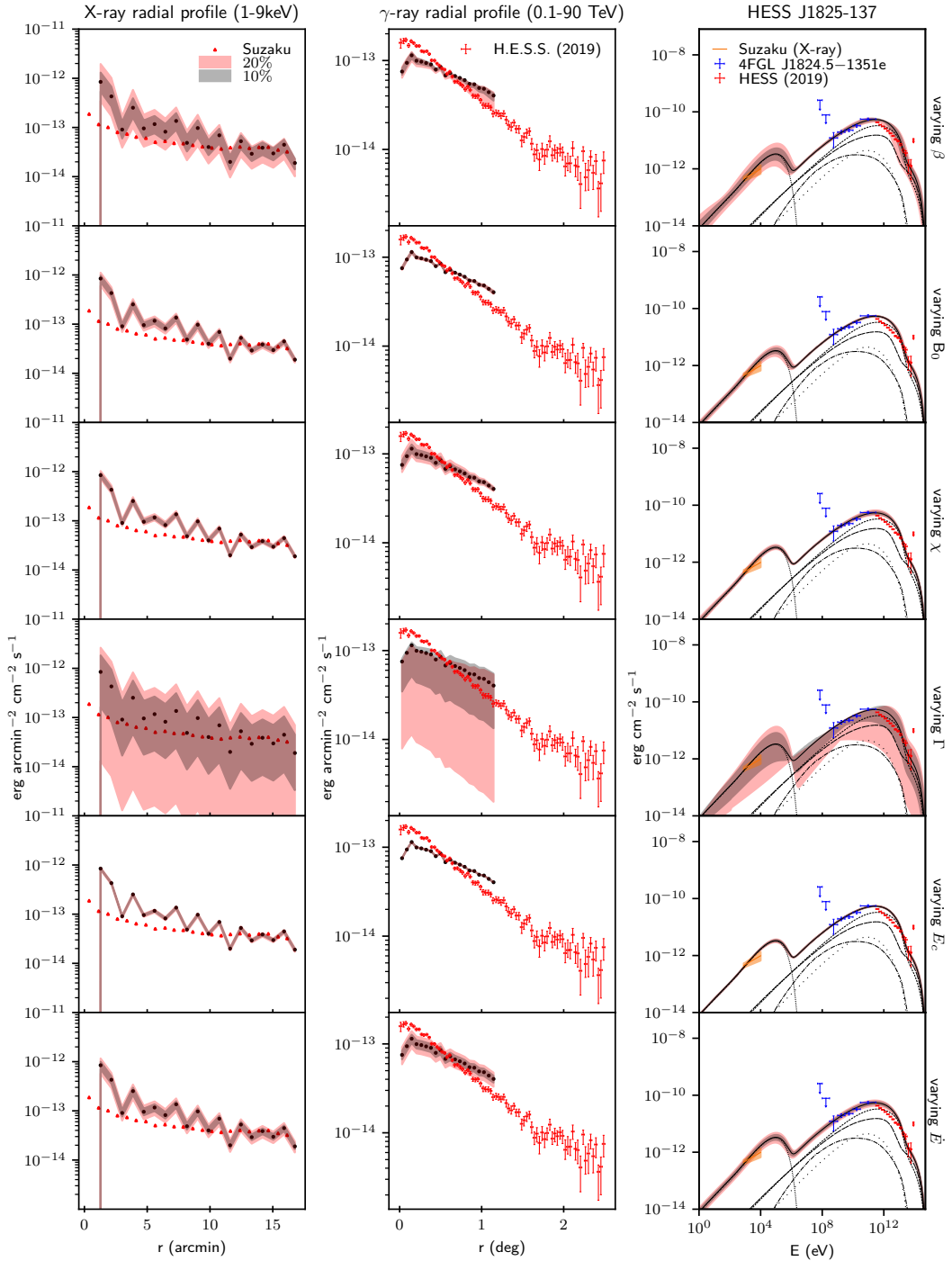


**Figure E2.** 40 kyr Model 2 as in Figure 5 but with 10% (grey shaded band) and 20% (pink shaded band) variation in parameters.

The cutoff energies for the 21 kyr and 40 kyr models are 45 TeV and 500 TeV respectively. As the cutoff energy for an exponential cutoff power-law increases, the energy spectra starts to follow a power-law. Hence, the systematic variation of  $E_C$  is less apparent for 40 kyr than 21 kyr as seen in the fourth row of Figure E1 and Figure E2 respectively.

#### APPENDIX F: ADDITIONAL FIGURES

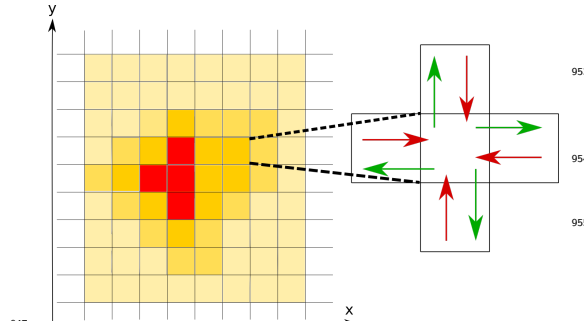


Figure F1: A 2D representation of the 3D grid used to numerically solve the transport equation (Equation 1). The zoomed in cell shows the flux of electrons in (red) and out (green) of the cell in one time step  $\Delta t$ .



Figure F4: The distance that electrons are transported before losing their energy through radiative cooling (synchrotron, inverse Compton and Bremsstrahlung) assuming purely diffusive (solid line) or advective transport (dashed line).

This paper has been typeset from a  $\text{\TeX}/\text{\LaTeX}$  file prepared by the author.



Figure F2: Total SED for a system of age 36 kyr Model 1 shown in green vs the 40 kyr Model 1 shown in Figure 5. The 36 kyr model has the same parameters as the 40 kyr model.



Figure F3: Total SED for a system with the same parameters as the 21 kyr Model 1 but with  $n = 2.0$  (black),  $n = 2.5$  (green) and  $n = 3.0$  (purple).



Figure F5. Comparison of Model 2 with an advective flow velocity of 0.001c (black), 0.002c (green) and 0.003c (purple)

# Chapter 9

## Conclusion and Future Work

This thesis investigated the origin of the X-ray to high-energy gamma-ray emission towards the extended TeV Pulsar Wind Nebula (PWN) HESS J1825-137 and adjacent source HESS J1826-130. PWN constitute the largest source class in the H.E.S.S. galactic plane survey (see Section 3.2.1) and have been identified as possible PeVatron source candidates; a source capable of accelerate cosmic rays greater than  $1 \text{ PeV} = 10^{15} \text{ eV}$  (see Section 2.2.4). The radio to gamma-ray emission towards HESS J1825-137 was modelled by linking cosmic-ray transport theory and radiative losses with ISM data towards HESS J1825-137.

This thesis first investigated the extended GeV emission towards the Galactic-south of HESS J1825-137 (named GeV-ABC) as revealed by Araya et al., (2019). The GeV emission was subdivided into three regions (GeV-A, GeV-B and GeV-C) based on the three peaks observed in the TS map by Araya et al., (2019). Using CO(1-0) data from the Nanten radio telescope, an analysis of the ISM towards GeV-ABC was undertaken in order to identify any association of gas clouds with the GeV emission. It was noted that a dense cloud of gas ( $n \approx 80 \text{ cm}^{-3}$ ) correlated with the physical position of GeV-B in the velocity range  $15 - 30 \text{ km s}^{-1}$  ( $1.6 - 2.8 \text{ kpc}$ ), coinciding with the distance estimate to LS 5039 of 2.5 kpc. The dense cloud also spatially correlated with a region of reduced H $\alpha$  emission and the H $\alpha$  rims detected by Stupar et al., (2008) and Voisin et al., (2016) that are consistent with the radius of the progenitor SNR of HESS J1825-137 ( $r_{\text{SNR}} \approx 120 \text{ pc}$ ).

The radio to gamma-ray emission towards GeV-ABC was then modelled using a single-zone of particles to determine the origin of cosmic rays within this region (see Chapter 6). This study investigated whether cosmic rays originated from the PWN and/or the progenitor SNR associated with HESS J1825-137. It found that the powering pulsar (PSR J1826-1334) must inject more than  $10^{37} \text{ erg s}^{-1}$  of electrons or more than  $10^{39} \text{ erg s}^{-1}$  of protons to power GeV-ABC, compared to the pulsar spin-down power of  $10^{36} \text{ erg s}^{-1}$ . Similarly, the progenitor SNR must inject  $> 10^{51} \text{ erg}$  of protons, compared to the canonical SNR cosmic-ray energy budget of  $10^{50} \text{ erg}$ . Unless the extended GeV reflects an earlier, more powerful epoch of the PWN or the progenitor SNR is a hypernova (with a cosmic-ray energy- budget of  $10^{51} \text{ erg}$ ), an accelerator associated with HESS J1825-137 is unlikely to be sole origin of cosmic rays towards GeV-ABC.

It was also postulated that the nearby binary system LS 5039 - either accretion onto the associated compact object or its progenitor SNR - could result in the cosmic rays that power GeV-ABC (see Chapter 6). It was ascertained through single-zone modelling that to power GeV-ABC, LS 5039 required an injection luminosity greater than the average accretion luminosity ( $\approx 10^{35} \text{ erg s}^{-1}$ ) or a minimum SNR energy budget of  $10^{51} \text{ erg}$ . Moreover, the estimated age of LS-5039 ( $\approx 0.1 - 1 \text{ Myr}$ ) suggests that the SNR would

be merging with the ISM. Therefore, an accelerator associated with LS 5039 by itself is unlikely to be the sole origin of cosmic rays responsible for GeV-ABC. A combination of an accelerator linked to HESS J1825-137 and LS 5039 could explain the GeV emission.

The next part of this thesis modelled a 3D distribution of electrons towards HESS J1825-137 (see Chapter 7) in order to predict the multiwavelength emission seen towards the PWN and to investigate the gamma-ray contamination of the nearby northern TeV source HESS J1826-130. This was achieved by numerically solving the cosmic-ray transport/loss equation over a 3D Cartesian grid of spatially-dependent number density and magnetic field using finite difference techniques (see Chapter 7). The H.E.S.S. Collaboration et al., (2019) suggested that both diffusive transport and advection towards lower Galactic longitudes was required to explain the asymmetric TeV morphology towards HESS J1825-137. Three different models were considered; Model 1 - isotropic diffusion, Model 2 - isotropic diffusion + advection and Model 3 - isotropic diffusion + advection + turbulent gas between HESS J1825-137 and HESS J1826-130 (see Chapter 8).

For a characteristic age of 21 kyr, Model 1 required an electron injection luminosity of  $10^{37}$  erg s $^{-1}$  to predict the multiwavelength SED, while an older age of 40 kyr required  $10^{35}$  erg s $^{-1}$ . This represents 1000% and 14% of the spin-down power of the pulsar respectively, suggesting that the true age of HESS J1825-137 is older than what the characteristic age suggests. Both ages could not explain the asymmetric gamma-ray morphology towards HESS J1825-137 and over-predicted the gamma-ray SED below 2 TeV towards HESS J1826-130.

The multiwavelength SED of HESS J1825-137 remained essentially unchanged when Model 2 introduced an advective flow of  $0.002c$  with the same input parameters as Model 1-40 kyr. The gamma-ray morphology was investigated in detail by taking slice profiles of the predicted gamma-ray flux map towards HESS J1825-137 and the uncorrelated HESS excess maps revealed by H.E.S.S. Collaboration et al., (2019). Model 2 was able to match the shape of the gamma-ray slice profile along Galactic longitude for photons  $< 1$  TeV and greater than 10 TeV. However, the slice profile between  $1 \text{ TeV} < E < 10 \text{ TeV}$  was shallower compared to the HESS excess slice, suggesting that the parent electrons were confined within the PWN before escaping into the ISM. Notably, Model 2 still over-predicted the gamma-ray emission  $< 2$  TeV towards HESS J1826-130.

Turbulent motion in the ISM results in an amplification of the magnetic field and acts as a barrier for electrons escaping into the ISM. Hence Model 3 introduced a shell of increased magnetic field gas around HESS J1826-130 to replicate the observed turbulent gas between HESS J1825-137 and HESS J1826-130 (Voisin et al., 2016). Model 3 found that an ISM shell with  $B > 60 \mu\text{G}$  around HESS J1826-130 was required to lower the gamma-ray emission to those estimated by HESS. However, the X-ray upper limit towards HESS J1826-130 constrained the shell to have a maximum strength of  $20 \mu\text{G}$ . This constraint violation suggests further refinement of the model is needed to fully disentangle the particle transport towards HESS J1825-137 and that the turbulent ISM may play a role in the emission from HESS J1826-130.

## Future Work

Models 1, 2 and 3 in Chapter 8 considered limited models of the PWN. For example, the detection of TeV halos around PWN like HESS J1825-137 suggest that the transport of electrons within the vicinity around the pulsar is suppressed compared to the surrounding ISM (e.g. see Evoli et al., (2018)). However, the model used in Chapter 8 did not consider the spatial dependence of diffusion. Similarly, it has been proposed that advection dominates close to the pulsar and diffusion dominates the outer reaches of the nebula (e.g. Giacinti et al., (2020); Recchia et al., (2021)), while the model here assumed isotropic diffusion with a constant 2D advective flow. Hence, future modelling towards HESS J825-137 and other PWN will consider diffusion and advection to be radially dependent on the distance to the lsar. The model also assumed that the position of the cosmic-ray source does not change over time. Asymmetry in the progenitor SNR will result in the pulsar gaining a kick-velocity up to  $300 \text{ km s}^{-1}$  (Kolb et al., 2017), leading to the powering pulsar being displaced up to  $\approx 6.5 \text{ pc}$  for the characteristic age of 21 kyr. This and asymmetry in the SNR reverse shock may contribute to the asymmetric gamma-ray morphology towards HESS J1825-137 and will be included in the future

Chapter 7 and Chapter 8 considered the pulsar to only be a source of electrons and neglected cosmic ray protons and positrons. However, studies such as Bell, (1992); Li et al., (2010); Ohira et al., (2018); Xin et al., (2019); Liu and Wang, (2021) suggest that PWN may have an additional hadronic component which would also contribute to the secondary emission of electrons from proton-proton interactions. Future implementation will consider the co-evolution of protons, positrons and electrons and their contribution to the SED of the PWN.

HESS J1825-137 is only one of the 20 confirmed PWN in the H.E.S.S. Galactic Plane Survey (H.E.S.S. Collaboration et al., 2018a). By applying a 3D model of particle transport towards a population of PWN, future work could investigate the evolution of PWN properties (e.g. multi-wavelength morphology and SED, injection spectrum and luminosity, ect). This would provide understanding on how cosmic rays and the surrounding ISM influences the evolution of PWN.

The next-generation Cherenkov Telescope Array with its improved sensitivity and angular resolution (CTA Consortium et al., 2019) will significantly increase the number of detected PWNe. Features in the gamma-ray morphology around known PWN and the SED at the highest energy ( $> 10 \text{ TeV}$ ) will be resolved in finer detail compared to current gamma ray instruments. The modelling conducted in Chapter 7 and Chapter 8 could be used to predict the gamma-ray morphology towards PWN and desugb future CTA observations using the python package `Gammapy` (Deil et al., 2017). The modelling conducted in this thesis is not limited to PWN and can be used to predict the multi-wavelength emission towards other particle accelerators such as SNRs, stellar clusters, ect.

# Appendix A

## Supernova Remnants

A SNR is the expanding remains (kinetic energy and cosmic rays) after a supernova event. SNRs have long been proposed as a site for cosmic ray acceleration (Baade and Zwicky, 1934b). In this section I will briefly describe the evolution of SNRs.

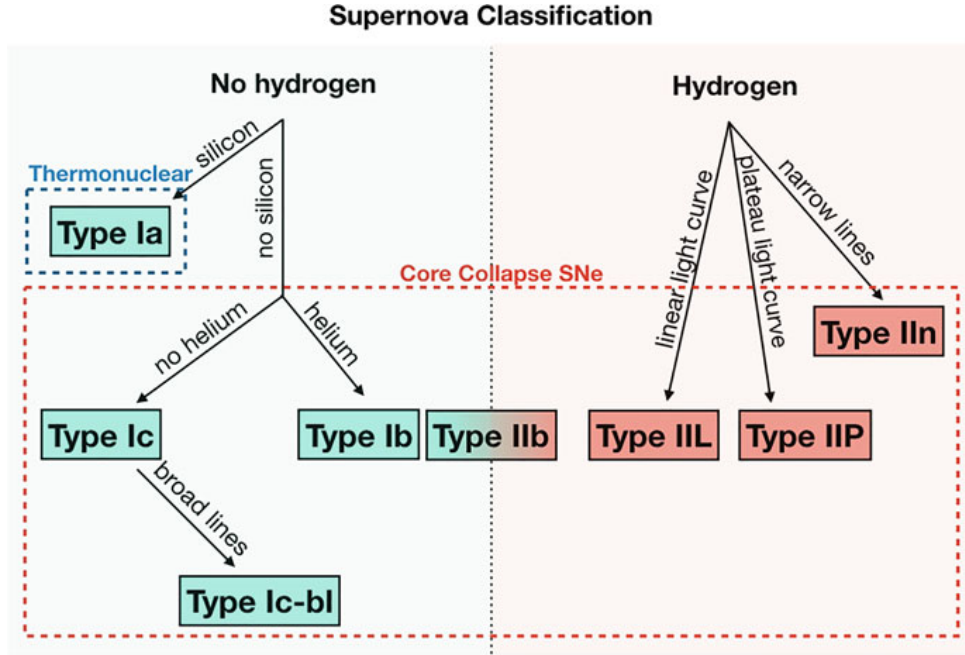


Figure A.1:  
Supernovae  
are historically  
categorised  
into different  
classifications  
based on their  
absorption line  
and light curves.  
Image courtesy  
of Vink, (2020).

### A.1 The supernova

Approximately two to three supernovae occur in the Milky Way per century (Mills et al., 1984; Tammann et al., 1994). Supernova are historically classified based on their light curves (a plot of the source's intensity vs time) and absorption lines. Type I supernovae tend to have no hydrogen absorption lines and light curves rapidly peak ( $\approx 1 - 2$  days) and then slowly decay (Vink, 2020). In contrast, Hydrogen absorption lines are observed in Type II supernovae and do not have as high a maximum in their light curves as Type I supernova (Vink, 2020). Type I and II supernova can be further subdivided based on the appearance of silicon or helium absorption lines and the shape of their light curve.

White dwarves are the remnant of stars whose mass was not sufficient to form a neutron star or black hole. As stars are typically born in groups, the white dwarf can accrete matter from its companion. This companion is normally another white dwarf or star. Once the mass of the white dwarf exceeds the Chandrasekhar limit ( $1.4 M_{\odot}$ ), electron degeneracy pressure cannot withhold gravitational collapse and the star goes supernova.

Supernovae with white dwarves as their progenitor are known as Type Ia supernova. A star with enough mass ( $\gtrsim 8 M_{\odot}$ ) undergo core collapse to form a neutron star or black hole. These type of supernova tend to form Type Ib, Type Ic and Type II supernovae. See Fig. A.1 for further classification of supernovae based on their absorption lines and light curves.

## A.2 Stages of a Supernova Remnant

A supernova releases around  $10^{53}$  erg of energy, with 99% of this energy being channelled into high-energy neutrinos. The remaining  $10^{51}$  erg mostly goes into kinetic energy. Approximately 10 to 20% of the kinetic energy is transferred into accelerating cosmic rays (Helder et al., 2012). The supernova ejects material into the ISM at supersonic speeds (up to 10% the speed of light). The interaction of ejected material with the ISM forms a shock wave ahead of the material which, in turn, creates a shell of plasma (Vink, 2020). The evolution of the SNR can be divided into four stages:

### A.2.1 Free Expansion Phase

Also classified as the ejecta-dominated phase, this phase occurs when the ejected mass from the supernova outweighs the mass of the swept up ISM ( $M_{ej} > M_{sw}$ ) and can last for hundreds of years up to a thousand years after the initial supernova (Reynolds, 2008). A supernova with kinetic energy  $E$  ejects material with speed (Bamba and Williams, 2022):

$$v = \sqrt{\frac{2E}{M_{ej}}} \approx 10^4 \quad [\text{km s}^{-1}] . \quad (\text{A.1})$$

The outermost shell interacts with the ISM forming a shock wave (forward shock) and a shell of ‘shocked’ plasma which radiatively cools and decelerates (Woltjer, 1972). The ejecta behind this shell is now moving faster than the shocked plasma shell and collides, forming a reverse shock which propagates inwards relative to the forward shock. SNRs in the free expansion phase tend to be bright in X-rays due to synchrotron emission from high-energy electrons. A SNR in its expansion phase is G1.9+0.3, it approximately 100 years old SNR and is situated close to the Galactic centre. (Reynolds et al., 2008)

### A.2.2 Sedov-Taylor Phase

When the swept up material outweighs the mass of the ejected material ( $M_{sw} > M_{ej}$ ), the Sedov-Taylor (aka energy-conservation phase) begins. Radiative losses (through thermal and synchrotron radiation) are negligible and the SNR remnant expands adiabatically with radius and velocity (Sedov, 1959):

$$\begin{aligned} R &\propto t^{\frac{2}{5}} \\ V &\propto t^{-\frac{3}{5}} . \end{aligned} \quad (\text{A.2})$$



Figure A.2: Illustration of the forward and reverse shocks of a SNR in its Sedov-Taylor phase of its evolution. Image courtesy of Vink, (2020)

Diffusive shock acceleration (see below) is believed to accelerate cosmic rays up to  $>$  TeV energies. These cosmic rays escape the SNR and interact with the surrounding ISM via proton-proton interactions to produce gamma-rays. SNRs in their Sedov-Taylor phase are still bright in X-rays through synchrotron radiation and lasts up to  $\approx 20$  kyr. Cassiopeia A is an example of a SNR entering its Sedov-Taylor phase (Truelove and McKee, 1999).

### A.2.3 Snow-Plough Phase

As the SNR ages, the SNR expansion slows down as seen in Eq. A.2. When the shock velocity reaches  $200 \text{ km s}^{-1}$  and temperatures are below  $10^6 \text{ K}$ , ionised atoms (e.g. hydrogen) recombine with free electrons and emit electromagnetic radiation in the radio-optical spectrum (Woltjer, 1972). This is known as the Snow-Plough phase where the expansion is governed by the conservation of momentum rather than energy (Vink, 2020). The age at which a SNR is estimated to reach its snow plough phase is governed by:

$$t_{\text{SP}} = 446 \left( \frac{E_{51}}{n_H \text{ cm}^{-3}} \right)^{\frac{1}{3}}, \quad (\text{A.3})$$

where  $n$  is the density of the ambient medium (Vink, 2020). An SNR in its Snow-Plough phase expands in a rate  $R \propto t^{1/4}$  (Woltjer, 1972). The SNR associated with HESS J1825-137 is believed to be entering the Snow-Plough phase based on the characteristic age of the associated pulsar and observed  $H\alpha$  lines (Voisin et al., 2016).

### Merging with the Interstellar Medium

The SNR expansion velocity continues to slow down until it reaches the speed of sound in the ISM and the SNR dissipates ( $\approx 10 \text{ km s}^{-1}$ ) (Woltjer, 1972). SNRs tend to have a life time approximately 1 million years.

# Appendix B

## Diffusive Shock Acceleration

At Earth, the energy spectrum of cosmic rays have been measured up to  $10^{20}$  eV (see Section 2.2.3). But how do cosmic rays reach these enormous energies? Fermi, in 1949, proposed a mechanism where cosmic rays are accelerated through the interaction with magnetic field irregularities in ISM gas clouds (Fermi, 1949). However, the amount of energy gained through these interactions was relatively small to explain the highest energy cosmic rays observed at Earth. Fermi's original theory was modified in the 1970's to consider the acceleration of cosmic rays as they travel through a shock wave generated by, for example, a SNR (Krymskii, 1977; Axford et al., 1977; Bell, 1978a; Bell, 1978b; Blandford and Ostriker, 1978). This is known as diffusive shock acceleration.

### B.1 Fermi's Original Theory

In Fermi's original theory, a cosmic ray with energy  $E_1$  scatters off a ISM gas cloud (travelling at velocity  $v_c$  in the lab frame) at angle  $\theta_1$  (see Fig. ??) and exits the cloud with energy  $E_2$  and angle  $\theta_2$ . Using Lorentz transformations, the original energy in the cloud frame (primed frame) is given by:

$$E'_1 = \gamma_c E_1 (1 - \beta_c \cos \theta_1) , \quad (\text{B.1})$$

where  $\beta_c = v_c/c$  and  $\gamma_c = 1/\sqrt{1-\beta_c^2}$ . The scattering is collisionless (elastic) in the reference frame of the cloud, giving  $E'_1 = E'_2$ . The final energy in the lab frame is then:

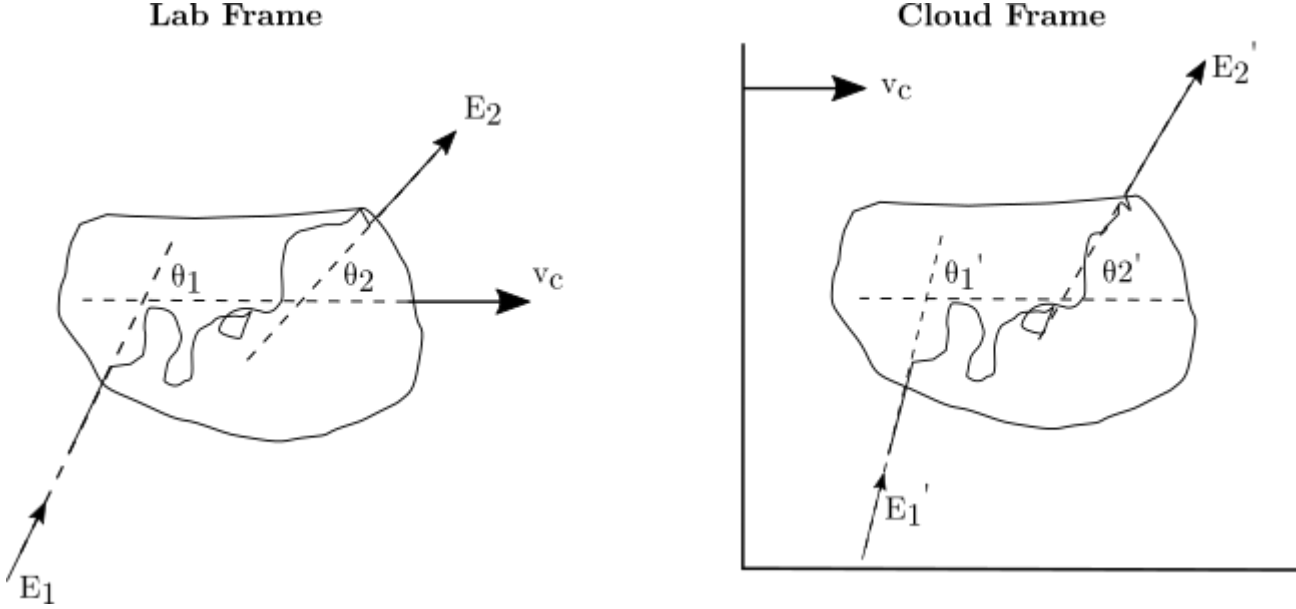
$$\begin{aligned} E_2 &= \gamma_c E'_2 (1 + \beta_c \cos \theta'_2) \\ &= \gamma_c^2 E_1 (1 + \beta_c \cos \theta'_2) (1 - \beta_c \cos \theta_1) . \end{aligned} \quad (\text{B.2})$$

The cosmic-ray fractional energy gain is then:

$$\begin{aligned} \frac{\Delta E}{E} &= \frac{E_2 - E_1}{E_1} \\ &= \frac{1 - \beta_c \cos \theta_1 + \beta_c \cos \theta_1 + \beta_c^2 \cos \theta_1 \cos \theta'_2}{E_1 (1 - \beta_c^2)} - 1 . \end{aligned} \quad (\text{B.3})$$

Considering the average fractional energy gain ( $\langle \Delta E/E \rangle$ ), the outgoing direction of the cosmic ray in the clouds reference frame is randomised, therefore  $\langle \cos \theta'_2 \rangle = 0$ . To calculate the average original cosmic-ray angle, consider the ISM cloud traveling a distance  $v_c t$  in a 'sea' of cosmic rays travelling at speed  $v_{\text{CR}}$  (see —). In time  $t$ , all cosmic rays in length  $l$  will enter the cloud. For relativistic cosmic rays ( $v_{\text{cr}} \gg v_c$ ):

$$\begin{aligned} L &= t \sqrt{v_{\text{CR}}^2 + v_c^2 - 2v_{\text{CR}}v_c \cos \theta_1} \\ &\approx t(v_{\text{CR}} - v_c \cos \theta_1) . \end{aligned} \quad (\text{B.4})$$



Cosmic ray enters a ISM cloud and scatters off magnetic field turbulence resulting in energy gain.

For a spherical cloud of radius  $r$  having cross section  $\sigma = \pi r^2$ , the collision rate,  $R$ , is:

$$\begin{aligned} R &= \frac{n_{\text{CR}} L \sigma}{t} \\ &= n_{\text{CR}} \sigma (v_{\text{CR}} - v_c \cos \theta_1) , \end{aligned} \quad (\text{B.5})$$

where  $n_{\text{CR}}$  is the cosmic-ray density. For an isotropic cosmic-ray distribution:

$$\frac{dn_{\text{CR}}}{d \cos \theta_1} = \frac{n_{\text{CR}}}{2}, \quad -1 < \cos \theta_1 < 1 , \quad (\text{B.6})$$

where  $-1 < \cos \theta_1 < 1$  considers all angles of  $\theta_1$ .

## B.2 Diffusive Shock Acceleration

A cosmic ray travelling upstream of the shock at velocity  $U_1$  and angle  $\theta_1$  will ‘pass’ through the shock and travel at velocity  $U_2$  and angle  $\theta_2$  downstream of the shock (see Fig. B.1). The magnetic fields upstream and downstream of the shock are  $B_1$  and  $B_2$  respectively.  $x$  and  $y$  is defined to be the direction perpendicular and parallel to the shock respectively. The compression ratio is defined to be the mass density ratio of the shocked and unshocked material:

$$r = \frac{\rho_2}{\rho_1} , \quad (\text{B.7})$$

where  $\rho$  is the density. From conservation of mass:

$$\begin{aligned} \rho_1 U_{1x} &= \rho_2 U_{2x} = A \\ \therefore U_{1x} &= r U_{2x} , \end{aligned} \quad (\text{B.8})$$

where  $A$  is a constant. From conservation of momentum:

$$U_{1y} = U_{2y} \quad (\text{B.9a})$$

$$A U_{1x} = A U_{2x} + P , \quad (\text{B.9b})$$

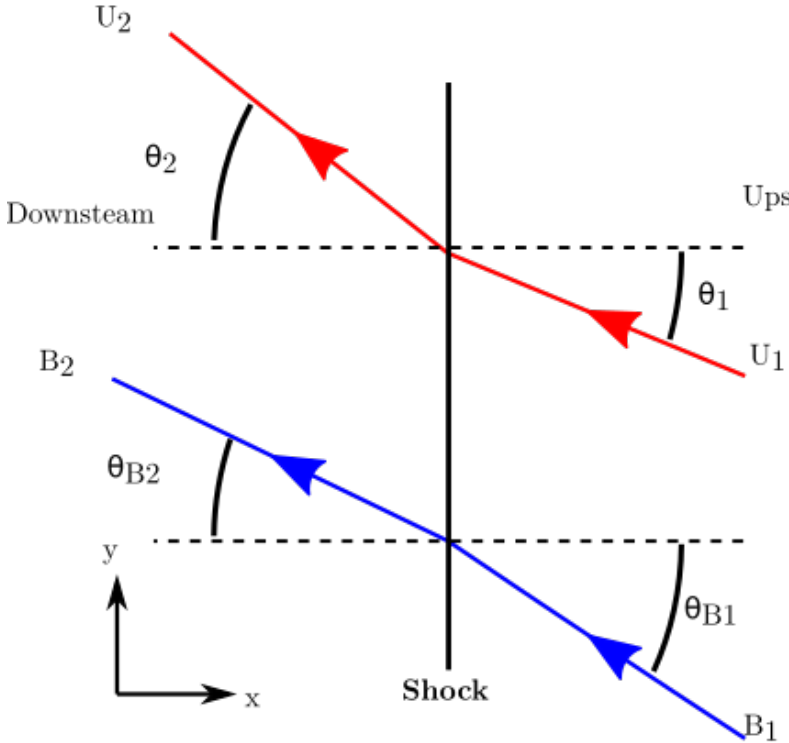


Figure B.1: A cosmic ray travels upstream of the shock at velocity  $U_1$  (relative to the shock) at angle  $\Theta_1$  and ‘passes’ through the shock downstream. The cosmic ray now has velocity  $U_2$  at angle  $\Theta_2$ .  $B_1$  and  $B_2$  are the magnetic fields upstream and downstream of the shock with angles  $\theta_{B1}$  and  $\theta_{B2}$  to the normal to the shock respectively.

with  $P$  being the pressure downstream. From the conservation of energy:

$$\frac{1}{2}AU_{1x}^2 = \frac{1}{2}U_{2x}^2 + U_{2x}(E + P) , \quad (\text{B.10})$$

it can be found that the compression ratio can be expressed in terms of the downstream internal energy  $E$ :

$$r = 1 + \frac{2E}{P} , \quad (\text{B.11})$$

and  $r$  takes values 4 and 7 for monatomic non-relativistic and relativistic gas respectively (Drury, 1983).

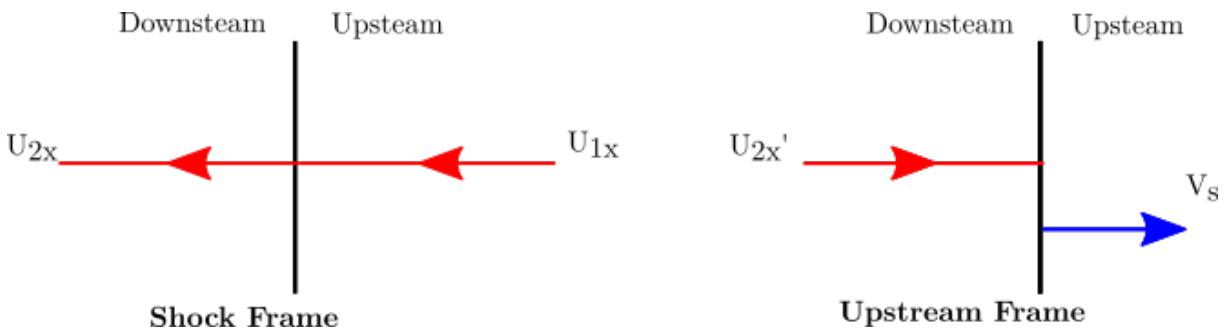


Figure B.2: In the reference frame of the shock, a cosmic ray travelling upstream of the shock (with velocity  $U_1$ ) to downstream of the shock (now travelling at velocity  $U_2$ ).  $B_1$  and  $B_2$  are the magnetic fields upstream and downstream of the shock with angles  $\theta_{B1}$  and  $\theta_{B2}$  to the normal to the shock respectively.

In the frame of the shock, the material upstream of the shock travels towards the shock

at  $U_1 = V_s$  (see Fig. B.2). Hence, the material downstream of the shock in the upstream reference frame (primed frame) travels at speed:

$$\begin{aligned} U'_{2x} &= U_{1x} - U_{2x} = V_s - \frac{V_s}{r} \\ \therefore \frac{U'_{2x}}{V_s} &= \frac{r-1}{r}, \end{aligned} \quad (\text{B.12})$$

For non-relativistic particles  $U'_{2x}/V_s = 3/4$ .

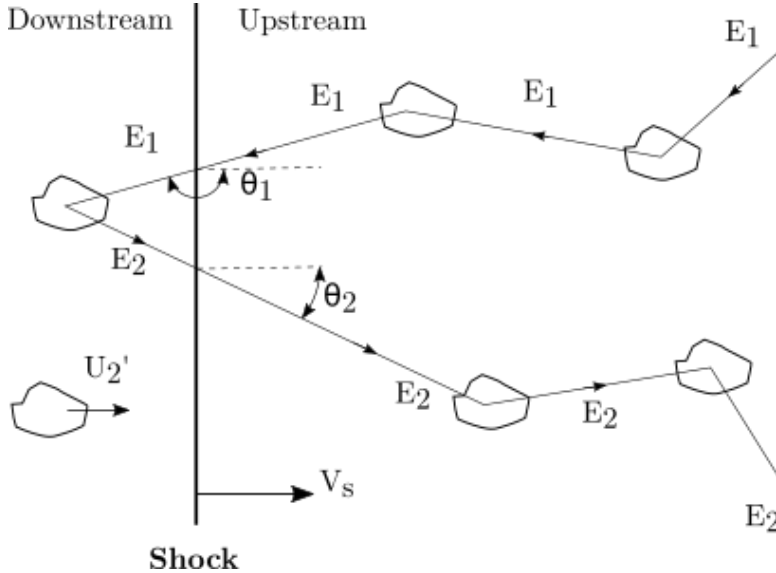


Figure B.3: In the reference frame of the material upstream of the shock, a cosmic ray of energy  $E_1$  travels upstream to downstream with no change of energy. The cosmic ray scatters off magnetic field turbulence in a cloud downstream of the shock and passes back upstream of the shock. This process can repeat or the cosmic ray can escape the system.

Now consider the scenario described in Fig. B.3, where cosmic ray of energy  $E_1$  and velocity  $v$  crosses upstream to downstream at angle  $\theta_1$  (in the upstream reference frame). Lorentz transformations gives the energy of the cosmic ray in the shock reference frame:

$$E'_1 = \gamma_d(E_1 - \beta_d p_1 \cos \theta_1 c), \quad (\text{B.13})$$

where  $\beta_d = v_d/c$ ,  $v_d$  is the velocity of the cosmic ray downstream,  $\gamma_d$  is the Lorentz factor downstream and  $p$  is the momentum. The energy and momentum of a cosmic ray is related by  $E \approx pc$ , therefore:

$$E'_1 = \gamma_d E_1 (1 - \beta_d \cos \theta_1). \quad (\text{B.14})$$

The cosmic ray then scatters of a downstream cloud and in the reference frame of the cloud  $E'_2 = E'_1$ . The cosmic ray then travels back upstream of the shock with energy:

$$\begin{aligned} E_2 &= \gamma_u E'_2 (1 + \beta \cos \theta'_2) \\ &= \gamma_d \gamma_u E_1 (1 - \beta_d \cos \theta_1) (1 + \beta \cos \theta'_2), \end{aligned} \quad (\text{B.15})$$

where  $\beta_u = v_u/c$ ,  $v_u$  is the velocity of the cosmic ray upstream and  $\gamma_u$  is the Lorentz factor upstream. Assuming the same velocity upstream and downstream ( $\beta = \beta_d = \beta_u$  and  $\gamma = \gamma_d = \gamma_u$ ), the fractional energy gain for one back and forth crossing is then:

$$\begin{aligned} \frac{\Delta E}{E} &= \frac{E_2 - E_1}{E_1} \\ &= \frac{1 - \beta \cos \theta_1 + \beta \cos \theta'_2 - \beta^2 \cos \theta'_2 \cos \theta_1}{1 - \beta^2} - 1. \end{aligned} \quad (\text{B.16})$$

Therefore, the average fractional energy is:

$$\left\langle \frac{\Delta E}{E} \right\rangle = \frac{1 - \beta \langle \cos \theta_1 \rangle + \beta \langle \cos \theta'_2 \rangle - \beta^2 \langle \cos \theta_1 \rangle \langle \cos \theta'_2 \rangle}{1 - \beta_{\text{cloud}}^2} - 1 . \quad (\text{B.17})$$

The average angle,  $\langle \cos \theta \rangle$ , can be found via:

$$\begin{aligned} \langle \cos \theta \rangle &= \frac{\int p(\cos \theta) \cos \theta \sin \theta d\theta}{\int_{\pi}^{\pi/2} p(\cos \theta) \sin \theta d\theta} \\ &= \frac{\int p(\cos \theta) \cos \theta d\cos \theta}{p(\cos \theta) d\cos \theta} \end{aligned} \quad (\text{B.18})$$

where  $p(\cos \theta)$  is the probability of a cosmic ray having angle  $\theta$ . The probability of a cosmic ray travelling upstream to downstream is proportional to the rate of particles per unit area travelling upstream to downstream:

$$p(\cos \theta_1) \propto R_{u \rightarrow d}(\theta_1) \approx -n_{CR} v \cos \theta_1 \quad [\text{m}^{-2} \text{s}^{-1}] , \quad (\text{B.19})$$

and  $90^\circ < \theta_1 < 180^\circ$  (see Fig. B.3) Similarly, the rate of cosmic rays crossing per unit area from downstream to upstream is defined by:

$$p(\cos \theta'_2) \propto R_{d \rightarrow u}(\theta'_2) \approx n_{CR} v \cos \theta'_2 \quad [\text{m}^{-2} \text{s}^{-1}] , \quad (\text{B.20})$$

with  $0^\circ < \theta'_2 < 90^\circ$  (see Fig. B.3). Therefore:

$$\begin{aligned} \langle \cos \theta_1 \rangle &= \frac{\int_{-1}^0 \cos \theta_1^2 d\cos \theta_1}{\int_{-1}^0 \cos \theta_1 d\cos \theta_1} = -\frac{2}{3} \\ \langle \cos \theta'_2 \rangle &= \frac{\int_0^1 \cos \theta'_2 d\cos \theta'_2}{\int_0^1 \cos \theta'_2 d\cos \theta'_2} = \frac{2}{3} . \end{aligned} \quad (\text{B.21})$$

Giving the average fractional energy gain:

$$\left\langle \frac{\Delta E}{E} \right\rangle = \frac{\beta^2 + \frac{4}{3}\beta + \frac{4}{9}\beta^2}{1 - \beta_{\text{cloud}}^2} . \quad (\text{B.22})$$

For a non-relativistic particle ( $\beta \ll 1$ ) and  $R = 4$  (see Eq. B.12):

$$\begin{aligned} \left\langle \frac{\Delta E}{E} \right\rangle &\approx \frac{4}{3}\beta = \frac{4}{3}U'_2 \\ &= \frac{4}{3}\left(\frac{R-1}{R}\right)\frac{V_s}{c} \\ &\approx \frac{V_s}{c} . \end{aligned} \quad (\text{B.23})$$

Each time the cosmic ray travels back and across the shock, the cosmic ray has increased its energy by a factor  $V_s/c$ .

# Appendix C

## Finite Difference Techniques applied to the Transport Equation

Finite difference techniques are utilised to solve differential equations numerically by approximating derivatives by finite differences. Often, these differential equations cannot be solved analytically unless in certain scenarios. For example, the transport equation (see Eq. 7.1) can only be solved for a impulsive source of cosmic rays. This section will describe the basics of finite difference techniques and the application to the transport equation.

### C.1 Diffusion

The diffusive component of the transport equation (see Eq. 7.1) is described by:

$$\frac{\partial n(\mathbf{r}, \gamma, t)}{\partial t} = \nabla \left( \bar{D} \cdot \nabla n(\mathbf{r}, \gamma, t) \right). \quad (\text{C.1})$$

A region of interstellar gas can be split into a 3D grid of voxels. Assuming that diffusion is isotropic ( $\bar{D} = D$ ), Eq. C.1 at position  $x, y, z$  and time  $t$  becomes:

$$\begin{aligned} \frac{\partial n(\mathbf{r}, \gamma, t)}{\partial t} \Big|_i^t &= \nabla D \cdot \nabla n + D \nabla^2 n \\ &= \sum_i \frac{\partial D}{\partial i} \frac{\partial n}{\partial i} + D_i \frac{\partial^2 n}{\partial i^2}, \end{aligned} \quad (\text{C.2})$$

where  $i$  considers the three Cartesian axes  $x, y$  and  $z$ . Assuming that diffusion is spatially independent ( $\frac{\partial D}{\partial i} = 0$ ). Taking the Taylor series expansion of  $n$  around point  $i$  becomes:

$$n_{i+\Delta i} = n_i + \Delta i \frac{\partial n}{\partial i} \Big|_{i+\Delta i} + \frac{\Delta i^2}{2} \frac{\partial^2 n}{\partial i^2} \Big|_{i+\Delta i} + \frac{\Delta i^3}{3!} \frac{\partial^3 n}{\partial i^3} \Big|_{i+\Delta i} + \dots \quad (\text{C.3a})$$

$$n_{i-\Delta i} = n_i - \Delta i \frac{\partial n}{\partial i} \Big|_{i-\Delta i} + \frac{\Delta i^2}{2} \frac{\partial^2 n}{\partial i^2} \Big|_{i-\Delta i} - \frac{\Delta i^3}{3!} \frac{\partial^3 n}{\partial i^3} \Big|_{i-\Delta i} + \dots \quad (\text{C.3b})$$

Assuming  $\delta i \ll 1$ , Eq. C.3 becomes:

$$n_{i+\Delta i} = n_i + \Delta i \frac{\partial n}{\partial i} \Big|_{i+\Delta i} + O(\Delta i^2) \quad (\text{C.4a})$$

$$n_{i-\Delta i} = n_i - \Delta i \frac{\partial n}{\partial i} \Big|_{i-\Delta i} + O(\Delta i^2), \quad (\text{C.4b})$$

where  $O(\Delta i^3)$  is truncation error due to higher orders. Rearranging Eq. C.4 to first order gives:

$$\frac{\partial n}{\partial i} \Big|_{i+\Delta i} \approx \frac{n_{i+\Delta i} - n_i}{\Delta i} \quad (\text{C.5a})$$

$$\frac{\partial n}{\partial i} \Big|_{i-\Delta i} \approx \frac{n_i - n_{i-\Delta i}}{\Delta i} , \quad (\text{C.5b})$$

where Eq. C.5a and Eq. C.5b are the forward and backward difference respectively. The central difference can be found by combining Eq. C.5a and Eq. C.5b:

$$\begin{aligned} \frac{\partial n}{\partial i} \Big|_{i+\Delta i} + \frac{\partial n}{\partial i} \Big|_{i-\Delta i} &= \frac{n_{i+\Delta i} - n_i}{\Delta i} + \frac{n_i - n_{i-\Delta i}}{\Delta i} \\ \therefore \frac{\partial n}{\partial i} \Big|_i &= \frac{n_{i+\Delta i} - n_{i-\Delta i}}{2\Delta i} . \end{aligned} \quad (\text{C.6})$$

The second derivative of  $n$  can be found by combining Eq. C.3a and Eq. C.3b up to the second order:

$$\begin{aligned} n_{i+\Delta i} + n_{i-\Delta i} &= 2n_i + 2 \frac{\Delta i^2}{2} \frac{\partial^2 n}{\partial i^2} \Big|_i \\ \frac{\partial^2 n}{\partial i^2} \Big|_i &= \frac{n_{i+\Delta i} + n_{i-\Delta i} - 2n_i}{\Delta i^2} . \end{aligned} \quad (\text{C.7})$$

Applying the forward difference to the LHS of Eq. C.2 and central difference to the RHS of Eq. C.2:

$$\frac{n_i^{t+\Delta t} - n_i^t}{\Delta t} = \sum_{i=x,y,z} \frac{D_{i+\Delta i} - D_{i-\Delta i}}{2\Delta i} \cdot \frac{n_{i+\Delta i}^t - n_{i-\Delta i}^t}{2\Delta i} + D_i \frac{n_{i+\Delta i}^t + n_{i-\Delta i}^t - 2n_i^t}{\Delta i^2} . \quad (\text{C.8})$$

For isotropic case of diffusion ( $\nabla D = 0$ , i.e.  $D_{i+\Delta i} = D_{i-\Delta i}$ ):

$$\begin{aligned} n_i^{t+\Delta t} &= n_i^t + \sum_{i=x,y,z} \frac{\Delta t}{\Delta i^2} D_i (n_{i+\Delta i}^t + n_{i-\Delta i}^t - 2n_i^t) \\ &= n_i^t + \sum_{i=x,y,z} \frac{\Delta t}{\Delta i^2} [D_i (n_{i+\Delta i}^t - n_i^t) + D_i (n_{i-\Delta i}^t - n_i^t)] . \end{aligned} \quad (\text{C.9})$$

i.e. Eq. C.9 is the solution of Eq. C.1 at time  $t + \Delta t$  using finite difference techniques.

### C.1.1 Stability of the Finite Difference

Von Neumann stability analysis (or Fourier stability analysis) can be used to check the numerical stability of finite difference techniques (Isaacson, 1966).

For a solution:

$$U(t + \Delta t, x) = \sum_{j=-n}^n C_j U(t, x + j\Delta x) , \quad (\text{C.10})$$

where there are  $2n+1$  points to calculate  $U(t + \Delta t, x)$ . The error ( $\epsilon_j^t$ ) is then defined to be

$$\epsilon_j^t = U_j^t - u_j^t , \quad (\text{C.11})$$

with  $u_j^t$  being the analytical solution at point  $j, t$ . Then,  $\epsilon_j$  satisfies Eq. C.12:

$$\epsilon(t + \Delta t, x) = \sum_{j=-n}^n C_j \epsilon(t, x + j\Delta x) , \quad (\text{C.12})$$

For linear differential equations with periodic boundary conditions, the error can be treated as a time-dependent Fourier expansion with wave number  $k$  (“Stochastic Partial Differential Equations” 2014).:

$$\epsilon(x, t) = A(t) e^{ikx} = A^t e^{ikx} , \quad (\text{C.13})$$

where Eq. C.13 is the time-dependent spatial Fourier expansion with wave number  $k$ . For the solution to be stable:

$$G = \left| \frac{A^{t+1}}{A^t} \right| \leq 1 , \quad (\text{C.14})$$

with  $G$  being the amplification factor. Therefore:

$$\begin{aligned} \epsilon_x^{t+1} &= A^{t+1} e^{ikx} \\ \epsilon_{x+1}^t &= A^t e^{ik(x+\Delta x)} \\ \epsilon_{x-1}^t &= A^t e^{ik(x-\Delta x)} . \end{aligned} \quad (\text{C.15})$$

Applying Von Newmann stability analysis to the transport equation, Eq. C.13 becomes:

$$\begin{aligned} A^{t+1} e^{ikx} &= A^t e^{ikx} + D' \left( A^t e^{ik(x+\Delta x)} + A^t e^{ik(x-\Delta x)} - 2A^t e^{ikx} \right) \\ \frac{A^{t+1}}{A^t} &= 1 + D' \left( e^{i\theta} + e^{-i\theta} - 2 \right) \\ &= 1 + D' (2 \cos \theta - 2) \\ &= 1 - 4D' \sin^2 \frac{\theta}{2} , \end{aligned} \quad (\text{C.16})$$

where  $D' = D\Delta t/\Delta x^2$  and  $\theta = k\Delta x$ . For the solution to be stable,  $\left| \frac{A^{t+1}}{A^t} \right| \leq 1$ . Hence:

$$\begin{aligned} 1 - 4D' \sin^2 \frac{k\Delta x}{2} &\geq -1 \\ \& 1 - 4D' \sin^2 \frac{k\Delta x}{2} \leq 1 . \end{aligned} \quad (\text{C.17})$$

As  $0 \leq \sin^2 \frac{k\Delta x}{2} \leq 1$ , Eq. C.9 is stable when:

$$\begin{aligned} D' &= D \frac{\Delta t}{\Delta x^2} \leq \frac{1}{2} \\ D &\leq \frac{1}{2} \frac{\Delta x^2}{\Delta t} . \end{aligned} \quad (\text{C.18})$$

i.e. finite difference techniques can be applied to the transport equation when the diffusion coefficient,  $D$ , is less than or equal to half of the ‘maximum’ diffusion coefficient implied by the voxel size and time step  $\Delta x^2/\Delta t$ .

## C.2 Advection

The advective component of the transport equation is given by:

$$\frac{\partial n(\mathbf{r}, \gamma, t)}{\partial t} = -\nabla(n\mathbf{v}_a) , \quad (\text{C.19})$$

where  $\mathbf{v}_a$  is the advective velocity of cosmic rays. Assuming  $\mathbf{v}_a$  is spatially independent:

$$\begin{aligned} \frac{\partial n(\mathbf{r}, \gamma, t)}{\partial t} &= -\mathbf{v}_a \nabla n \\ \left. \frac{\partial n}{\partial t} \right|_i &= -v_i \frac{\partial n}{\partial i} , \end{aligned} \quad (\text{C.20})$$

where  $i$  considers the three Cartesian axes  $x$ ,  $y$  and  $z$ . Applying the forward difference to the LHS of Eq. C.20 and the central difference to the RHS:

$$\begin{aligned} \frac{n_i^{t+\Delta t} - n_i^t}{\Delta t} &= - \sum_{i=x,y,z} v_i \frac{n_{i+\Delta i}^t - n_{i-\Delta i}^t}{2\Delta i} \\ n_i^{t+\Delta t} &= n_i^t - \frac{v_i}{2} \cdot \frac{\Delta t}{\Delta x} (n_{i+\Delta i}^2 - n_{i-\Delta i}^2) \\ &= n_i^t - \frac{v'}{2} (n_{i+\Delta i}^t - n_{i-\Delta i}^t) , \end{aligned} \quad (\text{C.21})$$

where  $v' = \frac{\Delta t}{\Delta x}$ . Applying the Von Neumann stability analysis to Eq. C.21:

$$\begin{aligned} A^{t+1} e^{ikx} &= A^t e^{ikx} + \frac{v'}{2} (e^{ikx} e^{ik\Delta x} - e^{ikx} e^{-ik\Delta x}) \\ \frac{A^{t+1}}{A^t} &= 1 - \frac{v'}{2} (e^{i\theta} - e^{-i\theta}) \\ &= 1 - iv' \sin \theta . \end{aligned} \quad (\text{C.22})$$

As  $|\frac{A^{t+1}}{A^t}| \leq 1$ :

$$\left| \frac{A^{t+1}}{A^t} \right| = 1 + v'^2 \sin^2 \theta \leq 1 . \quad (\text{C.23})$$

Therefore the numerical solution of advection that utilises a central finite difference is only stable when:

$$\sin^2 \theta = \sin^2(k\Delta x) \leq 0 . \quad (\text{C.24})$$

i.e. the solution is only stable when the error function (see Eq. C.11) has wave number:

$$k\Delta x = n\pi , \quad (\text{C.25})$$

where  $n = 0, 1, \dots$ . Therefore, the numerical solution of advection that utilises central finite difference methods is unstable. Instead, the forward and backward difference in spatial coordinates can be applied to Eq. C.20:

$$n_i^{t+\Delta t} = n_i^t - v' (n_{i+\Delta i}^t - n_i^t) , \quad \text{Forward Difference} \quad (\text{C.26a})$$

$$n_i^{t+\Delta t} = n_i^t - v' (n_i^t - n_{i-\Delta i}^t) , \quad \text{Backward Difference} . \quad (\text{C.26b})$$

Applying the Von Neumann analysis for the forward difference:

$$\begin{aligned}
\frac{A^{t+1}}{A^t} &= 1 - v' \left( e^{i\theta} - 1 \right) \\
&= 1 - v' (\cos \theta + i \sin \theta - 1) \\
&= 1 + v' (1 - \cos \theta) + i v' \sin \theta ,
\end{aligned} \tag{C.27}$$

and the backward difference:

$$\begin{aligned}
\frac{A^{t+1}}{A^t} &= 1 - v' \left( 1 - e^{-i\theta} \right) \\
&= 1 - v' (1 - \cos \theta + i \sin \theta) \\
&= 1 - v' (1 - \cos \theta) - i v' \sin \theta .
\end{aligned} \tag{C.28}$$

The forward and backward difference can be summarised as:

$$\frac{A^{t+1}}{A^t} = 1 \pm v' (1 - \cos \theta) \pm i v' \sin \theta , \tag{C.29}$$

Therefore:

$$\begin{aligned}
\left| \frac{A^{t+1}}{A^t} \right|^2 &= 1 + v'^2 + v'^2 \cos^2 \theta - 2v'^2 \cos \theta \pm 2c \mp 2v' \cos \theta + v'^2 \sin^2 \theta \\
&= 1 - 2v' (v' \cos \theta - v' \pm \cos \theta \mp 1) \\
&= 1 \mp 2v' (1 \mp v') (1 - \cos \theta) .
\end{aligned} \tag{C.30}$$

For the finite difference to be stable:

$$\begin{aligned}
1 &\geq \left| \frac{A^{t+1}}{A^t} \right| \\
1 &\geq \left| \frac{A^{t+1}}{A^t} \right|^2 \\
0 &\geq \mp 2v' (1 \mp v') (1 - \cos \theta) .
\end{aligned} \tag{C.31}$$

As  $(1 - \cos \theta) \geq 0$ :

$$1 \geq \pm v \frac{\Delta t}{\Delta x} . \tag{C.32}$$

i.e. Eq. C.32 is stable when a particle has speed less or equal to the ‘maximum’ speed ( $\Delta x / \Delta t$ ) implied by the voxel size and time step. When  $v \leq 0$ , only the forward difference is stable. Similarly, when  $v \geq 0$ , only the backward difference is stable.

# Appendix D

## Variance of diffusion in $n$ dimensions

The variance is a measurement of dispersion, comparing the standard deviation of a random variable to the population mean. The variance of function  $f(x)$  is defined as:

$$\begin{aligned}\text{Var}(X) &= \sigma^2 \\ &= E(X^2) - E(X)^2 \\ E(X^n) &= \int_{-\infty}^{\infty} x^n f(x) dx ,\end{aligned}\tag{D.1}$$

where  $E(X^n)$  is the expected value of variable  $X^n$ .

The distance that cosmic rays have travelled through diffusion (see Section 2.2.2 and Section 7.1) can be approximated by the radius containing  $1\sigma = 68\%$  of the particles,  $r_\sigma$ . This Appendix will calculate the variance (therefore  $r_\sigma$ ) for diffusion in 1D, 2D and 3D.

### D.1 1D Diffusion

For 1D diffusion, the solution to the transport equation for an impulsive accelerator injecting cosmic rays at  $t = 0$  and  $x = 0$  in a diffusion-only scenario (see Eq. 5.36a):

$$n(x) = \frac{1}{\sqrt{4\pi Dt}} \exp\left(-\frac{x^2}{4Dt}\right) .\tag{D.2}$$

Therefore:

$$\begin{aligned}E(x) &= \frac{1}{\sqrt{4\pi Dt}} \int_{-\infty}^{\infty} x \exp\left(-\frac{x^2}{4Dt}\right) dx \\ &= \frac{1}{\sqrt{4\pi Dt}} \left( -2Dt \exp\left(-\frac{x^2}{4Dt}\right) \Big|_{-\infty}^{\infty} + 2Dt \exp\left(-\frac{x^2}{4Dt}\right) \Big|_{-\infty}^{\infty} \right) \\ &= 0 ,\end{aligned}\tag{D.3}$$

and:

$$\begin{aligned}E(x^2) &= \frac{1}{\sqrt{4\pi Dt}} \int_{-\infty}^{\infty} x^2 \exp\left(-\frac{x^2}{4Dt}\right) dx \\ &= \frac{1}{\sqrt{4\pi Dt}} \left( \frac{\pi^{1/2} (4Dt)^{3/2}}{2} \right) \\ &= 2Dt .\end{aligned}\tag{D.4}$$

Giving the variance in 1D:

$$\text{Var}(x) = 2Dt , \quad (\text{D.5})$$

where  $R_\sigma = \sqrt{2Dt}$  represents the radius containing  $1\sigma \approx 68\%$  of cosmic rays.

## D.2 2D Diffusion

For 2D diffusion, the solution to the transport equation for an impulsive accelerator injecting cosmic rays at  $t = 0$  and  $r = 0$  in a diffusion-only scenario (see Eq. 5.36a):

$$\begin{aligned} n(x) &= \frac{1}{4\pi Dt} \exp\left(-\frac{r^2}{4Dt}\right) \\ r^2 &= x^2 + y^2 . \end{aligned} \quad (\text{D.6})$$

For two variables  $X$  and  $Y$  with expected values  $E(X)$  and  $E(Y)$ , the expected value of  $X + Y$  is:

$$E(X + Y) = E(X) + E(Y) . \quad (\text{D.7})$$

Therefore, the expected value of  $r^2$ :

$$\begin{aligned} E(r^2) &= E(x^2 + y^2) \\ &= E(x^2) + E(y^2) \\ &= 2Dt + 2Dt \\ &= 4Dt . \end{aligned} \quad (\text{D.8})$$

Giving the variance in 2D:

$$\text{Var}(r) = 4Dt . \quad (\text{D.9})$$

## D.3 3D Diffusion

For 3D diffusion, the solution to the transport equation for an impulsive accelerator injecting cosmic rays at  $t = 0$  and  $r = 0$  in a diffusion-only scenario (see Eq. 5.36a):

$$\begin{aligned} n(x) &= \frac{1}{\pi^{\frac{3}{2}} R_{\text{diff}}} \exp\left(-\frac{r^2}{R_{\text{diff}}^2}\right) \\ R_{\text{diff}} &= \sqrt{4Dt} , \end{aligned} \quad (\text{D.10})$$

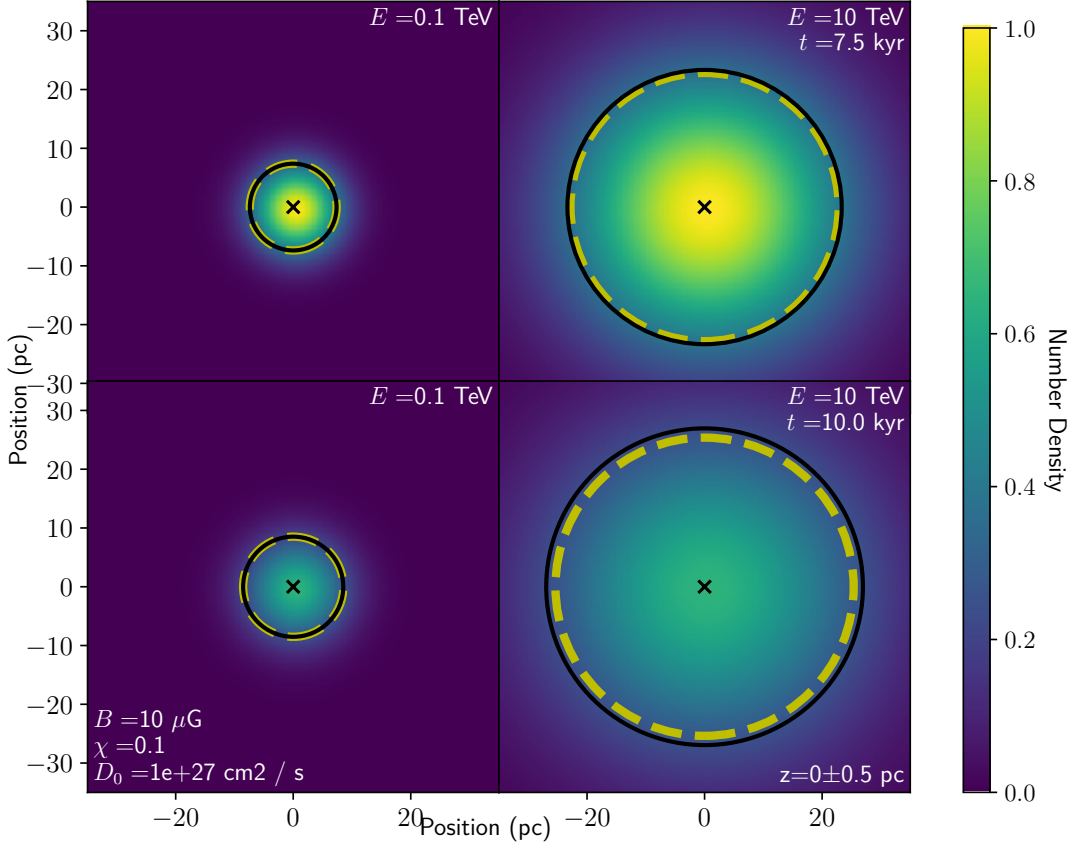
where  $r^2 = x^2 + y^2 + z^2$ . As with 2D diffusion:

$$\begin{aligned} E(r^2) &= E(x^2) + E(y^2) + E(z^2) \\ &= 2Dt + 2Dt + 2Dt \\ &= 6Dt . \end{aligned} \quad (\text{D.11})$$

Giving the variance in 3D:

$$\text{Var}(r) = 6Dt . \quad (\text{D.12})$$

The radius containing  $1\sigma = 68\%$  of cosmic rays  $R_\sigma = \sqrt{\text{Var}(r)} = \sqrt{6Dt}$  does not equate to the ‘diffusion distance’,  $R_{\text{diff}} = \sqrt{4Dt}$ , defined in literature (e.g. see Atoyan et al., (1995))



t (kyr)	E (TeV)	$R_{\text{var}} = \sqrt{4Dt}$ (pc)	$R_\sigma, 2\text{D}$ (pc)	$R_{\text{var}} = \sqrt{6Dt}$ (pc)	$R_\sigma, 3\text{D}$ (pc)
5.0	0.1	6.0	6.0	7.4	7.4
~	10	19.1	19.0	23.3	23.3
10	0.1	8.5	8.5	10.4	10.4
~	10	26.9	25.4	33.0	31.1

Figure D.1: Evolution of the electron number density for a diffusion-only scenario taken at  $z = 0 \pm 0.5$  pc along the line of sight. Electrons with energy 0.1 TeV and 10 TeV are injected at position  $x = y = z = 0$  (black cross) at  $t = 0$  into a uniform medium with magnetic field  $B = 10 \mu\text{G}$ ,  $\chi = 0.1$  and  $D_0 = 10^{27} \text{ cm}^2 \text{ s}^{-1}$  at 1 GeV. The electron number density is normalised to the maximum value in the 3D grid at  $t = 5.0$  kyr. The black and yellow-dashed circles represent the 2D variance radius ( $R_{\text{var}} = \sqrt{4Dt}$ ) and the radius containing 68% of electrons in the  $z = 0 \pm 0.5$  pc slice.

Note that by taking a slice along the 3D energy distribution (e.g.  $n = (x, y, z = 0)$ ), the radius ( $r^2 = x^2 + y^2$ ) containing 68% of cosmic rays reverts back to the 2D situation ( $R_\sigma = \sqrt{4Dt}$ ). This can be seen in Fig. D.1.

## **Appendix E**

### **Spectral Energy Distribution towards Cl\* 1806-20**

# Appendix F

## Miscellaneous Tables

Energy (GeV)	$b_1$	$b_2$	$b_3$	$\alpha(T_p)$	$\beta(T_p)$	$\gamma(T_p)$	$\lambda$
$1 \leq T_p < 5$	9.53	0.52	0.054	-	-	-	-
$T_{\text{thr}} \leq T_p \leq 1$	-	-	-	1.0	$\kappa$	0	-
$1 < T_p \leq 4$	-	-	-	1.0	$\mu + 2.45$	$\mu + 2.45$	3
$4 < T_p \leq 20$	-	-	-	1	$1.5\mu + 4.95$	$\mu + 1.50$	3
$20 < T_p \leq 100$	-	-	-	0.5	4.2	1	3
$T_p \geq 5$	9.13	0.35	0.00953	-	-	-	-
$T_p > 100$	-	-	-	0.5	4.9	1	3

$$\mu = \frac{5}{4}q^{5/4} \exp(-5q/4), \quad q = (T_p - 1 \text{ GeV})/m_p, \quad \kappa = 3.29 - \frac{1}{5}\theta_p^{-3/2}$$

Table F.1: Parameters for the hadronic gamma-ray spectra from a proton with kinetic energy  $T_p$  based on GEANT4 modelling by Kafexhiu et al., (2014).

# Bibliography

- Aartsen, M. G. et al. (2013). “Measurement of the cosmic ray energy spectrum with IceTop-73”. In: *Phys. Rev. D* 88.4, 042004, p. 042004. DOI: 10.1103/PhysRevD.88.042004.
- Abdo, A. A. et al. (2010). “The First Fermi Large Area Telescope Catalog of Gamma-ray Pulsars”. In: *ApJS* 187.2, pp. 460–494. DOI: 10.1088/0067-0049/187/2/460.
- Abdollahi, S. et al. (2020). “Fermi Large Area Telescope Fourth Source Catalog”. In: *ApJS* 247.1, 33, p. 33. DOI: 10.3847/1538-4365/ab6bcb.
- Abeysekara, A. U. et al. (2017). “Extended gamma-ray sources around pulsars constrain the origin of the positron flux at Earth”. In: *Science* 358.6365, pp. 911–914. DOI: 10.1126/science.aan4880.
- Abeysekara, A. U. et al. (2020). “Multiple Galactic Sources with Emission Above 56 TeV Detected by HAWC”. In: *Phys. Rev. Lett.* 124 (2), p. 021102. DOI: 10.1103/PhysRevLett.124.021102. URL: <https://link.aps.org/doi/10.1103/PhysRevLett.124.021102>.
- Abeysekara, A. U. et al. (2023). “The High-Altitude Water Cherenkov (HAWC) observatory in México: The primary detector”. In: *Nuclear Instruments and Methods in Physics Research A* 1052, 168253, p. 168253. DOI: 10.1016/j.nima.2023.168253.
- Abraham, J. et al. (2010). “Measurement of the energy spectrum of cosmic rays above  $10^{18}$  eV using the Pierre Auger Observatory”. In: *Physics Letters B* 685.4-5, pp. 239–246. DOI: 10.1016/j.physletb.2010.02.013.
- Abu-Zayyad, T. et al. (2013). “The Cosmic-Ray Energy Spectrum Observed with the Surface Detector of the Telescope Array Experiment”. In: *ApJ* 768.1, L1, p. L1. DOI: 10.1088/2041-8205/768/1/L1.
- Aharonian, F., J. Buckley, T. Kifune, and G. Sinnis (2008). “High energy astrophysics with ground-based gamma ray detectors”. In: *Reports on Progress in Physics* 71.9, 096901, p. 096901. DOI: 10.1088/0034-4885/71/9/096901.
- Aharonian, F. et al. (2005a). “A New Population of Very High Energy Gamma-Ray Sources in the Milky Way”. In: *Science* 307.5717, pp. 1938–1942. DOI: 10.1126/science.1108643.
- Aharonian, F. et al. (2006a). “Energy dependent  $\gamma$ -ray morphology in the pulsar wind nebula HESS J1825-137”. In: *A&A* 460.2, pp. 365–374. DOI: 10.1051/0004-6361:20065546.
- Aharonian, F. et al. (2006b). “The H.E.S.S. Survey of the Inner Galaxy in Very High Energy Gamma Rays”. In: *ApJ* 636.2, pp. 777–797. DOI: 10.1086/498013.
- Aharonian, F. et al. (2021a). “Construction and on-site performance of the LHAASO WFCTA camera”. In: *European Physical Journal C* 81.7, 657, p. 657. DOI: 10.1140/epjc/s10052-021-09414-z.
- Aharonian, F. et al. (2021b). “Observation of the Crab Nebula with LHAASO-KM2A - a performance study”. In: *Chinese Physics C* 45.2, 025002, p. 025002. DOI: 10.1088/1674-1137/abd01b.

- Aharonian, F. A. and A. M. Atoyan (1996). “On the emissivity of  $\pi^0$ -decay gamma radiation in the vicinity of accelerators of galactic cosmic rays.” In: *A&A* 309, pp. 917–928.
- Aharonian, F. A., A. M. Atoyan, and T. Kifune (1997). “Inverse Compton gamma radiation of faint synchrotron X-ray nebulae around pulsars”. In: *MNRAS* 291.1, pp. 162–176. DOI: 10.1093/mnras/291.1.162.
- Aharonian, F. A. et al. (2005b). “A possible association of the new VHE  $\gamma$ -ray source HESS J1825-137 with the pulsar wind nebula G18.0-0.7”. In: *A&A* 442.3, pp. L25–L29. DOI: 10.1051/0004-6361:200500180.
- Albert, A. et al. (2020). “3HWC: The Third HAWC Catalog of Very-high-energy Gamma-Ray Sources”. In: *ApJ* 905.1, 76, p. 76. DOI: 10.3847/1538-4357/abc2d8.
- Alpar, M. A., A. F. Cheng, M. A. Ruderman, and J. Shaham (1982). “A new class of radio pulsars”. In: *Nature* 300.5894, pp. 728–730. DOI: 10.1038/300728a0.
- Amato, E., D. Guetta, and P. Blasi (2003). “Signatures of high energy protons in pulsar winds”. In: *A&A* 402, pp. 827–836. DOI: 10.1051/0004-6361:20030279.
- Amenomori, M. et al. (2008). “The All-Particle Spectrum of Primary Cosmic Rays in the Wide Energy Range from  $10^{14}$  to  $10^{17}$  eV Observed with the Tibet-III Air-Shower Array”. In: *ApJ* 678.2, pp. 1165–1179. DOI: 10.1086/529514.
- Amenomori, M. et al. (2021). “First Detection of sub-PeV Diffuse Gamma Rays from the Galactic Disk: Evidence for Ubiquitous Galactic Cosmic Rays beyond PeV Energies”. In: *Phys. Rev. Lett.* 126 (14), p. 141101. DOI: 10.1103/PhysRevLett.126.141101. URL: <https://link.aps.org/doi/10.1103/PhysRevLett.126.141101>.
- Angüner, E. O. et al. (2017). “HESS J1826-130: A very hard  $\gamma$ -ray spectrum source in the galactic plane”. In: *6th International Symposium on High Energy Gamma-Ray Astronomy*. Vol. 1792. American Institute of Physics Conference Series, 040024, p. 040024. DOI: 10.1063/1.4968928.
- Apel, W. D. et al. (2013). “Ankle-like feature in the energy spectrum of light elements of cosmic rays observed with KASCADE-Grande”. In: *Phys. Rev. D* 87.8, 081101, p. 081101. DOI: 10.1103/PhysRevD.87.081101.
- Araya, M., A. M. W. Mitchell, and R. D. Parsons (2019). “Revealing a new region of gamma-ray emission in the vicinity of HESS J1825-137”. In: *MNRAS* 485.1, pp. 1001–1007. DOI: 10.1093/mnras/stz462.
- Arons, J. (1983). “Pair creation above pulsar polar caps : geometrical structure and energetics of slot gaps.” In: *ApJ* 266, pp. 215–241. DOI: 10.1086/160771.
- Atoyan, A. M., F. A. Aharonian, and H. J. Völk (1995). “Electrons and positrons in the galactic cosmic rays”. In: *Phys. Rev. D* 52.6, pp. 3265–3275. DOI: 10.1103/PhysRevD.52.3265.
- Axford, W. I., E. Leer, and G. Skadron (1977). “The Acceleration of Cosmic Rays by Shock Waves”. In: *International Cosmic Ray Conference*. Vol. 11. International Cosmic Ray Conference, p. 132.
- Baade, W. and F. Zwicky (1934a). “Cosmic Rays from Super-novae”. In: *Proceedings of the National Academy of Science* 20.5, pp. 259–263. DOI: 10.1073/pnas.20.5.259.
- (1934b). “On Super-novae”. In: *Contributions from the Mount Wilson Observatory* 3, pp. 73–78.
- (1934c). “Remarks on Super-Novae and Cosmic Rays”. In: *Physical Review* 46.1, pp. 76–77. DOI: 10.1103/PhysRev.46.76.2.
- Bamba, Aya and Brian J. Williams (2022). “Supernova Remnants: Types and Evolution”. In: *Handbook of X-ray and Gamma-ray Astrophysics*, 77, p. 77. DOI: 10.1007/978-981-16-4544-0\_88-1.

- Beck, Rainer (2001). "Galactic and Extragalactic Magnetic Fields". In: *Space Sci. Rev.* 99, pp. 243–260. DOI: 10.1023/A:1013805401252.
- Beck, Rainer and Richard Wielebinski (2013). "Magnetic Fields in Galaxies". In: *Planets, Stars and Stellar Systems. Volume 5: Galactic Structure and Stellar Populations*. Ed. by Terry D. Oswalt and Gerard Gilmore. Vol. 5, p. 641. DOI: 10.1007/978-94-007-5612-0\_13.
- Bell, A. R. (1978a). "The acceleration of cosmic rays in shock fronts - I." In: *MNRAS* 182, pp. 147–156. DOI: 10.1093/mnras/182.2.147.
- (1978b). "The acceleration of cosmic rays in shock fronts - II." In: *MNRAS* 182, pp. 443–455. DOI: 10.1093/mnras/182.3.443.
- (1992). "Cosmic ray acceleration in pulsar-driven supernova remnants." In: *MNRAS* 257, pp. 493–500. DOI: 10.1093/mnras/257.3.493.
- (2004). "Turbulent amplification of magnetic field and diffusive shock acceleration of cosmic rays". In: *MNRAS* 353.2, pp. 550–558. DOI: 10.1111/j.1365-2966.2004.08097.x.
- Berezinskii, V. S., S. V. Bulanov, V. A. Dogiel, and V. S. Ptuskin (1990). *Astrophysics of cosmic rays*. John Wiley & Sons, Inc.
- Bernlöhr, K. et al. (2003). "The optical system of the H.E.S.S. imaging atmospheric Cherenkov telescopes. Part I: layout and components of the system". In: *Astroparticle Physics* 20.2, pp. 111–128. DOI: 10.1016/S0927-6505(03)00171-3.
- Bethe, H. and W. Heitler (1934). "On the Stopping of Fast Particles and on the Creation of Positive Electrons". In: *Proceedings of the Royal Society of London Series A* 146.856, pp. 83–112. DOI: 10.1098/rspa.1934.0140.
- Blandford, R. D. and J. P. Ostriker (1978). "Particle acceleration by astrophysical shocks." In: *ApJ* 221, pp. L29–L32. DOI: 10.1086/182658.
- BLUMENTHAL, GEORGE R. and ROBERT J. GOULD (1970). "Bremsstrahlung, Synchrotron Radiation, and Compton Scattering of High-Energy Electrons Traversing Dilute Gases". In: *Rev. Mod. Phys.* 42 (2), pp. 237–270. DOI: 10.1103/RevModPhys.42.237. URL: <https://link.aps.org/doi/10.1103/RevModPhys.42.237>.
- Bogovalov, S. V. and D. V. Khangulyan (2002). "The Crab Nebula: interpretation of Chandra observations." In: *Astronomy Letters* 28, pp. 373–385. DOI: 10.1134/1.1484137.
- Bolatto, Alberto, Mark Wolfire, and Adam Leroy (2013). "The CO-to-H<sub>2</sub> conversion factor". In: *Annual Review of Astronomy and Astrophysics* 51. DOI: 10.1146/annurev-astro-082812-140944.
- Bombaci, I. (1996). "The maximum mass of a neutron star." In: *A&A* 305, p. 871.
- Braiding, Catherine et al. (2018). "The Mopra Southern Galactic Plane CO Survey—Data Release 3". In: *Publ. Astron. Soc. Australia* 35, e029, e029. DOI: 10.1017/pasa.2018.18.
- Brand, J. and L. Blitz (1993). "The velocity field of the outer galaxy." In: *A&A* 275, pp. 67–90.
- Breuhaus, M., B. Reville, and J. A. Hinton (2022). "Pulsar wind nebula origin of the LHAASO-detected ultra-high energy  $\gamma$ -ray sources". In: *A&A* 660, A8, A8. DOI: 10.1051/0004-6361/202142097.
- Breuhaus, M. et al. (2021). "Ultra-high Energy Inverse Compton Emission from Galactic Electron Accelerators". In: *ApJ* 908.2, L49, p. L49. DOI: 10.3847/2041-8213/abe41a.
- Brisbois, Chad, Petra Huentemeyer, and HAWC Collaboration (2018). "Understanding the Very High Energy Emission from the possible PWN 2HWC J2019+367 with HAWC". In: *APS April Meeting Abstracts*. Vol. 2018. APS Meeting Abstracts, B17.003, B17.003.

- Brose, R., I. Sushch, and J. Mackey (2022). “Core-collapse supernovae in dense environments - particle acceleration and non-thermal emission”. In: *MNRAS* 516.1, pp. 492–505. DOI: [10.1093/mnras/stac2234](https://doi.org/10.1093/mnras/stac2234).
- Burgess, Daniel A. et al. (2022). “The Eel Pulsar Wind Nebula: A PeVatron-candidate Origin for HAWC J1826-128 and HESS J1826-130”. In: *ApJ* 930.2, 148, p. 148. DOI: [10.3847/1538-4357/ac650a](https://doi.org/10.3847/1538-4357/ac650a).
- Cao, Zhen et al. (2021). “Ultrahigh-energy photons up to 1.4 petaelectronvolts from 12  $\gamma$ -ray Galactic sources”. In: *Nature* 594.7861, pp. 33–36. DOI: [10.1038/s41586-021-03498-z](https://doi.org/10.1038/s41586-021-03498-z).
- Cao, Zhen et al. (2023). “Measurement of ultra-high-energy diffuse gamma-ray emission of the Galactic plane from 10 TeV to 1 PeV with LHAASO-KM2A”. In: *arXiv e-prints*, arXiv:2305.05372, arXiv:2305.05372. DOI: [10.48550/arXiv.2305.05372](https://doi.org/10.48550/arXiv.2305.05372).
- Caprioli, D. and A. Spitkovsky (2014). “Simulations of Ion Acceleration at Non-relativistic Shocks. I. Acceleration Efficiency”. In: *ApJ* 783.2, 91, p. 91. DOI: [10.1088/0004-637X/783/2/91](https://doi.org/10.1088/0004-637X/783/2/91).
- Caraveo, Patrizia A. (2014). “Gamma-Ray Pulsar Revolution”. In: *ARA&A* 52, pp. 211–250. DOI: [10.1146/annurev-astro-081913-035948](https://doi.org/10.1146/annurev-astro-081913-035948).
- Cesarsky, C. J. and H. J. Volk (1978). “Cosmic Ray Penetration into Molecular Clouds”. In: *A&A* 70, p. 367.
- Cheng, K. S., C. Ho, and M. Ruderman (1986). “Energetic Radiation from Rapidly Spinning Pulsars. I. Outer Magnetosphere Gaps”. In: *ApJ* 300, p. 500. DOI: [10.1086/163829](https://doi.org/10.1086/163829).
- Chevalier, Roger A. (1977). “Was SN 1054 a Type II Supernova?” In: *Supernovae*. Ed. by David N. Schramm. Dordrecht: Springer Netherlands, pp. 53–61.
- Clemens, D. P. (1985). “Massachusetts-Stony Brook Galactic plane CO survey: the galactic disk rotation curve.” In: *ApJ* 295, pp. 422–436. DOI: [10.1086/163386](https://doi.org/10.1086/163386).
- Cristofari, P, S Gabici, R Terrier, and T B Humensky (2018). “On the search for Galactic supernova remnant PeVatrons with current TeV instruments”. In: *MNRAS* 479.3, pp. 3415–3421. DOI: [10.1093/mnras/sty1589](https://doi.org/10.1093/mnras/sty1589). URL: <https://doi.org/10.1093/mnras/sty1589>.
- Cristofari, Pierre (2021). “The Hunt for Pevatrons: The Case of Supernova Remnants”. In: *Universe* 7.9, p. 324. DOI: [10.3390/universe7090324](https://doi.org/10.3390/universe7090324).
- Cristofari, Pierre, Pasquale Blasi, and Elena Amato (2020). “The low rate of Galactic pevatrons”. In: *AP* 123, p. 102492. DOI: <https://doi.org/10.1016/j.astropartphys.2020.102492>. URL: <https://www.sciencedirect.com/science/article/pii/S0927650520300645>.
- Crutcher, Richard M., Benjamin Wandelt, Carl Heiles, Edith Falgarone, and Thomas H. Troland (2010). “Magnetic Fields in Interstellar Clouds from Zeeman Observations: Inference of Total Field Strengths by Bayesian Analysis”. In: *ApJ* 725.1, pp. 466–479. DOI: [10.1088/0004-637X/725/1/466](https://doi.org/10.1088/0004-637X/725/1/466).
- CTA* (). URL: <https://www.cta-observatory.org/>.
- CTA Consortium et al. (2019). *Science with the Cherenkov Telescope Array*. DOI: [10.1142/10986](https://doi.org/10.1142/10986).
- de Oña Wilhelmi, Emma, Rubén López-Coto, Elena Amato, and Felix Aharonian (2022). “On the Potential of Bright, Young Pulsars to Power Ultrahigh Gamma-Ray Sources”. In: *ApJ* 930.1, L2, p. L2. DOI: [10.3847/2041-8213/ac66cf](https://doi.org/10.3847/2041-8213/ac66cf).
- Deil, C. et al. (2017). “Gammapy - A prototype for the CTA science tools”. In: *35th International Cosmic Ray Conference (ICRC2017)*. Vol. 301. International Cosmic Ray Conference, 766, p. 766.
- Draine, Bruce T. (2011). *Physics of the Interstellar and Intergalactic Medium*.

- Drury, L. Oc. (1983). "REVIEW ARTICLE: An introduction to the theory of diffusive shock acceleration of energetic particles in tenuous plasmas". In: *Reports on Progress in Physics* 46.8, pp. 973–1027. DOI: 10.1088/0034-4885/46/8/002.
- Duncan, Robert C. and Christopher Thompson (1992). "Formation of Very Strongly Magnetized Neutron Stars: Implications for Gamma-Ray Bursts". In: *ApJ* 392, p. L9. DOI: 10.1086/186413.
- (1996). "Magnetars". In: *High Velocity Neutron Stars*. Ed. by R. E. Rothschild and R. E. Lingenfelter. Vol. 366. American Institute of Physics Conference Series, pp. 111–117. DOI: 10.1063/1.50235.
- Duvidovich, L., E. Giacani, G. Castelletti, A. Petriella, and L. Supán (2019). "A new study towards PSR J1826-1334 and PSR J1826-1256 in the region of HESS J1825-137 and HESS J1826-130". In: *A&A* 623, A115, A115. DOI: 10.1051/0004-6361/201834590.
- Eather, R. H. (1980). *Majestic lights. The aurora in science, history, and the arts*.
- Evoli, Carmelo, Tim Linden, and Giovanni Mornlino (2018). "Self-generated cosmic-ray confinement in TeV halos: Implications for TeV  $\gamma$ -ray emission and the positron excess". In: *Phys. Rev. D* 98.6, 063017, p. 063017. DOI: 10.1103/PhysRevD.98.063017.
- Evoli, Carmelo et al. (2017). "Cosmic-ray propagation with DRAGON2: I. numerical solver and astrophysical ingredients". In: *J. Cosmology Astropart. Phys.* 2017.2, 015, p. 015. DOI: 10.1088/1475-7516/2017/02/015.
- Faraday, Michael (1846). "Experimental Researches in Electricity. Nineteenth Series". In: *Philosophical Transactions of the Royal Society of London Series I* 136, pp. 1–20.
- Fermi, Enrico (1949). "On the Origin of the Cosmic Radiation". In: *Physical Review* 75.8, pp. 1169–1174. DOI: 10.1103/PhysRev.75.1169.
- Ferrière, Katia M. (2001). "The interstellar environment of our galaxy". In: *Reviews of Modern Physics* 73.4, pp. 1031–1066. DOI: 10.1103/RevModPhys.73.1031.
- Fukui, Y. et al. (2006). "NANTEN2 Project: CO and CI Survey of the Southern Sky". In: *IAU Special Session* 1, 21, p. 21.
- Gabici, S., S. Casanova, F. A. Aharonian, and G. Rowell (2010). "Constraints on the cosmic ray diffusion coefficient in the W28 region from gamma-ray observations". In: *SF2A-2010: Proceedings of the Annual meeting of the French Society of Astronomy and Astrophysics*. Ed. by S. Boissier, M. Heydari-Malayeri, R. Samadi, and D. Valls-Gabaud, p. 313.
- Gabici, Stefano, Felix A. Aharonian, and Pasquale Blasi (2007). "Gamma rays from molecular clouds". In: *Ap&SS* 309.1-4, pp. 365–371. DOI: 10.1007/s10509-007-9427-6.
- Gabici, Stefano et al. (2019). "The origin of Galactic cosmic rays: Challenges to the standard paradigm". In: *International Journal of Modern Physics D* 28.15, 1930022–339, pp. 1930022–339. DOI: 10.1142/S0218271819300222.
- Gaensler, Bryan M. and Patrick O. Slane (2006). "The Evolution and Structure of Pulsar Wind Nebulae". In: *ARA&A* 44.1, pp. 17–47. DOI: 10.1146/annurev.astro.44.051905.092528.
- Gallant, Yves A. and Jonathan Arons (1994). "Structure of Relativistic Shocks in Pulsar Winds: A Model of the Wisps in the Crab Nebula". In: *ApJ* 435, p. 230. DOI: 10.1086/174810.
- Gallant, Yves A., Masahiro Hoshino, A. B. Langdon, Jonathan Arons, and Claire E. Max (1992). "Relativistic, Perpendicular Shocks in Electron-Positron Plasmas". In: *ApJ* 391, p. 73. DOI: 10.1086/171326.
- Gelfand, Joseph D., Patrick O. Slane, and Weiqun Zhang (2009). "A Dynamical Model for the Evolution of a Pulsar Wind Nebula Inside a Nonradiative Supernova Remnant". In: *ApJ* 703.2, pp. 2051–2067. DOI: 10.1088/0004-637X/703/2/2051.

- Giacinti, G. et al. (2020). “Halo fraction in TeV-bright pulsar wind nebulae”. In: *A&A* 636, A113, A113. DOI: 10.1051/0004-6361/201936505.
- Giuliani, A. et al. (2010). “AGILE detection of GeV  $\gamma$ -ray emission from the SNR W28”. In: *A&A* 516, L11, p. L11. DOI: 10.1051/0004-6361/201014256.
- Gold, T. (1968). “Rotating Neutron Stars as the Origin of the Pulsating Radio Sources”. In: *Nature* 218.5143, pp. 731–732. DOI: 10.1038/218731a0.
- Goldreich, Peter and William H. Julian (1969). “Pulsar Electrodynamics”. In: *ApJ* 157, p. 869. DOI: 10.1086/150119.
- Gould, Robert J. (1965). “High-Energy Photons from the Compton-Synchrotron Process in the Crab Nebula”. In: *Phys. Rev. Lett.* 15.14, pp. 577–579. DOI: 10.1103/PhysRevLett.15.577.
- Greisen, Kenneth (1966). “End to the Cosmic-Ray Spectrum?” In: *Phys. Rev. Lett.* 16.17, pp. 748–750. DOI: 10.1103/PhysRevLett.16.748.
- Griffeth Stone, Alice et al. (2021). “Type Ia Supernova Models: Asymmetric Remnants and Supernova Remnant G1.9+0.3”. In: *ApJ* 923.2, 233, p. 233. DOI: 10.3847/1538-4357/ac300f.
- Grindlay, J. E., H. F. Helmken, R. H. Brown, J. Davis, and L. R. Allen (1975). “Evidence for the detection of gamma rays from Centaurus A at  $E_{gamma} \geq 3 \times 10^{11}$ eV.” In: *ApJ* 197, pp. L9–L12. DOI: 10.1086/181764.
- Haensel, P., A. Y. Potekhin, and D. G. Yakovlev (2007). *Neutron Stars 1 : Equation of State and Structure*. Vol. 326.
- Han, J. L., R. N. Manchester, A. G. Lyne, G. J. Qiao, and W. van Straten (2006). “Pulsar Rotation Measures and the Large-Scale Structure of the Galactic Magnetic Field”. In: *ApJ* 642.2, pp. 868–881. DOI: 10.1086/501444.
- HAWC* (). URL: <https://www.hawc-observatory.org/>.
- Heitler, W. (1954). *Quantum theory of radiation*.
- Helder, E. A. et al. (2012). “Observational Signatures of Particle Acceleration in Supernova Remnants”. In: *Space Sci. Rev.* 173.1-4, pp. 369–431. DOI: 10.1007/s11214-012-9919-8.
- HESS* (). URL: <https://www.mpi-hd.mpg.de/hfm/HESS/>.
- Hess, Victor F (1912). “Observations in low level radiation during seven free balloon flights”. In: *Phys. Zeit* 13, pp. 1084–1091.
- HESS Collaboration et al. (2016). “Acceleration of petaelectronvolt protons in the Galactic Centre”. In: *Nature* 531.7595, pp. 476–479. DOI: 10.1038/nature17147.
- H.E.S.S. Collaboration et al. (2018a). “The H.E.S.S. Galactic plane survey”. In: *A&A* 612, A1, A1. DOI: 10.1051/0004-6361/201732098.
- H.E.S.S. Collaboration et al. (2018b). “The population of TeV pulsar wind nebulae in the H.E.S.S. Galactic Plane Survey”. In: *A&A* 612, A2, A2. DOI: 10.1051/0004-6361/201629377.
- H.E.S.S. Collaboration et al. (2019). “Particle transport within the pulsar wind nebula HESS J1825-137”. In: *A&A* 621, A116, A116. DOI: 10.1051/0004-6361/201834335.
- H.E.S.S. Collaboration et al. (2020). “An extreme particle accelerator in the Galactic plane: HESS J1826-130”. In: *A&A* 644, A112, A112. DOI: 10.1051/0004-6361/202038851.
- Hewish, A., S. J. Bell, J. D. H. Pilkington, P. F. Scott, and R. A. Collins (1968). “Observation of a Rapidly Pulsating Radio Source”. In: *Nature* 217.5130, pp. 709–713. DOI: 10.1038/217709a0.
- Hillas, A. M. (1984). “The Origin of Ultra-High-Energy Cosmic Rays”. In: *ARA&A* 22, pp. 425–444. DOI: 10.1146/annurev.aa.22.090184.002233.

- (1985). “Cerenkov Light Images of EAS Produced by Primary Gamma Rays and by Nuclei”. In: *19th International Cosmic Ray Conference (ICRC19), Volume 3*. Vol. 3. International Cosmic Ray Conference, p. 445.
- Hinton, J. A. and W. Hofmann (2009). “Teraelectronvolt Astronomy”. In: *ARA&A* 47.1, pp. 523–565. DOI: [10.1146/annurev-astro-082708-101816](https://doi.org/10.1146/annurev-astro-082708-101816).
- Ikeuchi, S. (1998). “Evolution of Evolution of Superbubbles”. In: *IAU Colloq. 166: The Local Bubble and Beyond*. Ed. by Dieter Breitschwerdt, Michael J. Freyberg, and Joachim Truemper. Vol. 506, pp. 399–407.
- Isaacson, Eugene (1966). *Analysis of numerical methods*. eng. New York: Wiley.
- Jager, Ocker C. de and Arache Djannati-Ataï (2009). “Implications of HESS Observations of Pulsar”. In: *Neutron Stars and Pulsars*. Ed. by Werner Becker. Berlin, Heidelberg: Springer Berlin Heidelberg, pp. 451–479. DOI: [10.1007/978-3-540-76965-1\\_17](https://doi.org/10.1007/978-3-540-76965-1_17). URL: [https://doi.org/10.1007/978-3-540-76965-1\\_17](https://doi.org/10.1007/978-3-540-76965-1_17).
- Kafexhiu, Ervin, Felix Aharonian, Andrew M. Taylor, and Gabriela S. Vila (2014). “Parametrization of gamma-ray production cross sections for p p interactions in a broad proton energy range from the kinematic threshold to PeV energies”. In: *Phys. Rev. D* 90.12, 123014, p. 123014. DOI: [10.1103/PhysRevD.90.123014](https://doi.org/10.1103/PhysRevD.90.123014).
- Kawamura, Akiko et al. (2009). “THE SECOND SURVEY OF THE MOLECULAR CLOUDS IN THE LARGE MAGELLANIC CLOUD BY NANTEN. II. STAR FORMATION”. In: *A&AS* 184.1, p. 1. DOI: [10.1088/0067-0049/184/1/1](https://doi.org/10.1088/0067-0049/184/1/1). URL: <https://dx.doi.org/10.1088/0067-0049/184/1/1>.
- Kennel, C. F. and F. V. Coroniti (1984). “Confinement of the Crab pulsar’s wind by its supernova remnant.” In: *ApJ* 283, pp. 694–709. DOI: [10.1086/162356](https://doi.org/10.1086/162356).
- Kissmann, R. (2014). “PICARD: A novel code for the Galactic Cosmic Ray propagation problem”. In: *Astroparticle Physics* 55, pp. 37–50. DOI: [10.1016/j.astropartphys.2014.02.002](https://doi.org/10.1016/j.astropartphys.2014.02.002).
- Kolb, Christopher, John Blondin, Patrick Slane, and Tea Temim (2017). “Evolution of a Pulsar Wind Nebula within a Composite Supernova Remnant”. In: *ApJ* 844.1, 1, p. 1. DOI: [10.3847/1538-4357/aa75ce](https://doi.org/10.3847/1538-4357/aa75ce).
- Komissarov, S. S. and Y. E. Lyubarsky (2004). “Synchrotron nebulae created by anisotropic magnetized pulsar winds”. In: *MNRAS* 349.3, pp. 779–792. DOI: [10.1111/j.1365-2966.2004.07597.x](https://doi.org/10.1111/j.1365-2966.2004.07597.x).
- Kothes, Roland, Wolfgang Reich, and Bülent Uyaniker (2006). “The Boomerang PWN G106.6+2.9 and the Magnetic Field Structure in Pulsar Wind Nebulae”. In: *ApJ* 638.1, pp. 225–233. DOI: [10.1086/498666](https://doi.org/10.1086/498666).
- Koyama, K. et al. (1995). “Evidence for shock acceleration of high-energy electrons in the supernova remnant SN1006”. In: *Nature* 378.6554, pp. 255–258. DOI: [10.1038/378255a0](https://doi.org/10.1038/378255a0).
- Krumholz, Mark R., Roland M. Crocker, and Matt L. Sampson (2022). “Cosmic ray interstellar propagation tool using Itô Calculus (CRITIC): software for simultaneous calculation of cosmic ray transport and observational signatures”. In: *MNRAS* 517.1, pp. 1355–1380. DOI: [10.1093/mnras/stac2712](https://doi.org/10.1093/mnras/stac2712).
- Krymskii, G. F. (1977). “A regular mechanism for the acceleration of charged particles on the front of a shock wave”. In: *Akademii Nauk SSSR Doklady* 234, pp. 1306–1308.
- Kuiper, L. and W. Hermsen (2015). “The soft  $\gamma$ -ray pulsar population: a high-energy overview”. In: *MNRAS* 449.4, pp. 3827–3866. DOI: [10.1093/mnras/stv426](https://doi.org/10.1093/mnras/stv426).
- Lacy, J. H., R. Knacke, T. R. Geballe, and A. T. Tokunaga (1994). “Detection of Absorption by H 2 in Molecular Clouds: A Direct Measurement of the H 2:CO Ratio”. In: *ApJ* 428, p. L69. DOI: [10.1086/187395](https://doi.org/10.1086/187395).

- Lagage, P. O. and C. J. Cesarsky (1983). “The maximum energy of cosmic rays accelerated by supernova shocks.” In: *A&A* 125, pp. 249–257.
- Lazarian, Alex, Siyao Xu, and Yue Hu (2023). “Cosmic ray propagation in turbulent magnetic fields”. In: *Frontiers in Astronomy and Space Sciences* 10, 1154760, p. 1154760. DOI: 10.3389/fspas.2023.1154760.
- Lemoine, Martin (2016). “A corrugated termination shock in pulsar wind nebulae?” In: *Journal of Plasma Physics* 82.4, 635820401, p. 635820401. DOI: 10.1017/S0022377816000659.
- Lemoine, Martin and Guy Pelletier (2010). “On electromagnetic instabilities at ultra-relativistic shock waves”. In: *MNRAS* 402.1, pp. 321–334. DOI: 10.1111/j.1365-2966.2009.15869.x.
- LHAASO (). URL: <http://english.ihep.ac.cn/lhaaso/>.
- LHAASO collaboration (2021). “Performance of LHAASO-WCDA and Observation of Crab Nebula as a Standard Candle”. In: *arXiv e-prints*, arXiv:2101.03508, arXiv:2101.03508. DOI: 10.48550/arXiv.2101.03508.
- Li, Hui and Yang Chen (2010). “ $\gamma$ -rays from molecular clouds illuminated by accumulated diffusive protons from supernova remnant W28”. In: *MNRAS* 409.1, pp. L35–L38. DOI: 10.1111/j.1745-3933.2010.00944.x.
- Li, Hui, Yang Chen, and Li Zhang (2010). “Lepto-hadronic origin of gamma-rays from the G54.1+0.3 pulsar wind nebula”. In: *MNRAS* 408.1, pp. L80–L84. DOI: 10.1111/j.1745-3933.2010.00934.x. URL: <https://doi.org/10.1111/j.1745-3933.2010.00934.x>.
- Liu, Ruo-Yu and Xiang-Yu Wang (2021). “PeV Emission of the Crab Nebula: Constraints on the Proton Content in Pulsar Wind and Implications”. In: *ApJ* 922.2, 221, p. 221. DOI: 10.3847/1538-4357/ac2ba0.
- Livingstone, Margaret A. et al. (2007). “New phase-coherent measurements of pulsar braking indices”. In: *Ap&SS* 308.1-4, pp. 317–323. DOI: 10.1007/s10509-007-9320-3.
- Longair, Malcolm S. (2011). *High Energy Astrophysics*.
- Lorimer, D. R. and M. Kramer (2012). *Handbook of Pulsar Astronomy*.
- Lyubarsky, Y. and J. G. Kirk (2001). “Reconnection in a Striped Pulsar Wind”. In: *ApJ* 547.1, pp. 437–448. DOI: 10.1086/318354.
- Lyubarsky, Y. E. (2003). “The termination shock in a striped pulsar wind”. In: *MNRAS* 345.1, pp. 153–160. DOI: 10.1046/j.1365-8711.2003.06927.x.
- Ma, Xin-Hua et al. (2022). “Chapter 1 LHAASO Instruments and Detector technology”. In: *Chinese Physics C* 46.3, 030001, p. 030001. DOI: 10.1088/1674-1137/ac3fa6.
- Malkov, M. A., P. H. Diamond, R. Z. Sagdeev, F. A. Aharonian, and I. V. Moskalenko (2013). “Analytic Solution for Self-regulated Collective Escape of Cosmic Rays from Their Acceleration Sites”. In: *ApJ* 768.1, 73, p. 73. DOI: 10.1088/0004-637X/768/1/73.
- Manchester, R. N., G. B. Hobbs, A. Teoh, and M. Hobbs (2005). “The Australia Telescope National Facility Pulsar Catalogue”. In: *aj* 129.4, pp. 1993–2006. DOI: 10.1086/428488.
- Manolakou, K., D. Horns, and J. G. Kirk (2007). “Spectral evolution of non-thermal electron distributions in intense radiation fields”. In: *A&A* 474, pp. 689–700. DOI: 10.1051/0004-6361:20078298.
- Matthews, J. (2005). “A Heitler model of extensive air showers”. In: *Astroparticle Physics* 22.5, pp. 387–397. DOI: <https://doi.org/10.1016/j.astropartphys.2004.09.003>. URL: <https://www.sciencedirect.com/science/article/pii/S0927650504001598>.

- Meli, A. and J. J. Quenby (2003). "Particle acceleration in ultra-relativistic oblique shock waves". In: *Astroparticle Physics* 19.5, pp. 649–666. DOI: 10.1016/S0927-6505(02)00257-8.
- Melrose, D. B. (1980). *Plasma astrophysics: Nonthermal processes in diffuse magnetized plasmas. Volume 2 - Astrophysical applications.*
- Meyer, D. M. A., N. Langer, J. Mackey, P. F. Velázquez, and A. Gusdorf (2015). "Asymmetric supernova remnants generated by Galactic, massive runaway stars". In: *MNRAS* 450.3, pp. 3080–3100. DOI: 10.1093/mnras/stv898.
- Michelson, P. F., W. B. Atwood, and S. Ritz (2010). "Fermi Gamma-ray Space Telescope: high-energy results from the first year". In: *Reports on Progress in Physics* 73.7, 074901, p. 074901. DOI: 10.1088/0034-4885/73/7/074901.
- Millikan, R. A. and G. Harvey Cameron (1926). "High Frequency Rays of Cosmic Origin III. Measurements in Snow-Fed Lakes at High Altitudes". In: *Physical Review* 28.5, pp. 851–868. DOI: 10.1103/PhysRev.28.851.
- Mills, B. Y., A. J. Turtle, A. G. Little, and J. M. Durdin (1984). "A new look at radio supernova remnants." In: *Australian Journal of Physics* 37, pp. 321–357. DOI: 10.1071/PH840321.
- Mizuno, A. and Y. Fukui (2004). "Physical properties of molecular clouds as revealed by NANTEN CO survey: from the galactic center to the galactic warp". In: *Milky Way Surveys: The Structure and Evolution of our Galaxy*. Ed. by Dan Clemens, Ronak Shah, and Teresa Brainerd. Vol. 317. Astronomical Society of the Pacific Conference Series, p. 59.
- Mizuno, Norikazu et al. (2001). "First Results of a CO Survey of the Small Magellanic Cloud with NANTEN". In: *PASJ* 53.6, pp. L45–L49. DOI: 10.1093/pasj/53.6.L45.
- Modern Physical Chemistry A Molecular Approach* (2000). eng. 1st ed. 2000. New York, NY: Springer US.
- Morrison, P. (1958). "On gamma-ray astronomy". In: *Il Nuovo Cimento* 7.6, pp. 858–865. DOI: 10.1007/BF02745590.
- Nava, L. and S. Gabici (2013). "Anisotropic cosmic ray diffusion and gamma-ray production close to supernova remnants, with an application to W28". In: *MNRAS* 429.2, pp. 1643–1651. DOI: 10.1093/mnras/sts450.
- Nava, L., S. Gabici, A. Marcowith, G. Morlino, and V. S. Ptuskin (2016). "Non-linear diffusion of cosmic rays escaping from supernova remnants - I. The effect of neutrals". In: *MNRAS* 461.4, pp. 3552–3562. DOI: 10.1093/mnras/stw1592.
- Ohira, Yutaka, Shota Kisaka, and Ryo Yamazaki (2018). "Pulsar Wind Nebulae inside Supernova Remnants as Cosmic-Ray PeVatrons". In: 478.1, pp. 926–931. DOI: 10.1093/mnras/sty1159.
- Ormes, J. F., M. E. Ozel, and D. J. Morris (1988). "On the High-Energy Gamma-Ray Signature of Cosmic-Ray Sources". In: *ApJ* 334, p. 722. DOI: 10.1086/166873.
- Parthasarathy, A. et al. (2019). "Timing of young radio pulsars - I. Timing noise, periodic modulation, and proper motion". In: *MNRAS* 489.3, pp. 3810–3826. DOI: 10.1093/mnras/stz2383.
- Parthasarathy, A. et al. (2020). "Timing of young radio pulsars - II. Braking indices and their interpretation". In: *MNRAS* 494.2, pp. 2012–2026. DOI: 10.1093/mnras/staa882.
- Patterson, J R and A M Hillas (1983). "The relation of the lateral distribution of Cerenkov light from cosmic-ray showers to the distance of maximum development". In: *Journal of Physics G: Nuclear Physics* 9.11, pp. 1433–1452. DOI: 10.1088/0305-4616/9/11/015. URL: <https://doi.org/10.1088/0305-4616/9/11/015>.

- Persic, Massimo, Paolo Salucci, and Fulvio Stel (1996). “The universal rotation curve of spiral galaxies — I. The dark matter connection”. In: *MNRAS* 281.1, pp. 27–47. DOI: [10.1093/mnras/278.1.27](https://doi.org/10.1093/mnras/278.1.27).
- Porter, T. A., G. Jóhannesson, and I. V. Moskalenko (2022). “The GALPROP Cosmic-ray Propagation and Nonthermal Emissions Framework: Release v57”. In: *ApJS* 262.1, 30, p. 30. DOI: [10.3847/1538-4365/ac80f6](https://doi.org/10.3847/1538-4365/ac80f6).
- Porth, Oliver, Serguei S. Komissarov, and Rony Keppens (2014). “Three-dimensional magnetohydrodynamic simulations of the Crab nebula”. In: *MNRAS* 438.1, pp. 278–306. DOI: [10.1093/mnras/stt2176](https://doi.org/10.1093/mnras/stt2176).
- Principe, G. et al. (2020). “Energy dependent morphology of the pulsar wind nebula HESS J1825-137 with Fermi-LAT”. In: *A&A* 640, A76, A76. DOI: [10.1051/0004-6361/202038375](https://doi.org/10.1051/0004-6361/202038375).
- Prosekin, A. Yu., S. R. Kelner, and F. A. Aharonian (2015). “Transition of propagation of relativistic particles from the ballistic to the diffusion regime”. In: *Phys. Rev. D* 92.8, 083003, p. 083003. DOI: [10.1103/PhysRevD.92.083003](https://doi.org/10.1103/PhysRevD.92.083003).
- Protheroe, R. J., J. Ott, R. D. Ekers, D. I. Jones, and R. M. Crocker (2008). “Interpretation of radio continuum and molecular line observations of Sgr B2: free-free and synchrotron emission, and implications for cosmic rays”. In: *MNRAS* 390.2, pp. 683–692. DOI: [10.1111/j.1365-2966.2008.13752.x](https://doi.org/10.1111/j.1365-2966.2008.13752.x).
- Rand, Richard J. and Shrinivas R. Kulkarni (1989). “The Local Galactic Magnetic Field”. In: *ApJ* 343, p. 760. DOI: [10.1086/167747](https://doi.org/10.1086/167747).
- Recchia, S. et al. (2021). “Do the Geminga, Monogem and PSR J0622+3749  $\gamma$ -ray halos imply slow diffusion around pulsars?” In: *Phys. Rev. D* 104.12, 123017, p. 123017. DOI: [10.1103/PhysRevD.104.123017](https://doi.org/10.1103/PhysRevD.104.123017).
- Rees, M. J. and J. E. Gunn (1974). “The origin of the magnetic field and relativistic particles in the Crab Nebula”. In: *MNRAS* 167, pp. 1–12. DOI: [10.1093/mnras/167.1.1](https://doi.org/10.1093/mnras/167.1.1).
- Reid, M. J. et al. (2014). “Trigonometric Parallaxes of High Mass Star Forming Regions: The Structure and Kinematics of the Milky Way”. In: *ApJ* 783.2, 130, p. 130. DOI: [10.1088/0004-637X/783/2/130](https://doi.org/10.1088/0004-637X/783/2/130).
- Reynolds, S. P. (2008). “Supernova remnants at high energy.” In: *ARA&A* 46, pp. 89–126. DOI: [10.1146/annurev.astro.46.060407.145237](https://doi.org/10.1146/annurev.astro.46.060407.145237).
- Reynolds, Stephen P., B. M. Gaensler, and Fabrizio Bocchino (2012). “Magnetic Fields in Supernova Remnants and Pulsar-Wind Nebulae”. In: *Space Sci. Rev.* 166.1-4, pp. 231–261. DOI: [10.1007/s11214-011-9775-y](https://doi.org/10.1007/s11214-011-9775-y).
- Reynolds, Stephen P. et al. (2008). “The Youngest Galactic Supernova Remnant: G1.9+0.3”. In: *ApJ* 680.1, p. L41. DOI: [10.1086/589570](https://doi.org/10.1086/589570).
- Roberts, Mallory S. E., E. V. Gotthelf, Jules P. Halpern, Crystal L. Brogan, and Scott M. Ransom (2007). “Recent Observations of EGRET Pulsar Wind Nebulae”. In: *WE-Heraeus Seminar on Neutron Stars and Pulsars 40 years after the Discovery*. Ed. by W. Becker and H. H. Huang, p. 24.
- Rutherford, E. and E. N. Da C. Andrade (1913). “The Reflection of  $\gamma$  Rays from Crystals”. In: *Nature* 92.2296, p. 267. DOI: [10.1038/092267a0](https://doi.org/10.1038/092267a0).
- Sampson, Matt L. et al. (2023). “Turbulent diffusion of streaming cosmic rays in compressible, partially ionized plasma”. In: *MNRAS* 519.1, pp. 1503–1525. DOI: [10.1093/mnras/stac3207](https://doi.org/10.1093/mnras/stac3207).
- Sanders, D. B., N. Z. Scoville, and P. M. Solomon (1985). “Giant molecular clouds in the galaxy. II. Characteristics of discrete features.” In: *ApJ* 289, pp. 373–387. DOI: [10.1086/162897](https://doi.org/10.1086/162897).

- Sandström, Arne Eld, Eric Dyring, and Stig Lindgren (1960). “Dependence on Latitude of the Amplitude of the Diurnal Variation of Cosmic Rays”. In: *Nature* 187.4743, pp. 1099–1100. DOI: 10.1038/1871099b0.
- Schlickeiser, Reinhard (2002). *Cosmic Ray Astrophysics*.
- Schneider, A. S., C. J. Horowitz, J. Hughto, and D. K. Berry (2013). “Nuclear “pasta” formation”. In: *Phys. Rev. C* 88 (6), p. 065807. DOI: 10.1103/PhysRevC.88.065807. URL: <https://link.aps.org/doi/10.1103/PhysRevC.88.065807>.
- Schroeder, Frank et al. (2019). “High-Energy Galactic Cosmic Rays”. In: *BAAS* 51.3, 131, p. 131.
- Sedov, L. I. (Leonid Ivanovich) (1959). *Similarity and dimensional methods in mechanics*. eng. New York: Academic Press.
- Sironi, L., U. Keshet, and M. Lemoine (2015). “Relativistic Shocks: Particle Acceleration and Magnetization”. In: *Space Sci. Rev.* 191.1-4, pp. 519–544. DOI: 10.1007/s11214-015-0181-8.
- Skilling, J. (1975). “Cosmic ray streaming - I. Effect of Alfvén waves on particles.” In: *MNRAS* 172, pp. 557–566. DOI: 10.1093/mnras/172.3.557.
- Slane, Patrick (2017). “Pulsar Wind Nebulae”. In: *Handbook of Supernovae*. Ed. by Athem W. Alsabti and Paul Murdin. Cham: Springer International Publishing, pp. 2159–2179. DOI: 10.1007/978-3-319-21846-5\_95. URL: [https://doi.org/10.1007/978-3-319-21846-5\\_95](https://doi.org/10.1007/978-3-319-21846-5_95).
- Slane, Patrick, Andrei Bykov, Donald C. Ellison, Gloria Dubner, and Daniel Castro (2015). “Supernova Remnants Interacting with Molecular Clouds: X-Ray and Gamma-Ray Signatures”. In: *Space Sci. Rev.* 188.1-4, pp. 187–210. DOI: 10.1007/s11214-014-0062-6.
- Stanev, Todor. (2010). *High Energy Cosmic Rays*. eng. 2nd ed. 2010. Astronomy and Planetary Sciences. Berlin, Heidelberg: Springer Berlin Heidelberg.
- “Stochastic Partial Differential Equations” (2014). eng. In: *Stochastic Numerical Methods*. Weinheim, Germany: Wiley-VCH Verlag GmbH & Co. KGaA, pp. 287–326.
- Strong, A. W., I. V. Moskalenko, O. Reimer, S. Digel, and R. Diehl (2004). “The distribution of cosmic-ray sources in the Galaxy,  $\gamma$ -rays and the gradient in the CO-to-H<sub>2</sub> relation”. In: *A&A* 422, pp. L47–L50. DOI: 10.1051/0004-6361:20040172.
- Strong, Andrew W., Igor V. Moskalenko, and Vladimir S. Ptuskin (2007). “Cosmic-Ray Propagation and Interactions in the Galaxy”. In: *Annual Review of Nuclear and Particle Science* 57.1, pp. 285–327. DOI: 10.1146/annurev.nucl.57.090506.123011.
- Stupar, M., Q. A. Parker, and M. D. Filipović (2008). “Newly confirmed and candidate Galactic SNRs uncovered from the AAO/UKST H $\alpha$  survey”. In: *MNRAS* 390.3, pp. 1037–1054. DOI: 10.1111/j.1365-2966.2008.13761.x.
- Sturrock, P. A. (1971). “A Model of Pulsars”. In: *ApJ* 164, p. 529. DOI: 10.1086/150865.
- Tammann, G. A., W. Loeffler, and A. Schroeder (1994). “The Galactic Supernova Rate”. In: *ApJS* 92, p. 487. DOI: 10.1086/192002.
- Tanaka, Shuta J. and Fumio Takahara (2010). “A Model of the Spectral Evolution of Pulsar Wind Nebulae”. In: *ApJ* 715.2, pp. 1248–1257. DOI: 10.1088/0004-637X/715/2/1248.
- The Fermi Gamma-ray Space Telescope* (n.d.). URL: <https://fermi.gsfc.nasa.gov/>.
- The LHAASO Collaboration et al. (2021). “Peta-electron volt gamma-ray emission from the Crab Nebula”. In: *Science* 373.6553, pp. 425–430. DOI: 10.1126/science.abg5137. URL: <https://www.science.org/doi/abs/10.1126/science.abg5137>.
- The Magic Telescopes* (). URL: <https://magic.mpp.mpg.de/>.
- The Pierre Auger Collaboration et al. (2022). “A Catalog of the Highest-Energy Cosmic Rays Recorded During Phase I of Operation of the Pierre Auger Observatory”. In:

- J. Cosmology Astropart. Phys.*, arXiv:2211.16020, arXiv:2211.16020. DOI: 10.48550/arXiv.2211.16020.
- Thompson, Christopher and Robert Duncan (1993). “Neutron star dynamos and the origins of pulsar magnetism”. In: *ApJ* 408. DOI: 10.1086/172580.
- Thoudam, S. et al. (2016). “Cosmic-ray energy spectrum and composition up to the ankle: the case for a second Galactic component”. In: *A&A* 595, A33, A33. DOI: 10.1051/0004-6361/201628894.
- Torres, D. F., A. Cillis, J. Martín, and E. de Oña Wilhelmi (2014). “Time-dependent modeling of TeV-detected, young pulsar wind nebulae”. In: *Journal of High Energy Astrophysics* 1, pp. 31–62. DOI: 10.1016/j.jheap.2014.02.00110.48550/arXiv.1402.5485.
- Truelove, J. Kelly and Christopher F. McKee (1999). “Evolution of Nonradiative Supernova Remnants”. In: *ApJS* 120.2, pp. 299–326. DOI: 10.1086/313176.
- Uchiyama, Hideki, Hironori Matsumoto, Takeshi Go Tsuru, Katsuji Koyama, and Aya Bamba (2009). “Suzaku Observation of HESS J1825-137: Discovery of Largely-Extended X-Rays from PSR J1826-1334”. In: *PASJ* 61, S189. DOI: 10.1093/pasj/61.sp1.S189.
- van der Swaluw, E., A. Achterberg, Y. A. Gallant, and G. Tóth (2001). “Pulsar wind nebulae in supernova remnants. Spherically symmetric hydrodynamical simulations”. In: *A&A* 380, pp. 309–317. DOI: 10.1051/0004-6361:20011437.
- Van Etten, Adam and Roger W. Romani (2011). “Multi-zone Modeling of the Pulsar Wind Nebula HESS J1825-137”. In: *ApJ* 742.2, 62, p. 62. DOI: 10.1088/0004-637X/742/2/62.
- Vecchiotti, V., F. Zuccarini, F. L. Villante, and G. Pagliaroli (2022). “Unresolved Sources Naturally Contribute to PeV Gamma-Ray Diffuse Emission Observed by Tibet AS $\gamma$ ”. In: *ApJ* 928.1, 19, p. 19. DOI: 10.3847/1538-4357/ac4df4.
- VERITAS* (). URL: <https://veritas.sao.arizona.edu/>.
- Vieu, T., B. Reville, and F. Aharonian (2022). “Can superbubbles accelerate ultrahigh energy protons?” In: *MNRAS* 515.2, pp. 2256–2265. DOI: 10.1093/mnras/stac1901.
- Vincent, P. (2005). “H.E.S.S. Phase II”. In: *29th International Cosmic Ray Conference (ICRC29)*, Volume 5. Vol. 5. International Cosmic Ray Conference, p. 163.
- Vink, Jacco (2020). *Physics and evolution of supernova remnants*. eng. 1st ed. 2020. Astronomy and astrophysics library. Cham, Switzerland: Springer.
- Voisin, F. et al. (2016). “ISM gas studies towards the TeV PWN HESS J1825-137 and northern region”. In: *MNRAS* 458.3, pp. 2813–2835. DOI: 10.1093/mnras/stw473.
- Voisin, Fabien (2017). “Environment Studies of Pulsar Wind Nebulae and Their Interactions with the Interstellar Medium”. PhD thesis. University of Adelaide.
- Völk, Heinrich J. and Konrad Bernlöhr (2009). “Imaging very high energy gamma-ray telescopes”. In: *Experimental Astronomy* 25.1-3, pp. 173–191. DOI: 10.1007/s10686-009-9151-z.
- Wakely, S. P. and D. Horan (2008). “TeVCat: An online catalog for Very High Energy Gamma-Ray Astronomy”. In: *International Cosmic Ray Conference* 3, pp. 1341–1344.
- Weekes, T. C. et al. (1989). “Observation of TeV Gamma Rays from the Crab Nebula Using the Atmospheric Cerenkov Imaging Technique”. In: *ApJ* 342, p. 379. DOI: 10.1086/167599.
- Wilson, Thomas L. (2013). *Tools of Radio Astronomy*. eng. 6th ed. 2013. Astronomy and Astrophysics Library. Berlin, Heidelberg: Springer Berlin Heidelberg.
- Woltjer, L. (1964). “X-Rays and Type I Supernova Remnants.” In: *ApJ* 140, pp. 1309–1313. DOI: 10.1086/148028.
- (1972). “Supernova Remnants”. In: *ARA&A* 10, p. 129. DOI: 10.1146/annurev.aa.10.090172.001021.

- Xin, Yuliang, Houdun Zeng, Siming Liu, Yizhong Fan, and Daming Wei (2019). “VER J2227+608: A Hadronic PeVatron Pulsar Wind Nebula?” In: *ApJ* 885.2, 162, p. 162. doi: [10.3847/1538-4357/ab48ee](https://doi.org/10.3847/1538-4357/ab48ee).
- Yao, J. M., R. N. Manchester, and N. Wang (2017). “A New Electron-density Model for Estimation of Pulsar and FRB Distances”. In: *ApJ* 835.1, 29, p. 29. doi: [10.3847/1538-4357/835/1/29](https://doi.org/10.3847/1538-4357/835/1/29).
- Zatsepin, G. T. and V. A. Kuz'min (1966). “Upper Limit of the Spectrum of Cosmic Rays”. In: *Soviet Journal of Experimental and Theoretical Physics Letters* 4, p. 78.
- Zavlin, V. E. and G. G. Pavlov (2002). “Modeling Neutron Star Atmospheres”. In: *Neutron Stars, Pulsars, and Supernova Remnants*. Ed. by W. Becker, H. Lesch, and J. Trümper, p. 263.
- Zettili, Noureddine. (2001). *Quantum mechanics : concepts and applications*. eng. Chichester ; Wiley.